THE UNIVERSITY
of ADELAIDE

Understanding Marine Magnetotellurics

by

Jake MacFarlane

In fulfilment of the requirements for the degree of

Doctor of Philosophy

April 2022

Department of Earth Sciences

School of Physical Sciences

The University of Adelaide

Dedicated to those who suffer from anxiety and depression.

Contents

Declaration **xi**

Acknowledgements **xiii**

Abstract **xv**

1 Introduction **1**

2 The Oceanic Magnetotelluric Method **7**
2.1 Expanding Maxwell's Equations 8
2.2 EM Fields In The Earth's Atmosphere 10
2.3 EM Induction In A Homogeneous Earth 10
2.3.1 Skin Depth 11
2.4 EM Induction In A Layered Earth 12
2.4.1 EM Induction in a 2D Earth 14
2.5 EM Induction In A 3-Dimensional Earth 15
2.6 Source Fields 15
2.7 EM Induction In The Earth's Oceans 16
2.8 Conclusions 21

3 An Oceanic Mantle Electrical Conductivity Reference Model **23**
3.1 Introduction 23
3.2 Bulk Conductivity 28
3.2.1 Temperature (T) 31
3.2.2 Matrix Conductivity (σ_m) 31
3.2.3 Melt Conductivity (σ_{SiO_2}, σ_{CO_2}) & Melt Fraction (F) 33
3.3 Results 37
3.4 Discussion 38
3.5 Conclusions 42

4 Hybrid Oceanic-Continental MT Response **43**
4.1 APPLE Experiment . . . 45
4.1.1 Data Collection . . . 46
4.2 Tidal Signal . . . 49
4.3 Solar Quiet Daily Variation . . . 49
4.4 Fast Fourier Transformation . . . 60
4.5 Signal-To-Noise Ratio . . . 60
4.6 Magnetotelluric Impedance . . . 73
4.7 Discussion . . . 89
4.8 Conclusions . . . 104

5 Insights On The Oceanic Upper Mantle **105**
5.1 3-Dimensional Continental Inversion Model . . . 107
5.2 2-Dimensional Forward Modelling . . . 127
5.3 Reference Model . . . 130
5.4 Discussion . . . 135
5.5 Conclusions . . . 139

6 Summary and Conclusion **153**
6.1 An Oceanic Mantle Electrical Conductivity Reference Model . . . 153
6.2 A Hybrid Oceanic-Continental MT Response Approach . . . 154
6.3 Insights On The Oceanic Upper Mantle . . . 154

A Reference Model Electrical structure Versus Depth **157**

B 3-Dimensional Inversion Versus Depth **179**

Bibliography **194**

List of Tables

3.1 Pacific Ocean Survey Data 27

4.1 APPLE Survey Data 49

A.1 Reference Model Electrical Structure Versus Depth 158

B.1 3-Dimensional Inversion Resistivity Versus Depth 180

List of Figures

1.1 Pacific Ocean Station Map 2
1.2 Oceanic Lithosphere Temperature Pseudosection 4
1.3 Pacific Ocean Sea Floor Age 5

2.1 Global Skin-Depth Period 17
2.2 Coast Effect Singularity Peak 18
2.3 Thin-Sheet Schematic 19
2.4 Adjustment Distance 20
2.5 Global Adjustment Distance Map 22

3.1 Pacific Ocean Sea Floor Age 25
3.2 Pacific Ocean Station Map 26
3.3 Reference Model Schematic Diagram 28
3.4 Model Conductivity Pseudosection 29
3.5 Model Volatile Mass Fraction Distribution 30
3.6 Model Temperature Profile 32
3.7 Model Matrix Phase Proportion 34
3.8 Model Melt Fraction 36
3.9 Pacific Ocean Hashin-Shtrikman Limits 39
3.10 Pacific Ocean MT Conductance 40

4.1 Antarctica, Canada, North America, and South America Bathymetry Location Map 44
4.2 APPLE CSEM Inversion Model 45
4.3 APPLE Bathymetry Location Map 47
4.4 APPLE Cluster Bathymetry Location Map 48
4.5 Rhonda Linear Periodogram - E_x and E_y With Tides 50
4.6 Rhonda Linear Periodogram - B_x and B_y With Tides 51
4.7 Opus Linear Periodogram - E_x and E_y With Tides 52
4.8 Opus Linear Periodogram - B_x and B_y With Tides 53
4.9 sDome Linear Periodogram - B_x and B_y 54

4.10 Tidal Signal - Ex . . . 55
4.11 Tidal Signal - Ey . . . 56
4.12 Tidal Signal - Bx . . . 57
4.13 Tidal Signal - By . . . 58
4.14 Tidal Signal - sDome . . . 59
4.15 Rhonda Logarithmic Periodogram - E_x and E_y . . . 61
4.16 Rhonda Logarithmic Periodogram - B_x and B_y . . . 62
4.17 Igor Logarithmic Periodogram - E_x and E_y . . . 63
4.18 Igor Logarithmic Periodogram - B_x and B_y . . . 64
4.19 Trevor Logarithmic Periodogram - E_x and E_y . . . 65
4.20 Trevor Logarithmic Periodogram - B_x and B_y . . . 66
4.21 Ulysses Logarithmic Periodogram - E_x and E_y . . . 67
4.22 Ulysses Logarithmic Periodogram - B_x and B_y . . . 68
4.23 Opus Logarithmic Periodogram - E_x and E_y . . . 69
4.24 Opus Logarithmic Periodogram - B_x and B_y . . . 70
4.25 Kermit Logarithmic Periodogram - E_x and E_y . . . 71
4.26 sDome Logarithmic Periodogram - B_x and B_y . . . 72
4.27 Rhonda Time Series . . . 74
4.28 Igor Time Series . . . 75
4.29 Trevor Time Series . . . 76
4.30 Kermit Time Series . . . 77
4.31 Ulysses Time Series . . . 78
4.32 Opus Time Series . . . 79
4.33 Impedance Comparison - Z_{XX} (Cluster) . . . 80
4.34 Impedance Comparison - Z_{XX} (Transect) . . . 81
4.35 Impedance Comparison - Z_{YY} (Cluster) . . . 82
4.36 Impedance Comparison - Z_{YY} (Transect) . . . 83
4.37 ρ_{app} & Φ Comparison - Z_{XX} (Cluster) . . . 84
4.38 ρ_{app} & Φ Comparison - Z_{XX} (Transect) . . . 85
4.39 ρ_{app} & Φ Comparison - Z_{YY} (Cluster) . . . 86
4.40 ρ_{app} & Φ Comparison - Z_{YY} (Transect) . . . 87
4.41 Impedance Comparison - Z_{XY} (Cluster) . . . 90
4.42 Impedance Comparison - Z_{XY} (Transect) . . . 91
4.43 Impedance Comparison - Z_{YX} (Cluster) . . . 92
4.44 Impedance Comparison - Z_{YX} (Transect) . . . 93
4.45 ρ_{app} & Φ Comparison - Z_{XY} (Cluster) . . . 94
4.46 ρ_{app} & Φ Comparison - Z_{XY} (Transect) . . . 95
4.47 ρ_{app} & Φ Comparison - Z_{YX} (Cluster) . . . 96
4.48 ρ_{app} & Φ Comparison - Z_{YX} (Transect) . . . 97
4.49 Rhonda Coherence . . . 98

4.50 Igor Coherence . . . 99
4.51 Trevor Coherence . . . 100
4.52 Kermit Coherence . . . 101
4.53 Ulysses Coherence . . . 102
4.54 Opus Coherence . . . 103

5.1 Location Map For APPLE, USArray, and CONUS data . . . 106
5.2 Californian Phase Tensors (1,000 s) . . . 108
5.3 Californian Phase Tensors (3,000 s) . . . 109
5.4 Californian Phase Tensors (7,000 s) . . . 110
5.5 Californian Phase Tensors (30,000 s) . . . 111
5.6 3D Inversion Mesh . . . 113
5.7 California 3D Inversion - Horizontal Slice (1 km to 10 km) . . . 114
5.8 California 3D Inversion - Horizontal Slice (20 km to 200 km) . . . 115
5.9 California 3D Inversion - Cross-Section Location Map . . . 116
5.10 California 3D Inversion - Northern Cross-Section . . . 117
5.11 California 3D Inversion - Central Cross-Section . . . 118
5.12 California 3D Inversion - Southern Cross-Section . . . 119
5.13 Great Valley Sequence . . . 120
5.14 California Depth to the Mohorovičić discontinuity and LAB . . . 121
5.15 Continental Resistivity Versus Depth . . . 122
5.16 3D Inversion - Apparent Resistivity Invariant (100 s and 300 s) . . . 123
5.17 3D Inversion - Apparent Resistivity Invariant (1,000 s and 3,000 s) . . . 124
5.18 3D Inversion - Phase Invariant (100 s and 300 s) . . . 125
5.19 3D Inversion - Phase Invariant (1,000 s and 3,000 s) . . . 126
5.20 APPLE Bathymetry Location Map . . . 128
5.21 APPLE Cluster Bathymetry Profile . . . 131
5.22 APPLE Transect Bathymetry Profile . . . 132
5.23 APPLE Ocean Age Map . . . 133
5.24 APPLE Melt Fraction . . . 134
5.25 APPLE Conductivity Hashin-Shtrikman Limits . . . 136
5.26 APPLE CSEM Inversion Model . . . 137
5.27 APPLE Forward Model . . . 138
5.28 Rhonda TE-Mode Results . . . 140
5.29 Rhonda TM-Mode Results . . . 141
5.30 Igor TE-Mode Results . . . 142
5.31 Igor TM-Mode Results . . . 143
5.32 Trevor TE-Mode Results . . . 144
5.33 Trevor TM-Mode Results . . . 145
5.34 Kermit TE-Mode Results . . . 146
5.35 Kermit TM-Mode Results . . . 147

5.36 Ulysses TE-Mode Results 148
5.37 Ulysses TM-Mode Results 149
5.38 Opus TE-Mode Results 150
5.39 Opus TM-Mode Results 151

Declaration

I certify that this work contains no material which has been accepted for the award of any other degree or diploma in my name, in any university or other tertiary institution and, to the best of my knowledge and belief, contains no material previously published or written by another person, except where due reference has been made in the text. In addition, I certify that no part of this work will, in the future, be used in a submission in my name, for any other degree or diploma in any university or other tertiary institution without the prior approval of the University of Adelaide and where applicable, any partner institution responsible for the joint-award of this degree.

I give permission for the digital version of my thesis to be made available on the web, via the University's digital research repository, the Library Search and also through web search engines, unless permission has been granted by the University to restrict access for a period of time.

I acknowledge the support I have received for my research through the provision of an Australian Government Research Training Program Scholarship.

Jake MacFarlane 20/4/2022

Acknowledgements

First, I would like to thank everyone who graciously provided the data they had collected from the Pacific Ocean. Their contributions were integral to my analysis. Similarly, I would also like to thank everyone who has worked with the APPLE data over the past two decades. Their indirect contribution to this project is greatly appreciated.

In addition, I would like to thank the staff at both the SCRIPPS Institution of Oceanography (San Diego, California) and the Institute of Geophysics (Boční II, Prague). Their hospitality made my trips abroad considerably less stressful.

I am thankful for the patience and understanding of my supervisors Graham Heinson, Stephan Thiel, and Derrick Hasterok. Without your help I would have given up on this project years ago. I would also like to thank Kiyoshi Baba and Josef Pek for their invaluable guidance throughout my project.

I would like to extend my most humble gratitude to Goran Boren, Yohannes Lemma Didana, Ben Kay, Paul Soeffky, John Souders, and Nigel Rees. Their kind nature has been a constant source of encouragement. In addition, thank you to Dennis Conway and Ben Kay for reviewing my thesis.

I would also like to thank my partner Robyn Williamson and our two cats named Cuddlebug and Dewdrop. I love you all dearly. Furthermore, I thank the friends and family who have followed me through this journey.

Finally, I would like to thank Samuel Jennings for sharing this thesis template. Figures were generated using GeoTools (CGG Multi-Physics Imaging, Milan), GMT 5 (Wessel et al., 2013), MatLab (MATLAB, 2019).

Abstract

The theory of plate tectonics proposes that the Earth's lithosphere is separated into rigid plates which are capable of motion through interactions with the underlying asthenosphere. Following its adoption in the 1960's, it has become the prominent theory used to understand geodynamic processes within the Earth. The mechanisms of tectonism are of particular interest due to their implications regarding the formation of economic resources. Despite numerous studies attempting to characterise these mechanisms, the lithosphere-asthenosphere rheological contrast (LARC) remains an enigmatic component of plate tectonic theory.

The magnetotelluric (MT) method is of particular interest when investigating the upper mantle as it is primarily sensitive to electrical conductivity. From electrical conductivity, conclusions regarding the temperature, pressure, physical and chemical state, porosity, and permeability of rocks can be inferred. This thesis examines laboratory conductivity measurements with ocean-bottom MT data collected from the Pacific Ocean. From these data, I create an upper mantle reference model for electrical conductivity and propose a hybrid MT impedance which improves the bandwidth and confidence intervals of ocean-bottom MT data.

Between 50 km and 100 km depth, MT data predicts variable electrical conductivity structures. My reference model is able to encapsulate this variability with a function which varies according to hydration, partial melt, and the age of the overlying oceanic lithospheric. For 200 km to 400 km, the hydrated end-member of this reference model predicts the convergence of conductivity structures with increasing depth observable in published conductivity structures. As such, this reference model constrains the presence of hydration and partial melt within the LARC for a range of lithospheric ages and is a representative model of the Earth's oceanic lithosphere and asthenosphere.

Following an analysis of ocean-bottom EM field observations, I observe the attenuation of magnetic field variations by the conductive ocean water. This attenuation results in MT impedances which are difficult to interpret using available modelling algorithms. In contrast, the calculation of a hybrid MT impedance using ocean-bottom electric and continental magnetic fields is observed to improve the signal-to-noise ratio. This improved signal-to-noise ratio extends the usable bandwidth of ocean-bottom MT data from just over one decade to approximately four decades. It is important to note that this impedance represents the normalisation of ocean-bottom electric fields using

continental magnetic fields. As a consequence, alterations must be made to modelling algorithms before attempting to reproduce hybrid impedances.

Finally, a case study is conducted to assess the validity of my reference model and hybrid impedance. To do so, structurally simple forward models of both standard and hybrid impedances are calculated. The conductivity structure of this model was constrained by a 3-Dimensional inversion of continental MT data, controlled source EM (CSEM) data, and my reference model. From this model, hybrid impedances are observed to reproduces four decades of data measured by numerous receivers. From this evidence, I conclude that my reference model constrains the LARC and that it realistically represents the upper mantle. Additionally, I conclude that my hybrid impedance is a useful alternative to traditional MT impedance when conducting ocean-bottom MT studies.

Thesis Supervisors: Prof. Graham Heinson, Dr. Stephan Thiel, and Dr. Derrick Hasterok

Chapter 1

Introduction

In the early 20^{th} century Alfred Wegener found evidence of a single supercontinent, now known as Pangea, from which the current landmasses had fragmented (Wegener, 1912; Reinke-Kunze, 1994). This would later develop into the theory of plate tectonics following observations supporting Wegener's theory (Heezen, 1960; Dietz, 1961; Hess, 1962; Vine and Matthews, 1963; Morley and Larochelle, 1964). The theory of plate tectonics describes the motion of lithospheric plates, which comprise the Earth's rigid shell, through their interaction with an underlying ductile asthenosphere. Despite the adoption of plate tectonic theory, a consensus is yet to be reached regarding the cause of the contrast in rheology between the lithosphere and asthenosphere. Evidence of a sharp transition between the lithosphere and asthenosphere from seismological studies precludes a purely thermal origin due to its diffusive nature (Kawakatsu et al., 2009; Karato, 2012). Instead, authors suggest hydration (Karato and Jung, 1998; Mei and Kohlstedt, 2000; Karato and Jung, 2003; Karato, 2012), partial melting (Kohlstedt, 2002; Hirschmann, 2010) or both.

The MT method is of particular interest when investigating these hypotheses due to its sensitivity to enhanced electrical conductivity caused by partial melt, hydration, and temperature (Khan, 2016). The MT method is a passive technique developed in the 1950s by Tikhonov (1950) and Cagniard (1953) which measured EM fields induced within the Earth by naturally occurring variations in electric and magnetic source fields. The induced EM fields vary due to the electrical conductivity σ (also presented as resistivity $\rho = 1/\sigma$) of the Earth. For geophysical studies, electrical conductivity is defined as the ability of subsurface structures to conduct electrical currents. From this parameter, geophysicists relate EM field measurements to geological structures using laboratory rock conductivity measurements. The range of source field frequencies available when utilising the MT method ($\sim 10^{-5}$ Hz to $\sim 10^{4}$ Hz) allows the MT method to probe depths from ~ 10 m to > 500 km as per the EM skin depth equation:

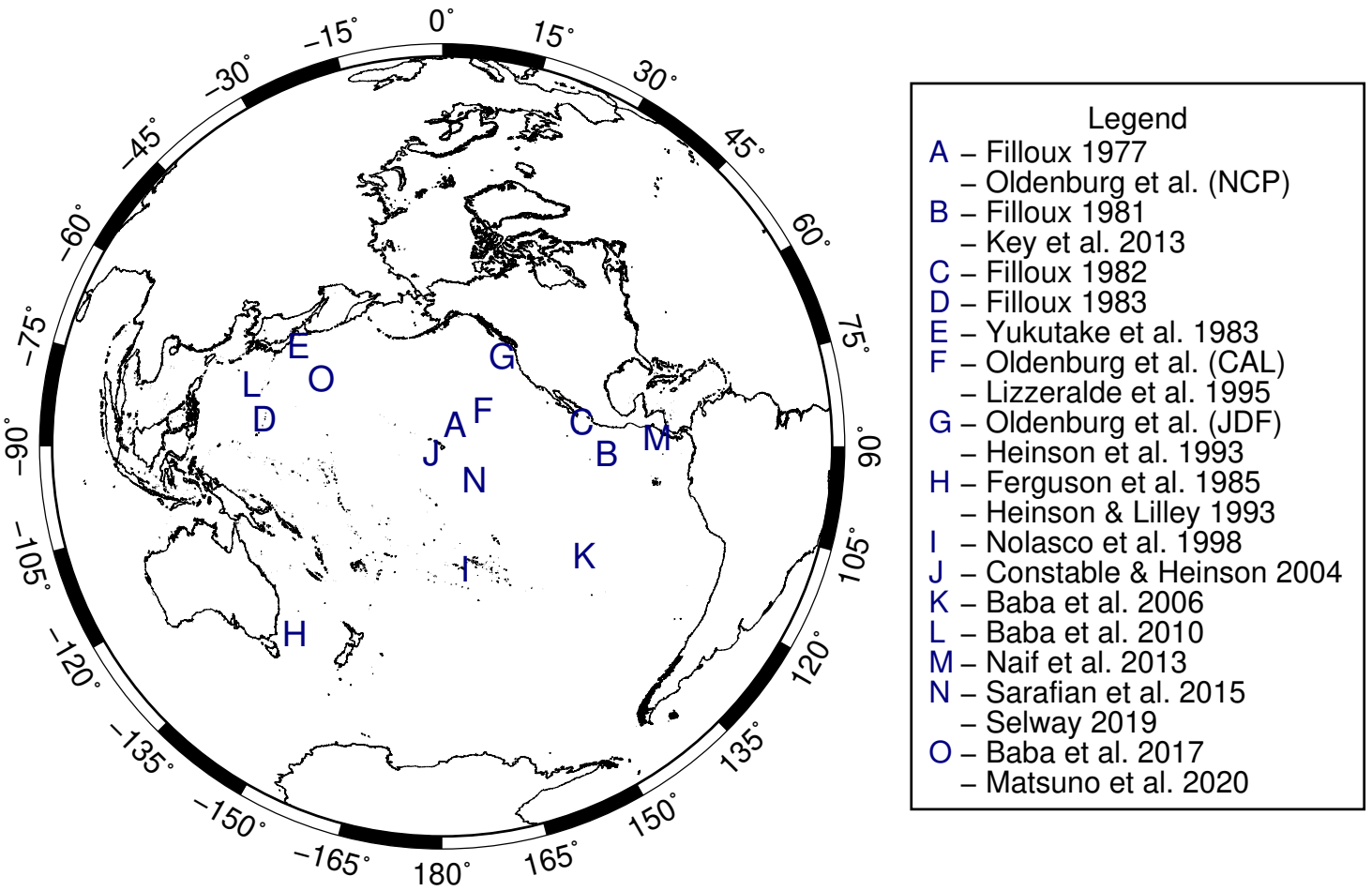

Figure 1.1: Azimuthal equidistant projection of the Pacific centred on Hawaii, United States of America. Letters denote the location of ocean-bottom MT surveys from the Pacific Ocean. Multiple studies denoted by the same letter were approximately from the same location.

$$\delta(\omega) = \sqrt{\frac{2}{\mu_0 \omega \sigma}}. \tag{1.1}$$

Eq. 1.1 defines the depth at which EM fields are attenuated to 1/e of their surface amplitude. Beyond this depth, EM fields are increasingly insensitive to the Earth's conductivity structure (Simpson and Bahr, 2005). Consequently, the EM skin depth equation represents a measure of the penetration depth of EM signal.

Oceanic lithosphere forms at mid-ocean ridges following the cooling of basaltic magma. This compositional homogeneity and the subsidence caused by conductive cooling results in a simpler geology and higher electrical resistivity when compared to continental lithosphere (Evans et al., 2005; Baba et al., 2006; Kawakatsu et al., 2009; Karato, 2012; Key et al., 2013; Naif et al., 2013). Furthermore, MT impedance calculated at the bottom of an infinitely wide ocean of uniform thickness is only sensitive to subsurface conductivity structures. As additional complexity is introduced, in the form of undulating bathymetry (Baba et al., 2006), tectonic boundaries (Key et al., 2013; Naif et al., 2013), and coastlines (Key and Constable, 2011; Worzewski et al., 2012; Wang et al., 2019), EM fields are distorted from a 1-Dimensional response. However, the magnitude of this distortion is inversely proportional to the period of the EM fields. Therefore, long period MT data, such as those utilised when investigating the LARC, are able to recover subsurface conductivity structures (Heinson and Constable, 1992).

Geophysicists utilise the high resistivity and simple geology of oceanic lithosphere to investigate the Earth's upper mantle by deploying MT receivers on the ocean floor (Fig. 1.1; Poehls and von Herzen (1976); Filloux (1977, 1981, 1982, 1983); Yukutake et al. (1983); Oldenburg et al. (1984); Ferguson et al. (1985); Heinson and Lilley (1993); Heinson et al. (1993); Lizarralde et al. (1995); Sinha et al. (1997); Nolasco et al. (1998); Sinha et al. (1998); Heinson et al. (2000); Constable and Heinson (2004); Baba et al. (2006); Jegen et al. (2009); Baba et al. (2010); Matsuno et al. (2010); Gallardo et al. (2012); Key et al. (2013); Myer et al. (2013); Naif et al. (2013); Sarafian et al. (2015); Jegen et al. (2016); Kapinos et al. (2016); Baba et al. (2017a,b); Selway and O'Donnell (2019); Wang et al. (2019); Matsuno et al. (2020). Oceanic lithosphere forms at mid-ocean ridges which then cools conductively and thickens with time (Figs 1.2 & 1.3). The presence of coastlines complicates ocean-bottom MT studies by attenuating the calculated apparent resistivity (Heinson and Constable, 1992). Despite this, the MT study of Naif et al. (2013) inferred the LARC is the result of partial melting between 45 km and 70 km depth beneath 23-Myr-old oceanic lithosphere from offshore Nicaragua. In contrast, Sarafian et al. (2015) and Selway and O'Donnell (2019) utilised MT data collected on 70-Myr-old oceanic lithosphere from the central Pacific Ocean. These authors inferred the LARC is caused by either hydration (Sarafian et al.,

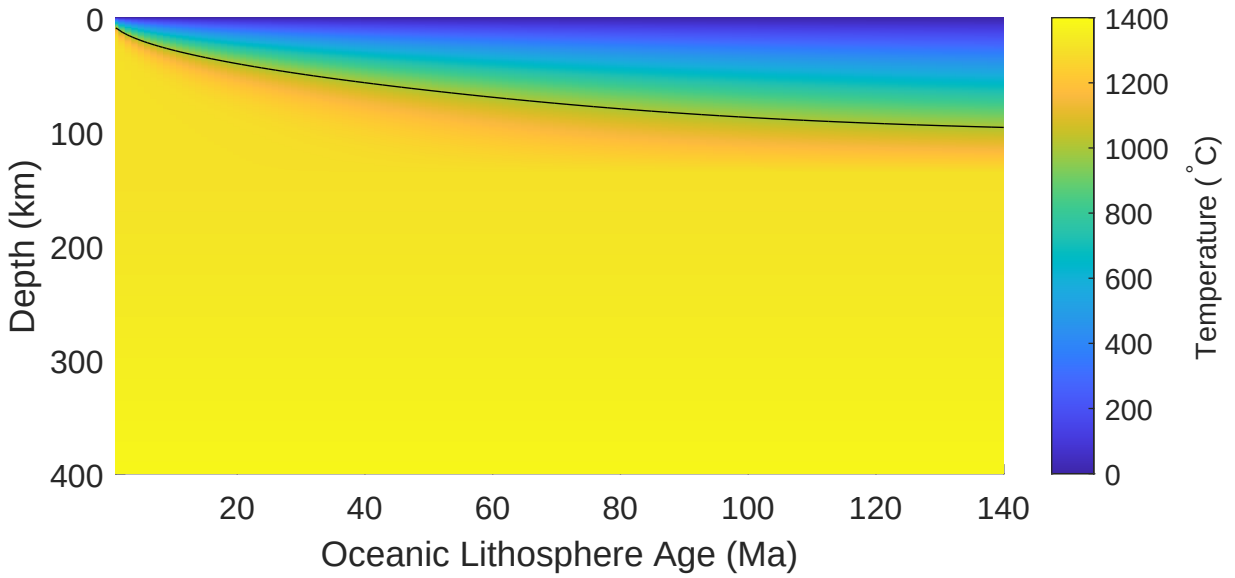

Figure 1.2: Pseudosection of temperature (°C) as a function of depth (km) and oceanic lithosphere age (Ma). The contour represents 1,000 °C and represents the conductive cooling and thickening of oceanic lithosphere.

2015) or partial melt (Selway and O'Donnell, 2019). The goal of this dissertation is to unify ocean-bottom MT measurements from the Pacific Ocean floor into a representative conductivity model of the Earth's oceanic crust and upper mantle. Such a model would allow geophysicists to ascertain the conditions which give rise to the contrast in rheology between the lithosphere and asthenosphere which has implications regarding our understanding of the mechanisms of plate motion. In addition, a representative conductivity model will allow future ocean-bottom MT studies to readily interpret the Earth's lithospheric and asthenospheric conductivity structures. Following an outline of the theory pertinent to this thesis, I present the formulation of my conductivity model. This model characterises the conductivity structure of the upper mantle as a function of oceanic lithosphere age and is formulated from a collation of MT studies from the Pacific Ocean. I then present an analysis of MT impedance and propose a hybrid impedance comprised of ocean-floor electric fields and quasi-surface magnetic fields. This alternative form of MT impedance is observed to result in an increase in the stability of measured responses. Finally, I utilise previously unpublished data to present a forward-modelling case study of the oceanic lithosphere and asthenosphere. This case study investigates the efficacy of both the conductivity model and hybrid impedance.

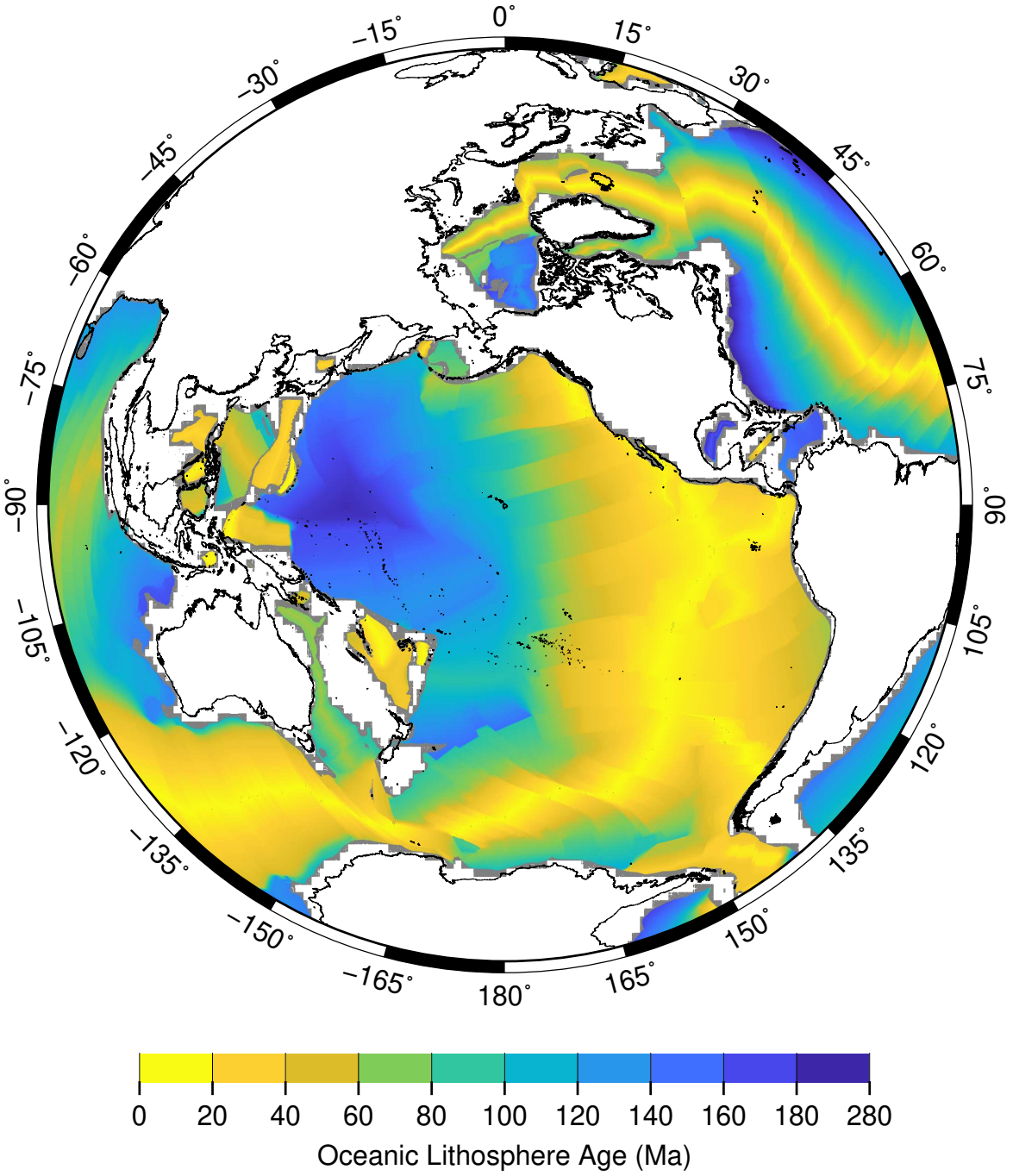

Figure 1.3: Azimuthal equidistant projection of the Pacific Ocean centred on Hawaii. Map coloured with respect to oceanic lithosphere age (Ma) data from Müller et al. (2016).

Chapter 2

The Oceanic Magnetotelluric Method

The behaviour of EM fields at any frequency in a linear, isotropic medium is described by the following set of partial differential equations (PDEs):

$$\nabla \bullet \mathbf{D} = \eta, \tag{2.1}$$

$$\nabla \bullet \mathbf{B} = 0, \tag{2.2}$$

$$\nabla \times \mathbf{E} = -\frac{\partial \mathbf{B}}{\partial t}, \tag{2.3}$$

$$\nabla \times \mathbf{H} = \mathbf{j} + \frac{\partial \mathbf{D}}{\partial t}. \tag{2.4}$$

This collection of PDEs is known as Maxwell's equations. Gauss's Law for electric fields (Eq. 2.1) states that the electric displacement $\mathbf{D}$ (C/m^2) on a closed surface is equal to the charge enclosed by that surface and will later be used to define the volume charge density η in a conductive medium. Conversely, Gauss's Law for magnetic fields (Eq. 2.2) states that magnetic induction $\mathbf{B}$ (T) forms a closed loop. Faraday's Law of induction (Eq. 2.3) states that a time varying magnetic induction $\mathbf{B}$ will generate an electric field $\mathbf{E}$ (V/m) in a closed loop orientated orthogonal to $\mathbf{B}$. Ampere's Law (Eq. 2.4) states that magnetic intensity $\mathbf{H}$ (A/m) is related to the current density $\mathbf{j}$ (A/m^2) and a time varying $\mathbf{D}$ in a similar fashion.

These equations are valid for both ocean-bottom and continental MT studies. However, ocean-bottom MT studies vary from their continental counterparts in a number of fundamental ways. First, ocean-bottom MT measurements are taken within a conductive environment. In contrast, continental MT measurements are taken within the electrically insulating atmosphere. Second, magnetic fields at the base of the oceans are distorted and attenuated as a result of the resistive oceanic lithosphere.

Finally, the accumulation of charges along the conductivity contrast between the ocean and the continent induces electric fields. The lateral extent at which these fields influence ocean-bottom MT responses is increased due to the aforementioned resistive oceanic lithosphere.

2.1 Expanding Maxwell's Equations

To relate the EM fields described by Maxwell's equations to the EM properties of the medium they are propagating through, the following equations are required:

$$\mathbf{j} = \sigma \mathbf{E}, \tag{2.5}$$

$$\mathbf{B} = \mu \mathbf{H}, \tag{2.6}$$

$$\mathbf{D} = \varepsilon \mathbf{E}. \tag{2.7}$$

Electrical conductivity σ (S/m) is the measure of a medium's ability to transport electrical charge. This is the parameter which the MT method is sensitive to and relates the current density $\mathbf{j}$ to the electric field $\mathbf{E}$ through Ohm's Law. In the MT method, the most general representation of electrical conductivity in an isotropic medium is a 3×3 symmetric tensor (σ) in Cartesian coordinates. Magnetic permeability μ (H/m), represented by $\mu = \mu_0 \mu_r$, is defined as the ability of a medium to accommodate magnetic induction and relates the magnetic induction $\mathbf{B}$ to the magnetic intensity $\mathbf{H}$. Here, μ_0 is the magnetic permeability of free space, and μ_r is the relative value for a specific material. Finally, electrical permittivity ε (F/m) is a measure of a medium's ability to interact with an electric field and become polarised by the field. It is related to the permittivity of free space ε_0 and the relative value for a specific material ε_r through a similar relationship $\varepsilon = \varepsilon_0 \varepsilon_r$ and relates the electric displacement $\mathbf{D}$ to the electric field $\mathbf{E}$. For the MT method, variations in electrical permittivity ε and magnetic permeability μ are considered negligible when compared to the variations in bulk rock conductivity, that is $\partial\sigma \gg \partial\varepsilon_r$ and $\partial\sigma \gg \partial\mu_r$. Therefore, I assume the free-space values for these variables ($\mu \approx \mu_0 = 4\pi \times 10^{-7}$ H/m and $\varepsilon \approx \varepsilon_0 = 8.85 \times 10^{-12}$ F/m).

To solve Maxwell's equations for EM induction within a medium, these equations are decoupled and defined in terms of $\mathbf{E}$ and $\mathbf{B}$ only using the quasi-static approximation. This condition states that time-varying displacement currents are negligible when compared to time-varying conduction currents and allows us to neglecting the displacement current in Maxwell's equations (Simpson and Bahr, 2005). Having established the material relationships and quasi-static approximation, Maxwell's equations can be rewritten in terms of $\mathbf{E}$ and $\mathbf{B}$ as follows:

$$\nabla \bullet \mathbf{E} = \frac{\eta}{\varepsilon_0}, \tag{2.8}$$

$$\nabla \bullet \mathbf{B} = 0, \tag{2.9}$$

$$\nabla \times \mathbf{E} = -\frac{\partial \mathbf{B}}{\partial t}, \tag{2.10}$$

$$\nabla \times \mathbf{B} = \mu_0 \mathbf{j} = \mu_0 \sigma \mathbf{E}. \tag{2.11}$$

Furthermore, the quasi-static approximation allows us to show that the current density will satisfy $\nabla \bullet \mathbf{j} = 0$. The divergence of Eq. 2.11, noting the vector calculus identities which state $\nabla \bullet (\nabla \times \mathbf{A}) \equiv 0$ and $\nabla \bullet (x\mathbf{A}) = x\nabla \bullet \mathbf{A} + \nabla x \bullet \mathbf{A}$ where x is a scalar field, produces the following (Simpson and Bahr, 2005):

$$\nabla \bullet (\nabla \times \mathbf{B}) = \nabla \bullet \mathbf{j} = (\sigma \nabla \bullet \mathbf{E} + \nabla \sigma \bullet \mathbf{E}) = 0. \tag{2.12}$$

This states that the current density $\mathbf{j}$ is solenoidal and all conduction current flows in closed circuits (Weaver, 1994). When combined with Eq. 2.8, the volume charge density in a conductive medium is given by the following expression:

$$\eta = -\frac{\nabla \sigma \bullet \mathbf{E}}{\sigma} \varepsilon_0, \tag{2.13}$$

which states that electric charges can only accumulate in regions where the conductivity has a non-vanishing gradient ($\nabla \sigma \neq 0$). A similar method applied to Ampere's Law (Eq. 2.11) shows that $\nabla \bullet \mathbf{B}$ is a constant ($\frac{\partial}{\partial t} \nabla \bullet \mathbf{B} = 0$) and therefore Eq. 2.9 is true at all times. These results show that Eq. 2.10 and Eq. 2.11 are the only equations required to fully describe the behaviour of quasi-static fields.

Having rewritten Maxwell's equations in terms of only $\mathbf{E}$ and $\mathbf{B}$, the diffusion of EM fields through an electrically conductive medium can be defined. Beginning with Faraday's law and remembering the vector calculus identity for the Laplacian ($\nabla^2 \mathbf{A}$) $\nabla \times (\nabla \times \mathbf{A}) = \nabla(\nabla \bullet + A) - \nabla^2 \mathbf{A}$ where $\mathbf{A}$ is a vector field, the following equations are defined (Simpson and Bahr, 2005):

$$\nabla \times (\nabla \times \mathbf{E}) = \nabla(\nabla \bullet \mathbf{E}) - \nabla^2 \mathbf{E} = -\frac{\partial}{\partial t}(\nabla \times \mathbf{B}). \tag{2.14}$$

Substituting Eq. 2.8 and Eq. 2.9 into the above equation produces:

$$\nabla^2 \mathbf{E} + \nabla \left(\frac{\nabla \sigma \bullet \mathbf{E}}{\sigma} \right) = \mu_0 \sigma \frac{\partial \mathbf{E}}{\partial t}. \tag{2.15}$$

Applying the same method to Ampere's Law results in (Simpson and Bahr, 2005):

$$\nabla^2 \mathbf{B} + \nabla \sigma \times (\nabla \times \mathbf{B}) = \mu_0 \sigma \frac{\partial \mathbf{B}}{\partial t}. \tag{2.16}$$

Together these equations define the diffusive nature of EM fields.

2.2 EM Fields In The Earth's Atmosphere

Of particular interest to the MT method is EM induction within the Earth's atmosphere. Source fields travelling through the Earth's atmosphere are assumed to be far enough away from their ionospheric source that they can be approximated as a uniform, plane-wave ($\partial/\partial x = \partial/\partial y = 0$) travelling in the $\hat{\mathbf{z}}$ direction with a harmonic time dependence of $e^{i\omega t}$ where $\omega = 2\pi f$ is the angular frequency defined by the frequency f (both in Hz) of the source field. Furthermore, this region is assumed to be a perfect insulator ($\sigma = \nabla\sigma = 0$) and therefore the equations governing EM induction (Eq. 2.15 and Eq. 2.16) simplify to (Simpson and Bahr, 2005):

$$\frac{\partial^2 \mathbf{E}}{\partial z^2} = 0, \tag{2.17}$$

$$\frac{\partial^2 \mathbf{B}}{\partial z^2} = 0. \tag{2.18}$$

From these assumptions it becomes clear by expanding the curl for both the E and B fields as per Eq. 2.10 and Eq. 2.11 that the vertical components of these EM fields are unable to reach the Earth's surface ($E_z = B_z = 0$). However, considering an electric field polarised in the x-direction E_x and a magnetic field polarised in the y-direction B_y both of which propagate in the $\hat{\mathbf{z}}$ direction, Eq. 2.17 becomes:

$$\frac{\partial^2 E_x}{\partial z^2} = 0. \tag{2.19}$$

From this, it follows that the first spatial derivative of E_x in the $\hat{\mathbf{z}}$ must be a constant. In conjunction with Faraday's Law, this shows the solution for B_y in air is a constant (Cagniard, 1953):

$$B_y = -\frac{1}{i\omega}\frac{\partial E_x}{\partial z} = B_0, \tag{2.20}$$

and, through integration, the solution for E_x will be a linear function of z (Cagniard, 1953):

$$E_x = \int_{-\infty}^{\infty} -i\omega B_y \, \partial z = -i\omega B_0 z + E_0. \tag{2.21}$$

2.3 EM Induction In A Homogeneous Earth

To describe EM induction within the Earth, it is convenient to first describe the geoelectrical model of a homogeneous half-space. This scenario is defined by a constant non-zero σ ($\nabla\sigma = 0$) causing the PDEs Eq. 2.15 and Eq. 2.16 to reduce to (Simpson and Bahr, 2005):

$$\nabla^2 \mathbf{E} = \mu_0 \sigma \frac{\partial \mathbf{E}}{\partial t}, \tag{2.22}$$

$$\nabla^2 \mathbf{B} = \mu_0 \sigma \frac{\partial \mathbf{B}}{\partial t}. \tag{2.23}$$

As both these equations have the same form, the diffusion of EM fields within a homogeneous Earth can be described using a general field $\mathbf{F} \in \{\mathbf{E}, \mathbf{B}\}$. To satisfy Maxwell's equations within a half-space, this general field is as follows (Simpson and Bahr, 2005):

$$\mathbf{F} = \mathbf{F}_1 \mathrm{e}^{-kz} \mathrm{e}^{i\omega t} + \mathbf{F}_2 \mathrm{e}^{kz} \mathrm{e}^{i\omega t}, \tag{2.24}$$

where F_1 and F_2 are the fields at the surface and k is the propagation constant. However, the field F must diminish as $z \to \infty$ which implies that $F_2 = 0$ must be true. As a consequence, the Earth cannot generate EM energy and instead it must be dissipated or absorbed. Differentiating Eq. 2.24 with respect to time allows the definition of a Laplacian for the general field similar to Eq. 2.22 and Eq. 2.23 as the following:

$$\nabla^2 \mathbf{F} = i\omega \mu_0 \sigma \mathbf{F}. \tag{2.25}$$

Having assumed a homogeneous Earth, $\mathbf{F}$ cannot vary in the x and y directions ($\partial \mathbf{F}/\partial x = \partial \mathbf{F}/\partial y = 0$) causing the Laplacian to reduce to the following:

$$\frac{\partial^2 \mathbf{F}}{\partial z^2} = k^2 \mathbf{F}, \tag{2.26}$$

from which the propagation constant of the EM fields k (m^{-1}) can be defined:

$$k = \sqrt{i\omega\mu_0\sigma} = \sqrt{\frac{\mu_0\omega\sigma}{2}} + i\sqrt{\frac{\mu_0\omega\sigma}{2}}. \tag{2.27}$$

2.3.1 Skin Depth

A useful parameter when studying EM fields is the EM skin depth δ. This parameter describes the depth at which EM fields attenuate to 1/e of their initial value. From Eq. 2.27, the skin-depth can be defined by the following:

$$\delta(\omega) = \frac{1}{\Re(k)} = \sqrt{\frac{2}{\mu_0\omega\sigma}}. \tag{2.28}$$

This skin depth is inversely proportional to the square root of frequency and conductivity. As such, high frequency signals or signals which propagate through regions of high conductivity result in low penetration depths. Naturally, higher penetration depths are caused by low frequency signals or regions of low conductivity.

2.4 EM Induction In A Layered Earth

To characterise EM induction within a 1-Dimensional Earth, the Earth is defined in terms of N layers extending infinitely in the x- and y-directions at depths $z = \{z_1, z_2, \ldots, z_N\}$. These layers are characterised by electrical conductivities $\sigma = \{\sigma_1, \sigma_2, \ldots, \sigma_N\}$ which varies in the vertical direction ($\partial\sigma/\partial x = \partial\sigma/\partial y = 0$). As a result, a homogeneous solution for the diffusion equation in the form of Eq. 2.24 can be found within each layer (Simpson and Bahr, 2005):

$$E_{xn}(k_n, \omega), = \mathbf{E}_{1n}\mathrm{e}^{-ikz}\mathrm{e}^{i\omega t} + \mathbf{E}_{2n}\mathrm{e}^{kz}\mathrm{e}^{i\omega t}, \tag{2.29}$$

which can be combined with Faraday's Law to give the following relationship between orthogonal EM fields:

$$B_{yn}(k_n, \omega) = \frac{k}{i\omega}\left(\mathbf{E}_{1n}\mathrm{e}^{-ikz}\mathrm{e}^{i\omega t} - \mathbf{E}_{2n}\mathrm{e}^{kz}\mathrm{e}^{i\omega t}\right). \tag{2.30}$$

This allows for the creation a transfer function for each layer from the ratio of Eq. 2.29 and Eq. 2.34 as follows:

$$Z_{ij} = \frac{E_i}{B_j} = \frac{i\omega}{k} = \sqrt{\frac{\omega}{\mu_0\sigma}}\sqrt{i} = \sqrt{\frac{\omega\rho}{2\mu_0}} + i\sqrt{\frac{\omega\rho}{2\mu_0}}, \tag{2.31}$$

where $(i, j) \in (x, y)$ and $i \neq j$. While MT instruments measure magnetic induction $\mathbf{B}$, MT studies typically define the impedance in terms of $\mathbf{H}$. Therefore, the above equations are redefined as:

$$Z_{ij} = \frac{E_i}{H_j} = \frac{i\omega\mu_0}{k} = \sqrt{\frac{\omega\mu_0}{\sigma}}\sqrt{i} = \sqrt{\frac{\omega\mu_0\rho}{2}} + i\sqrt{\frac{\omega\mu_0\rho}{2}}, \tag{2.32}$$

from which the Schmucker-Weidelt transfer function Schmucker (1973); Weidelt (1973) can be defined:

$$C_n(k_n, \omega) = \frac{E_{xn}(k_n, \omega)}{i\omega\mu_0 B_{yn}(k_n, \omega)}. \tag{2.33}$$

This transfer function varies as a function of z as the propagation constant changes with layer conductivity $k = \sqrt{i\omega\mu_0\sigma_n}$. In addition, the field components which constitute the transfer function must be continuous across the interfaces which comprise our 1-Dimensional Earth model. Combining the transfer functions from the top and bottom of the n-th layer generates Wait's recursion formula (Wait, 1954):

$$C_n(z_{n-1}) = \frac{1}{k_n}\frac{k_n C_{n+1}(z_n) + tanh(k_n l_n)}{1 + k_n C_{n+1}(z_n) tanh(k_n l_n)}, \tag{2.34}$$

where $l_n = z_n - z_{n-1}$. This formula enables the calculation of transfer function at the top of the n-th layer assuming the transfer function from the top of the $n + 1$th

layer is known. The final layer N is defined as a homogeneous half-space and as such the transfer function may be calculated using Eq. 2.33.

As the penetration depth of the EM fields, and subsequently the number of layers they are sensitive to, is a function of angular frequency, the apparent resistivity ρ_a can be defined. The apparent resistivity represents the average resistivity ascertained from Wait's recursion formula as if it were an equivalent uniform half-space. For each layer, the apparent resistivity is as follows:

$$\rho_{a_n}(\omega) = \frac{1}{\mu_0 \omega} |Z_n(\omega)|^2. \tag{2.35}$$

A consequence of this is that for penetration depths shallower than z_1, the apparent resistivity represents the conductivity of this first layer $1/\sigma_1$. However for penetration depths beyond the first layer, the apparent resistivity will asymptote to the apparent resistivity of the N-th layer penetrated, that is to say ρ_a tends to $1/\sigma_n$. As a result, sufficiently thin layers may be unable to be resolved. Similar to the apparent resistivity, the impedance phase is now also a depth-weighted value. The impedance phase for each layer is determined via the following equation:

$$\phi_n(\omega) = \arctan\left(\frac{\Im Z_n(\omega)}{\Re Z_n(\omega)}\right). \tag{2.36}$$

Within a homogeneous layer, the impedance phase is fixed to 45°. However, by comparing two models it is possible to show that ϕ will be greater than 45° when transitioning to a more conductive layer and ϕ will be less than 45° when transitioning to a more resistive layer. The first model consists of an infinitely resistive layer of thickness $h = l_1$ overlying a more conductive half-space. These conditions result in $\sigma_1/\sigma_2 \ll 1$ which subsequently means $|q_1 C_2| \ll 1$. The second model consists of an infinitely thin conductive layer with a conductance of $\tau = \sigma_1 l_1$ overlying a comparatively resistive half-space. As such, $l_1 \ll |C_2|$. In addition, the property $|q_1| l_1 \ll 1$ is true for both models and results in $\tanh(q_1 l_1) \equiv q_1 l_1$. These conditions cause the transfer functions to behave as follows for the first model:

$$C_1 = C_2 + l_1 = C_2 + h, \tag{2.37}$$

and the second model respectively:

$$C_2 = \frac{C_2}{1 + i\omega\mu_0 \tau C_2}. \tag{2.38}$$

As a result, the first model results in an increase to $\Re(C_1)$ causing the impedance phase to deflect to angles greater than 45° while the second model results in an increase to $\Im(C_1)$ causing the impedance phase to be deflected to angles smaller than 45° (Simpson and Bahr, 2005).

2.4.1 EM Induction in a 2D Earth

The introduction of additional complexity to our model of the Earth in the form of a lateral heterogeneity in the $\hat{\mathbf{y}}\hat{\mathbf{z}}$ plane allows for the description of EM induction within a 2-Dimensional Earth. Introducing this lateral heterogeneity causes both electrical conductivity and EM fields to vary in both the horizontal $\hat{\mathbf{y}}$ and vertical $\hat{\mathbf{z}}$ directions. As such, $\partial\mathbf{F}/\partial x = 0$ is true for the purposes solving the Laplacian within a 2-Dimensional Earth. Furthermore, the electric and magnetic fields are no longer necessarily orthogonal to each other (Vozoff, 1991). As a result, a 2×2 tensor, called the general impedance tensor, is now required to describe the relationship between $\mathbf{E}$ and $\mathbf{B}$ components. This tensor reduces to the 1D case when the condition $Z_{xy} = -Z_{yx}$ is true and is given by (Simpson and Bahr, 2005):

$$\begin{pmatrix} E_x \\ E_y \end{pmatrix} = \begin{pmatrix} Z_{xx} & Z_{xy} \\ Z_{yx} & Z_{yy} \end{pmatrix} \begin{pmatrix} B_x \\ B_y \end{pmatrix}. \tag{2.39}$$

An additional outcome of introducing a lateral heterogeneity is that σ_y and E_y must be discontinuous to ensure the conservation of current as per Ohm's Law (Eq. 2.5). It is therefore convenient to represent the field components in terms of a transverse electric (TE) polarisation:

$$\frac{\partial E_x}{\partial y} = \frac{\partial B_z}{\partial t} = i\omega B_z, \tag{2.40}$$

$$\frac{\partial E_x}{\partial z} = \frac{\partial B_y}{\partial t} = -i\omega B_y, \tag{2.41}$$

$$\frac{\partial B_z}{\partial y} - \frac{\partial B_y}{\partial z} = \frac{\partial E_x}{\partial t} = \mu_0 \sigma E_x, \tag{2.42}$$

and a transverse magnetic (TM) polarisation:

$$\frac{\partial B_x}{\partial y} = \frac{\partial E_z}{\partial t} = \mu_0 \sigma E_z, \tag{2.43}$$

$$\frac{\partial B_x}{\partial z} = \frac{\partial E_y}{\partial t} = -\mu_0 \sigma E_y, \tag{2.44}$$

$$\frac{\partial E_z}{\partial y} - \frac{\partial E_y}{\partial z} = \frac{\partial B_x}{\partial t} = i\omega B_x, \tag{2.45}$$

which combine fields orientated parallel to the lateral heterogeneity (E_x & B_x) with their constituents (E_y, E_z, B_y, & B_z). Following Eq. 2.41 and Eq. 2.44, it becomes

apparent that the impedances for orthogonal fields are described by these polarisations. As such, the impedance tensor reduces to an anti-diagonal form comprised of TE- and TM-polarisation impedance:

$$\begin{pmatrix} 0 & Z_{xy} \\ Z_{yx} & 0 \end{pmatrix} = \begin{pmatrix} 0 & Z_{TE} \\ Z_{TM} & 0 \end{pmatrix}. \tag{2.46}$$

For the 2-Dimensional scenario described earlier, it is possible for the general impedance tensor (Eq. 2.39) to reduce to the polarised tensor through the utilisation of a rotation matrix $\mathbf{R}$:

$$\mathbf{R} = \begin{pmatrix} \cos\theta & \sin\theta \\ -\sin\theta & \cos\theta \end{pmatrix}, \tag{2.47}$$

and its transpose R^T via:

$$\mathbf{Z}^{'} = \mathbf{R}\mathbf{Z}\mathbf{R}^T, \tag{2.48}$$

where θ represents the angle between the measurement axis (x, y, z) and the axis of the lateral heterogeneity $(x^{'}, y^{'}, z^{'})$, $\mathbf{Z}$ is the general impedance tensor, and $\mathbf{Z}^{'}$ is its anti-diagonal form.

2.5 EM Induction In A 3-Dimensional Earth

Representation of a 3-Dimensional Earth through the introduction of an additional lateral heterogeneity within the $\hat{\mathbf{x}}\hat{\mathbf{z}}$ plane causes electrical conductivity to vary in all directions. As such, the EM field components are interconnected and require that all field components be solved to describe the diffusion of EM fields through a 3-Dimensional Earth. This interconnectivity causes the general impedance tensor (Eq. 2.39) to become asymmetrical with non-zero components in all locations (Simpson and Bahr, 2005).

$$\begin{pmatrix} Z_{xx} & Z_{xy} \\ Z_{yx} & Z_{yy} \end{pmatrix} \neq 0 \tag{2.49}$$

.

2.6 Source Fields

Interactions between the Earth and a variety of EM phenomena result in induced EM fields which are utilised by the MT method. These induced fields have periods ranging from 10^{-3} s to 100,000 s (10^{-5} Hz to 1,000 Hz frequency). However, a reduction in the power spectrum occurs for periods between 0.2 s and 2 s. This reduction, referred to as the MT dead-band, reaches a maximum at a period of 1 s (Geiermann and Schill, 2010). The MT dead-band represents the change between the two primary inductive mechanisms within the Earth and results in a reduction in MT data quality (Simpson

and Bahr, 2005). There are additional dead-bands in MT data at periods between 1 s and 10 s, and periods greater than 1,000 s associated with the noise characteristics of MT receivers (Chave et al., 2012).

Induced fields with periods greater than 1 s are a consequence of interactions between solar wind and the Earth's magnetosphere. As the solar wind reaches the Earth's magnetic field, a secondary electric field is generated within the ionosphere which, in turn, generates an electric current. This electric current subsequently induces a magnetic field which propagates to the Earth's surface as a plane wave for periods less than 100,000 s at mid-latitudes (Srivastava, 1965; Chave et al., 2012)

Saline water with an average conductivity of 3.3 S/m comprises the Earth's oceans (Tyler et al., 2017). This further limits the bandwidth available to ocean-bottom MT studies by requiring a minimum source field period. For instance, to penetrate an average ocean depth of 3,700 m (Amante and Eakins, 2009) a period of 178 s is required (Fig. 2.1) as per the skin depth equation (Simpson and Bahr, 2005).

2.7 EM Induction In The Earth's Oceans

In the early 1900s Chapman (1923) discovered that induced EM fields are distorted by conductive water associated with the Earth's oceans. Further developed by numerous authors (De Wet, 1949; Price, 1949; Ashour, 1950) and recognised as a global phenomenon by Bullard and Parker (1970), this distortion has been described by Fainberg (1980) as one of the principal problems of modern geomagnetism.

Due to the 24, 12, 8, and 6 hour periodicity of the Earth's magnetic field and the 12.45 hour periodicity of tidal activity, an electrical current is established within the oceans as per Maxwell equations. Spatial variations associated with coastline geometry and bathymetry further complicates the induced current (Schnepf et al., 2014, 2015; Tyler et al., 2017).

While this electrical current is small, it is able to move freely within Earth's oceans and subsequently induces significant EM fields. Furthermore, magnetic fields undergo further attenuation as the resistivity of the ocean floor increases (Key, 2003).

For ocean-bottom MT surveys, the Transerve Magnetic (TM) mode exhibits dampened apparent resistivity curves whereas the Transverse Electric (TE) mode exhibits a singularity peak in the apparent resistivity (Fig. 2.2). For the TM mode, electrical current flowing towards the coast results in a discrepancy in the current density between the ocean and the continent. As a consequence, the electric field perpendicular

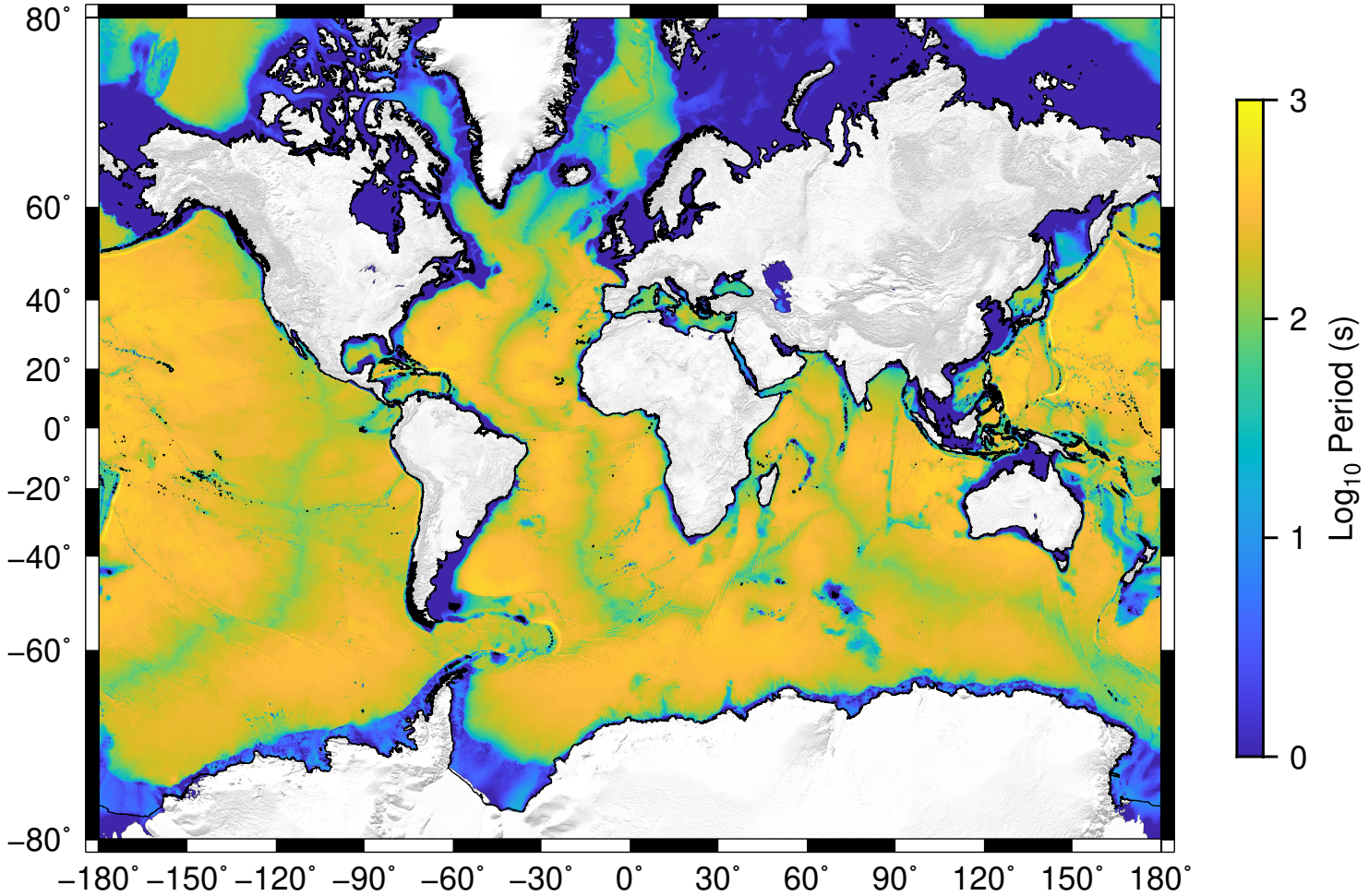

Figure 2.1: Global skin-depth period map calculated from ocean depths as presented by Amante and Eakins (2009) in the ETOPO1 dataset. This image represents the signal period required to calculate the Earth's oceans assuming an average ocean-water conductivity of 3.3 S/m (Tyler et al., 2017).

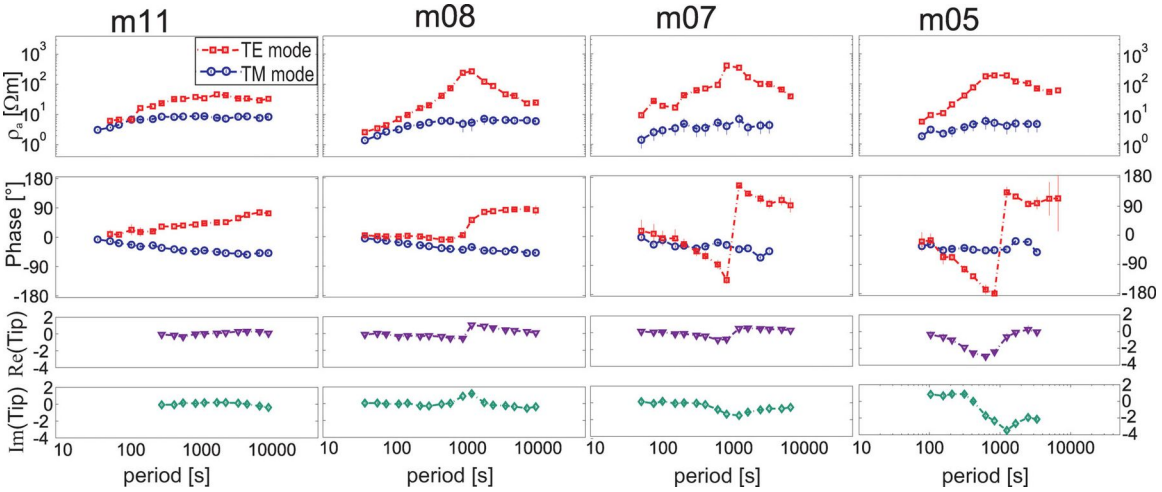

Figure 2.2: Response functions of marine MT stations deployed offshore Costa Rica by Worzewski et al. (2012). The uppermost panels display apparent resistivity calculated from measured responses and display the singularity peak within the TE-mode which is associated with the coast effect. The remaining panels display phase and tipper components.

to the coastline is reduced which dampens apparent resistivities. For the TE mode, electrical current flowing parallel to the coastline results in a similar current density discrepancy as the TM mode. However, the reduction of the electric field parallel to the coastline causes the magnetic field perpendicular to the coastline to approach 0 as $\delta E_x/\delta y \gg \delta E_x/\delta z$ (Eqs 2.40 and 2.41). This results in discontinuous magnetic fields at the conductivity contrast (Dawson, 1983). However, the EM response to the coastline dissipates much more rapidly in the TE mode than the TM mode as distance increases away from the conductivity contrast. To understand this distortion, Price (1949) developed the theory of EM induction in thin sheets. The thin sheet approximation represents the Earth's surface using an infinitesimally thin layer. The conductance of this layer is defined by the depth integral of conductivity for the portion of Earth it represents. Price (1949) showed that the effect of this layer can be reduced in such a way that they can be considered a modification of the boundary conditions at the Earth's surface. This approximation requires the skin depth and horizontal wavelength of the source field to be larger than the thickness of the surface layer. As a result, the thin sheet approximation is only valid for long period source fields.

However, the model of Price (1949) requires the thin sheet be embedded within a non-conducting medium. To address this, Ranganayaki (1978) developed a generalised thin sheet approximation which allows for a layered conductivity structure beneath the thin sheet. This addition allows the thin sheet approximation to represent the oceanic

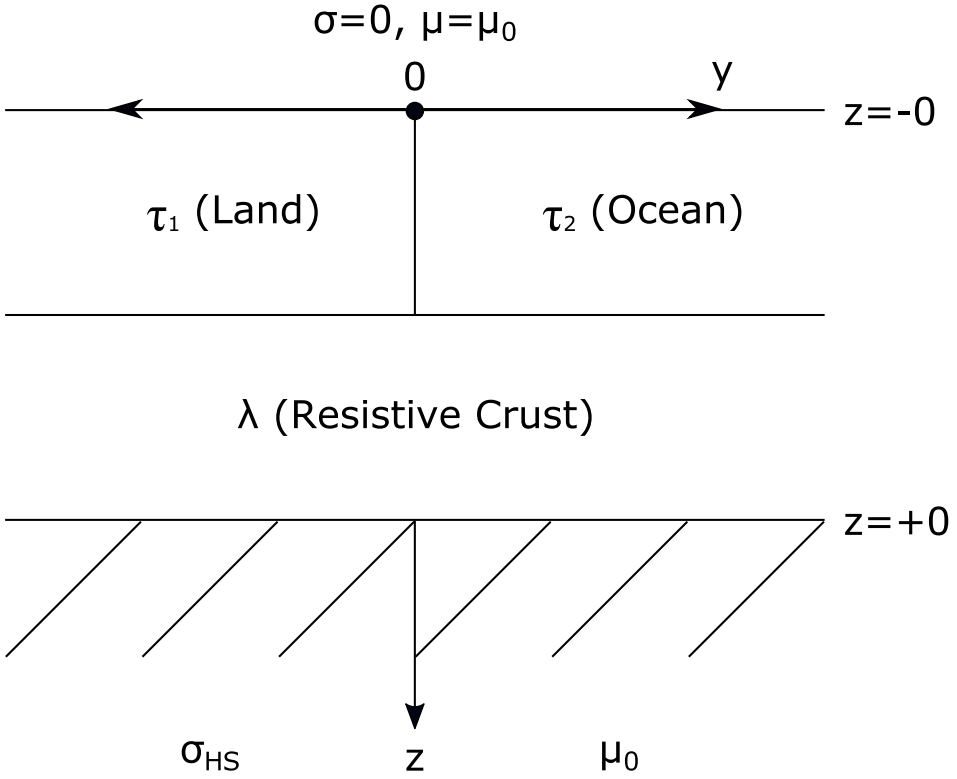

Figure 2.3: Schematic diagram of the thin-sheet approximation of Dawson et al. (1982). τ_1 represents the resistance of the continent, τ_2 represents the resistance of the ocean, λ represents the oceanic lithosphere, and σ_{HS} represents an underlying conductive half-space. Finally, -0 and +0 represent the top and bottom of the thin-sheet.

lithosphere beneath the model of Price (1949). Furthermore, the approximation of Ranganayaki (1978) is capable of predicting EM induction due to a 2-Dimensional surface thin sheet. Dawson (1979) further extended this approximation to predict induction due to a 3-Dimensional surface thin sheet. As a consequence, the thin sheet approximation is capable of modelling the change in conductivity associated with the ocean-continent boundary.

According to controlled source (EM) soundings, the resistivity of oceanic lithosphere is between 10,000 Ωm and 20,000 Ωm resulting in a resistance of 10^9 Ωm^2 (Cox et al., 1986; Chesley et al., 2019). Chesley et al. (2019) found the resistivity structure of oceanic lithosphere to be anisotropic between the depths of 11 km to 20 km. They found the electrical resistivity to be $\sim$29 times larger in the vertical plane parallel to the paleo-ridge. However, MT data lacks resolution and is insensitive to anisotropy within the uppermost oceanic lithosphere (Cox, 1981; Chesley et al., 2019). As a consequence, I utilise a resistance of 10^9 Ωm^2 for the oceanic lithosphere thin sheet.

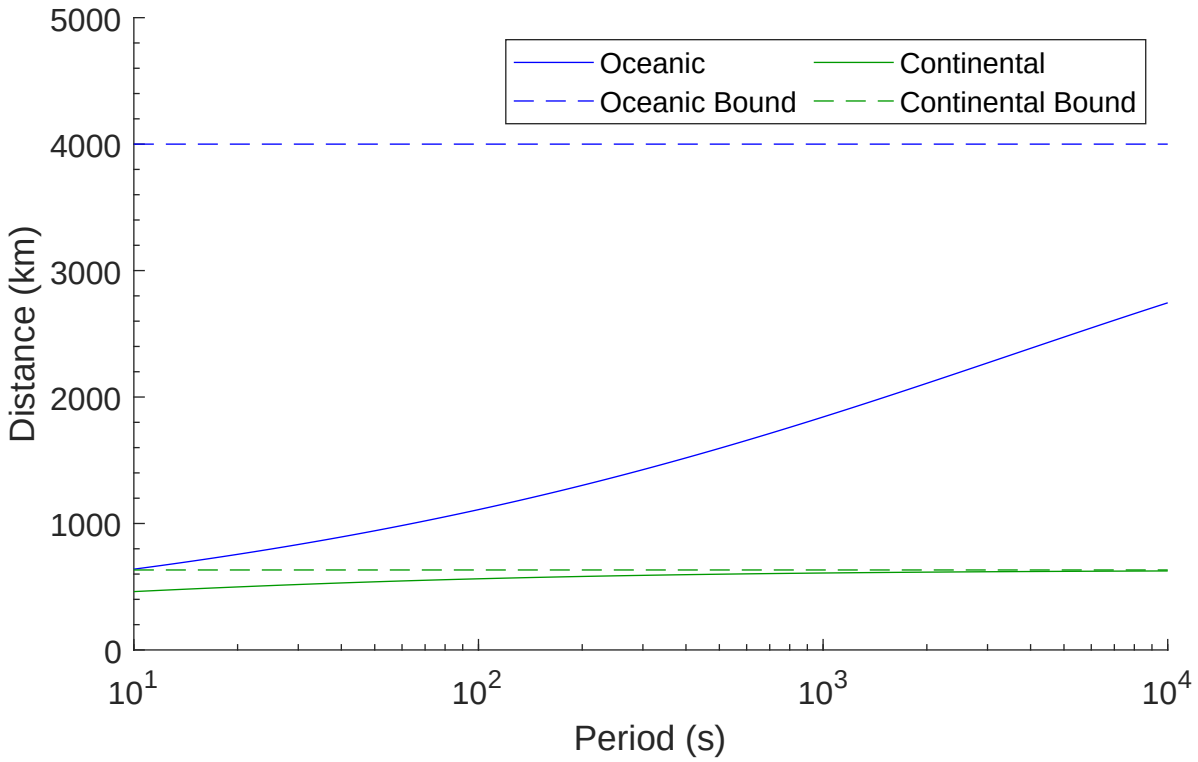

Figure 2.4: Adjustment distance calculated for $\tau_1 = 400$ S, $\tau_2 = 1.6 \times 10^4$ S, $\lambda = 10^9$ Ωm^2 (Cox et al., 1986; Chesley et al., 2019), $\sigma_{HS} = 100$ S/m. The solid lines correspond to the frequency dependent adjustment distance calculated from Eq. 2.51. The frequency independent adjustment distance (dashed line) calculated from Eq. 2.50 represents the maximum bound of the frequency dependent adjustment distance.

Ranganayaki and Madden (1980) recognised that the vertical flow of current through the conductive thin-sheet is inhibited if an underlying resistive thin-sheet (Fig. 2.3). As a result, charges accumulate across the boundary between the two thin sheets which causes a discontinuity in the horizontal electric fields while the magnetic fields remain unaffected. From this analysis Ranganayaki and Madden (1980) proposed the concept of an adjustment distance. This horizontal adjustment distance is analogous to the EM skin depth (Eq. 2.28) and represents the distance at which EM fields induced at the 2-Dimensional boundary within a thin sheet attenuate to 1/e of their initial value (Ranganayaki and Madden, 1980; Weaver and Dawson, 1992). Ranganayaki and Madden (1980) defined the horizontal adjustment distance d as:

$$d(j) = \sqrt{\tau_j \lambda}, \tag{2.50}$$

where τ is the conductance of the thin sheet, λ is the depth integral of resistivity

for the thin sheet, and the index j refers to the oceanic or continental thin sheet. The horizontal adjustment distance was then further refined by Weaver and Dawson (1992) to include a frequency component f:

$$d_j = \frac{\sqrt{\tau_j \lambda}}{\Re\sqrt{1 - \frac{\tau_j \chi_j}{\sigma}}}, \tag{2.51}$$

$$\chi_j = \frac{1}{\lambda\alpha} - \sqrt{\frac{1}{(2\lambda\alpha)^2} - \frac{1}{\tau_j \lambda} + i\alpha^2}, \tag{2.52}$$

$$\alpha = \sqrt{\omega\mu_0\sigma}. \tag{2.53}$$

Here, τ is the conductance of the thin sheet, λ is the depth integral of resistivity for the thin sheet, σ is the conductivity of the half-space beneath the thin sheets, ω is the angular frequency.

2.8 Conclusions

Interactions between EM fields induced within the Earth and conductive ocean water complicates the interpretation of MT data. From the horizontal adjustment distance, it becomes clear that these issues are exacerbated for ocean-bottom MT studies. This is due to the 3-Dimensional nature of coastline boundaries and the resistivity of oceanic lithosphere. This phenomenon manifests itself as dampened apparent resistivities for the TM mode and a singularity peak in the apparent resistivity of the TE mode. As a consequence, care must be taken when utilising MT data from the Earth's ocean to ascertain information regarding subsurface conductivity structures.

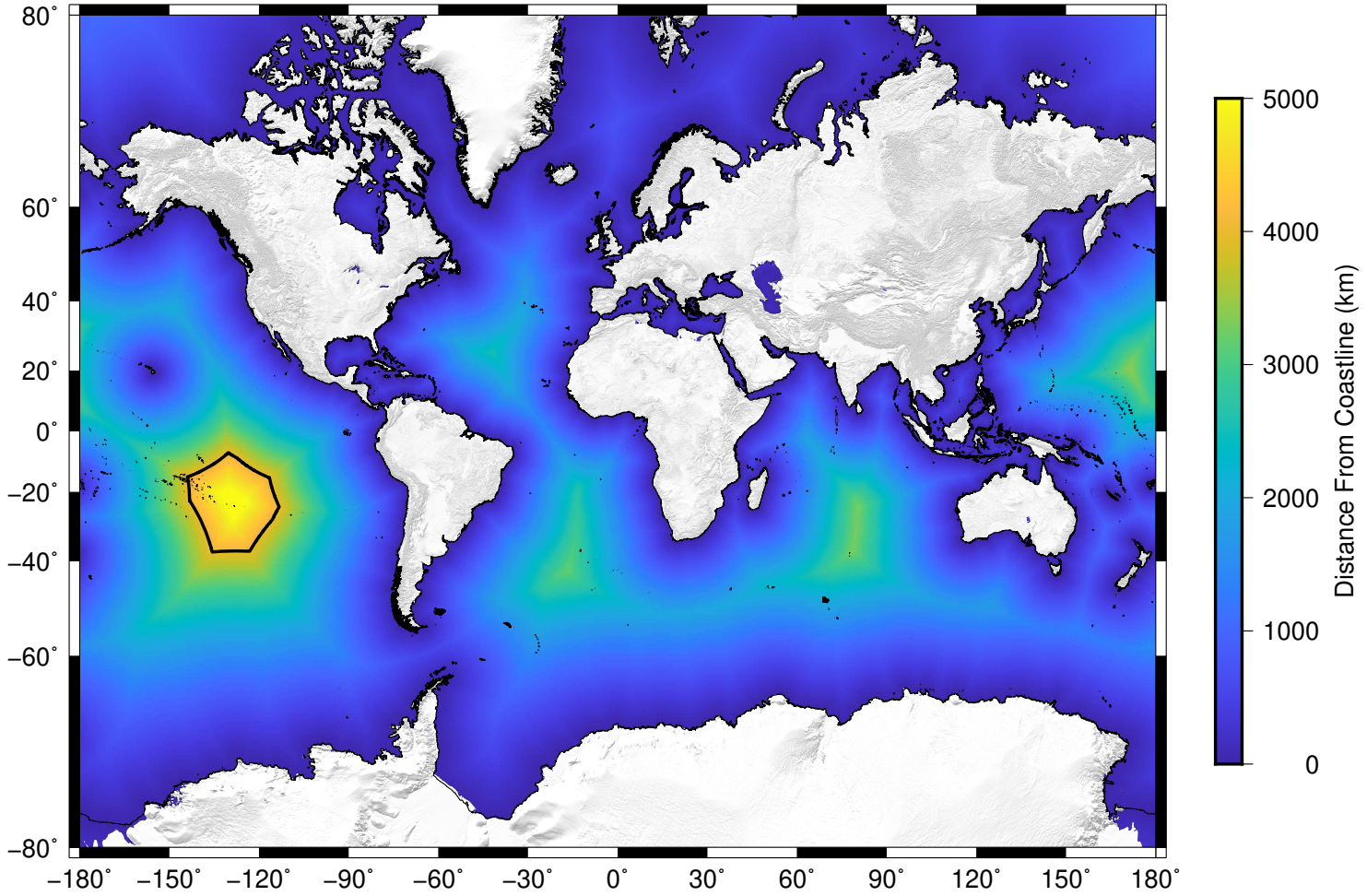

Figure 2.5: Global adjustment distance map with adjustment distance calculated for $\tau_1 = 400$ S, $\tau_2 = 1.6 \times 10^4$ S, $\lambda = 10^9$ Ωm^2 (Cox et al., 1986), $\sigma = 100$ S/m. Distances are calculated from the Global Self-consistent, Hierarchical, High-resolution Geography Database of Wessel and Smith (1996). For this calculation I ignore islands with an area of less than 10,000 km^2. The black line represents the oceanic adjustment distance bound calculated from Eq. 2.50.

Chapter 3

An Oceanic Mantle Electrical Conductivity Reference Model

Studies attempting to constrain the LARC have attributed this phenomenon to the presence of hydration, partial melt, or both. In addition to this disagreement, these studies fail to consider how the geodynamic processes which result in the LARC evolve with the age of the overlying lithosphere. As a consequence, the LARC remains a point of contention which limits our understanding of plate tectonic theory. The aim of this chapter is to construct a representative model of the Earth's oceanic lithosphere and asthenosphere incorporating the age of the oceanic lithosphere from laboratory conductivity measurements and four decades of MT studies from the Pacific Ocean. By comparing my reference model to conductivity structures interpreted from Pacific Ocean MT surveys and global conductivity models derived from satellite magnetic field data, I conclude that this conductivity model serves as a representative model of the Earth's oceanic lithosphere and asthenosphere. Furthermore, I conclude that this reference model can reconcile hydration and partial melt within the asthenosphere and constrain the aforementioned rheological contrast for a range of lithospheric ages. As depth increases beyond the rheological contrast, I conclude that the conductivity structure of the upper mantle becomes homogeneous and hydrated.

3.1 Introduction

The electrical conductivity of the Earth is an important parameter in studies of the crust and mantle. Understanding the electrical structure of the Earth allows us to make statements regarding the temperature, pressure, physical and chemical state, porosity, and permeability of rocks at depths ranging from the near surface into the deep mantle. Furthermore, electrical conductivity can be used to constrain geophysical models which aren't directly sensitive to the physical processes which generate high conduc-

tivities. As such, EM methods, which are primarily sensitive to electrical conductivity, are striving to produce accurate representations of the Earth's conductivity structure. Of particular interest is the electrical structure associated with the rheological contrast between the lithosphere and asthenosphere. Constraining the conditions which give rise to this contrast in rheology will subsequently constrain a large portion of the Earth and has implications regarding our understanding of the mechanisms of plate motion. However, MT surveys are yet to come to a consensus regarding conductivity structure of the oceanic lithosphere and asthenosphere (Naif et al., 2013; Sarafian et al., 2015; Baba et al., 2017b; Selway and O'Donnell, 2019). Furthermore, questions regarding the robustness of these studies remain due to their limited consideration for how these conductivity structures evolve with respect to lithospheric age (Fig. 3.1).

In this chapter I propose a solution for these issues. The chapter begins with the definition of my conductivity model from which I aim to constrain the Earth's upper mantle. This model utilises Hashin-Shtrikman (HS) bounds to characterise the bulk conductivity of the mantle in terms of a resistive matrix, comprised of either dry or hydrated mantle minerals, and partial melt, comprised of silicate and carbonatite melt. To ensure this model incorporates temporal variations in conductivity structure, the temperature component of my reference model is calculated as a function of lithospheric age. I then assess the validity of this model by comparing the resulting conductivity structures to conductivity structures collated from the past four decades of MT studies from the Pacific Ocean (Fig. 3.2 and Tab. 3.1). From my analysis, I find my proposed conductivity model is capable of unifying the varied upper mantle conductivity structures from Pacific Ocean MT studies into a single model. This model also corroborates the hypothesis of hydration within the upper mantle while restricting partial melt to regions underlying young oceanic lithosphere.

It is worth noting that the data central to this analysis is likely to differ in quality due to a number of factors. Furthermore, most of these MT studies are situated offshore California and Hawaii. However my aim is to identify a standard conductivity model for the upper mantle from which conductivity anomalies may be identified, comparable to standard seismic velocity models. As such, I believe subtle variations due to innovations over the past 50 years and the uneven distribution of MT studies from the Pacific Ocean will be of negligible importance. Furthermore, inconsistencies in conductivity structures interpreted from data collected from nearby regions were identified in the study of Baba et al. (2017b) complicates the issue of data quality even today.

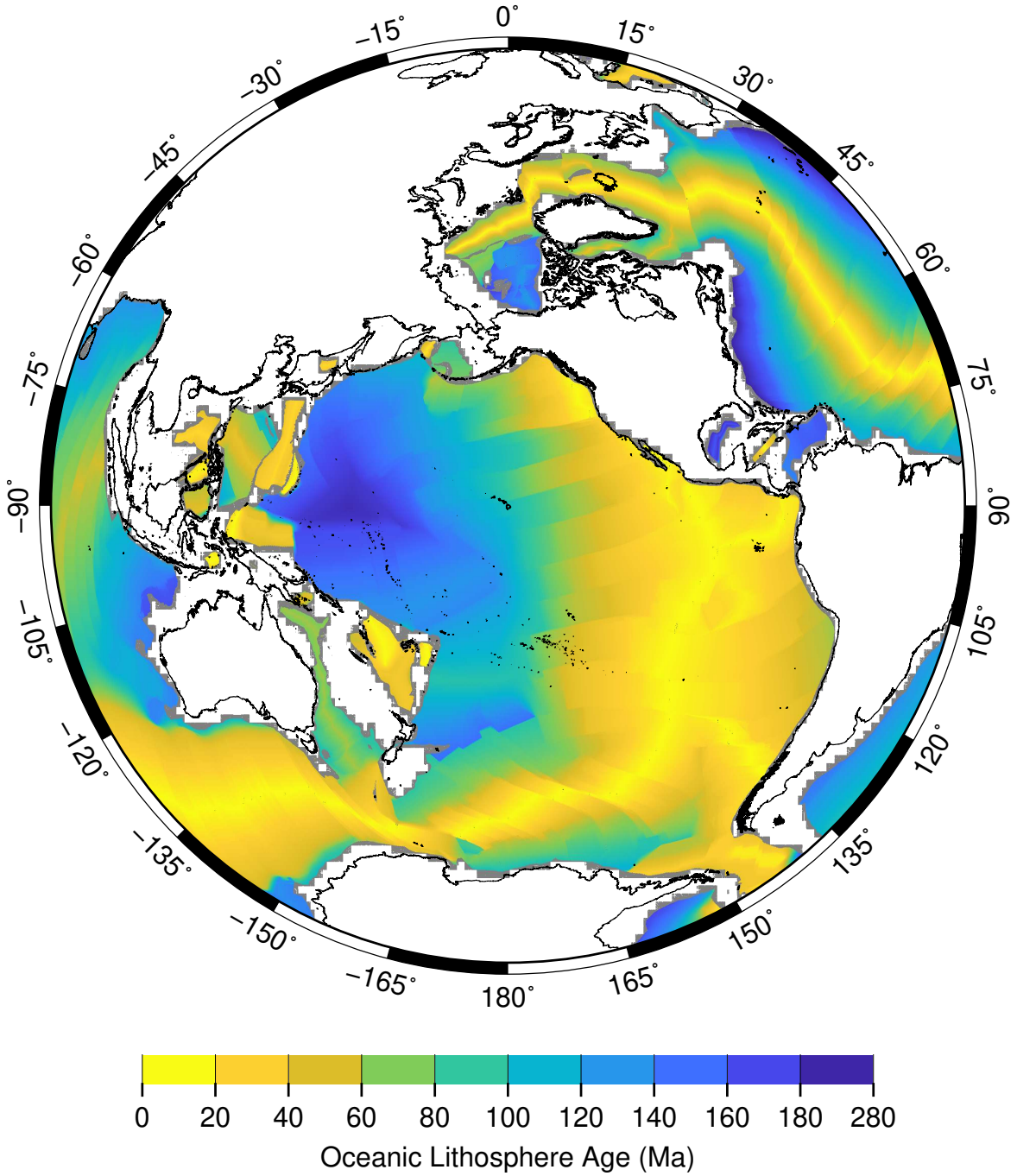

Figure 3.1: Azimuthal equidistant projection of the Pacific Ocean centred on Hawaii, United States of America. Map coloured with respect to oceanic lithosphere age (Ma) data from Müller et al. (2016).

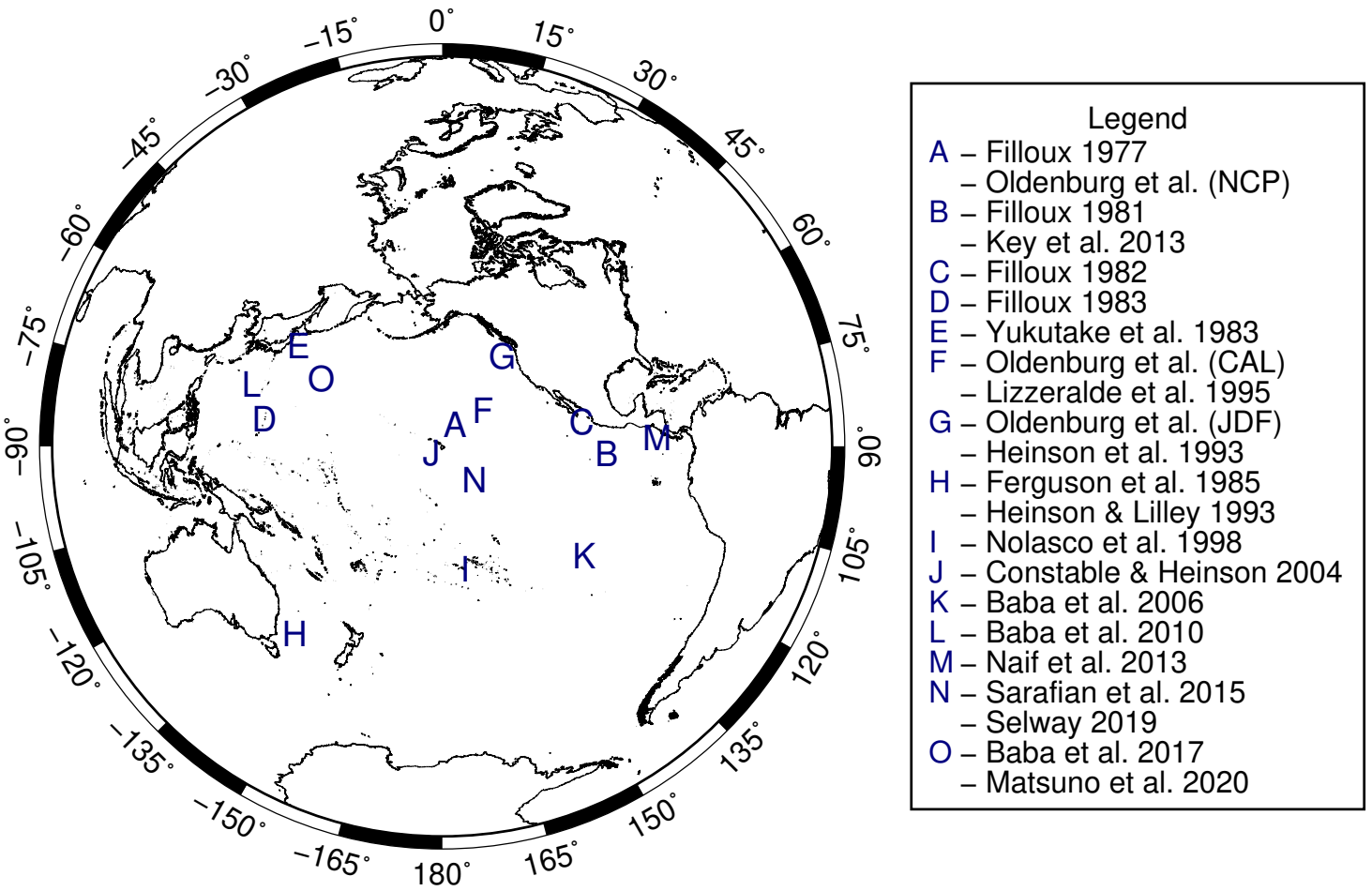

Figure 3.2: Azimuthal equidistant projection of the Pacific centred on Hawaii. Letters denote the location of ocean-bottom MT surveys from the Pacific Ocean. Multiple studies denoted by the same letter were approximately from the same location.

Table 3.1: Averaged MT survey locations from the Pacific Ocean. Oceanic lithosphere age data from Müller et al. (2016). ! denotes studies which had their resistivity profile estimated from published Figs. * denotes studies which had their longitude and latitude estimated.

Author	Latitude °	Longitude °	Oceanic Lithosphere Age (Ma)
Filloux (1977) Fig. 5	26.6	-151.2	66.8
Filloux (1981) Fig. 6 - Station 1 !	12.1	-103.5	0.6
Filloux (1981) Fig. 6 - Station 2 !	12.3	-102.8	2.1
Filloux (1982) Fig. 7 - Model A !	21.2	-108.9	5.2
Filloux (1983) Fig. 7 - Station 1 !	18.0	144.5	3.2
Filloux (1983) Fig. 7 - Station 2 !	18.1	146.8	146.9
Yukutake et al. (1983) Fig. 6 - 10 Layer !	39.5	145.3	131.5
Oldenburg et al. (1984) Fig. 2 - CAL !	29.4	-140.1	67.2
Oldenburg et al. (1984) Fig. 2 - JDF !*	47.0	-129.0	0.3
Oldenburg et al. (1984) Fig. 2 - NCP !	26.6	-151.2	66.8
Ferguson et al. (1985) Fig. 4 - Solid Line !	-37.6	156.0	55.4
Heinson and Lilley (1993) Fig. 8 Model Y !*	-39.0	155.0	58.2
Heinson et al. (1993) Fig. 10 !	44.5	-130.4	0.1
Lizarralde et al. (1995) Fig. 7a - Horizontal Average	31.2	-142.3	47.5
Nolasco et al. (1998) Fig. 6a	-17.8	-148.7	68.7
Constable and Heinson (2004) Fig. 7 - Western Edge !	17.9	-159.0	98.1
Baba et al. (2006) Fig. 3a - Above Ridge Axis !*	-16.0	-113.0	0.0
Baba et al. (2010) Fig. 7	24.8	137.1	25.6
Naif et al. (2013) *	10.0	-87.5	23.4
Key et al. (2013) *	9.3	-104.3	0.0
Sarafian et al. (2015) Fig. 5	9.2	-145.6	70.4
Baba et al. (2017b) Fig. 11 - Area A	39.5	156.2	131.3
Baba et al. (2017b) Fig. 11 - Area B	31.5	163.6	139.9
Baba et al. (2017b) Fig. 11 - Area C	28.8	147.9	149.8
Baba et al. (2017b) Fig. 11 - Area D *	31.0	163.0	141.4
Selway and O'Donnell (2019)	9.2	-145.6	70.4
Matsuno et al. (2020) Fig. 14 - A-2	39.5	156.2	131.3
Matsuno et al. (2020) Fig. 14 - B-2	31.5	163.6	139.9

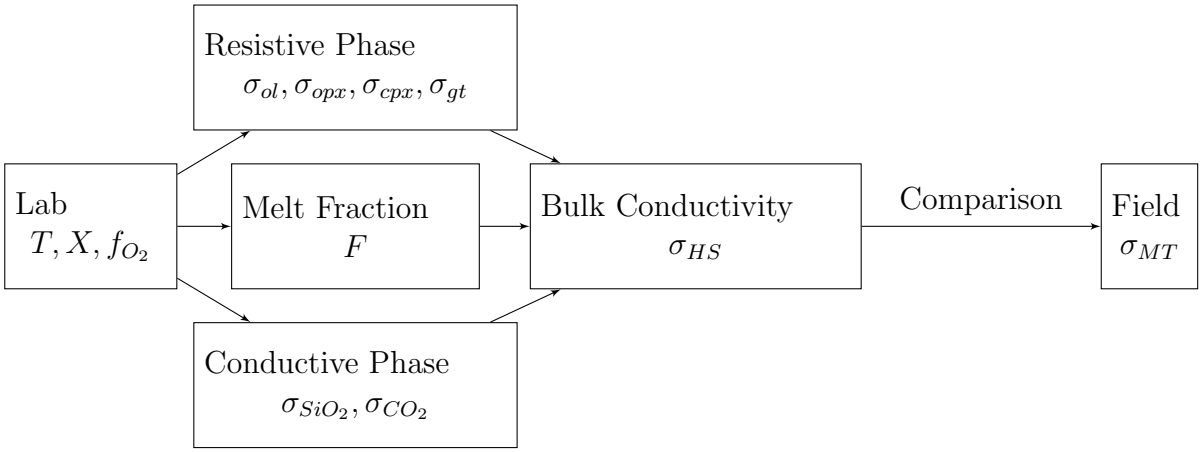

Figure 3.3: Schematic diagram describing the work flow of our proposed reference model.

3.2 Bulk Conductivity (σ^+_{HS} & σ^-_{HS})

I calculate the bulk conductivity of the upper mantle for an unknown distribution of conductive and resistive phases via HS bounds (Hashin and Shtrikman, 1962) (Fig. 3.4). HS bounds represent the narrowest conductivity bounds for a multiphase system with an interconnected (σ^+_{HS}) and disconnected (σ^-_{HS}) conductive phase (Hashin and Shtrikman, 1962) via the following equations:

$$\sigma^+_{HS} = \sigma_c + \frac{1-F}{\frac{1}{\sigma_m - \sigma_c} + \frac{F}{3\sigma_c}}, \tag{3.1}$$

$$\sigma^-_{HS} = \sigma_m + \frac{F}{\frac{1}{\sigma_c - \sigma_m} + \frac{1-F}{3\sigma_m}}. \tag{3.2}$$

The resistive phase represents a matrix conductivity (σ_m). Typically, the upper mantle consists of 60 - 80% olivine with the remaining 20 - 40% consisting of clinopyroxene, orthopyroxene, garnet, and minor phases (Khan, 2016). The conductive phase σ_c represents silicate and carbonatite melt conductivities (σ_{SiO_2} and σ_{CO_2} respectively). Early work by Shankland and Waff (1977) found that a melt fraction of a few percent is capable of satisfying conductivity anomalies within this region of the Earth. Evidence supports H_2O and CO_2 concentrations of $X_{H_2O} = 200 \pm 50$ ppm and $X_{CO_2} = 100 \pm 20$ ppm respectively (Hirschmann, 2018). However, the solubility of H_2O decreases with respect to temperature (Özaydın and Selway, 2020). As such, I utilise H_2O and CO_2 concentrations of $X_{H_2O} = 100$ ppm and $X_{CO_2} = 60$ ppm which are determined from mid-ocean ridge basalts (Hirschmann et al., 2009; Hirschmann and Dasgupta, 2009). These volatiles are then partitioned between the matrix and

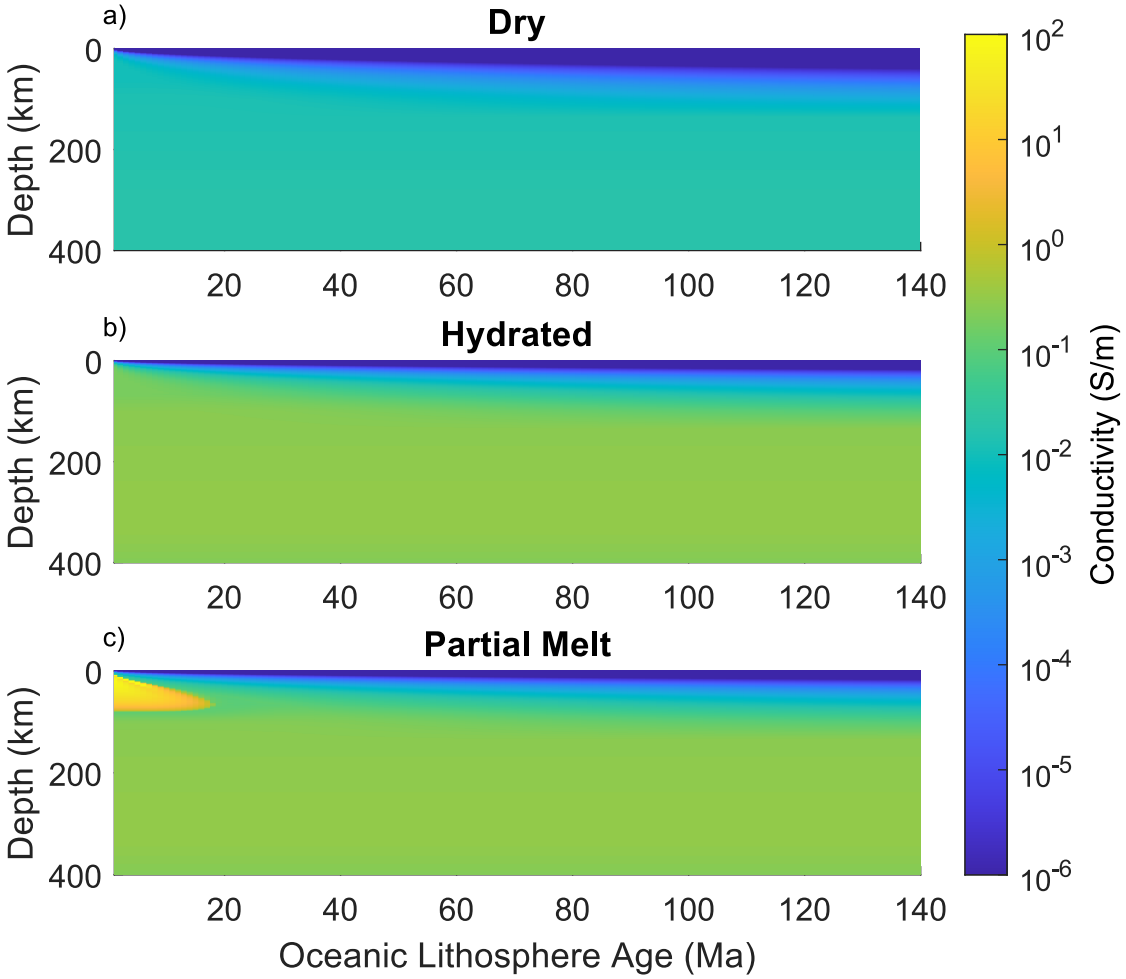

Figure 3.4: a), b), and c) display a pseudosection of the bulk conductivity as calculated by my forward model as a function of depth beneath the ocean floor (km) and oceanic lithosphere age (Ma) assuming the upper mantle is dry, hydrated, or partially melted respectively.

conductive phases using the equations of Katz et al. (2003). The concentration of H_2O and CO_2 is then further partitioned between the constituent components of the conductive phase (Fig. 3.5). Increasing the concentrations of H_2O and CO_2 would further depress the solidus and increase the melt fraction F within our reference model. Subsequently, σ^+_{HS} would increase and approach σ_c as relative proportion of the conductive and resistive phases are governed by the melt fraction F. Furthermore, this model makes no distinction between mantle minerals when partitioning water within the solid phase. This causes the model to overestimate the matrix conductivity from mantle minerals. However, testing found that our conclusions are unaffected by this overestimation.

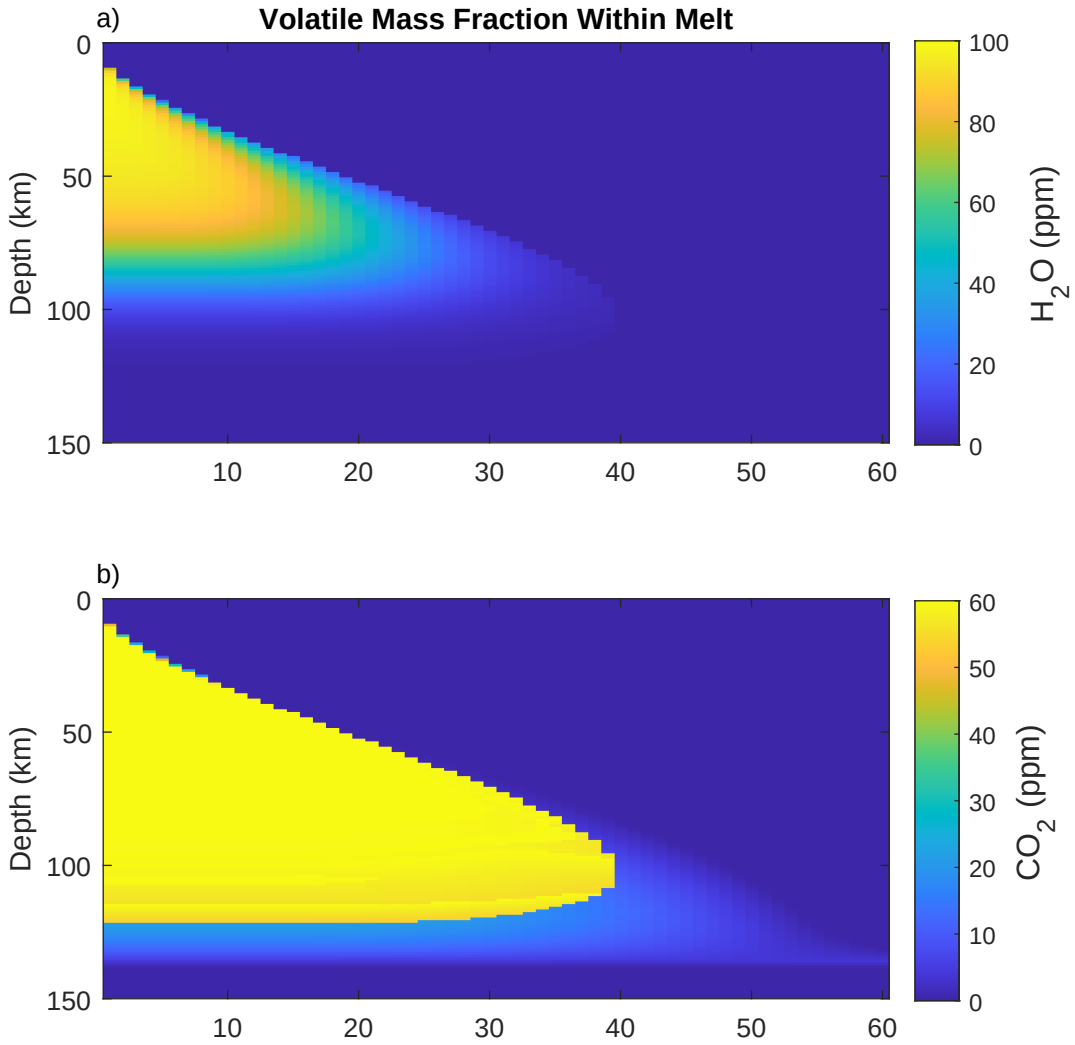

Figure 3.5: a) and b) display the distribution of H_2O and CO_2 within the melt phase function of depth (km) and oceanic lithosphere age (Ma).

3.2.1 Temperature (T)

It is important to remember that conductivity is governed by an Arrhenius relationship (Tyburczy and Fisler, 2013; Khan, 2016) as given by:

$$\sigma = \sigma_0 \exp\left(-\frac{H}{\kappa_B T}\right) \tag{3.3}$$

Therefore, I calculate temperature as a function of depth beneath the ocean floor and oceanic lithospheric age (Fig. 3.6). The following temperature calculations assume no thermal anomalies exist within the mantle. I utilise the model of Hasterok (2013) to define the geothermal gradient for regions of the Earth which primarily transport heat via thermal conduction. Within this region temperatures increase rapidly with depth. However as depth approaches the asymptotic plate thickness of 90 km, temperatures asymptote towards the mantle temperature of 1,364 K (Hasterok, 2013). Beyond the asymptotic plate thickness, heat is primarily transported via convection resulting in temperatures which increase slowly via adiabatic processes. As such, an adiabatic geothermal gradient of 0.3 $°C$ is assumed for this region resulting in the temperature relation:

$$T(z,t) = \begin{cases} \frac{T_m z}{L} + \frac{2}{\pi}\left(\sum_{n=1}^{\infty} \frac{\sin(C_n z)\exp\left(-C_n^2 \kappa t\right)}{n}\right) & \text{if } z \leq L \\ T_m + \delta T z \text{ if } z > L \end{cases}, \tag{3.4}$$

$$C_n = \frac{n\pi}{L},$$

$$\kappa = \frac{k}{\rho_m C_p},$$

where κ is thermal diffusivity ($mm^2\ s^{-1}$), $k = 3.5$ W m^{-1} K^{-1} is thermal conductivity, $\rho_m = 3{,}320$ kg m^{-3} is the mantle density, and $C_p = 1{,}168$ J kg^{-1} K^{-1} is the specific heat capacity. A recent analysis of oceanic lithosphere thermal models by Richards et al. (2018) has shown a temperature-dependent thermal conductivity $k(t)$ which decreases from 7 W m^{-1} K^{-1} to 2 W m^{-1} K^{-1} over temperatures ranging from 0 °C to 1,600 °C. While this results in more accurate temperature calculations, results presented by McKenzie et al. (2005) suggest negligible differences when comparing the temperature profiles calculated from k and $k(t)$.

3.2.2 Matrix Conductivity (σ_m)

I utilise HS limits to calculate the matrix conductivity via the following:

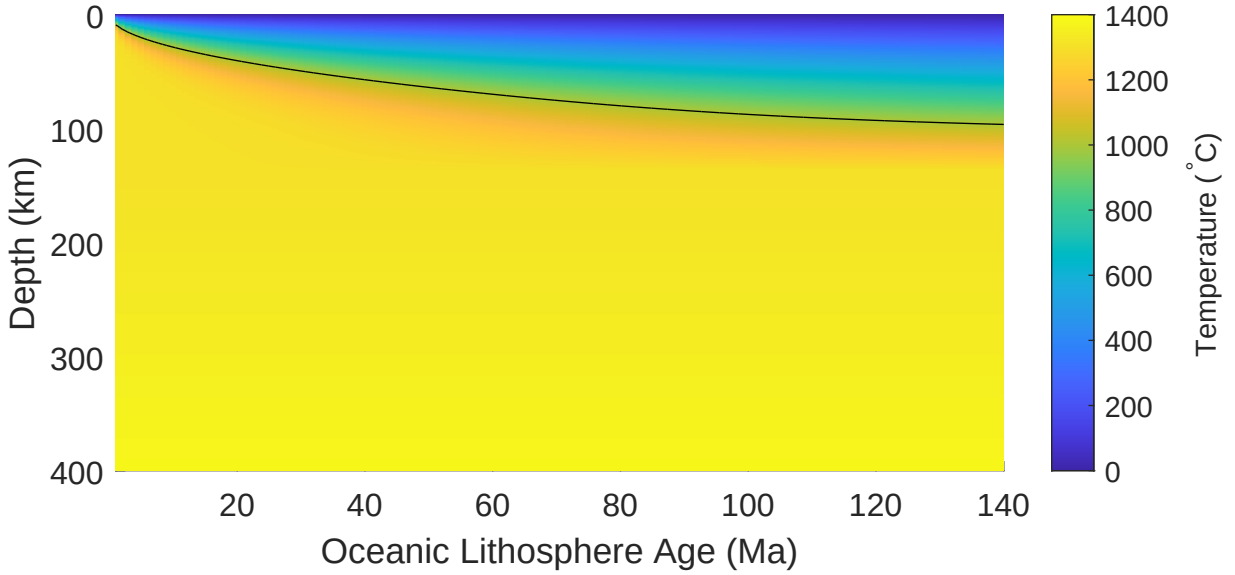

Figure 3.6: Temperature as a function of depth beneath the ocean floor (km) and oceanic lithosphere age (Ma). The black line represents a constant temperature of 1,000°C.

$$\sigma_{m\ HS\pm} = \left(\sum_{i=1}^{N} \frac{X_i}{\sigma_i + 2\sigma_\pm} \right) - 2\sigma_\pm. \tag{3.5}$$

where σ_i is the individual mineral conductivities (Fig. 3.7a), X_i is their respective phase proportion (Fig. 3.7b), and $\sigma_\pm$ corresponds to the maximum or minimum of the N mineral phases present.

As such, I first determine the proportions of olivine, orthopyroxene, clinopyroxene, and garnet (X^{ol}, X^{opx}, X^{cpx}, and X^{gt} respectively) within the upper mantle as a function of depth beneath the ocean floor (Fig. 3.7b) via a simplified version of the mantle mineral phase proportions presented by Stixrude and Lithgow-Bertelloni (2011). For simplicity, this model assumes the composition of the mantle is laterally homogeneous.

The conductivities of hydrous olivine are then calculated via a combination of the SEO3 model of Constable (2006) for the Quartz-Fayalite-Magnetite buffer and the universal hydrous olivine model of Gardés et al. (2014):

$$\sigma_{SEO3} = Fe^*_{Mg}\mu_{Mg}e + 2V''_{Mg}\mu_{Mg}e, \tag{3.6}$$

$$\sigma_{UHO} = \sigma_{0H_2O} X_{H_2O} \exp\left(-\frac{\Delta H_{H_2O} - \alpha X_{H_2O}^{1/3}}{\kappa_B T(z,t)}\right), \tag{3.7}$$

$$\sigma_{ol} = \sigma_{SEO3} + \sigma_{UHO}, \tag{3.8}$$

where σ_0 is the pre-exponential conductivity (S/m), $H = E + PV$ is activation enthalpy (kJ mol^{-1}), P is pressure (Pa), E is activation energy (kJ mol^{-1}), V is activation volume (m^3), T is temperature (K), and κ_B is Boltzmann's constant (eV). It is important to note the following alteration to the SEO3 model was made to correct for variable iron content (Hirsch et al., 1993):

$$X_{Fe} = (b_{Fe} + d_{Fe}) 5.536 C_{Fe}^{0.727}, \tag{3.9}$$

$$\mu_{Fe} = 1.22 \times 10^{-5} \exp\left(-\frac{2.0265 - 2.14 X_{Fe}^{1/3}}{\kappa_B T}\right), \tag{3.10}$$

where X_{Fe} is the concentration of iron, b_{Fe} is the iron defect concentration, d_{Fe} is the oxygen fugacity component of Constable (2006), C_{Fe} is the concentration of Fe^{3+} polarons, and μ_{Fe} is the mobility of iron. The remaining two hydrous minerals within my model are orthopyroxene and clinopyroxene. I utilise the models of Zhang et al. (2012) and Yang et al. (2011) to define orthopyroxene and clinopyroxene respectively:

$$\sigma_{opx} = \sigma_{0h} \exp\left(-\frac{H_h}{\kappa_B T(z,t)}\right) + \sigma_{0p} X_{H_2O} \exp\left(-\frac{H_p - \alpha X_{H_2O}^{1/3}}{\kappa_B T(z,t)}\right), \tag{3.11}$$

$$\sigma_{cpx} = \sigma_{0h} \exp\left(-\frac{H_h}{\kappa_B T(z,t)}\right) + \sigma_{0p} X_{H_2O}^{r} \exp\left(-\frac{H_p}{\kappa_B T(z,t)}\right). \tag{3.12}$$

The final mineral conductivity I define is the conductivity of anhydrous garnet utilising the model of Yoshino et al. (2008):

$$\sigma_{gt} = \sigma_{0h} \exp\left(-\frac{H_h}{\kappa_B T(z,t)}\right). \tag{3.13}$$

3.2.3 Melt Conductivity (σ_{SiO_2}, σ_{CO_2}) & Melt Fraction (F)

Zones of high conductivity within the asthenosphere have previously been attributed to partial melt (Naif et al., 2013). Therefore, the conductive phase represents the

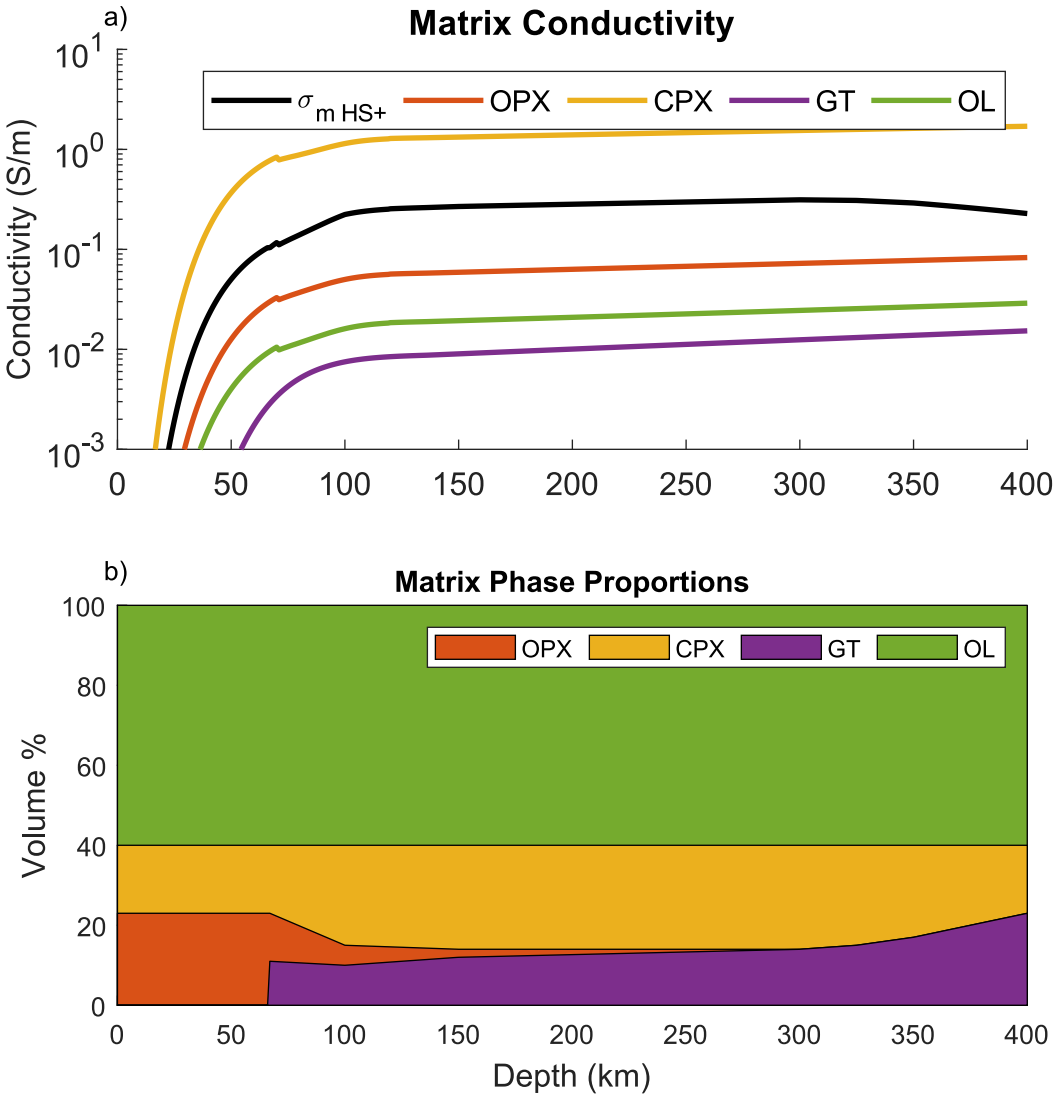

Figure 3.7: a) displays the electrical conductivity as a function of depth beneath the ocean floor (km) for orthopyroxene (Orange line), clinopyroxene (Yellow line), garnet (Purple line), olivine (Green line), and the HS upper limit calculated for the matrix (Black line). b) displays the phase proportion of orthopyroxene (Orange), clinopyroxene (Yellow), garnet (Purple), and olivine (Green) within the upper mantle as a function of depth beneath the ocean floor (km).

conductivity of silicate and carbonatite melt (σ_{SiO_2} and σ_{CO_2} respectively) via the models of Pommier and Le-Trong (2011) and Gaillard et al. (2008):

$$\sigma_{SiO_2} = \sigma_0^{SiO_2} \exp\left(-\frac{H_{SiO_2}}{kT}\right), \tag{3.14}$$

$$\sigma_{CO_2} = \sigma_0^{CO_2} \exp\left(-\frac{H_{CO_2}}{kT}\right), \tag{3.15}$$

where $\sigma_0^{SiO_2}$, $\sigma_0^{CO_2}$, H_{SiO_2} and H_{CO_2} represent the pre-exponential conductivity (S/m) and activation enthalpy (kJ mol^{-1}) for molten silicates and carbonatites respectively. However, evidence suggests melt fractions of up to $\sim 1\%$ are only likely to be present around mid-ocean ridges with significantly less melt available elsewhere (Hirschmann, 2010). Therefore to avoid overestimating available melt fraction, I combine results of Katz et al. (2003) and Dasgupta et al. (2007) to calculate available silicate and carbonatite melt fractions within the asthenosphere (Fig. 3.8a and b respectively). This model calculates the melt distribution from solidus temperatures and assumes that all melt is able to be extracted from the mantle. By comparing Fig. 3.8a) and b), we observe that our model predicts the fractional crystallisation of carbonatite rocks from the total melt fraction as its SiO_2 content increases (Yaxley et al., 2022). It is important to consider the significant drop in melt productivity ($\delta F/\delta T$) associated with the depletion of clinopyroxene resulting in a change from a melting reaction dominated by CPX melting to one dominated by OPX melting (Hirschmann et al., 1998). For this reason, I first calculate the melt fraction while clinopyroxene is available:

$$F_{Cpx-Out} = \frac{M_{Cpx}}{R_{Cpx}}, \tag{3.16}$$

where M_{Cpx} corresponds to the weight fraction of clinopyroxene within the sample being melted and R_{Cpx} is the reaction coefficient of clinopyroxene. From this, I then define the total melt fraction available via:

$$F = \begin{cases} \frac{T-(T_{Solidus}-\Delta T(X_{H_2O}(X_{H_2O}^{Bulk},P,F))-\Delta T(X_{CO_2}(X_{CO_2}^{Bulk},P,F)))}{T_{Liquidus}^{Lherz}-T_{Solidus}}^{1.5} & F \leq F_{Cpx-Out} \\ F_{Cpx-Out} + (1-F_{Cpx-Out})\left(\frac{T-T_{Cpx-Out}}{T_{Liquidus}-T_{Cpx-Out}}\right)^{1.5} & F > F_{Cpx-Out} \end{cases}. \tag{3.17}$$

From the total melt fraction, I'm able to define the silicate melt fraction F_{SiO_2} as a function of total melt fraction F and carbonatite melt fraction F_{CO_2}:

$$F_{SiO_2} = F - F_{CO_2}, \tag{3.18}$$

where carbonatite melt fraction is calculated via the ratio of carbonatite melt fraction to total melt fraction R estimated from Dasgupta et al. (2005):

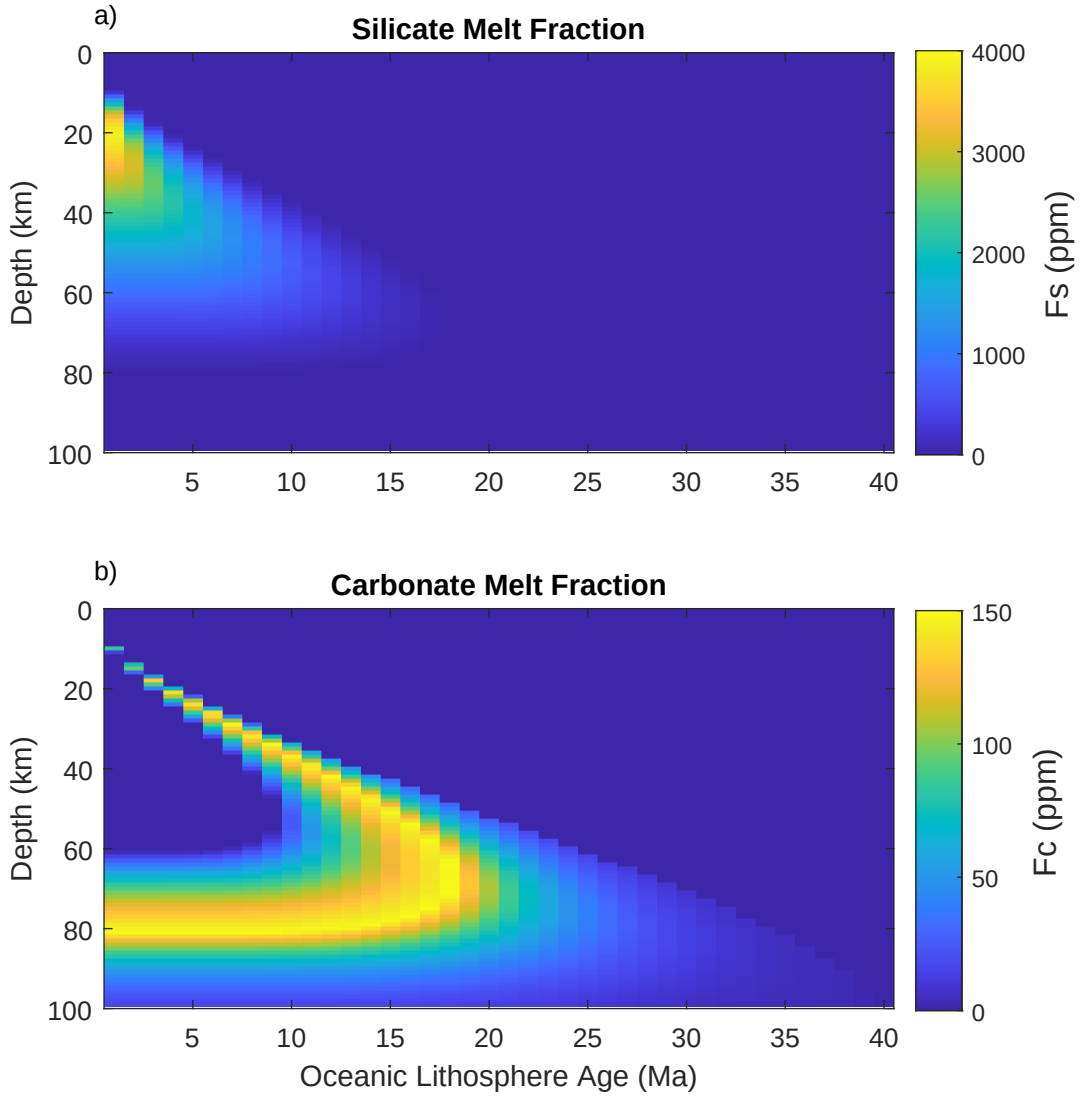

Figure 3.8: a) and b) display the melt fraction as a function of depth beneath the ocean floor (km) and oceanic lithosphere age (Ma) for silicate and carbonatite based melt respectively.

$$F_{CO_2} = F \times R. \tag{3.19}$$

$$R = -0.21488 + 3.0253 \times X_{CO_2}^{melt}. \tag{3.20}$$

$$X_{CO_2}^{melt} = \frac{X_{CO_2}^{bulk}}{D^{CO_2} + F(1 - D^{CO_2})}. \tag{3.21}$$

3.3 Results

Conductivity structures interpreted from Pacific Ocean seafloor MT show the presence of three distinct domains within the Earth which exhibit vastly different conductivity structures (Fig. 3.9). The first domain, between 50 km to 100 km, is defined by a wide range of conductivities which vary with respect to the age of the overlying oceanic lithosphere. Conductivities associated with the oldest oceanic lithosphere agree with the global conductivity model of Grayver et al. (2017). This model utilises time-varying magnetospheric and tidal magnetic fields. The motionally induced ocean currents which generate tidal magnetic fields experience galvanic coupling with the Earth. This enhances their sensitivity to resistive subsurface structures (Grayver et al., 2017). These secondary fields are measured by low-orbit satellites and inverted. From this inversion, both a structurally smooth L_2-norm (Fig. 3.9, green) and a structurally sparse L_1-norm (Fig. 3.9, magenta) solution was calculated (Fig. 3.9). HS upper and lower limits calculated for a partially melted and dry upper mantle underlying oceanic lithosphere of 1 Ma (Fig. 3.9, solid red line) and 140 Ma (Fig. 3.9, solid blue line) respectively envelop these conductivities.

The second domain, between 100 km and 200 km, represents an intermediate of surrounding domains with the global conductivity model of Grayver et al. (2017) shifting from the lower to the upper HS limit. This shift is also present in the measured conductivity profiles underlying older oceanic lithosphere. However, measured conductivity profiles underlying young oceanic lithosphere instead approximates the HS upper limit over a much smaller depth range. Due to the variable nature of the measured conductivity profiles with respect to depth within this domain, layer-averaged conductivies were not calculated. The third domain, between 200 km and 400 km, is defined by a homogenisation of conductivities towards the global conductivity model (Grayver et al., 2017).

Measured layer-averaged conductivities for the first domain, 50 km to 100 km, decrease rapidly for increasing lithospheric ages $\leq$ 50 Ma beyond which a linear decrease is observed (Fig. 3.10a). Modelled layer-averaged conductivities for both dry and hydrated

asthenospheres are unable to reproduce the variability observed for lithospheric ages ≤ 50 Ma. However, a hydrated asthenosphere is necessary to reproduce the magnitude of measured layer-averaged conductivities for ages > 50 Ma. In contrast, a partially melted asthenosphere produces layer-averaged conductivities which reproduce both the ≤ 50 Ma variability and the layer-averaged conductivity magnitudes.

Within the third domain, 200 km to 400 km, layer-averaged conductivities remain constant regardless of lithospheric age (Fig. 3.10b). At this depth melt is unstable due to high solidus temperatures for realistic H_2O contents (Hirschmann et al., 2009), and thus only dry and hydrated layer-averaged conductivities are considered. For this domain, both a dry and hydrated conductivity model reproduces the constant layer-averaged conductivity. However, only a hydrated upper mantle is capable of reproducing the magnitude of measured layer-averaged conductivities for this domain.

3.4 Discussion

Through an analysis of MT data from the Pacific Ocean across regions of varying lithospheric age, I identify 3 domains with distinct conductivity structures within the Earth. HS limits represent the upper and lower bounds of bulk conductivity for a resistive matrix with a perfectly interconnected and disconnected conductive phase (Hashin and Shtrikman, 1962) respectively. As such they represent the limits of conductivities possible for such a two-phase system. The HS upper limit for a partially melted upper mantle is observed to drop below a hydrated upper mantle (Fig. 3.10a). I interpret this response to be caused by the dehydration of the matrix by small amounts of melt. This partial melt is insufficient to counteract the dehydration of the matrix and results in a decrease in bulk conductivity. For the depth range of the first domain, 50 km to 100 km, I observe a relationship between conductivity and lithospheric age which I interpret a being representative of asthenospheric material (Fig. 3.10a). Forward modelled HS upper limit conductivities calculated for dry, hydrated, and partially melted upper mantle minerals show this domain is compatible with a primarily hydrated asthenosphere with some degree of partial melt beneath young oceanic lithosphere (Fig. 3.10). As such, my model predicts partial melting between 50 km and 100 km depth (Fig. 3.9). This depth range is compatible with the results of Baba et al. (2006), Key et al. (2013), and Naif et al. (2013) who found evidence supporting the presence of partial melt at depths shallower than 100 km for young oceanic lithosphere. Consequently, from this model I infer evidence supporting the hypothesis of enhanced conductivity due to a hydrated asthenosphere for depths shallower than 100 km with partial melting required under young oceanic lithosphere. Lastly, the second domain is interpreted to be an average of the first and third domains. This is caused by the volumetric nature

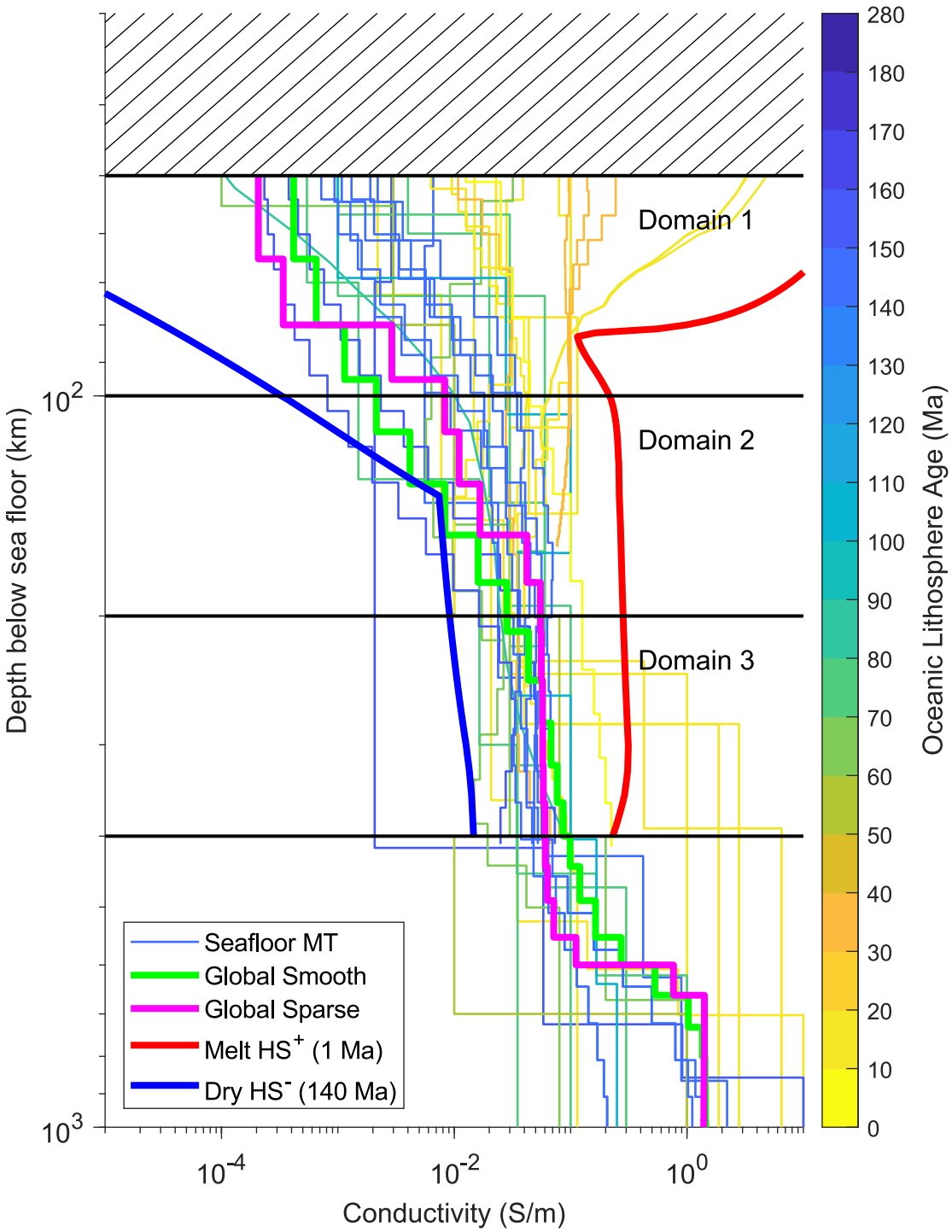

Figure 3.9: Conductivity structures from the Pacific Ocean coloured with respect to oceanic lithosphere age (Ma) data from Müller et al. (2016). Green and magenta lines correspond to the global conductivity model of Grayver et al. (2017). Red and blue lines correspond to Hashin-Shtrikman limits calculated by my conductivity model. The red line represents the Hashin-Shtrikman upper limit beneath 1 Ma oceanic lithosphere assuming partial melt. The blue line represents the Hashin-Shtrikman lower limit beneath 140 Ma oceanic lithosphere assuming no H_2O and CO_2.

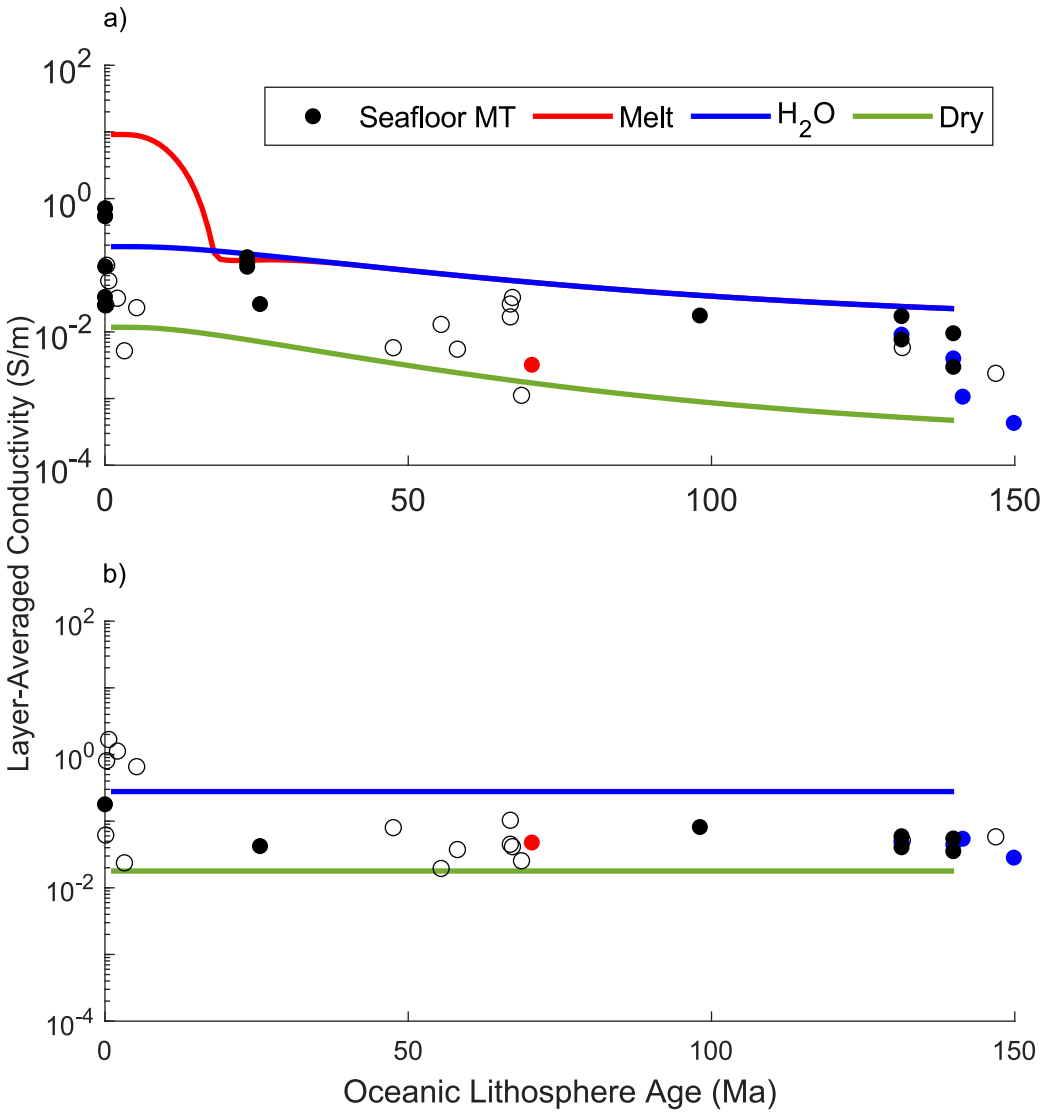

Figure 3.10: a) displays layer-averaged conductivities for domain 1 defined between 50 km and 100 km whereas b) displays layer-averaged conductivities for domain 3 defined between 200 km and 400 km. Lines represent the Hashin-Shtrikman upper limits calculated from my upper mantle conductivity model. Circles represent the layer-averaged conductivities calculated from MT surveys. Filled circles correspond to studies published after the year 2000. The red circle corresponds to the study of Sarafian et al. (2015) while the blue circles correspond to the study of Baba et al. (2017b)

of the MT method. As the skin depth increases, this average asymptotes towards the conductivity structure of third domain. As a result, I exclude the second domain from further analysis.

When investigating the third domain, between 200 km to 400 km depth, I observe that conductivities become largely homogenised towards a value comparable to the global conductivity model of Grayver et al. (2017) (Fig. 3.9 & 3.10b). Together with the depth of this domain, I interpret it as being representative of a largely homogeneous upper mantle. As partial melt is unstable at this depth, it is subsequently removed from my analysis of this domain (Hirschmann et al., 2009). Furthermore, I believe the cluster of pre-year-2000 layer-averaged conductivity outliers at approximately 0 Ma are due to modelling limitations. These limitations result in much thicker resistive layers more akin to the 660 km discontinuity (Grayver et al., 2017) as seen in Fig. 3.9, and therefore are neglected. Furthermore, instability at these depths may be a consequence of the long periods required to sample these depths which result in limited data availability. However, forward modelled HS upper limit conductivities calculated for dry, hydrated upper mantle minerals show most of the data for this region is compatible with hydration (Fig. 3.10b). Additionally, these results corroborate the results of Sarafian et al. (2015) who found evidence supporting the presence of significant hydration within the upper mantle. As such, I interpret these results as evidence supporting the hypothesis of hydration within the upper mantle. In conjunction with my earlier conclusion, I interpret these results as evidence supporting a standard conductivity model of the Earth which is devoid of thermal and compositional anomalies consisting of a hydrated upper mantle with limited amounts of partial melting restricted to young oceanic lithosphere.

Finally, measured conductivities within the first domain are observed to increase rapidly for young lithospheric ages beyond which a linear decrease is observed (Figs 3.9 & 3.10a). This may suggest the presence of a percolation threshold within the asthenosphere. I define a percolation threshold as the point beyond which the mean fracture aperture results in an interconnected fluid pathway subsequently enhancing fluid permeability and bulk conductivity (Kirkby and Heinson, 2017). As the mean aperture size decreases past the percolation threshold, the melt within our model will become trapped within the solid matrix. At this point, the bulk conductivity will represent the HS^{-} limit. This supports the hypothesis of unextractable melt within the matrix presented by Karato (2014) and Holtzman (2016). However, additional data is required to better constrain how conductivity varies within the asthenosphere for lithospheric ages $\leq$ 50 Ma.

3.5 Conclusions

Numerous studies have deployed MT receivers on the Earth's ocean floor. By taking advantage of the highly resistive and geologically simple nature of oceanic lithosphere, these studies aim to constrain the rheological contrast between the lithosphere and asthenosphere. However, a consensus is yet to be reached with these studies proposing the presence of hydration or partial melt within the asthenosphere. Furthermore, these studies fail to consider how this conductivity structure evolves with respect to lithospheric age. In this chapter, I created a conductivity model by combining laboratory conductivity measurements with a wealth of ocean-bottom MT data from the Pacific Ocean. This conductivity model serves as a representative model of the Earth's oceanic lithosphere and asthenosphere by integrating the age of the oceanic lithosphere. From this model, I'm able to reconcile hydration and partial melt within the asthenosphere and constrain the aforementioned rheological contrast for a range of lithospheric ages. As depth increases beyond the rheological contrast, I conclude that the conductivity structure of the mantle becomes homogeneous and hydrated. These conclusions have implications regarding our understanding of the mechanisms of plate motion.

Chapter 4

A Hybrid Oceanic-Continental MT Response Approach

The goal of the MT method is to constrain the subsurface conductivity structure of the Earth by utilising naturally occurring EM fields to measure induction within the Earth. For marine MT, these fields are attenuated and distorted by the non-uniform shape of the Earth's oceans, heterogeneities in the oceanic crust, and mantle electrical conductivity. In addition, induced magnetic fields are further attenuated and distorted by the vertical contrast in electrical conductivity between ocean water and oceanic lithosphere. This approximately four order of magnitude variation (Chesley et al., 2019) limits the usable bandwidth of ocean-bottom MT responses as a function of ocean depth. Away from mid-ocean ridges, hot-spots, and subduction zones, the magnitude of the inductive effects caused by heterogeneities in the Earth's oceans overshadows those of subsurface conductivity structures (Constable and Heinson, 2004; Naif et al., 2013; Key et al., 2013). This issue is so prolific it is considered one of the principal problems in modern geomagnetism (Fainberg, 1980; Key and Constable, 2011; Worzewski et al., 2012; Grayver et al., 2017; Wang et al., 2019). Despite this, oceanic MT studies continue to utilise EM field measurements collected from the bottom of the Earth's oceans. This may result in the inconsistencies in conductivity structures interpreted from data collected from nearby regions identified in the study of Baba et al. (2017b).

In this chapter I propose a strategy to address this in the form of a hybrid MT impedance. The chapter begins with an overview of the Anisotropy and Physics of the Pacific Lithosphere Experiment (APPLE) situated 800 km to 1,100 km offshore California, from which I source my MT data. Following an analysis of ocean-bottom EM fields, I identify the attenuation of induced ocean-bottom magnetic fields. This attenuation results in inconsistencies between adjacent receivers. Subsequently I investigate a hybrid impedance which utilises ocean-bottom electric fields and quasi-surface

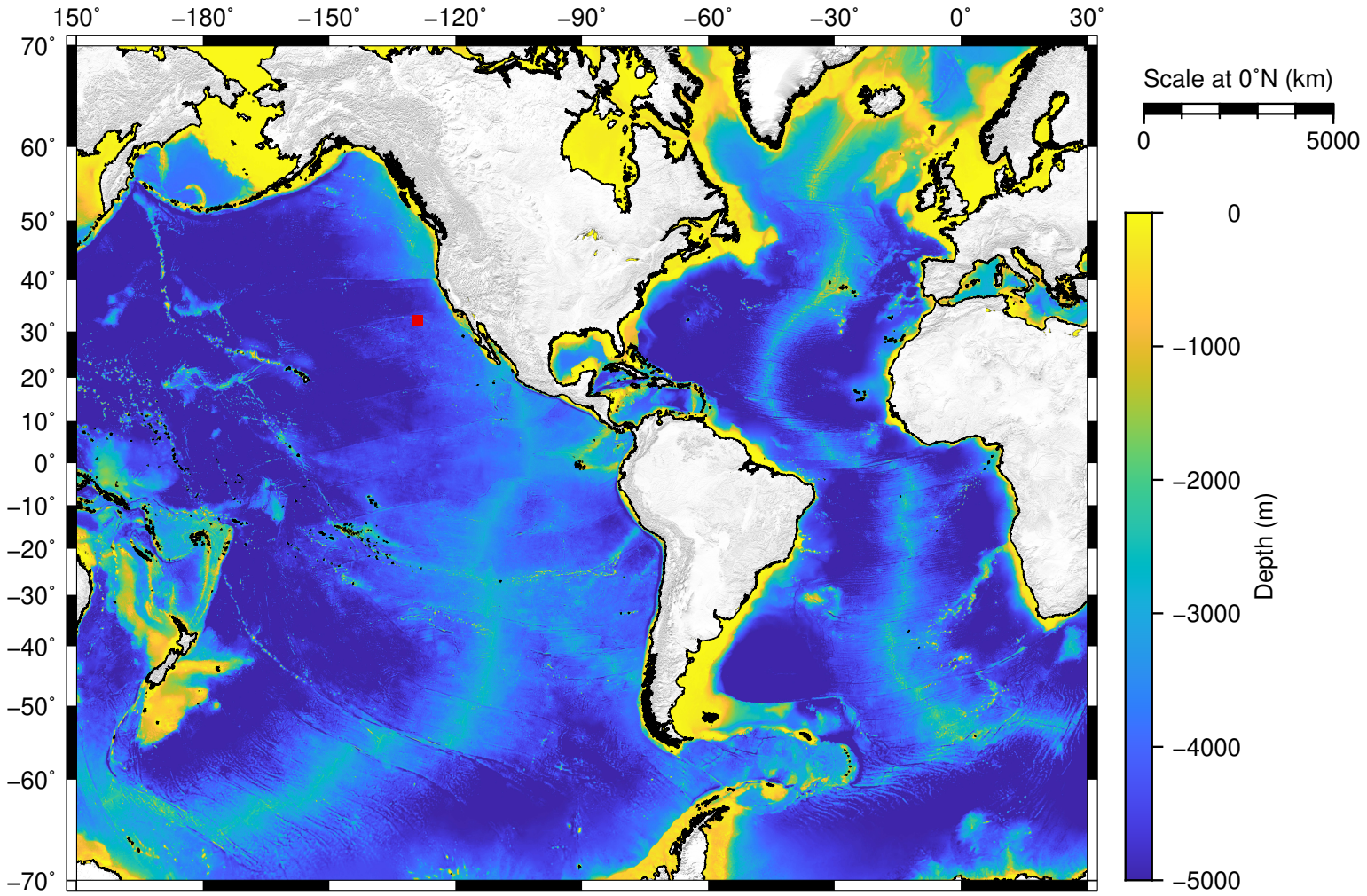

Figure 4.1: Bathymetry location map of Antarctica, Canada, North America, and South America. The red square corresponds to the centre of the APPLE cluster. The basemap utilises the ETOPO1 dataset of Amante and Eakins (2009).

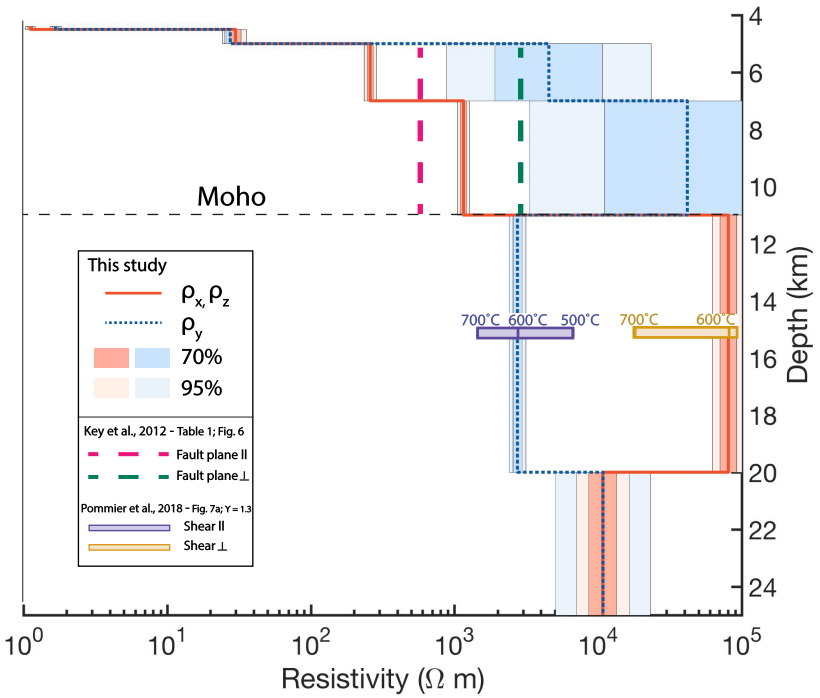

Figure 4.2: Preferred resistivity model with 70% and 95% confidence intervals derived from a linearised uncertainty analysis of Chesley et al. (2019). Orange, solid, and blue, dashed lines show resistivity in the paleo-ridge-parallel (x-z) plane and paleo-spreading (y) direction, respectively, for this study. Overlain dashed pink and green lines are resistivities for hydrated bending fault plane parallel and perpendicular directions, respectively, from the Middle America Trench (Key et al., 2012). Experimentally measured conductivity for sheared olivine samples (Pommier et al. (2018); shear strain = 1.3) extrapolated to lower temperatures for the shear parallel direction (purple rectangle) and shear plane perpendicular direction (gold rectangle).

magnetic fields. From this analysis, I find the calculation of a hybrid impedance extends the bandwidth of data collected during the APPLE study from just over one decade to approximately four decades. In conclusion, I propose that future oceanic MT studies should neglect to measure ocean-bottom horizontal magnetic fields and instead utilise hybrid impedances.

4.1 APPLE Experiment

The APPLE data were collected from MT receivers deployed offshore California between February and August 2001. This location was chosen for its simple bathymetry

and distance from major active tectonic boundaries (Fig. 4.1). Furthermore, the continental margin presents a relatively straight boundary from North America to South America (Fig. 4.1). The experiment sought to identify anisotropy within the Pacific plate via the collection of both controlled-source EM (CSEM) and MT data. From the CSEM data, Chesley et al. (2019) found evidence of significant electrical anisotropy within oceanic lithosphere which they interpreted to be the result of sub-vertical porosity induced by ridge-parallel normal faulting (Fig. 4.2). EM fields measured during the APPLE study are orientated such that the X and Y axes correspond to geographic east and north respectively. Furthermore, problems with the Kermit receiver during the APPLE study resulted in this receiver only measuring 8 hours of horizontal magnetic fields. As a consequence, the Kermit receiver utilises the horizontal magnetic fields measured by the nearby Trevor receiver.

4.1.1 Data Collection

The ocean-bottom receivers utilised during the APPLE study were comprised of a Flinders University (South Australia, Australia) three-component 0.1 nT fluxgate magnetometer and a Scripps Institution of Oceanography (California, United States of America) two-component silver chloride electrometer utilising a 10 m dipole (Constable, 2013). Both the magnetometer and electrometer had a sampling interval of 20 s. These receivers were deployed along a profile extending perpendicular to the north-south trend of the subducted Pacific-Farallon spreading centre. This results in an oblique view of the coastline and the current spreading direction (Figs 4.3, 4.4, and Tab. 4.1). The fossil spreading direction of Pacific-Farallon spreading centre is observable in the east-west trend of the Murray fracture zone situated north of the APPLE cluster (Michaud et al., 2006; Matthews et al., 2011) (Fig. 4.3). This spreading centre was terminated approximately 20 Ma following the breakup of the Farallon plate into the Cocos, Nazca, and Antarctic plates (Mammerickx et al., 1980). The current spreading direction is a consequence of this reorganisation following the establishment of a series of spreading centres throughout Baja California approximately 6 Ma to 10 Ma (Umhoefer, 2011). This current spreading direction is observable in the northwest-southeast trend of the Fieberling Tablemount, Fred Speiss Tablemount, and Hoke Seamount situated between the APPLE cluster and the Kermit ocean-bottom receiver (Fig. 4.3).

It is convenient to differentiate the MT receivers into groups based on the average ocean depth. The first group consist of four receivers deployed on the abyssal plain in ocean depths of $\leq$ 4,000 m and comprises 800 km of the approximately 1,100 km transect. Of these four receivers, two were deployed adjacent to the continental slope. The second group consists of the remaining five receivers which were deployed approximately 1,100 km offshore within a 30 km radius centred on 32.2°N 129°W in

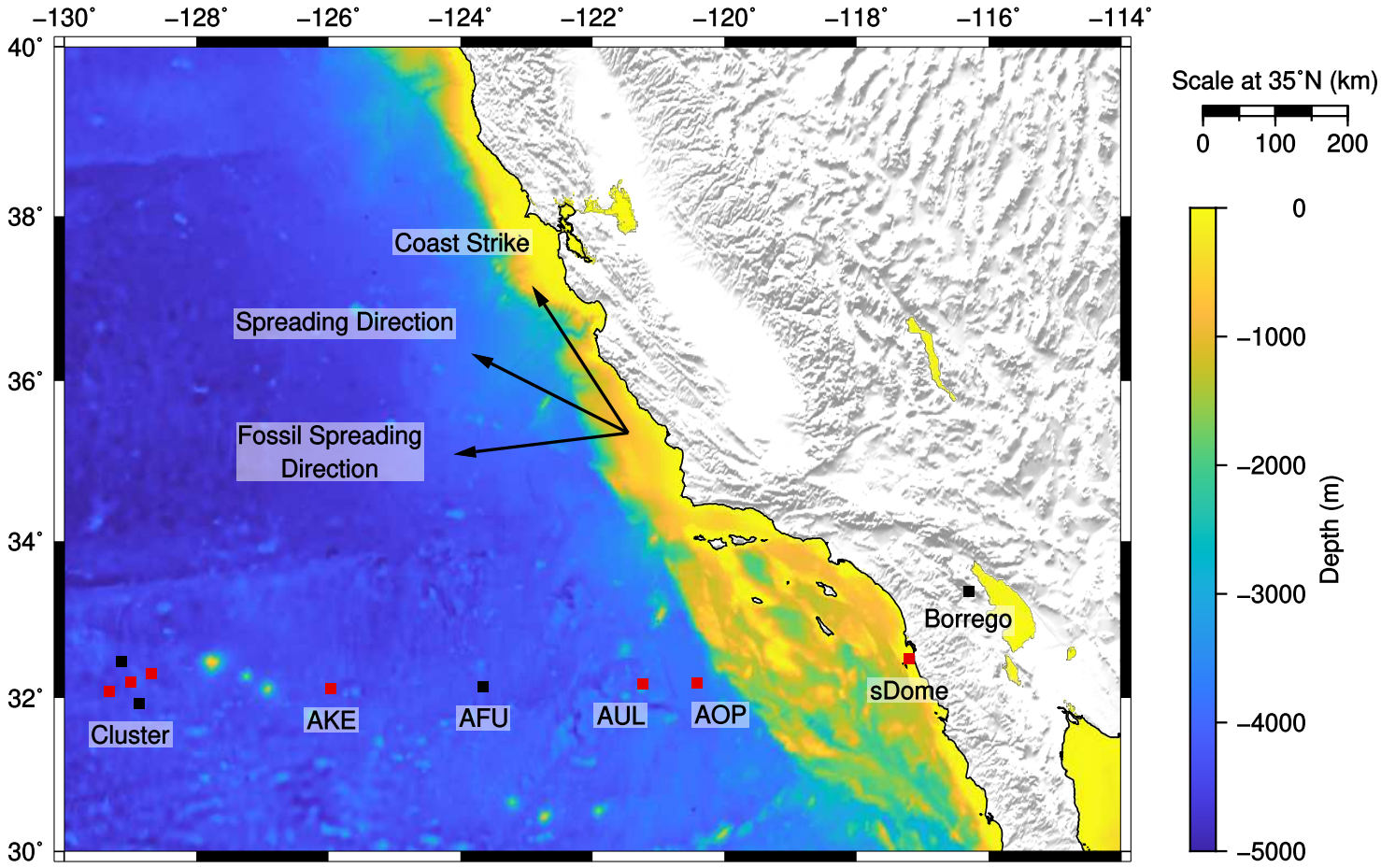

Figure 4.3: Bathymetry location map of the APPLE survey from offshore California with MT stations displayed as squares. Red squares correspond to stations utilised during Chapter 4 and Chapter 5. The arrows display the strike of the coastline, the fossil spreading direction, and the current spreading direction. The basemap utilises the ETOPO1 dataset of Amante and Eakins (2009). At 32°N latitude, the 1 arc-minute resolution of the ETOPO1 dataset corresponds to a distance of 1,600 m.

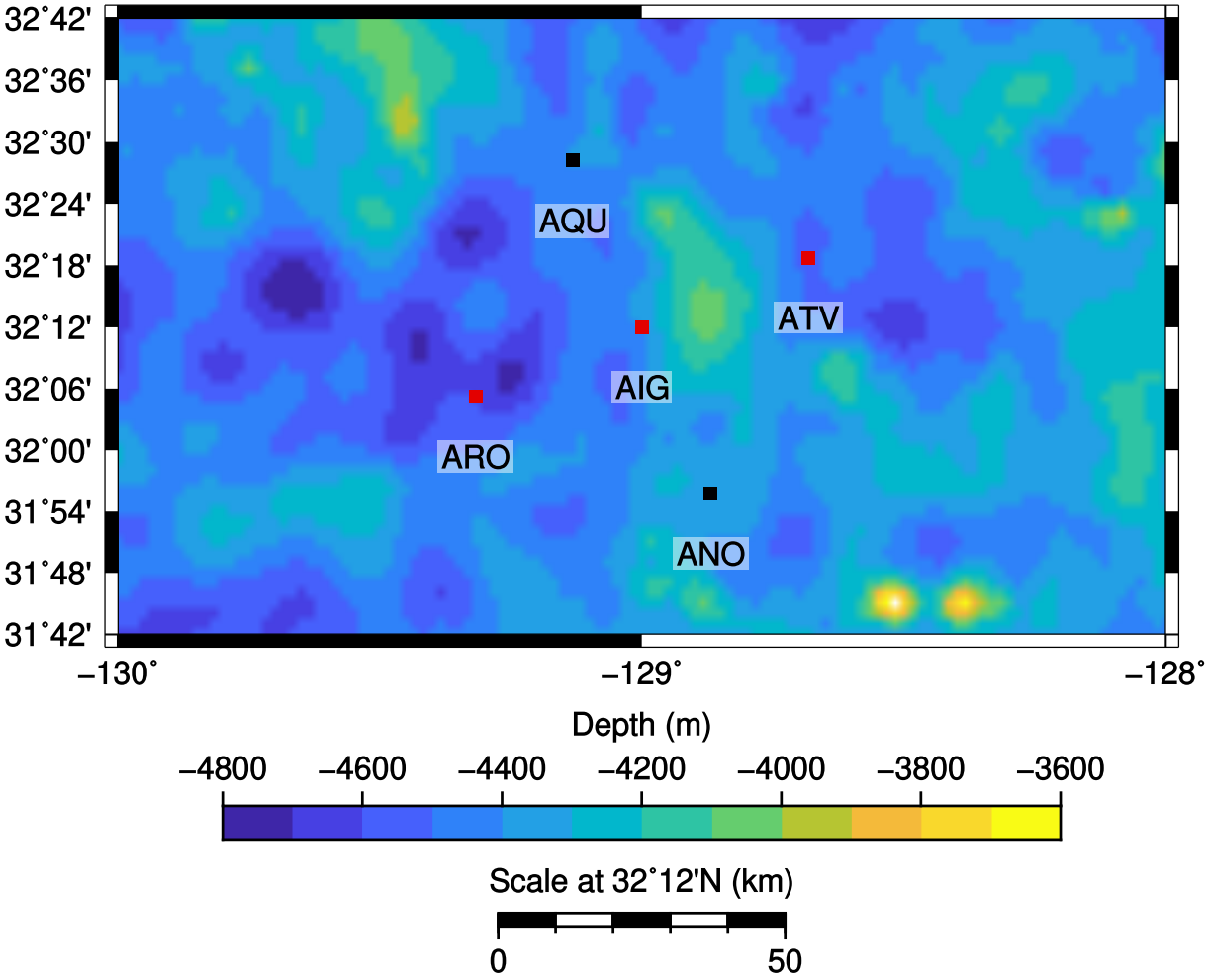

Figure 4.4: Bathymetry location map of the cluster portion of the APPLE survey from offshore California with MT stations displayed as squares. Red squares correspond to stations utilised during Chapter 4 and Chapter 5. The basemap utilises the ETOPO1 dataset of Amante and Eakins (2009).

ocean depths of 4,000 m to 4,500 m. These sites form a cross shape and allow for an assessment of local bathymetric effects via comparison of measured electromagnetic fields and the creation of an average ocean floor magnetotelluric response. In addition a three-component magnetometer was deployed at the Scripps Institution of Oceanography (California, United States of America).

It is important to note that the bathymetry of this region is poorly constrained as the 1 arc-minute resolution of the ETOPO1 dataset of Amante and Eakins (2009) corresponds to a distance of approximately 1,600 m at a latitude of 32°N. Furthermore, the sediment thickness on the ocean-floor is unknown. However, abrupt features in

Table 4.1: Locations of the APPLE MT instruments as well as their geographic coordinates and water depths as recorded by the instruments.

Name	Latitude °	Longitude °	Instrument Depth (m)	Location
Rhonda (ARO)	32.08	-129.32	4101	Cluster
Quail (AQU)	32.47	-129.13	4344	Cluster
Igor (AIG)	32.20	-129.00	4451	Cluster
Noddy (ANO)	31.93	-128.87	4351	Cluster
Trevor (ATV)	32.32	-128.68	4325	Cluster
Kermit (AKE)	32.12	-125.97	4165	Transect
Fuzzy (AFU)	32.15	-123.67	4129	Transect
Ulysses (AUL)	32.18	-121.25	3807	Continental slope
Opus (AOP)	32.18	-120.42	3855	Continental slope
sDome	32.50	-117.20	0	SIO, San Diego

bathymetry and sediment thickness are unlikely to be resolved by the ocean-bottom MT receivers due to the large distance between adjacent receivers.

4.2 Tidal Signal

The MT impedance is defined as the ratio of the horizontal electric and magnetic fields measured at the surface. While this is generally successful for continental studies, this methodology is problematic for ocean-bottom studies. In particular, EM fields induced by the motion of ocean water within the geoelectric field must first be removed before calculating impedance. The gravitational fields of the Moon serve as the primary driving force behind the motion of ocean water. As the moon orbits the Earth, its gravitational fields establish tidal bulges on opposite sides of the Earth. The periodicity of this process is 12.5 hours, corresponding to the Earth's tidal period (Chave et al., 2012). Figs 4.5 to 4.9 display the electric and magnetic fields measured during the APPLE study by the Rhonda, Opus, and sDome receivers. From these Figs, I observe a peak in both the electric and magnetic fields at 1.9 Cycles per Day (cpd) which corresponds to the tidal period of the Earth's ocean. I interpret this peak to be EM fields induced by the principal lunar (M2) signal.

4.3 Solar Quiet Daily Variation

Further complicating ocean-bottom MT studies is the induction of EM fields by solar quiet (S_q) daily variation. The S_q daily variation is caused by variations in the absorption of solar radiation within the atmosphere. This establishes an electrical

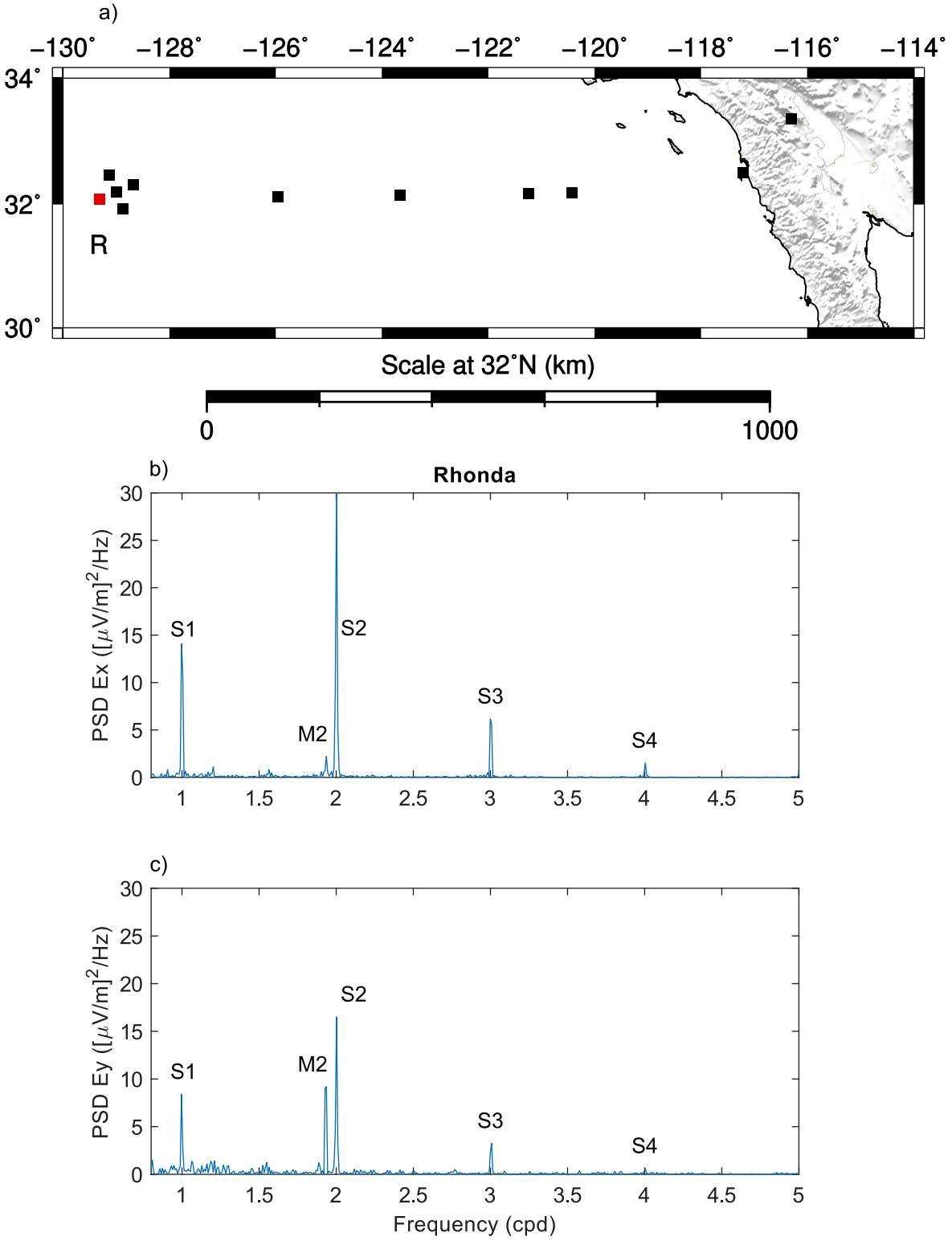

Figure 4.5: a) displays APPLE MT stations as squares. Red squares denote plotted stations. b) and c) display the power of E_x and E_y respectively as a function of frequency measured by the Rhonda receiver. Frequency is displayed in Cycles per Day (cpd).

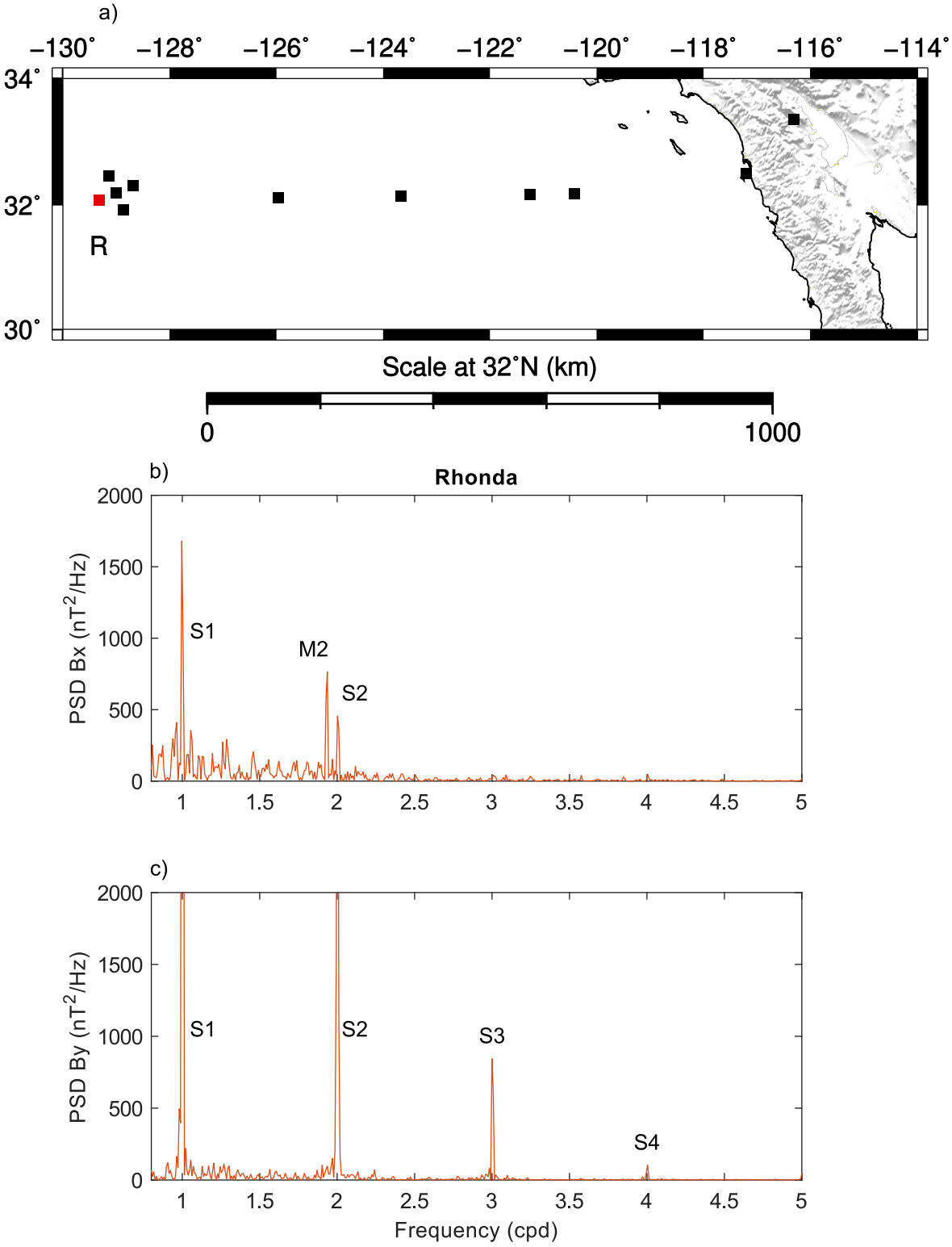

Figure 4.6: a) displays APPLE MT stations as squares. Red squares denote plotted stations. b) and c) display the power of B_x and B_y respectively as a function of frequency measured by the Rhonda receiver. Frequency is displayed in Cycles per Day (cpd).

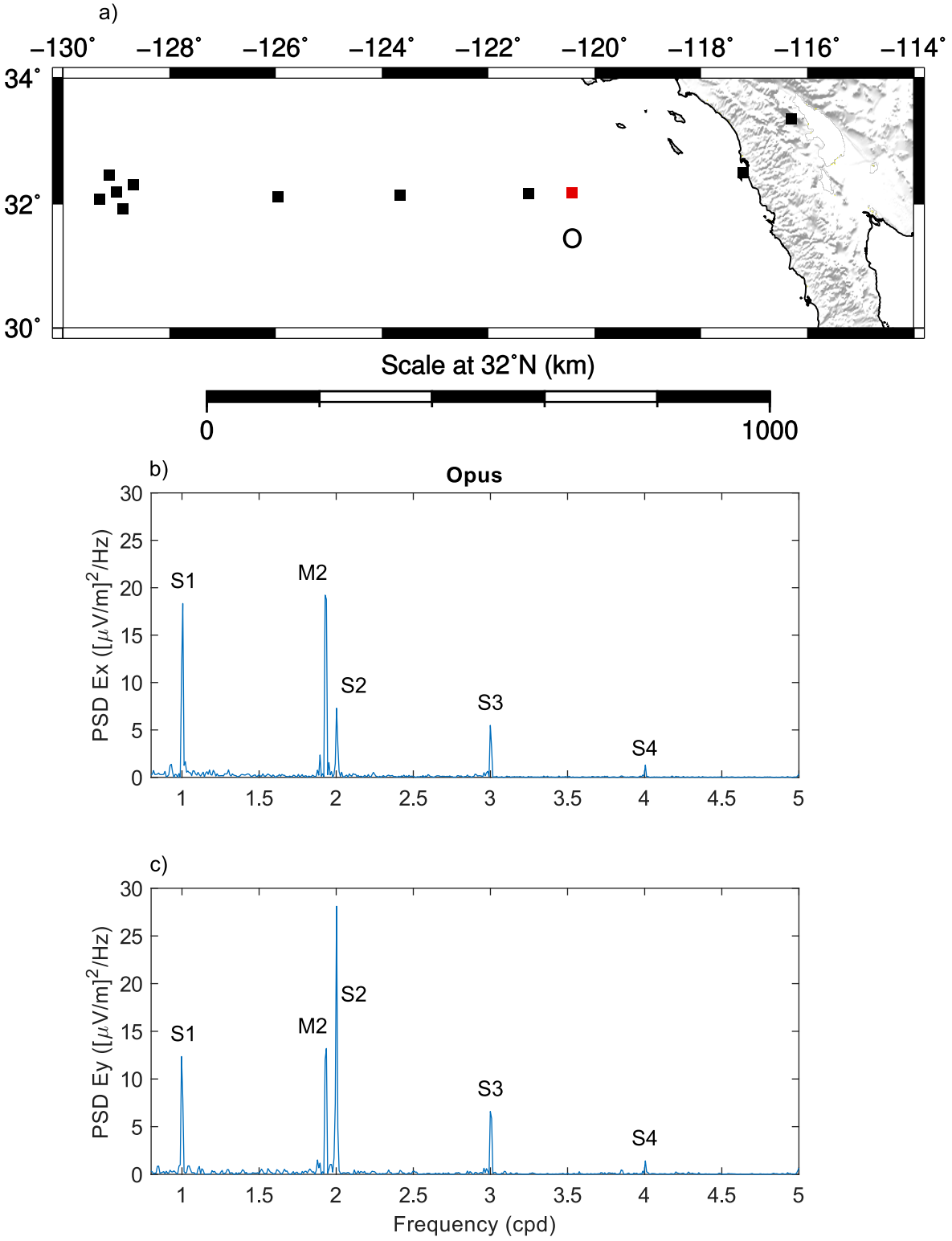

Figure 4.7: a) displays APPLE MT stations as squares. Red squares denote plotted stations. b) and c) display the power of E_x and E_y respectively as a function of frequency measured by the Opus receiver. Frequency is displayed in Cycles per Day (cpd).

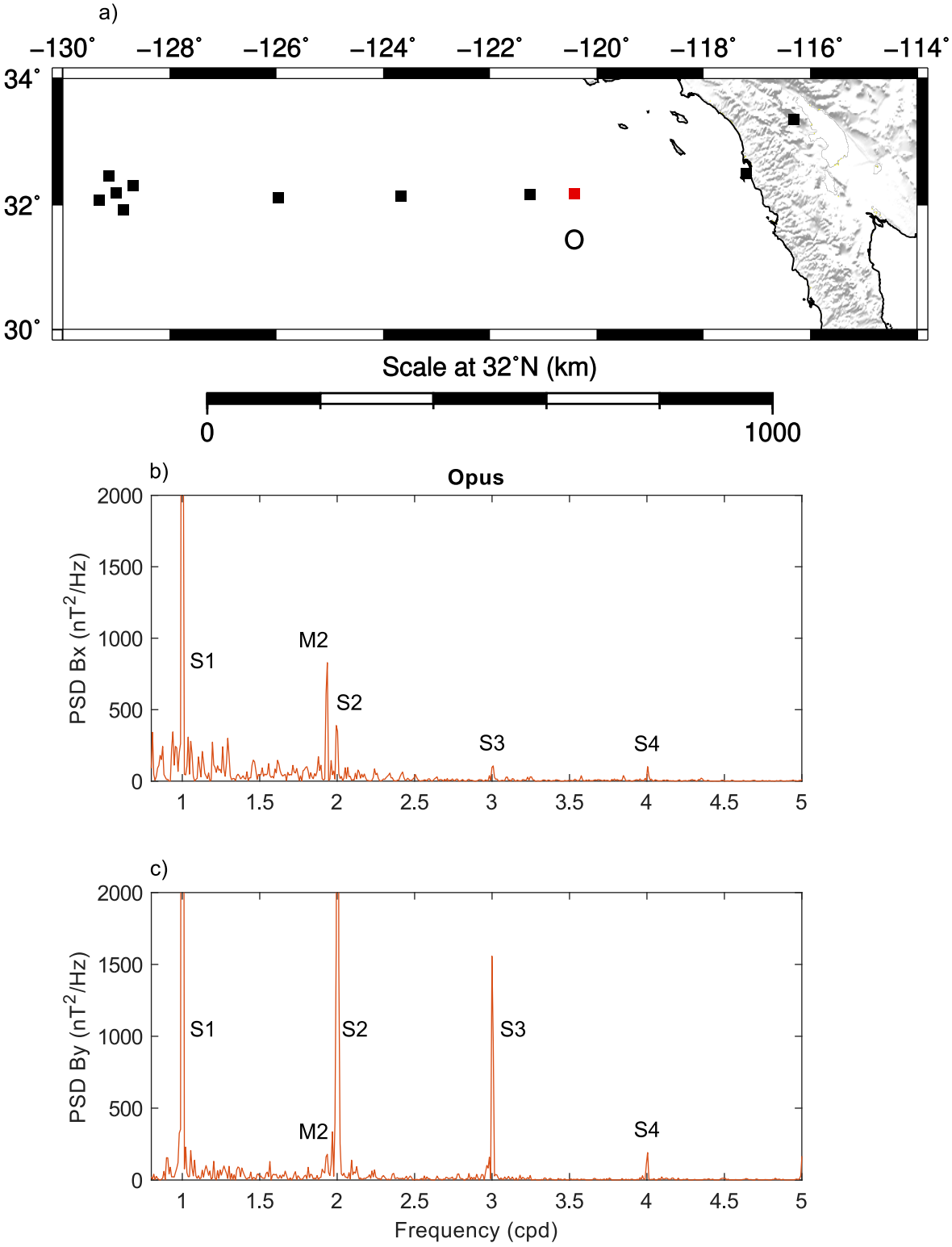

Figure 4.8: a) displays APPLE MT stations as squares. Red squares denote plotted stations. b) and c) display the power of B_x and B_y respectively as a function of frequency measured by the Opus receiver. Frequency is displayed in Cycles per Day (cpd).

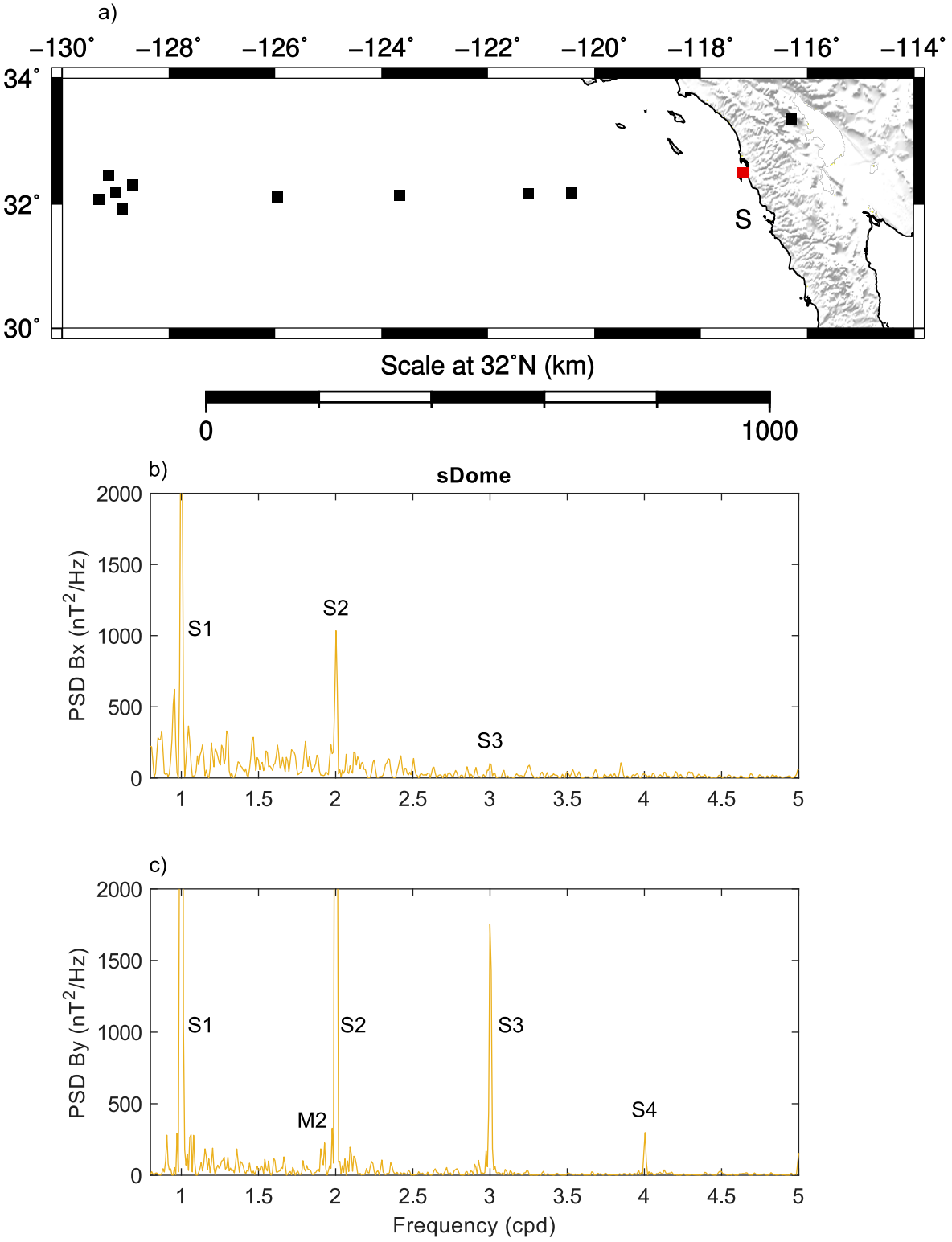

Figure 4.9: a) displays APPLE MT stations as squares. Red squares denote plotted stations. b) and c) display the power of B_x and B_y respectively as a function of frequency measured by the sDome receiver. Frequency is displayed in Cycles per Day (cpd).

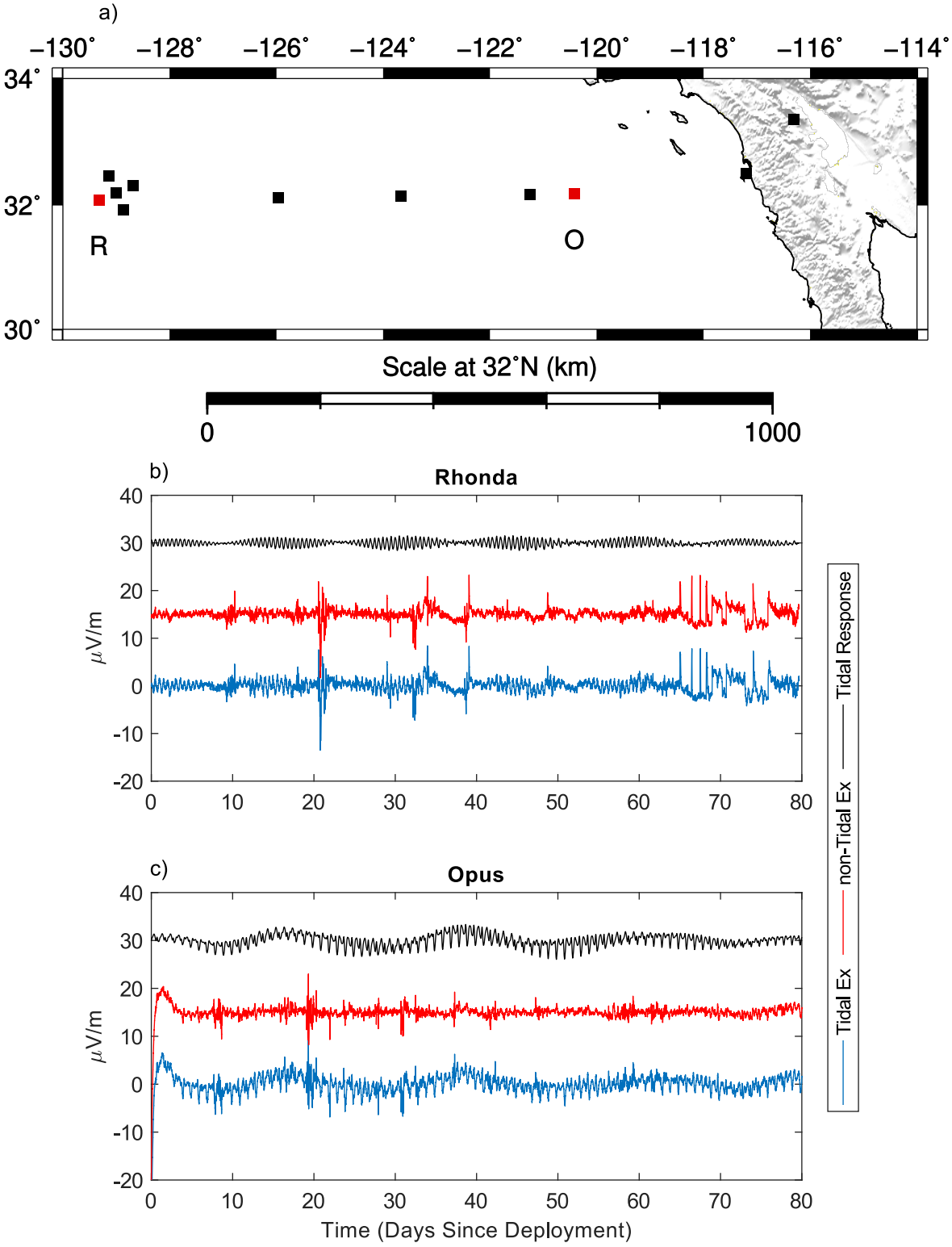

Figure 4.10: a) displays APPLE MT stations as squares. Red squares denote plotted stations. b) and c) displays E_x field data measured by the Rhonda and Opus receivers. The blue and red lines correspond to electric field data with and without tidal signals. The black line corresponds to the tidal signal removed during processing. This line can be generated by subtracting the non-tidal response from the tidal response. Red and black lines are offset along the y-axis to aid with readability.

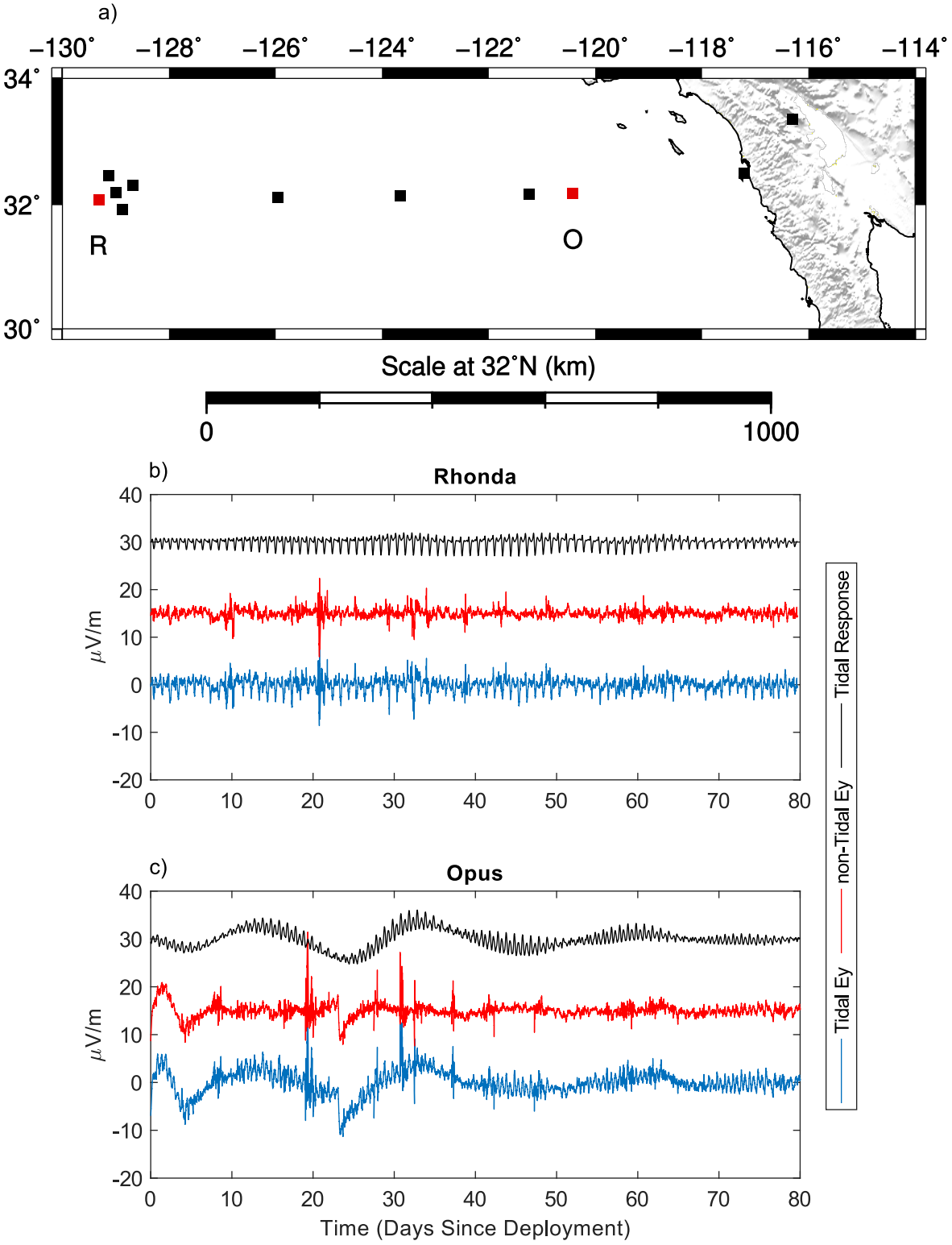

Figure 4.11: a) displays APPLE MT stations as squares. Red squares denote plotted stations. b) and c) displays E_y field data measured by the Rhonda and Opus receivers. The blue and red lines correspond to electric field data with and without tidal signals. The black line corresponds to the tidal signal removed during processing. This line can be generated by subtracting the non-tidal response from the tidal response. Red and black lines are offset along the y-axis to aid with readability.

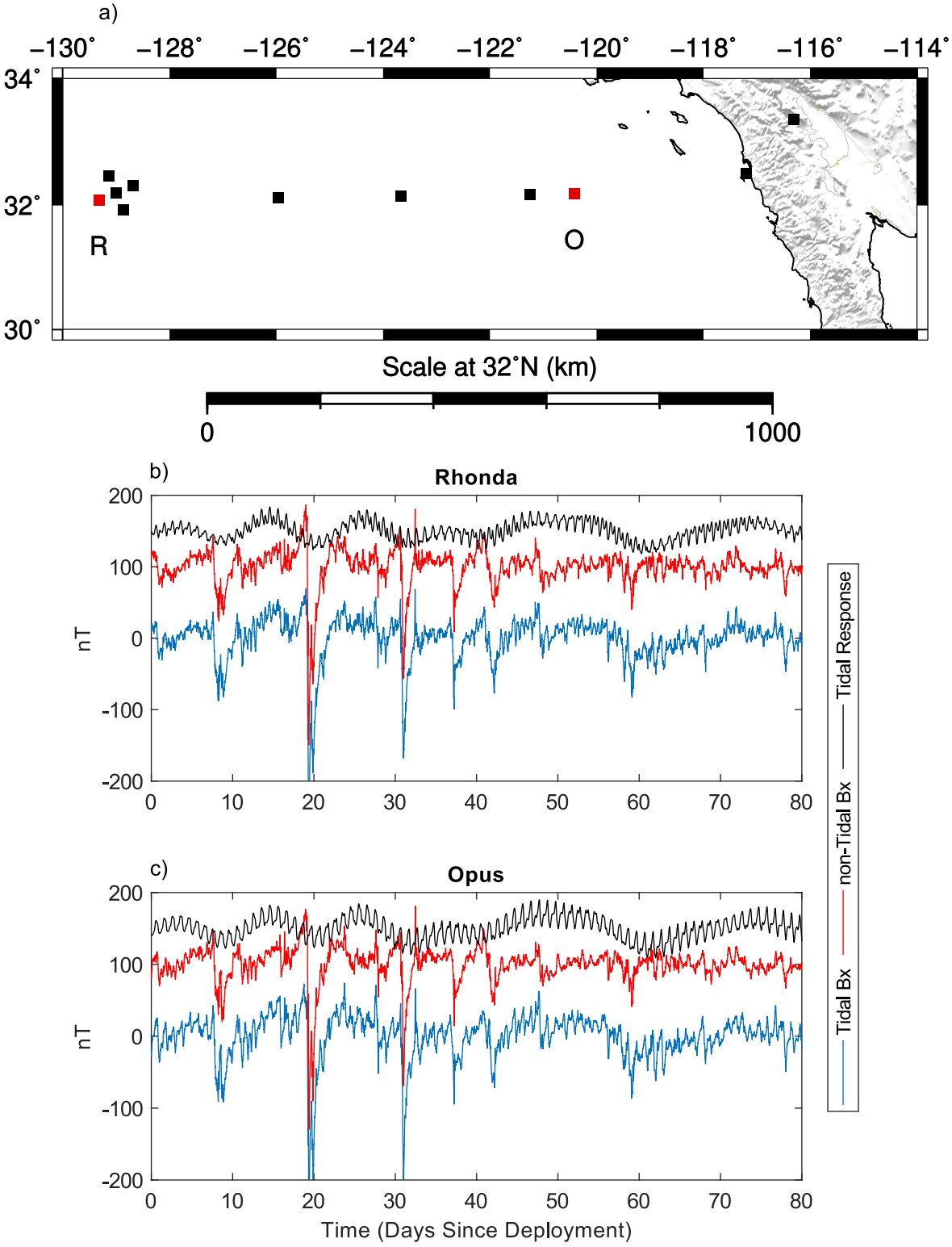

Figure 4.12: a) displays APPLE MT stations as squares. Red squares denote plotted stations. b) and c) displays B_x field data measured by the Rhonda and Opus receivers. The blue and red lines correspond to magnetic field data with and without tidal signals. The black line corresponds to the tidal signal removed during processing. This line can be generated by subtracting the non-tidal response from the tidal response. Red and black lines are offset along the y-axis to aid with readability.

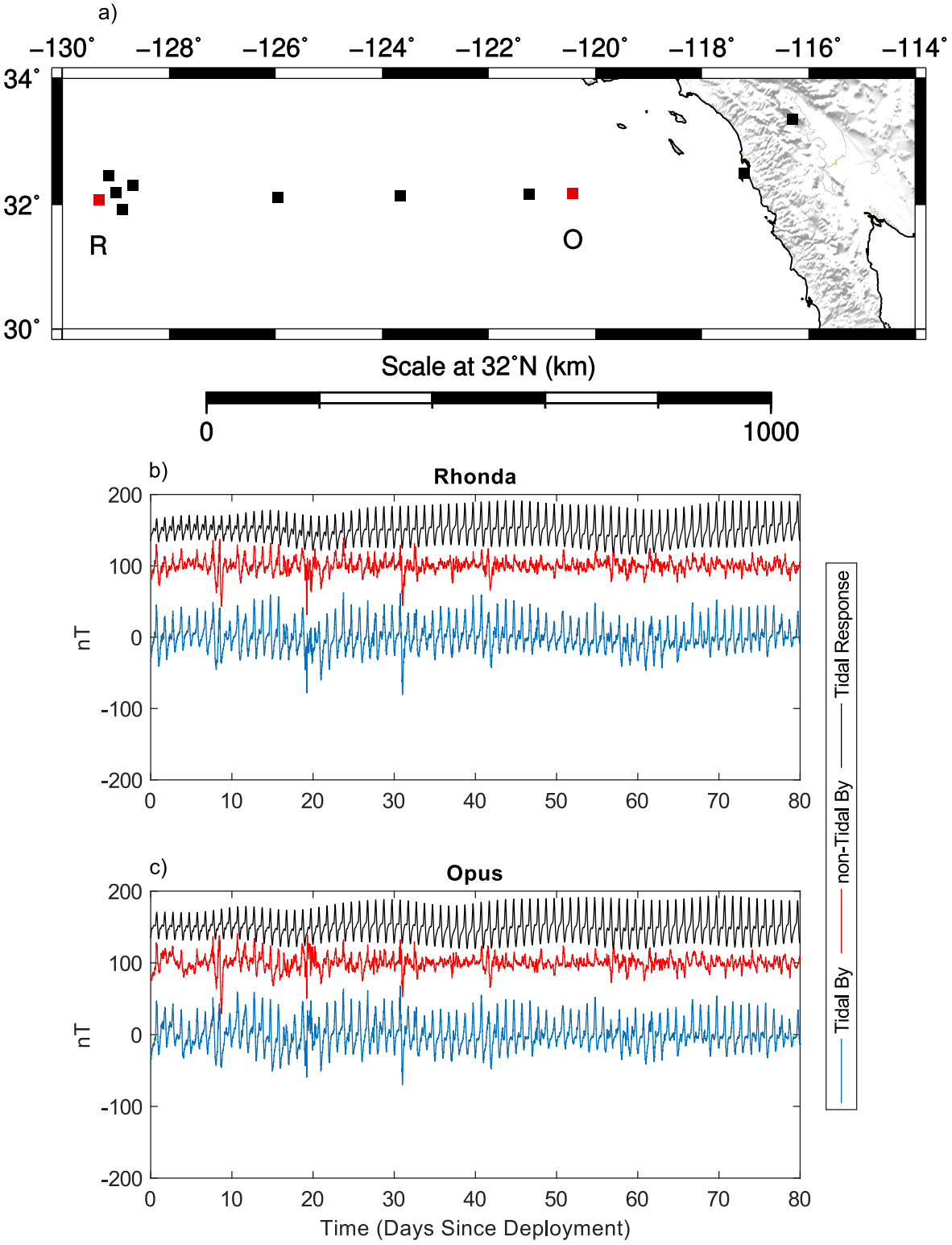

Figure 4.13: a) displays APPLE MT stations as squares. Red squares denote plotted stations. b) and c) displays B_y field data measured by the Rhonda and Opus receivers. The blue and red lines correspond to magnetic field data with and without tidal signals. The black line corresponds to the tidal signal removed during processing. This line can be generated by subtracting the non-tidal response from the tidal response. Red and black lines are offset along the y-axis to aid with readability.

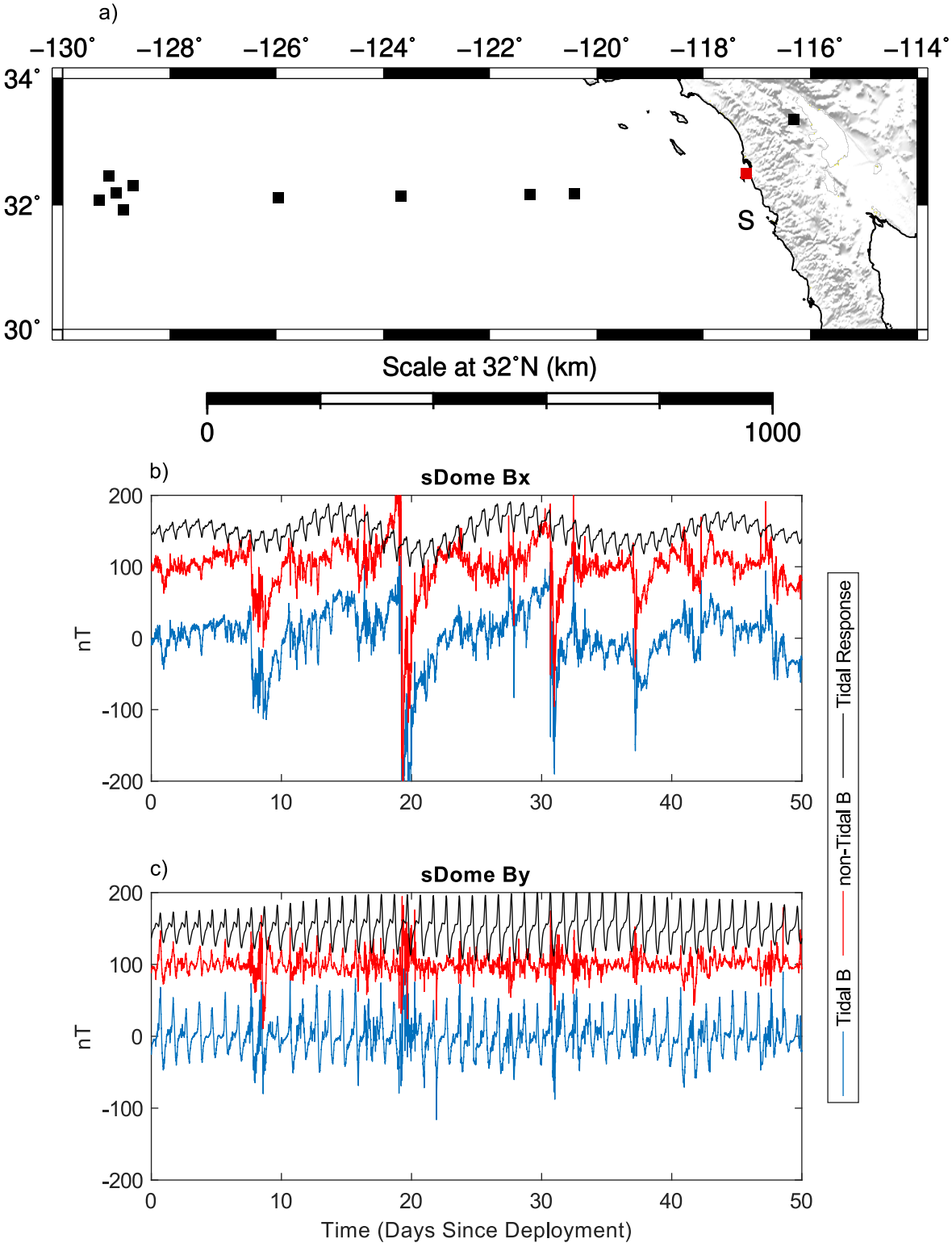

Figure 4.14: a) displays APPLE MT stations as squares. Red squares denote plotted stations. b) displays B_x field data measured by the sDome receiver. c) displays B_y field data measured by the sDome receiver. The blue and red lines correspond to magnetic field data with and without tidal signals. The black line corresponds to the tidal signal removed during processing. This line can be generated by subtracting the non-tidal response from the tidal response. Red and black lines are offset along the y-axis to aid with readability.

current within the ionosphere which varies as the Earth rotates with respect to the sun and induces non-planar fields. The periodicity of this process is 24 hours and corresponds to the Earth's rotational period with respect to the sun (Chave et al., 2012). From Figs 4.5 to 4.9, I observe numerous peaks in both the electric and magnetic fields. In particular, the peak at 1 cpd corresponds to the Earth's rotational period with respect to the sun. As such, I interpret this peak to be EM fields induced by the diurnal solar (S1) signal. Additional peaks are observed at 2 cpd, 3 cpd, and 4 cpd which I interpret to be EM fields induced by harmonics of the S1 signal.

4.4 Fast Fourier Transformation

Following the identification of EM fields induced by the motion of the ocean and S_q daily variations, I conduct a fast Fourier transformation (FFT) to remove their influence. Figs 4.10 to 4.14 display the horizontal EM fields measured by the Rhonda, Opus, and sDome receivers prior to and following the removal of tidal and S_q fields. From these Figs, I observe that the tidal and S_q fields substantially distort the EM fields measured during the APPLE study. Furthermore, I observe that the amount of distortion within measured electric fields increases as the receiver approaches the continental margin. Once the tidal and S_q fields are removed, I observe similar electric fields at all receivers. Subsequently, I conclude that I have successfully removed the EM fields induced by the motion of the ocean and S_q daily variations from the ocean-bottom MT data collected during the APPLE survey. As such, I conclude that EM noise associated with the motion of the ocean and S_q daily variations don't cause the instability observed in impedance.

4.5 Signal-To-Noise Ratio

Following the successful removal of EM noise associated with the Earth's ocean and ionosphere by FFT, I analyse the signal-to-noise ratio at each receiver. An inverse relationship between the power spectral density (PSD) and frequency, referred to as pink noise, defines the relationship between EM field attenuation and signal frequency (Junge, 1994; Simpson and Bahr, 2005). At sufficient frequencies, instrumentation within MT receivers generate a source of constant magnetic fields which obscures natural signals (Constable, 2013). As ocean depth increases, this source of noise occurs at higher frequencies. I observe this relationship in all EM field measurements to a frequency of 100 cpd. Beyond this frequency, ocean-bottom electric and sDome magnetic fields are observed to continue this relationship. In contrast, ocean-bottom magnetic fields are observed to maintain their power independent of frequency indicative of instrument noise. The frequency at which I observe this phenomenon is

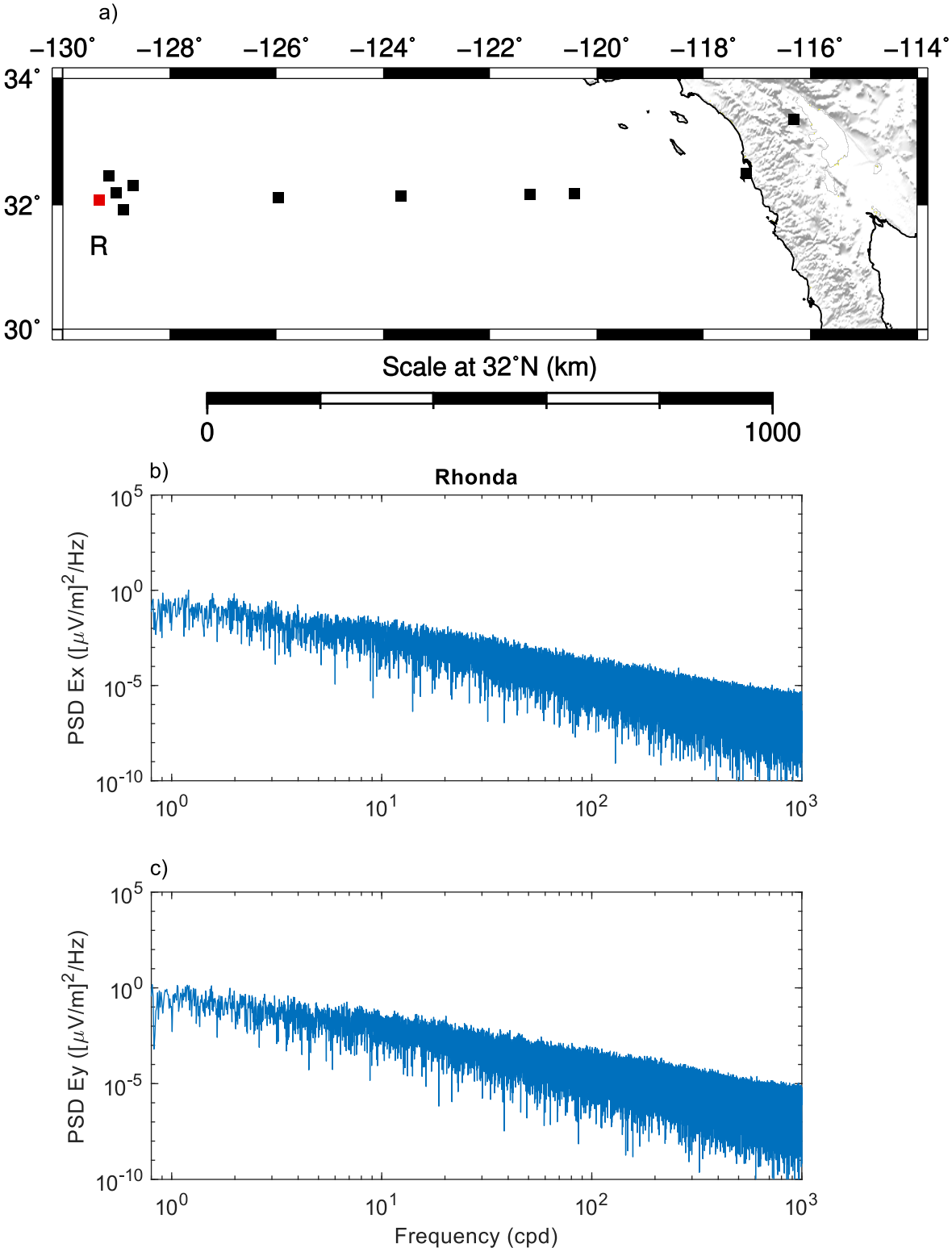

Figure 4.15: a) displays APPLE MT stations as squares. Red squares denote plotted stations. b) and c) display the power of E_x and E_y respectively as a function of frequency measured by the Rhonda receiver. Frequency is displayed in Cycles per Day (cpd).

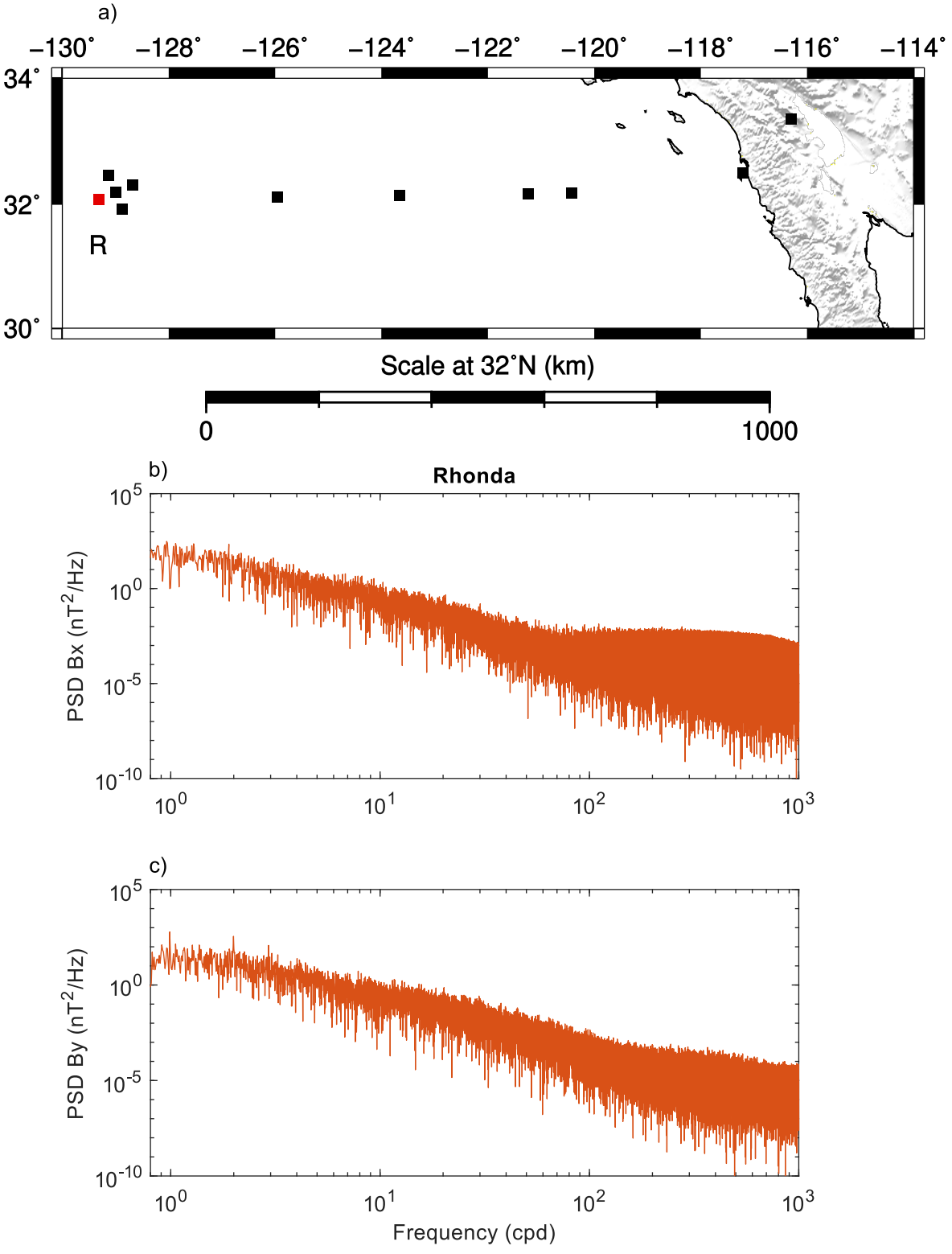

Figure 4.16: a) displays APPLE MT stations as squares. Red squares denote plotted stations. b) and c) display the power of B_x and B_y respectively as a function of frequency measured by the Rhonda receiver. Frequency is displayed in Cycles per Day (cpd).

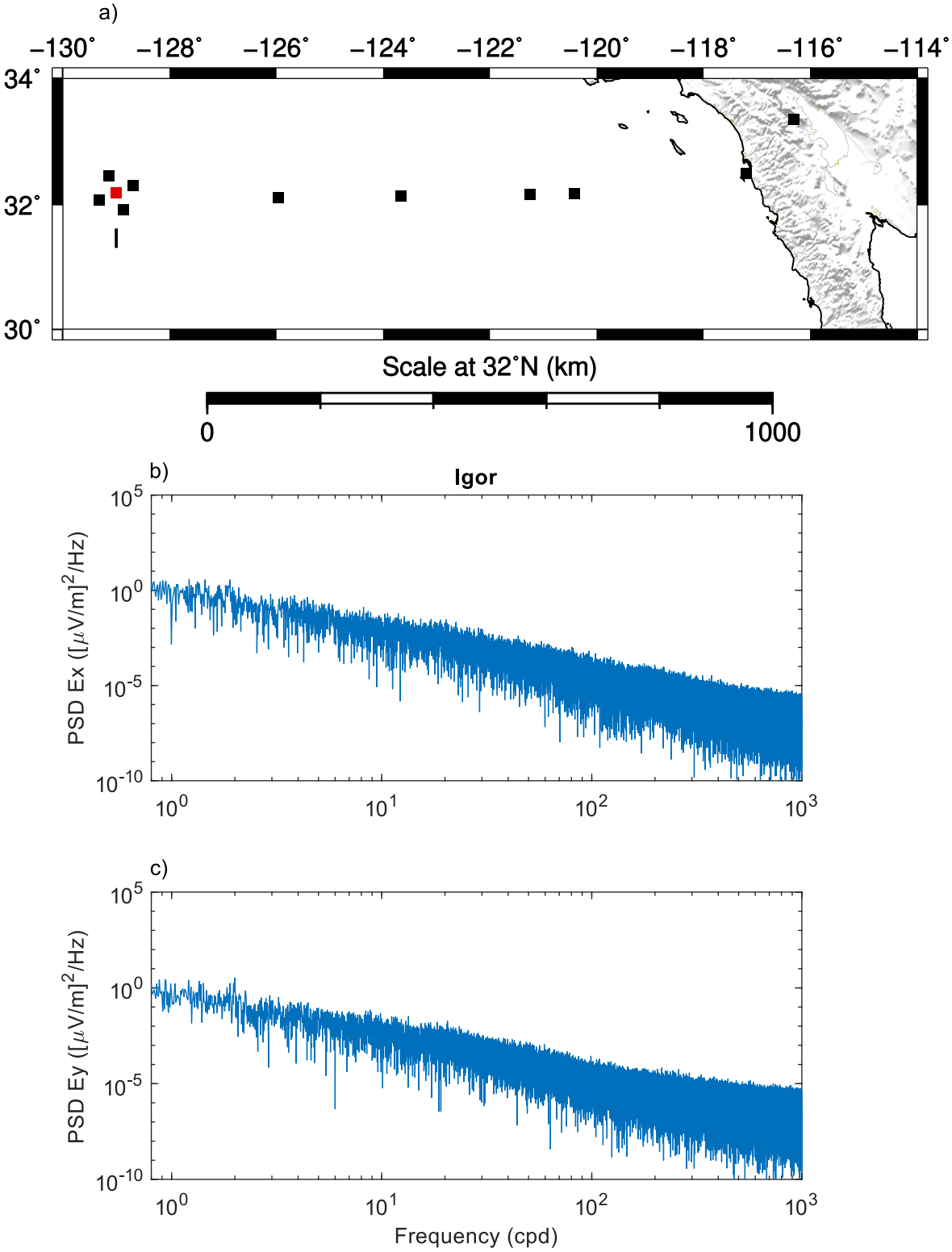

Figure 4.17: a) displays APPLE MT stations as squares. Red squares denote plotted stations. b) and c) display the power of E_x and E_y respectively as a function of frequency measured by the Igor receiver. Frequency is displayed in Cycles per Day (cpd).

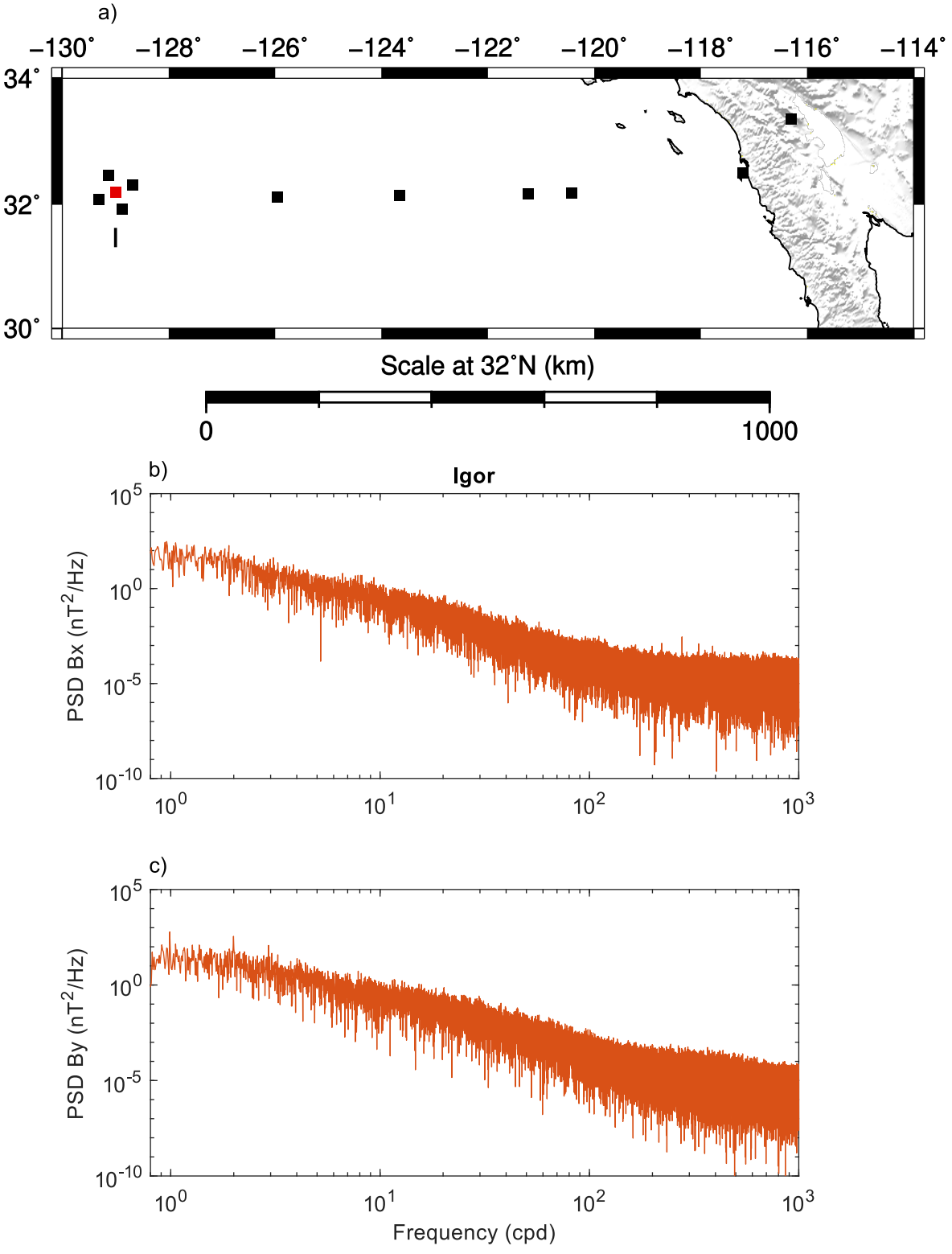

Figure 4.18: a) displays APPLE MT stations as squares. Red squares denote plotted stations. b) and c) display the power of B_x and B_y respectively as a function of frequency measured by the Igor receiver. Frequency is displayed in Cycles per Day (cpd).

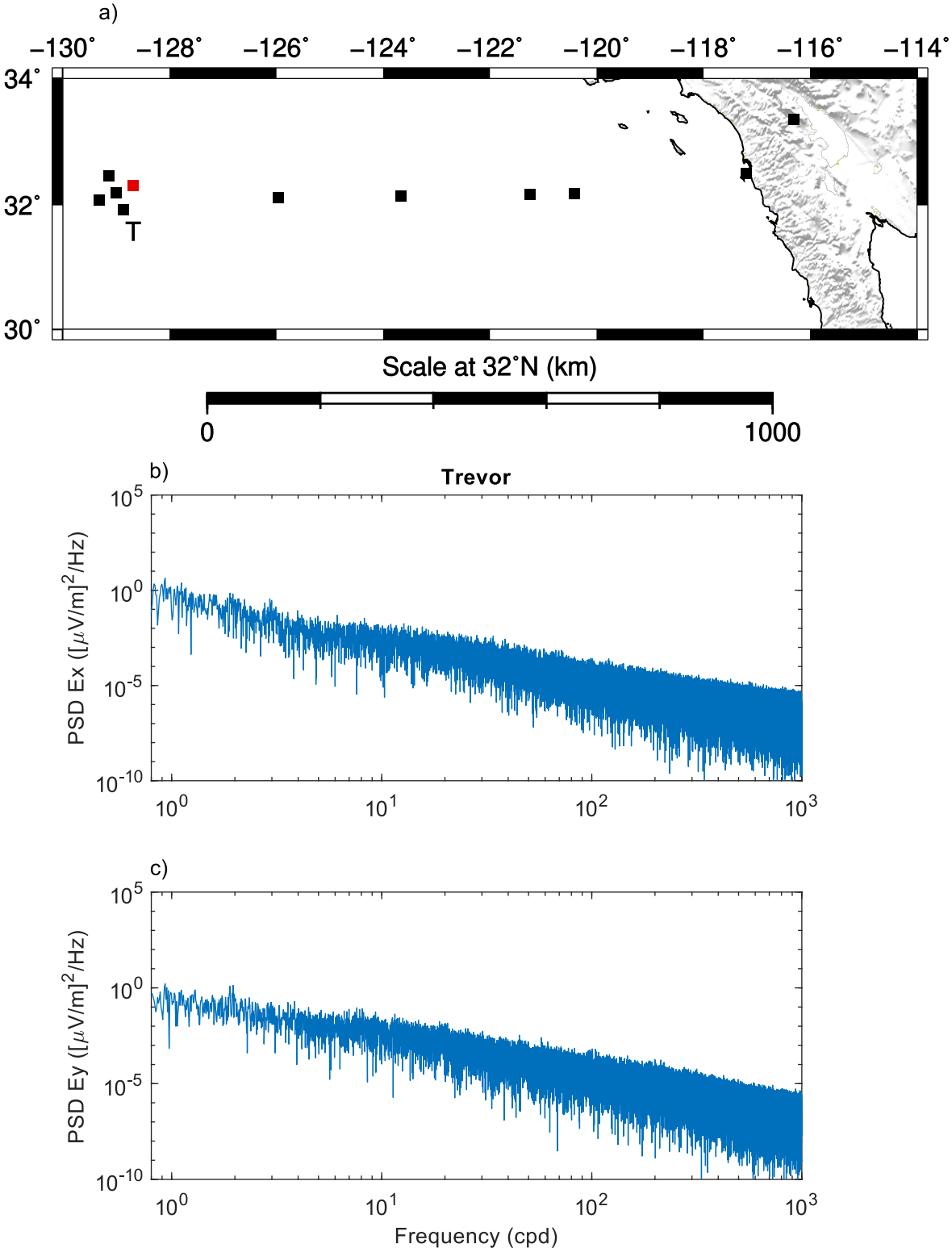

Figure 4.19: a) displays APPLE MT stations as squares. Red squares denote plotted stations. b) and c) display the power of E_x and E_y respectively as a function of frequency measured by the Trevor receiver. Frequency is displayed in Cycles per Day (cpd).

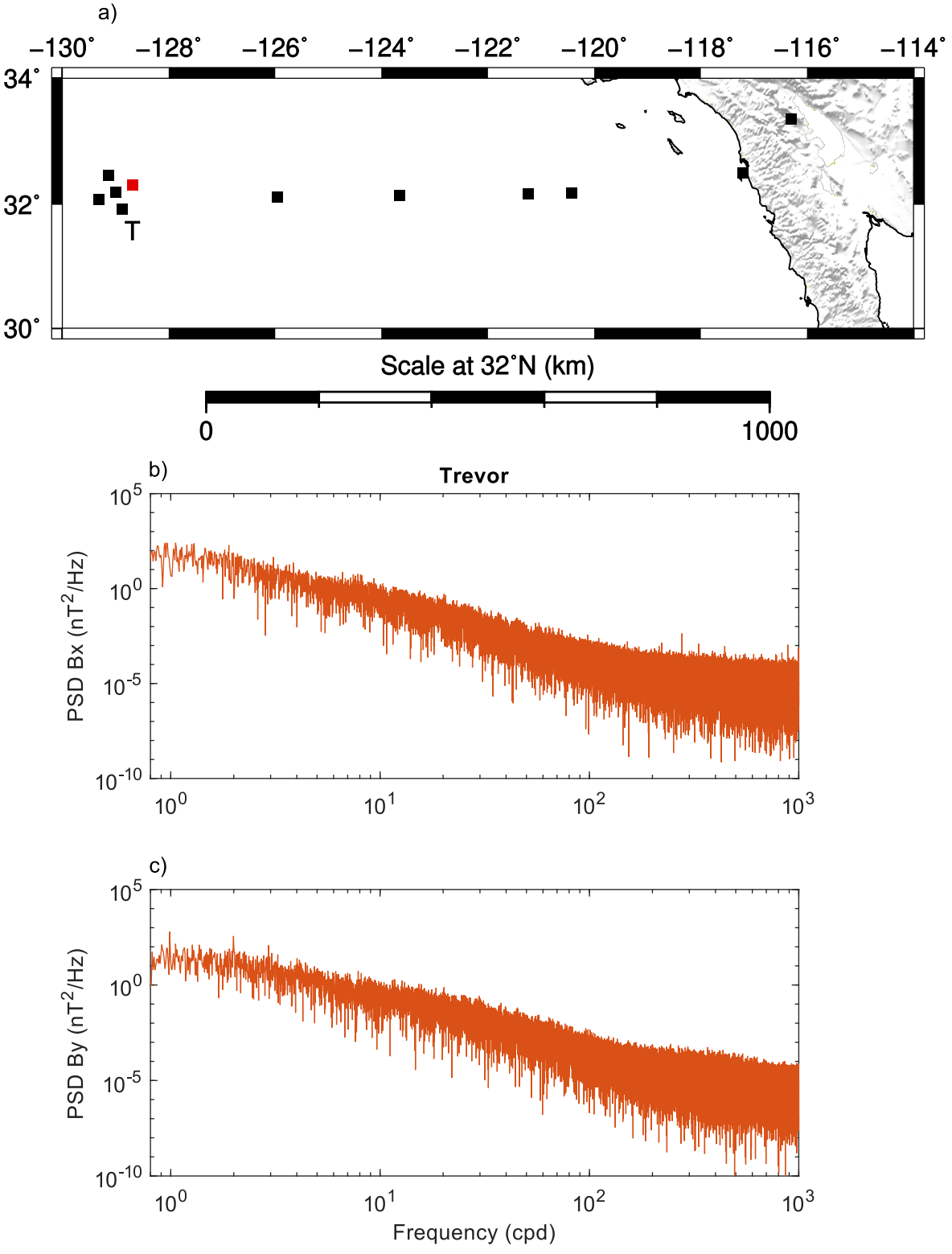

Figure 4.20: a) displays APPLE MT stations as squares. Red squares denote plotted stations. b) and c) display the power of B_x and B_y respectively as a function of frequency measured by the Trevor receiver. Frequency is displayed in Cycles per Day (cpd).

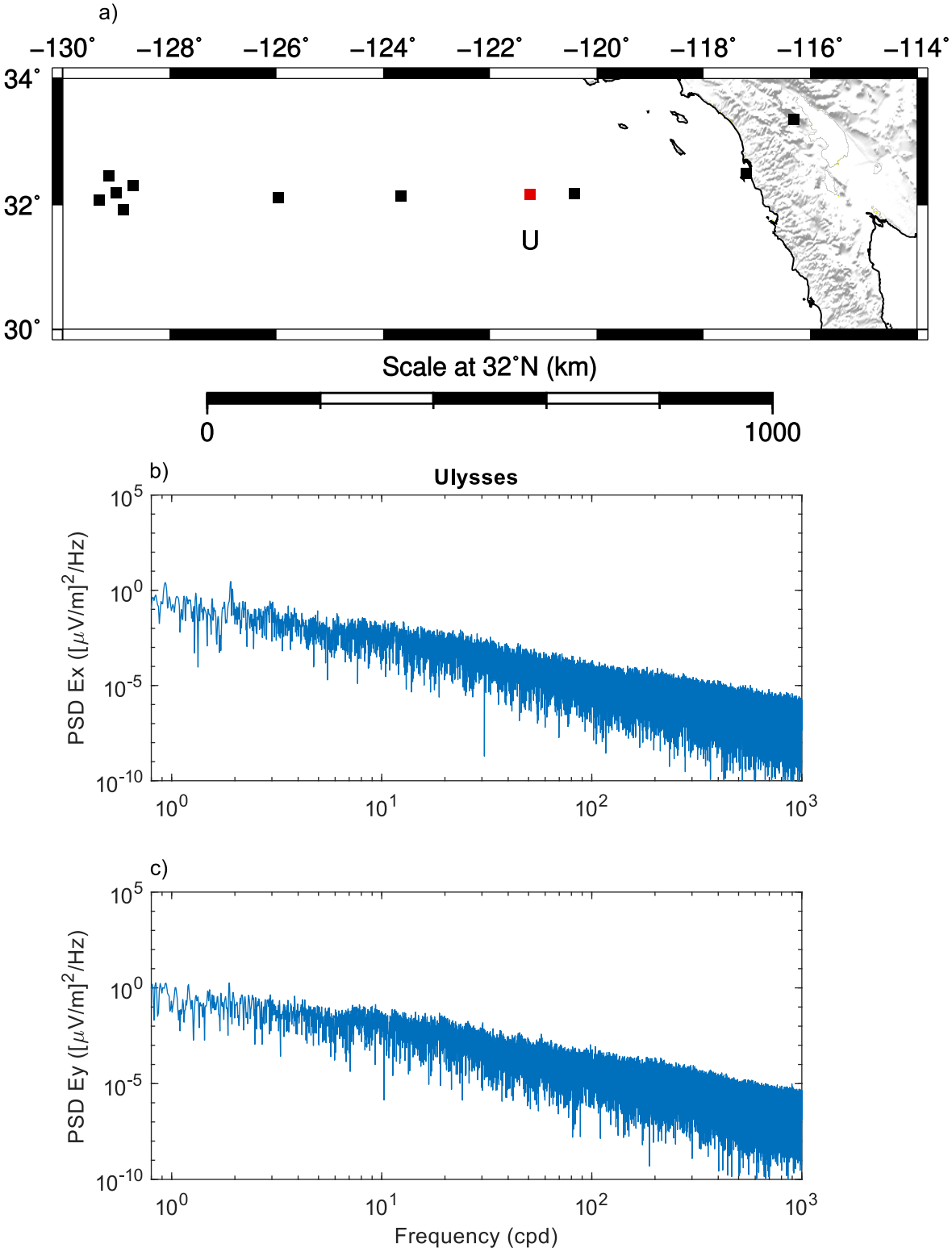

Figure 4.21: a) displays APPLE MT stations as squares. Red squares denote plotted stations. b) and c) display the power of E_x and E_y respectively as a function of frequency measured by the Ulysses receiver. Frequency is displayed in Cycles per Day (cpd).

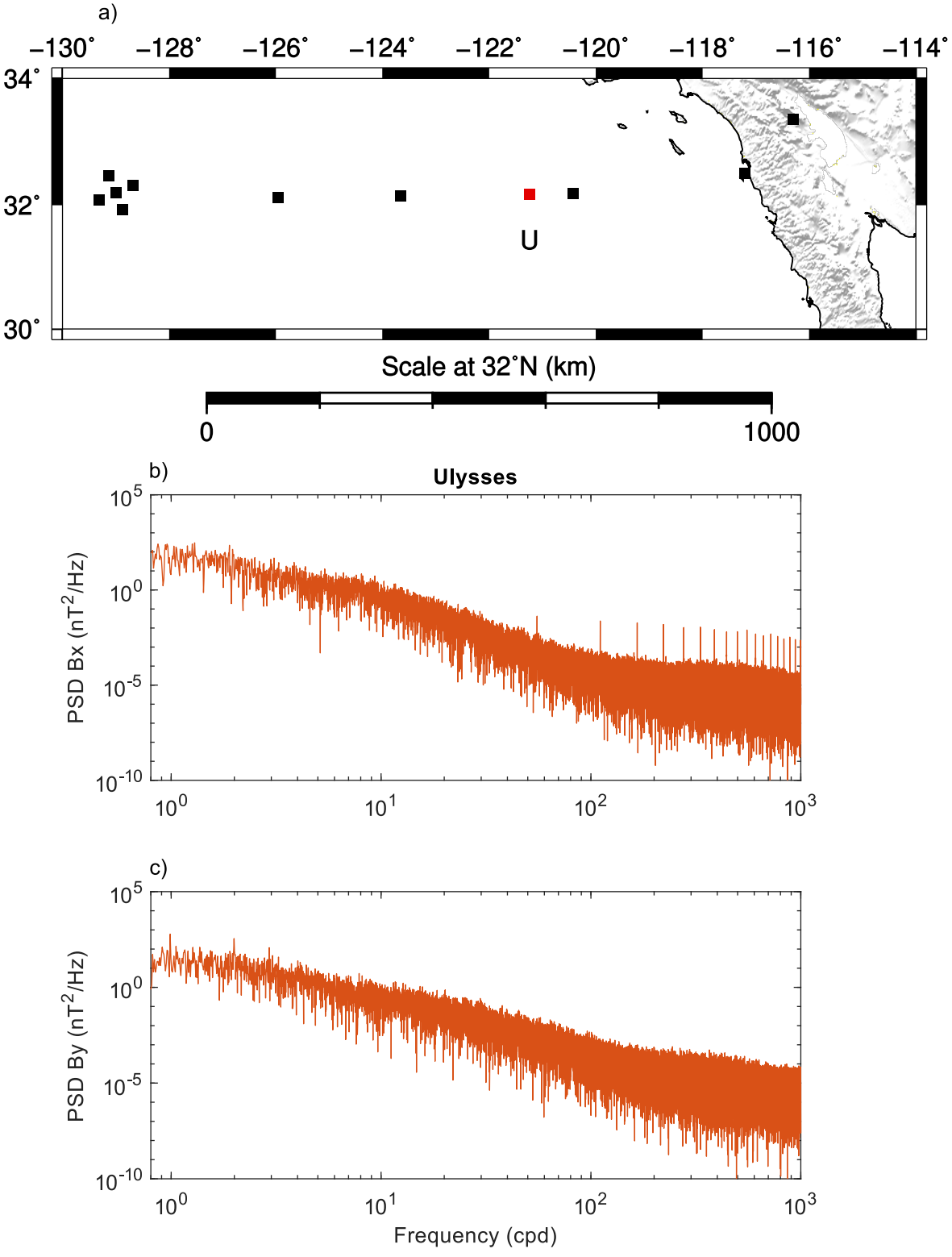

Figure 4.22: a) displays APPLE MT stations as squares. Red squares denote plotted stations. b) and c) display the power of B_x and B_y respectively as a function of frequency measured by the Ulysses receiver. Frequency is displayed in Cycles per Day (cpd).

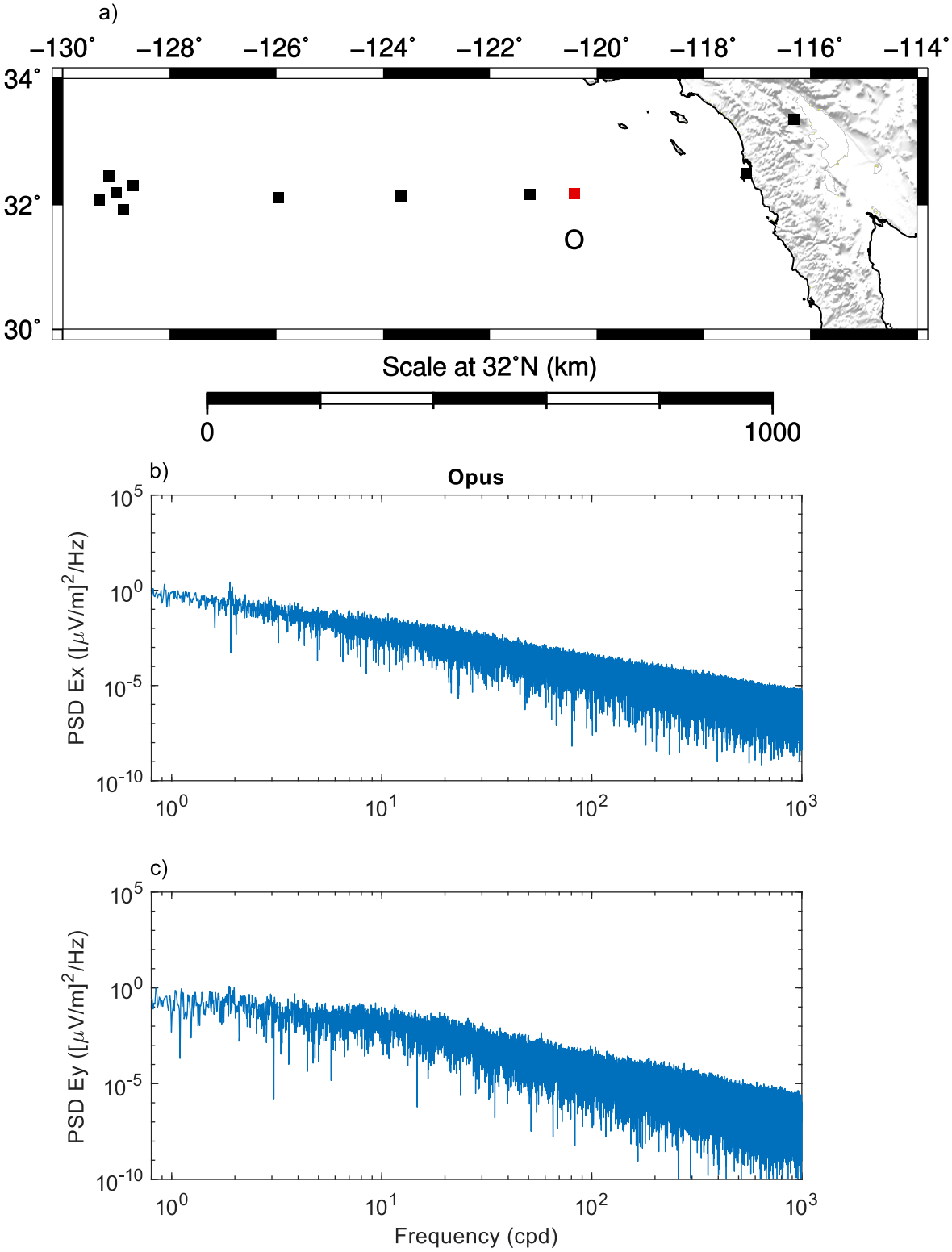

Figure 4.23: a) displays APPLE MT stations as squares. Red squares denote plotted stations. b) and c) display the power of E_x and E_y respectively as a function of frequency measured by the Opus receiver. Frequency is displayed in Cycles per Day (cpd).

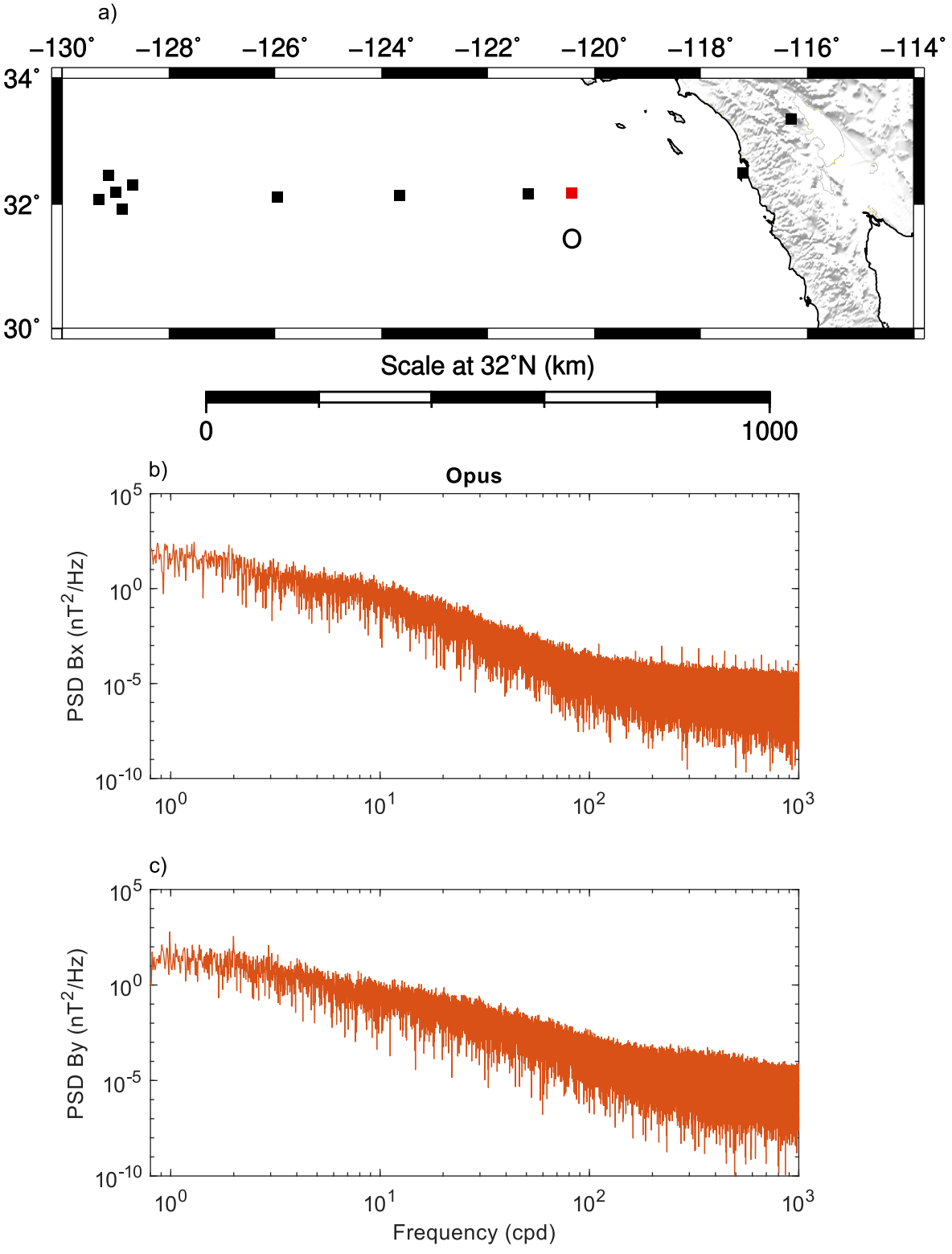

Figure 4.24: a) displays APPLE MT stations as squares. Red squares denote plotted stations. b) and c) display the power of B_x and B_y respectively as a function of frequency measured by the Opus receiver. Frequency is displayed in Cycles per Day (cpd).

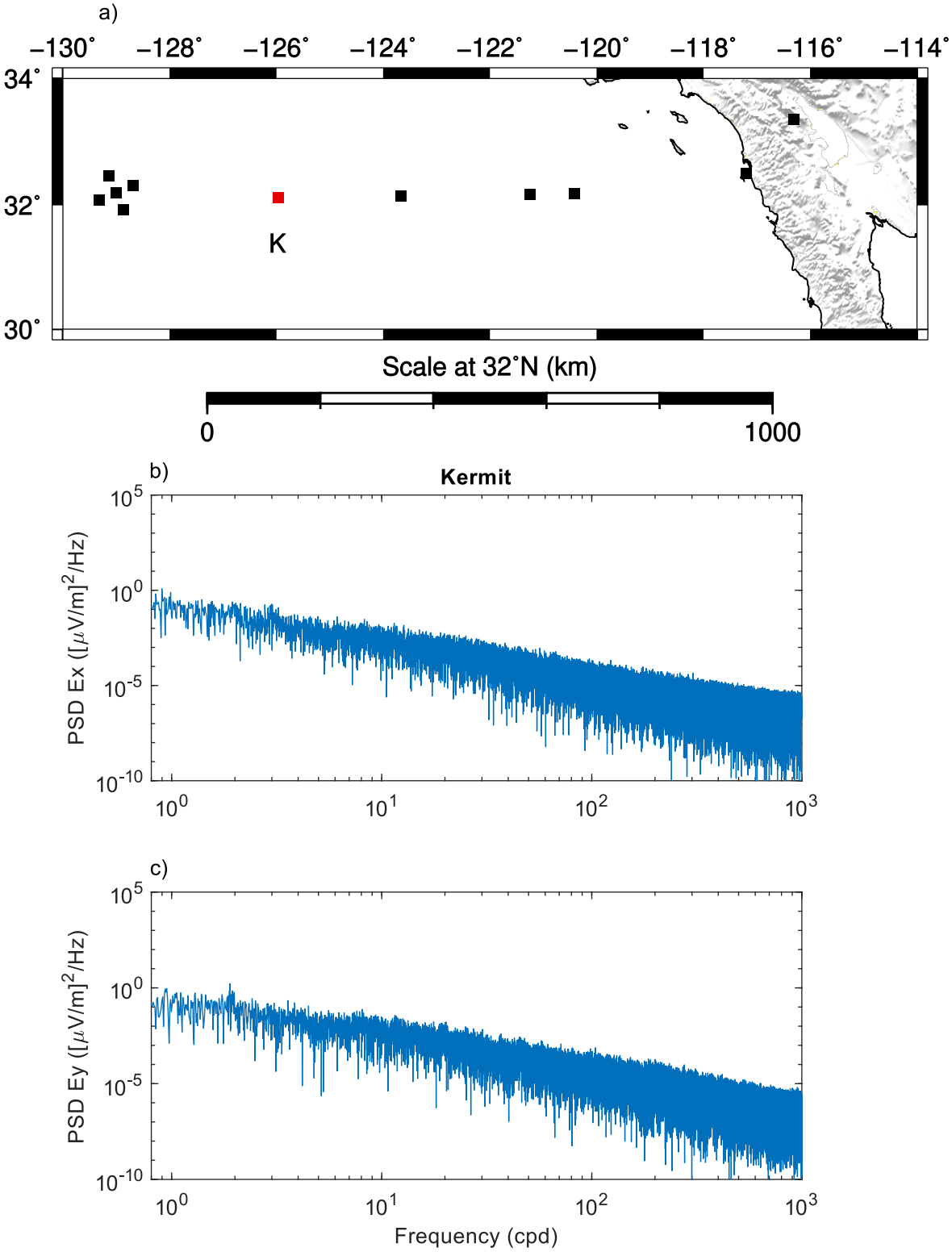

Figure 4.25: a) displays APPLE MT stations as squares. Red squares denote plotted stations. Following instrument issues, Kermit utilises Trevor magnetic fields. b) and c) display the power of E_x and E_y respectively as a function of frequency measured by the Kermit receiver. Frequency is displayed in Cycles per Day (cpd).

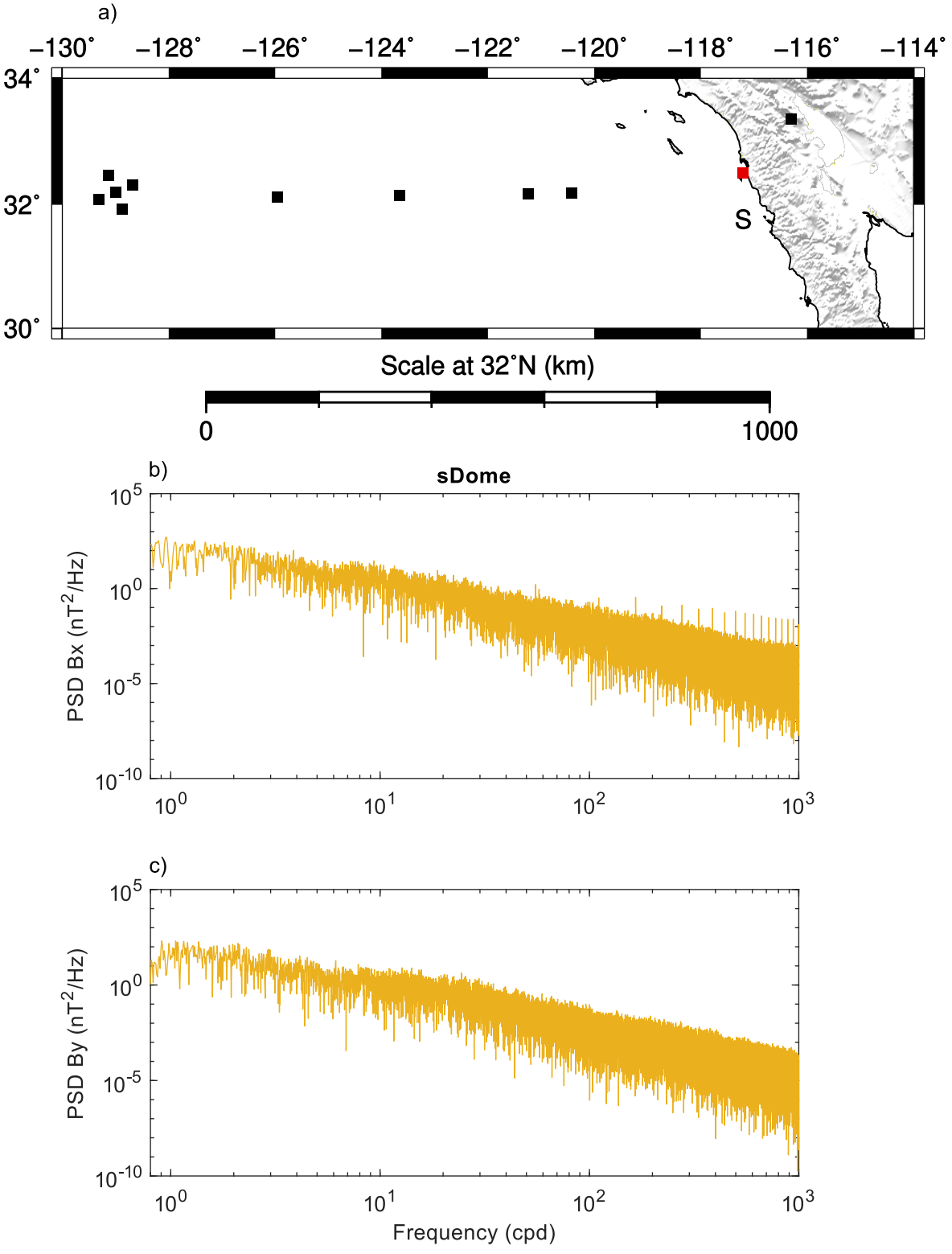

Figure 4.26: a) displays APPLE MT stations as squares. Red squares denote plotted stations. b) and c) display the power of B_x and B_y respectively as a function of frequency measured by the sDome receiver. Frequency is displayed in Cycles per Day (cpd).

approximately an order of magnitude lower than what is presented by Constable (2013). However, Chesley et al. (2019) determined that the near-surface resistivity for this region is considerably larger than the 1,000 Ωm presented by Constable (2013). Furthermore, the average ocean depth for the APPLE survey is greater than those presented by Constable (2013). From these factors, I conclude that the noise floor for the fluxgate magnetometers utilised during the APPLE survey is reduced to 100 cpd. As such, I conclude from these observations that the poor signal-to-noise ratio of ocean-bottom magnetic fields is a cause of unstable ocean-bottom MT impedances. To further investigate the signal-to-noise issues which contaminate ocean-bottom magnetic fields, I plot a 24 hour segment of measured field data (Figs 4.27 to 4.32). I choose the 19^{th} day to 20^{th} day due to the prominent EM signal recorded at approximately the 6^{th} hour of the 19^{th} day of recording. For ocean-bottom electric and sDome magnetic fields, I observe consistent expressions of coherent signal. In contrast, the ocean is observed to act as a high-pass filter upon ocean-bottom magnetic fields. The cut-off frequency of this filter is observed to be inversely proportional to the ocean depth and coastline distance at the location of the receiver. As these factors decrease, I observe ocean-bottom magnetic signal asymptotes toward a low frequency approximation of sDome surface magnetic signal.

These observations corroborate my earlier conclusion that ocean-bottom magnetic field measurements cause instability in ocean-bottom MT impedance. To address this issue, I propose the calculation of a hybrid impedance utilising ocean-bottom electric and ocean-surface magnetic field measurements to increase the stability of calculated impedances and improve our ability to resolve subsurface conductivity structures via oceanic MT studies. In order to measure ocean-surface magnetic fields, a three-component magnetometer would be required to continuously measure the pitch, yaw, and roll of the instrument. While technically feasible, it is unlikely that a dedicated magnetometer capable of taking high frequency pitch, yaw, and roll measurements will be developed and deployed on the ocean surface for multiple months. As such, I utilise sDome magnetic field measurements as a quasi-surface response.

4.6 Magnetotelluric Impedance

Figs 4.33 to 4.36 display Z_{XX} and Z_{YY} components of standard and hybrid impedances. From these Figs, I observe highly variable and poorly constrained values for Z_{XX} and Z_{YY} when calculating standard impedance. In contrast, Z_{XX} and Z_{YY} for hybrid impedances are well constrained and vary smoothly between periods. The apparent resistivity and phase calculated from Z_{XX} exhibit similar characteristics (Figs 4.37 to 4.40). In contrast, the apparent resistivity and phase response of Z_{YY} is observed to be poorly constrained for both standard and hybrid impedance. I interpret these

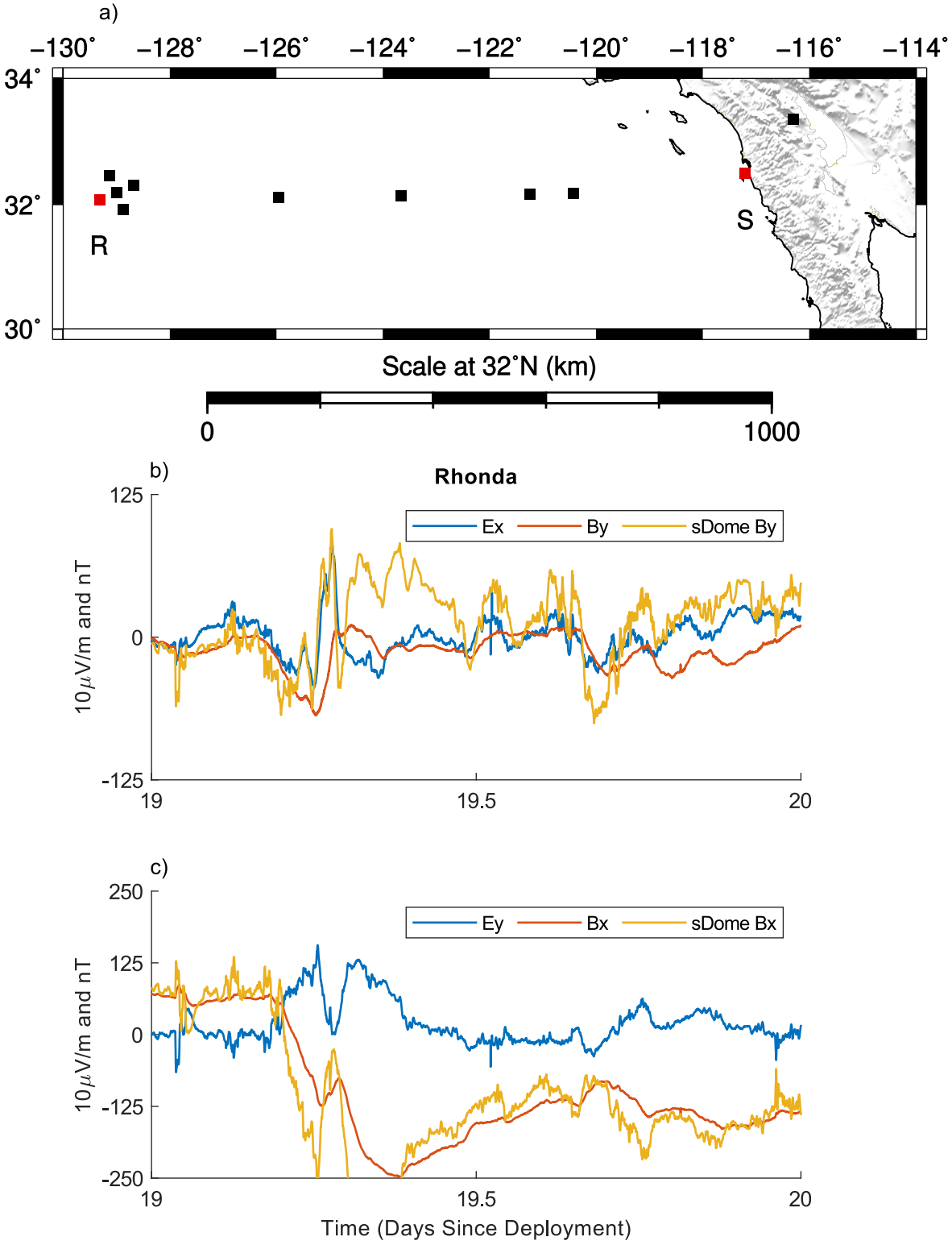

Figure 4.27: a) displays APPLE MT stations as squares. Red squares denote plotted stations. b) displays a 24 hour segment of E_x and B_y fields measured by the Rhonda receiver alongside B_y sDome receiver field measurements. c) displays a 24 hour segment of E_y and B_x fields measured by the Rhonda receiver alongside B_x sDome receiver field measurements.

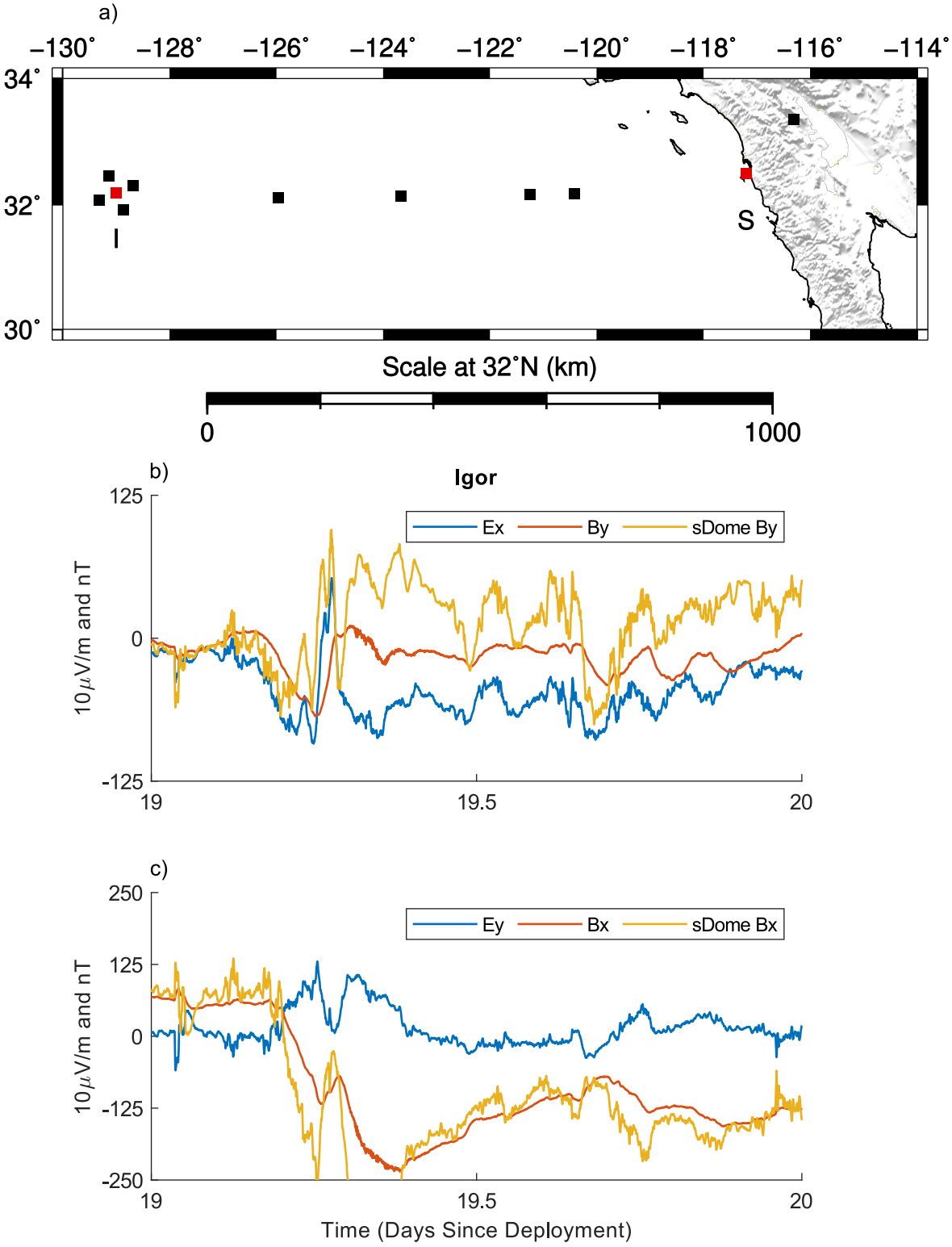

Figure 4.28: a) displays APPLE MT stations as squares. Red squares denote plotted stations. b) displays a 24 hour segment of E_x and B_y fields measured by the Igor receiver alongside B_y sDome receiver field measurements. c) displays a 24 hour segment of E_y and B_x fields measured by the Igor receiver alongside B_x sDome receiver field measurements.

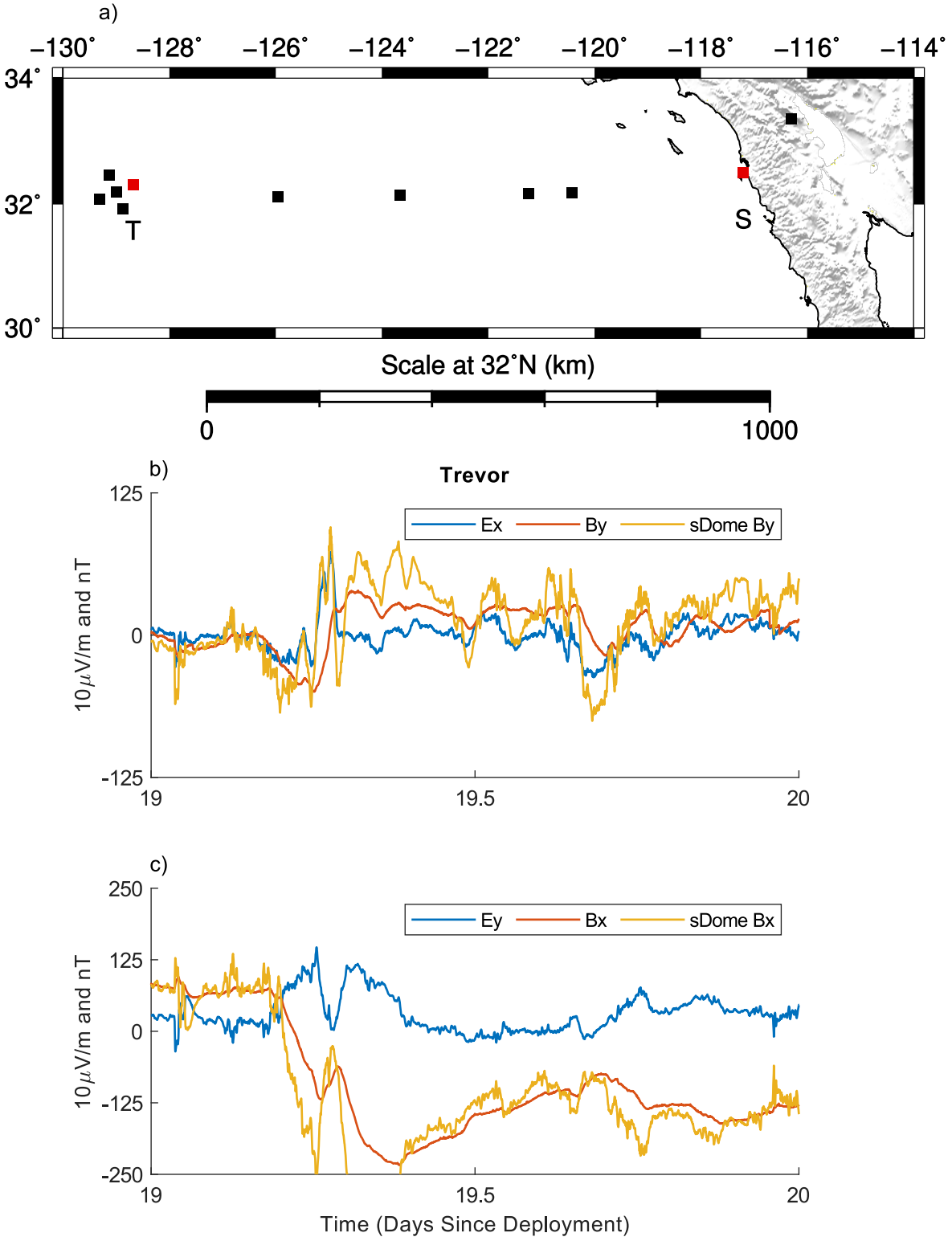

Figure 4.29: a) displays APPLE MT stations as squares. Red squares denote plotted stations. b) displays a 24 hour segment of E_x and B_y fields measured by the Trevor receiver alongside B_y sDome receiver field measurements. c) displays a 24 hour segment of E_y and B_x fields measured by the Trevor receiver alongside B_x sDome receiver field measurements.

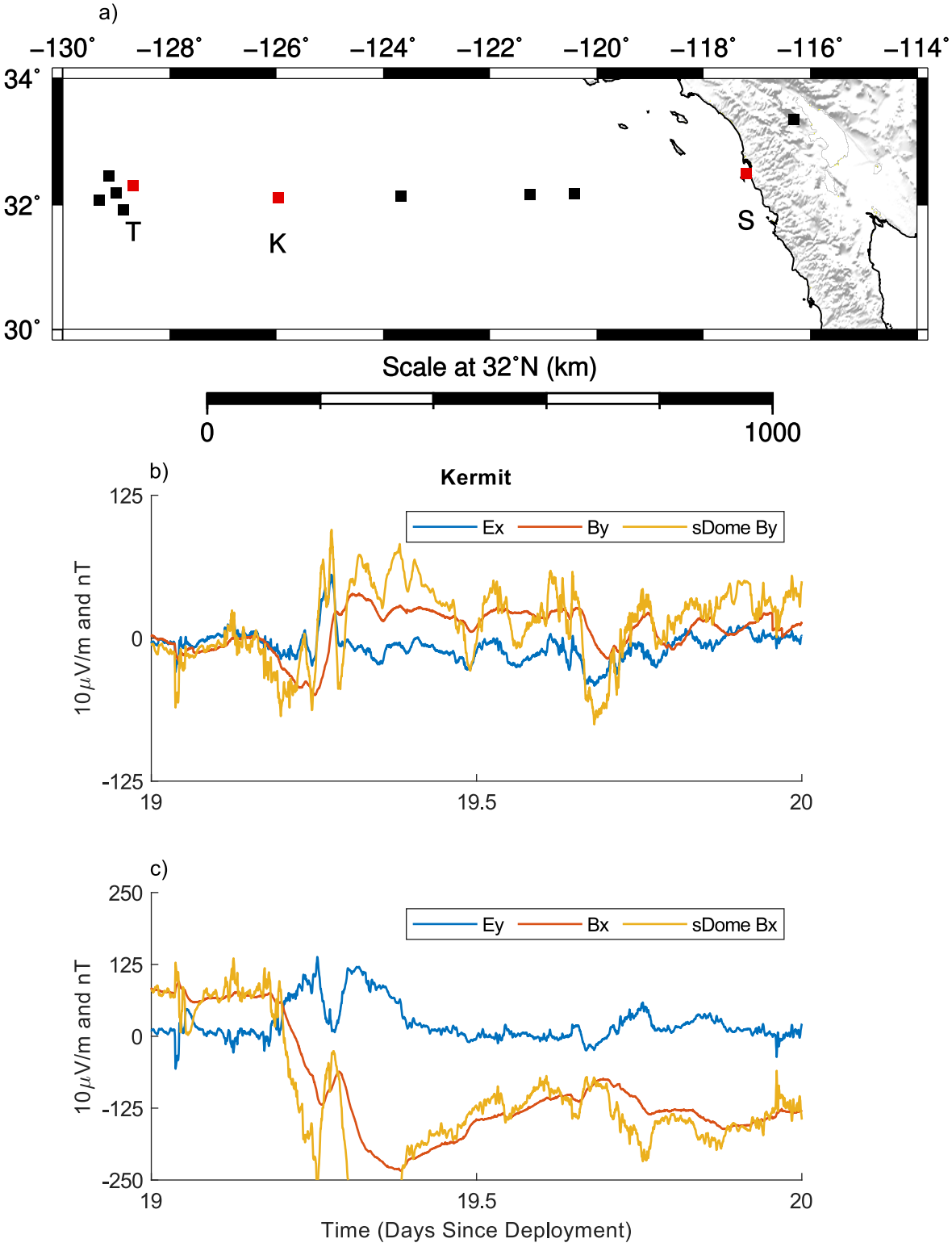

Figure 4.30: a) displays APPLE MT stations as squares. Red squares denote plotted stations. Following instrument issues, Kermit utilises Trevor magnetic fields. b) displays a 24 hour segment of E_x and B_y fields utilised by the Kermit receiver alongside B_y sDome receiver field measurements. c) displays a 24 hour segment of E_y and B_x fields utilised by the Kermit receiver alongside B_x sDome receiver field measurements.

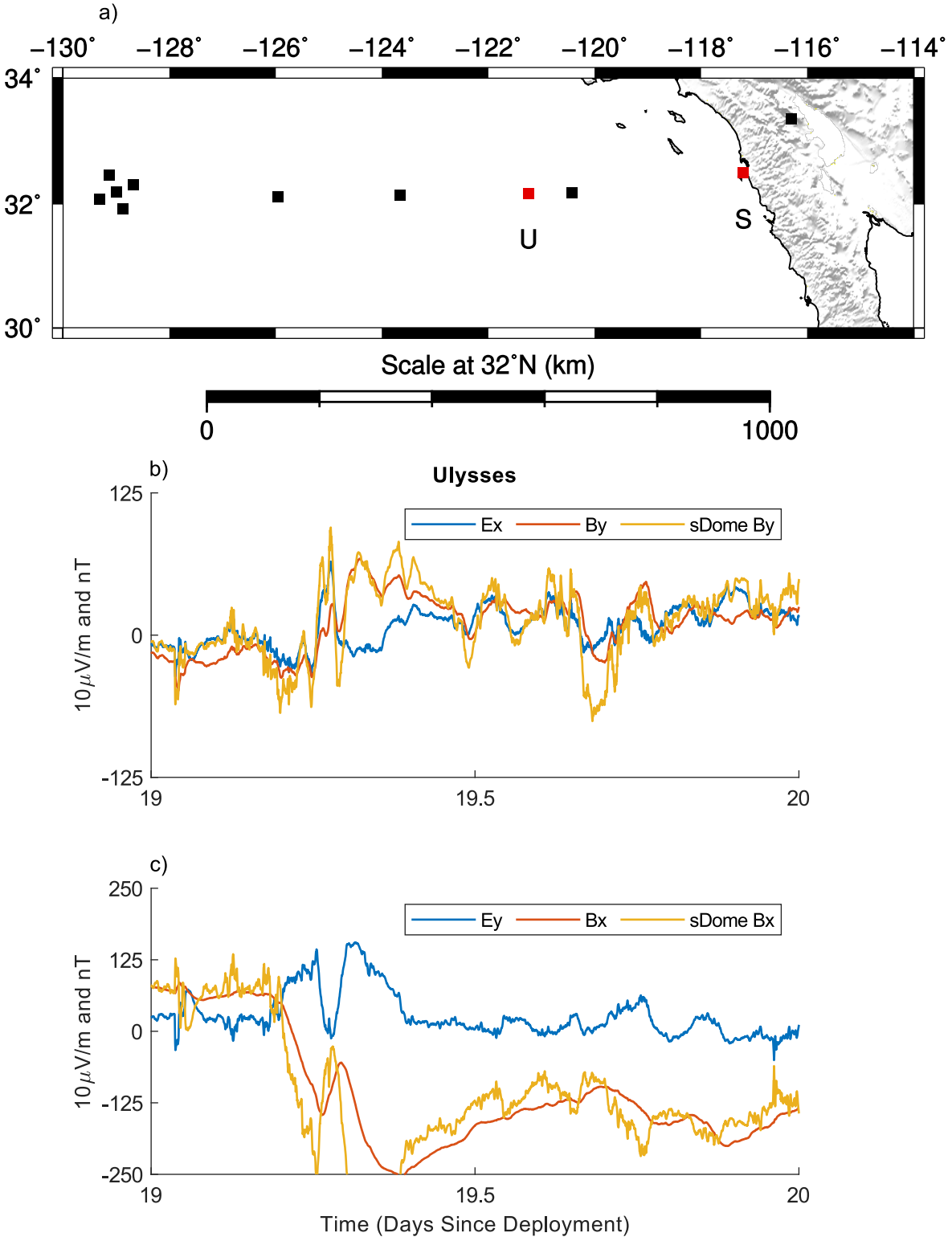

Figure 4.31: a) displays APPLE MT stations as squares. Red squares denote plotted stations. b) displays a 24 hour segment of E_x fields measured by the Ulysses receiver alongside B_y sDome receiver field measurements. c) displays a 24 hour segment of E_y and B_x fields measured by the Ulysses receiver alongside B_x sDome receiver field measurements.

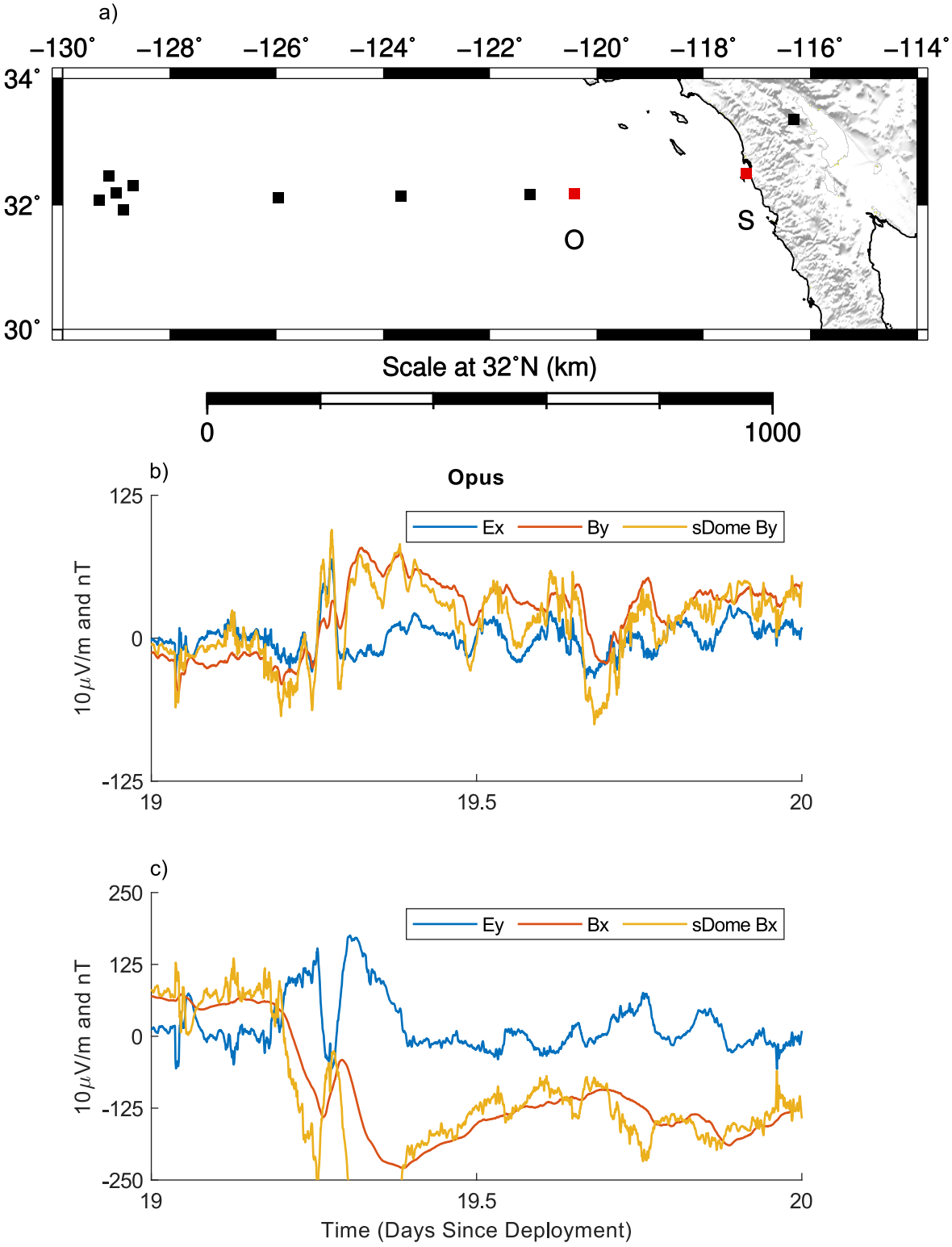

Figure 4.32: a) displays APPLE MT stations as squares. Red squares denote plotted stations. b) displays a 24 hour segment of E_x and B_y fields measured by the Opus receiver alongside B_y sDome receiver field measurements. c) displays a 24 hour segment of E_y and B_x fields measured by the Opus receiver alongside B_x sDome receiver field measurements.

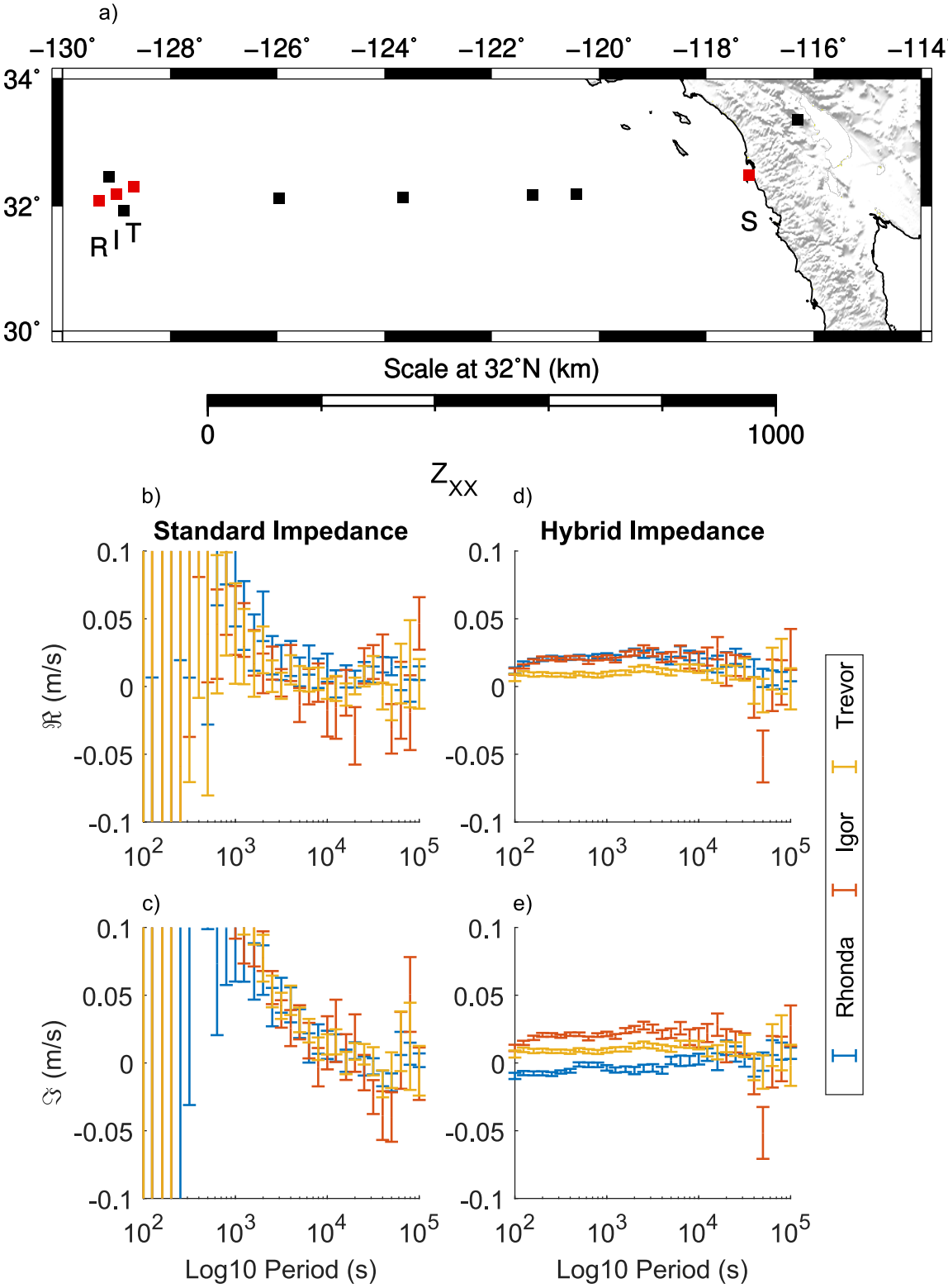

Figure 4.33: a) displays APPLE MT stations as squares. Red squares denote plotted stations. b) and c) display the $\Re$ and $\Im$ for standard impedance. d) and e) display the $\Re$ and $\Im$ for hybrid impedance. Blue, orange, and yellow data points correspond to the Z_{XX} component calculated from Rhonda, Igor, and Trevor receivers respectively.

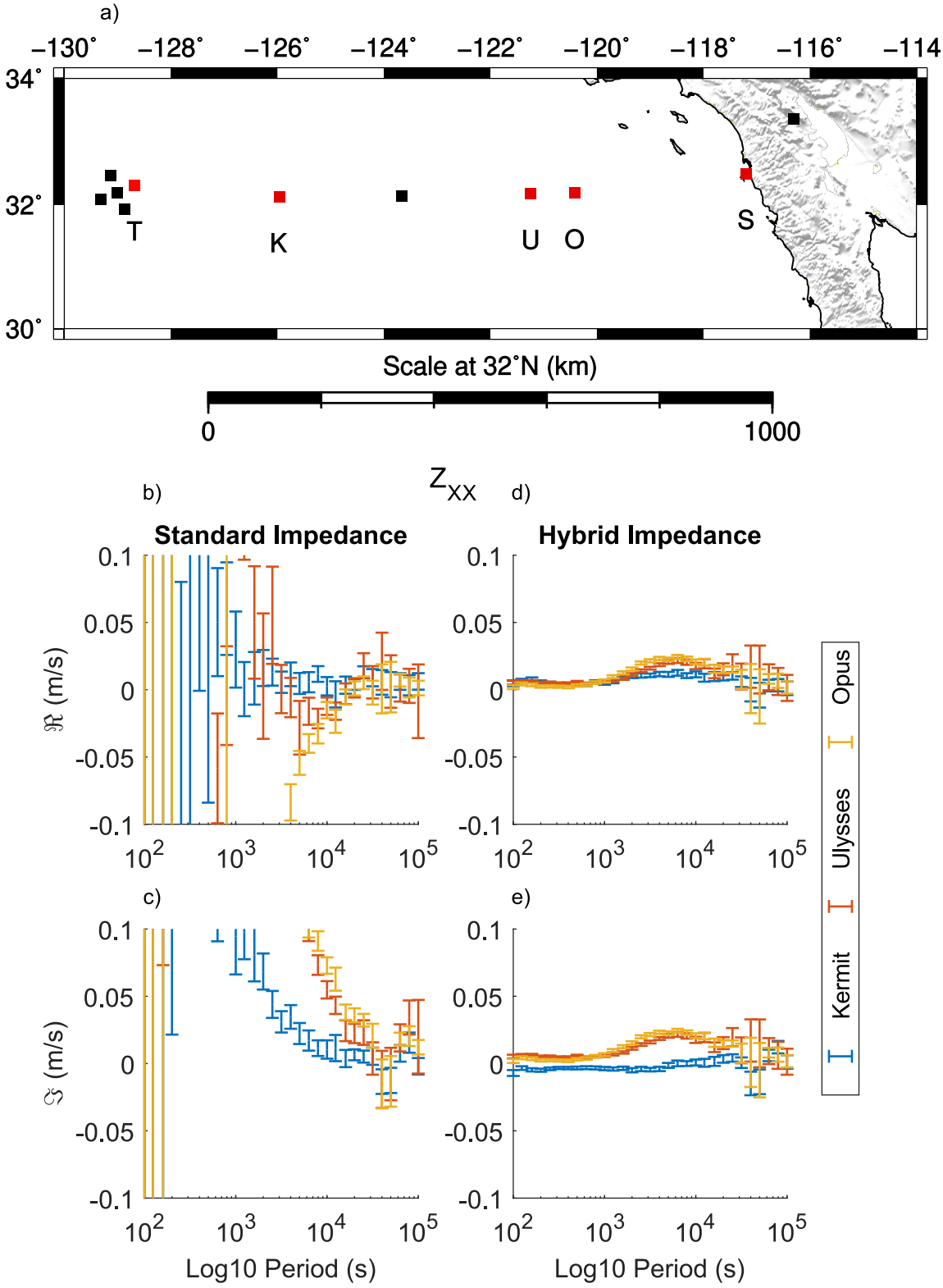

Figure 4.34: a) displays APPLE MT stations as squares. Red squares denote plotted stations. Following instrument issues, Kermit utilises Trevor magnetic fields. b) and c) display the $\Re$ and $\Im$ for standard impedance. d) and e) display the $\Re$ and $\Im$ for hybrid impedance. Blue, orange, and yellow data points correspond to the Z_{XX} component calculated from Kermit, Ulysses, and Opus receivers respectively.

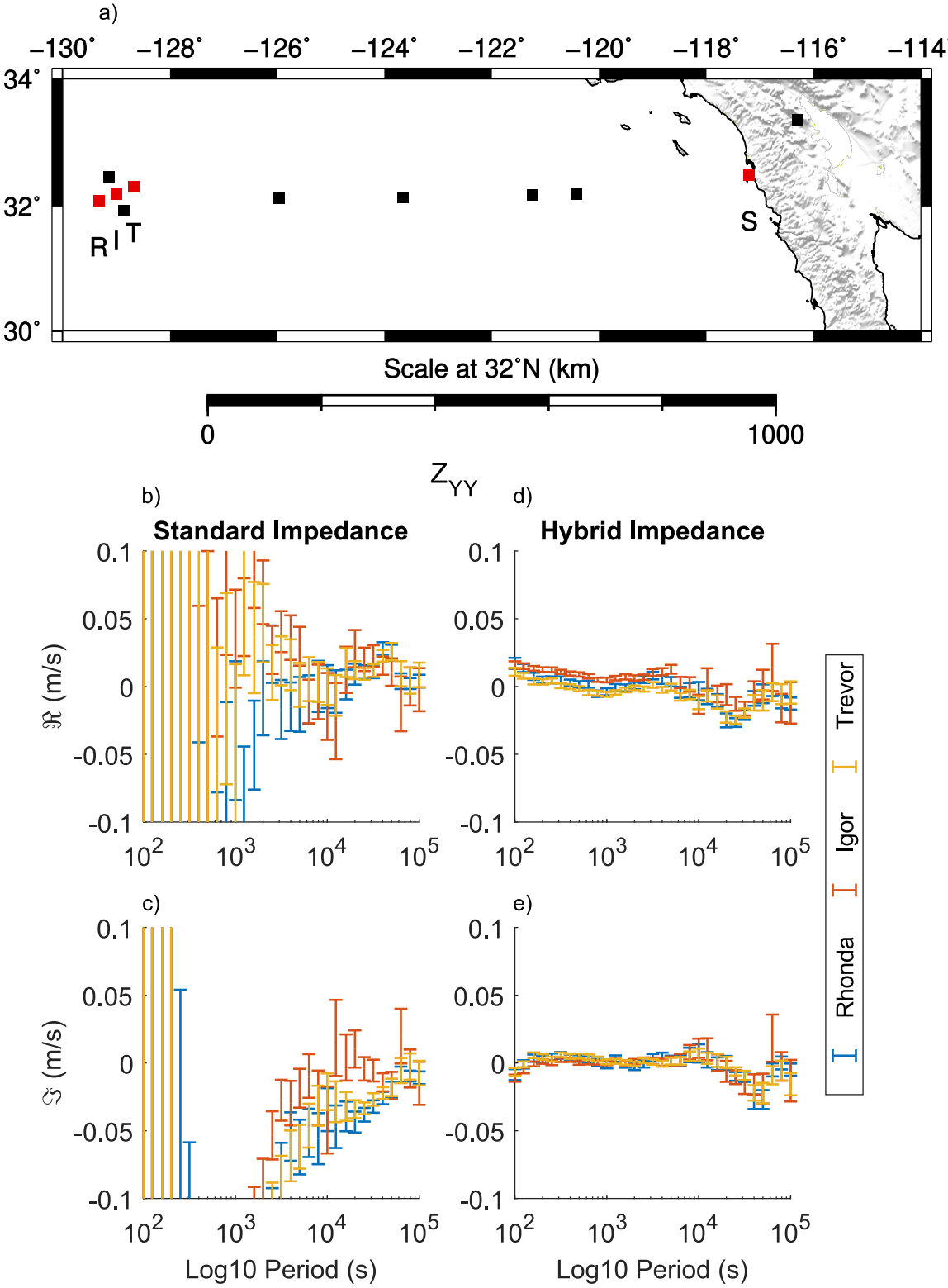

Figure 4.35: a) displays APPLE MT stations as squares. Red squares denote plotted stations. b) and c) display the $\Re$ and $\Im$ for standard impedance. d) and e) display the $\Re$ and $\Im$ for hybrid impedance. Blue, orange, and yellow data points correspond to the Z_{YY} component calculated from Rhonda, Igor, and Trevor receivers respectively.

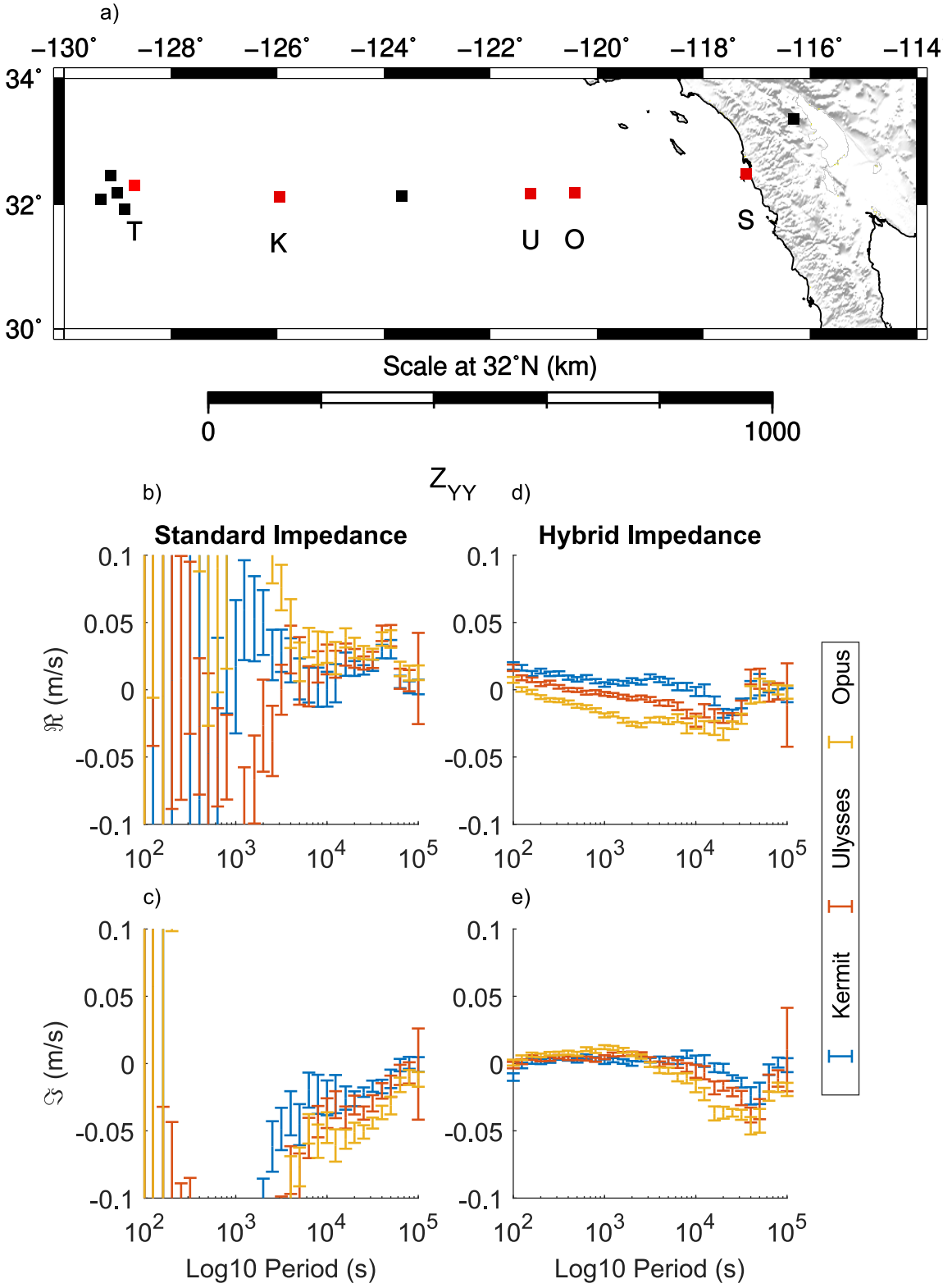

Figure 4.36: a) displays APPLE MT stations as squares. Red squares denote plotted stations. Following instrument issues, Kermit utilises Trevor magnetic fields. b) and c) display the $\Re$ and $\Im$ for standard impedance. d) and e) display the $\Re$ and $\Im$ for hybrid impedance. Blue, orange, and yellow data points correspond to the Z_{YY} component calculated from Kermit, Ulysses, and Opus receivers respectively.

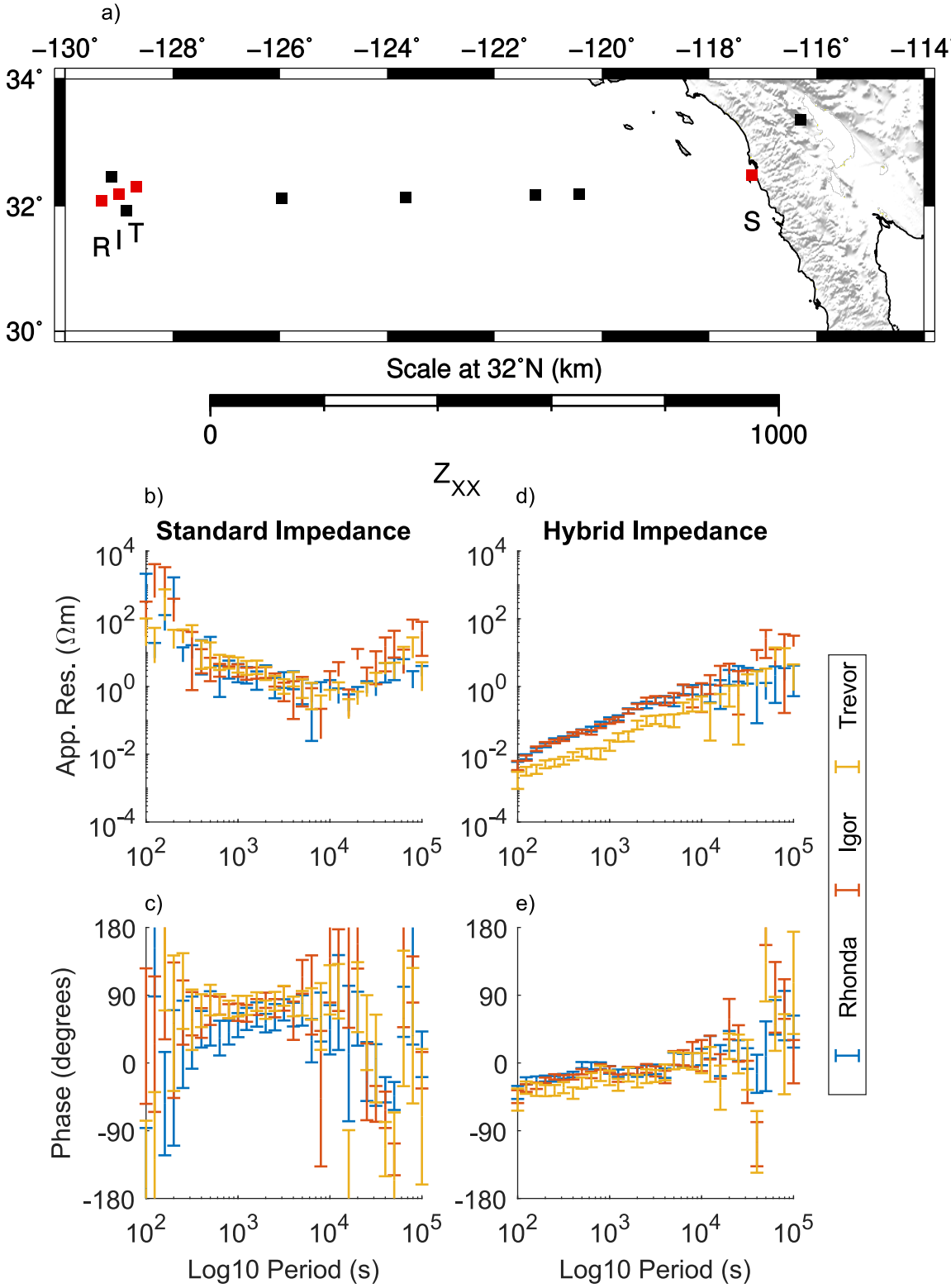

Figure 4.37: a) displays APPLE MT stations as squares. Red squares denote plotted stations. b) and c) display apparent resistivity and phase for a standard impedance. d) and e) display apparent resistivity and phase for a hybrid impedance. Blue, orange, and yellow data points correspond to the Z_{XX} component calculated from Rhonda, Igor, and Trevor receivers respectively.

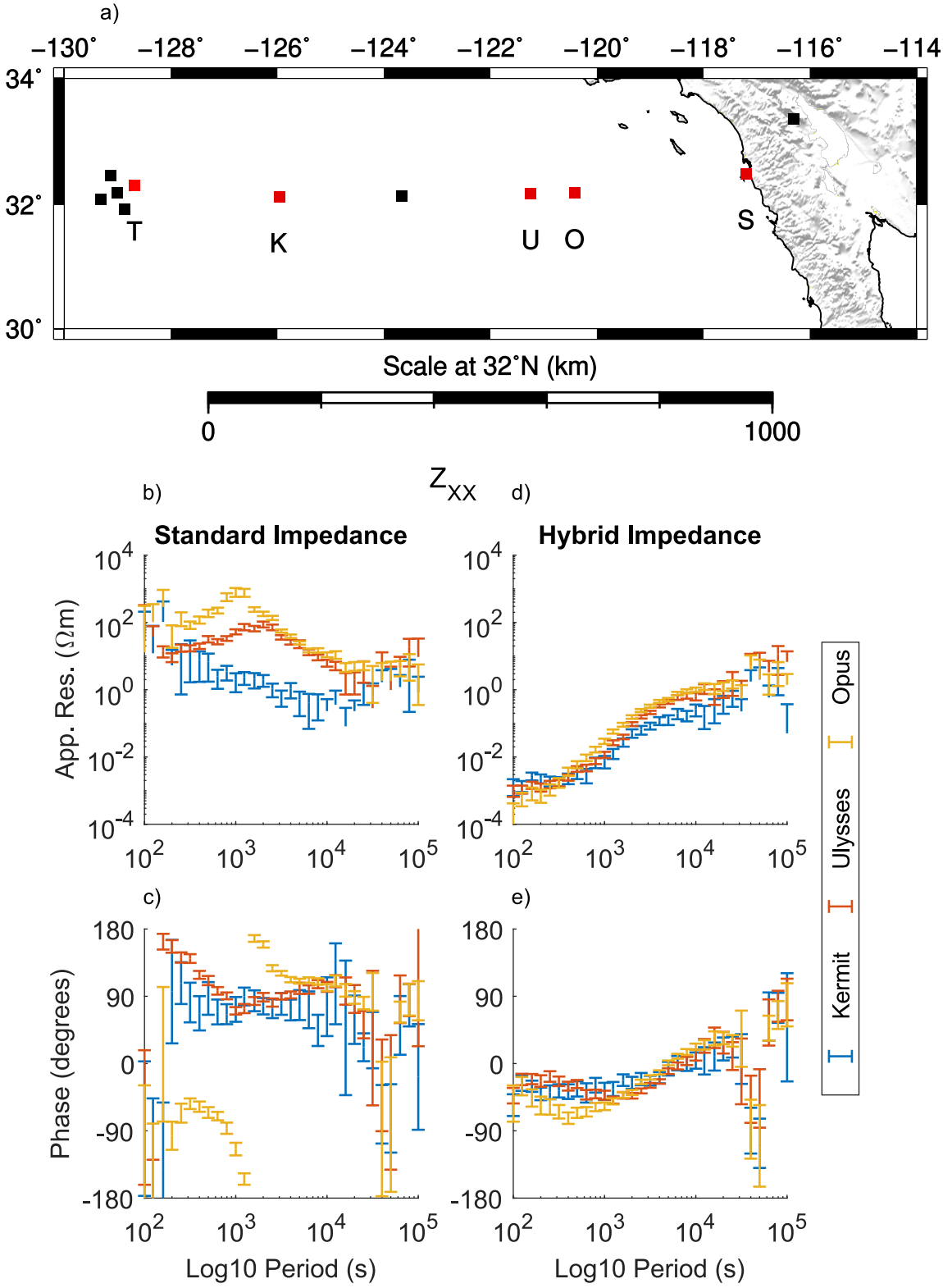

Figure 4.38: a) displays APPLE MT stations as squares. Red squares denote plotted stations. Following instrument issues, Kermit utilises Trevor magnetic fields. b) and c) display apparent resistivity and phase for a standard impedance. d) and e) display apparent resistivity and phase for a hybrid impedance. Blue, orange, and yellow data points correspond to the Z_{XX} component calculated from Kermit, Ulysses, and Opus receivers respectively.

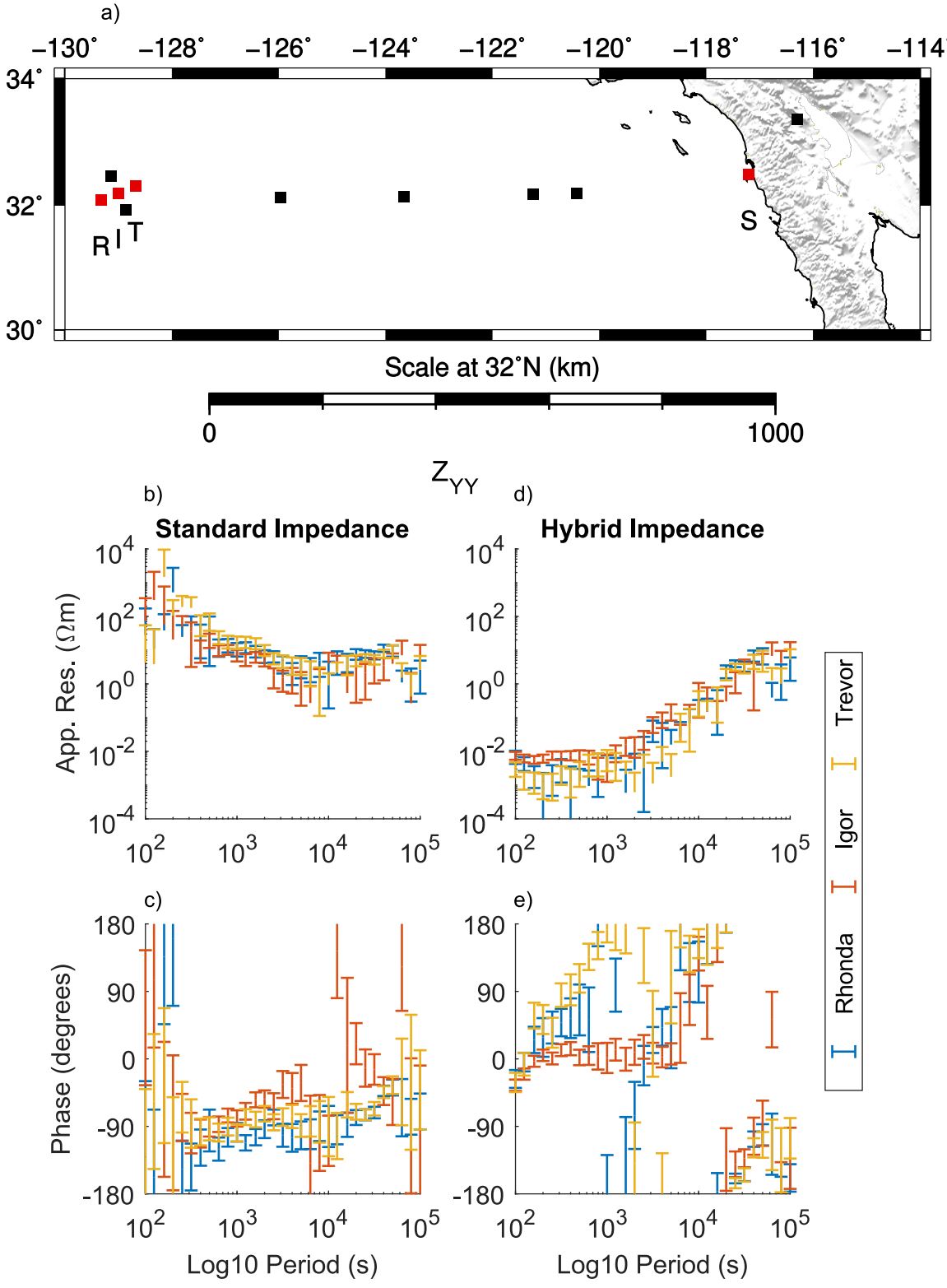

Figure 4.39: a) displays APPLE MT stations as squares. Red squares denote plotted stations. b) and c) display apparent resistivity and phase for a standard impedance. d) and e) display apparent resistivity and phase for a hybrid impedance. Blue, orange, and yellow data points correspond to the Z_{YY} component calculated from Rhonda, Igor, and Trevor receivers respectively.

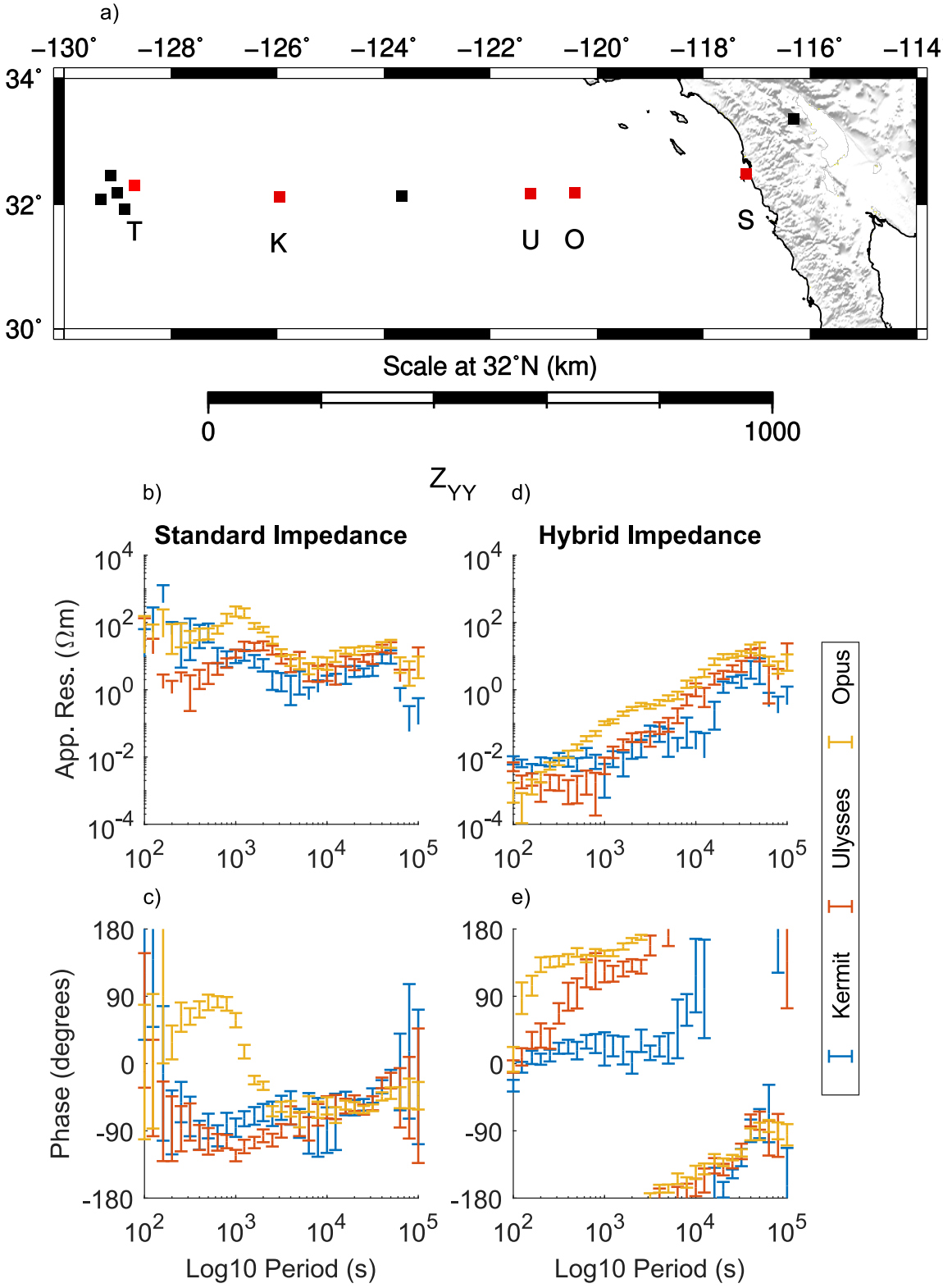

Figure 4.40: a) displays APPLE MT stations as squares. Red squares denote plotted stations. Following instrument issues, Kermit utilises Trevor magnetic fields. b) and c) display apparent resistivity and phase for a standard impedance. d) and e) display apparent resistivity and phase for a hybrid impedance. Blue, orange, and yellow data points correspond to the Z_{YY} component calculated from Kermit, Ulysses, and Opus receivers respectively.

responses to be a consequence of utilising sDome B_y fields. As the sDome receiver is closer to the coastline than its ocean-bottom counter parts, the effects of E_x on B_y are more pronounced. As a result, the magnitude of Z_{YY} is reduced which causes instability in apparent resistivity and phase when compared to standard impedance.

I then display Z_{XY} and Z_{YX} for standard and hybrid impedances (Figs 4.41 to 4.44) in addition to apparent resistivity and phase responses (Figs 4.45 to 4.48). From these Figs, I observe improved confidence intervals for periods greater than 1,000 s when comparing standard impedance to my proposed hybrid impedance. I interpret this observation to be evidence supporting the use of a hybrid MT impedance as a strategy to address ocean-bottom MT impedance instability. For periods shorter than 1,000 s, errors are observed to increase. In contrast, hybrid impedances exhibit well constrained values for this period range. I interpret this response to be an expression of poor signal-to-noise ratio as observed at high frequencies in the PSD response of ocean-bottom magnetic field. Subsequently, these observations corroborate my earlier conclusion that ocean-bottom magnetic field measurements cause instability in ocean-bottom MT impedance. Furthermore, these observations provide further evidence supporting the use of a hybrid MT impedance as a strategy to address ocean-bottom MT impedance instability.

In addition to the impedance, I calculate the coherence between (E_x,B_y) and (E_y,B_x) EM fields measured by all receivers. The coherence of EM fields represents the extent to which the PSD an EM field can be predicted from another EM field using a linear relationship. Additionally, I analyse the zero coherence between these pairs of EM fields. The zero coherence represents the extent to which the PSD of an EM field can be predicted by a random synthetic time series. When the coherence and zero coherence values are approximately equal, the relationship between PSD is poorly resolved.

Figs 4.49 to 4.54 display the coherence and zero coherence at each receiver location for standard and hybrid impedance fields. The coherence and zero coherence become approximately equal for periods less than 100 s when utilising standard impedance fields. In contrast, the zero coherence remains small for this period range when utilising hybrid impedance. This observation further corroborates my conclusion that ocean-bottom magnetic field measurements cause instability in ocean-bottom MT impedance. For periods greater than 100 s, I observe large coherence values compared to zero coherence values for periods between 100 s and 10,000 s for both standard and hybrid impedance fields. However, I observe larger zero coherence values when utilising standard impedance fields. This verifies my observations of improved confidence intervals when comparing standard and hybrid impedance. Subsequently, I interpret this observation as evidence supporting the use of a hybrid MT impedance. Beyond 10,000 s,

ocean-bottom electric and quasi-surface magnetic fields result in coherence and zero coherence values which are comparable to those calculated from ocean-bottom fields. From this observation, I expect minimal improvements beyond 10,000 s when calculating hybrid impedance. However, it is important to note that improving the confidence intervals for periods shorter than 10,000 s constrains permissible geoelectric structures for periods beyond 10,000 s.

4.7 Discussion

Through an analysis of EM fields measured during APPLE, I identified an alternative form of impedance for use in ocean-bottom MT studies. It is important to note that this hybrid impedance doesn't represent a discrete EM response of the Earth due to the spatial distance between receivers. The geological structure of the APPLE region is assumed to consist of a 2-Dimensional coastline orientated towards 327° above a 1-Dimensional oceanic lithosphere. As a result, the impedance tensor can be rotated into a coordinate frame parallel and perpendicular to the coastline. In this configuration diagonal elements of the impedance tensor reduce to zero.

Diagonal elements of the hybrid impedance are observed to better approximate this condition when compared to standard impedance (Figs 4.33 to 4.34 and Figs 4.35 to 4.36). Furthermore, I observe improvements in the confidence intervals of all impedance tensor elements at all periods when calculating hybrid impedance which subsequently improves the confidence intervals of apparent resistivity and phase information calculated from hybrid impedances (Figs 4.33 to 4.48). Lastly, hybrid impedances are observed to be less sensitive to the proximity of the continental margin allowing for easier comparison between ocean-bottom receivers. From these observations, I conclude that hybrid impedance improves the bandwidth and confidence intervals of ocean-bottom MT data.

The apparent resistivity is observed to decrease at short periods towards the conductivity of ocean water for both the diagonal and off-diagonal components of hybrid impedance. I interpret this decrease in resistivity to be a consequence of generating hybrid impedances. As this process involves utilising magnetic fields from the ocean surface, the resulting apparent resistivity represents ocean water conductivity at short periods. Furthermore, the plane-wave assumption degrades for periods greater than 10,000 s (Pulkkinen et al., 2006). However, these periods allow us to improve the confidence intervals for the intervening periods. This improvement subsequently reduces the uncertainty when interpreting geological structures within the Earth. Therefore, I propose future ocean-bottom MT studies utilise hybrid impedances when attempting to investigate the electrical structure of the Earth.

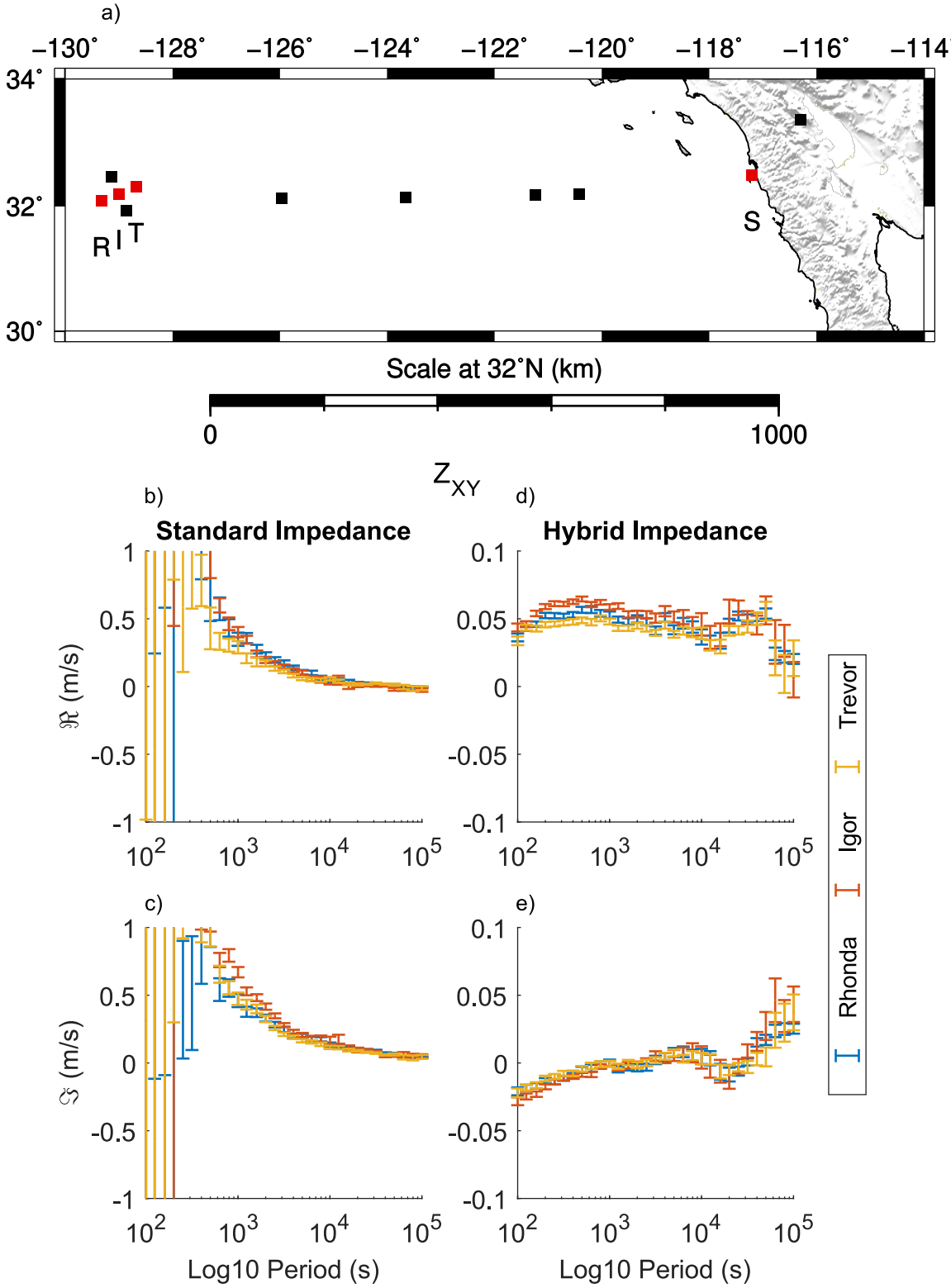

Figure 4.41: a) displays APPLE MT stations as squares. Red squares denote plotted stations. b) and c) display the $\Re$ and $\Im$ for the Z_{XY} component for standard impedance. d) and e) display the $\Re$ and $\Im$ for the Z_{XY} component for hybrid impedance. Blue, orange, and yellow data points correspond the Rhonda, Igor, and Trevor receivers respectively. When presenting hybrid responses, the Y-axis is reduced by an order of magnitude to improve readability.

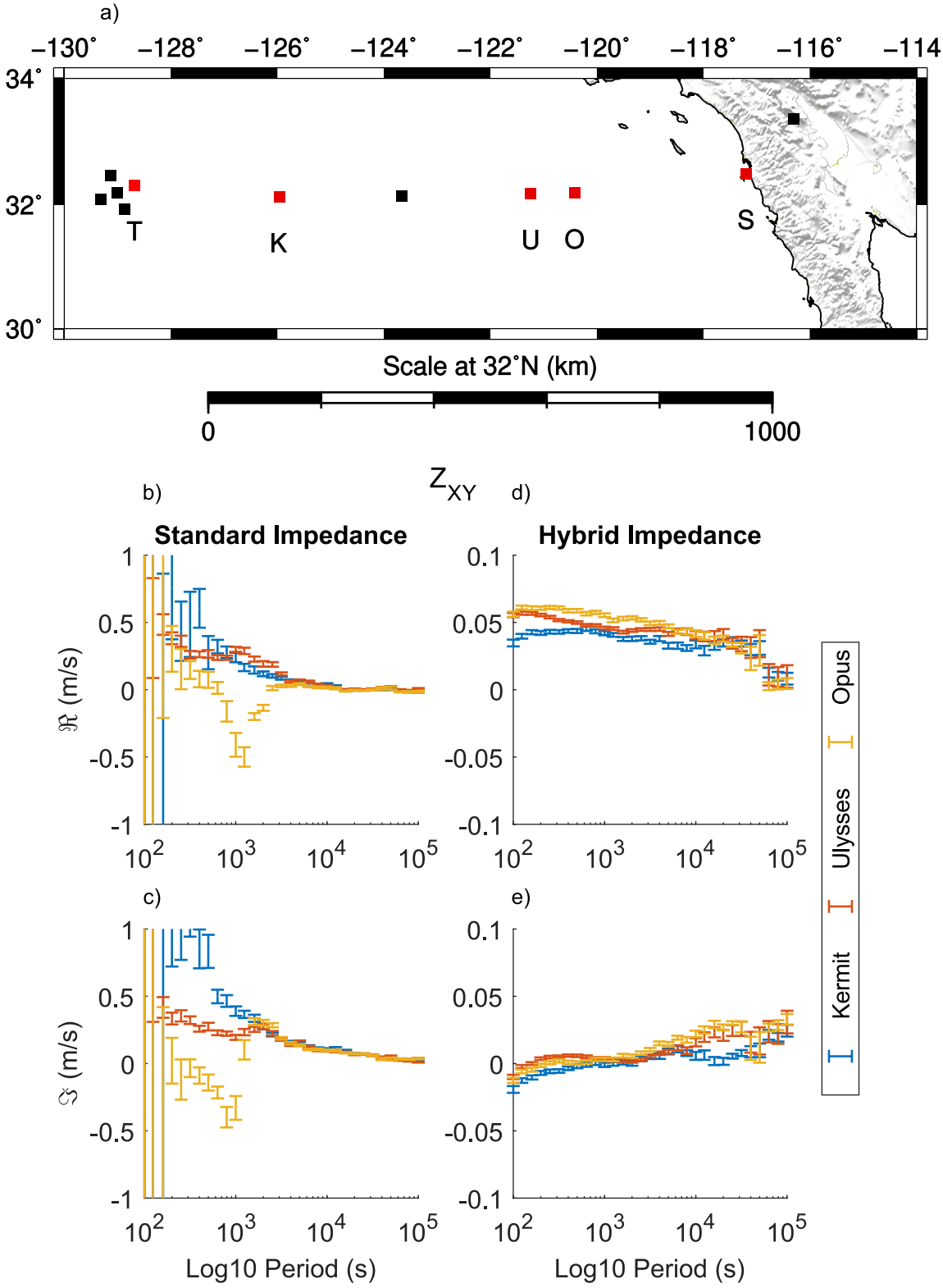

Figure 4.42: a) displays APPLE MT stations as squares. Red squares denote plotted stations. Following instrument issues, Kermit utilises Trevor magnetic fields. b) and c) display the $\Re$ and $\Im$ for standard impedance. d) and e) display the $\Re$ and $\Im$ for hybrid impedance. Blue, orange, and yellow data points correspond to the Z_{XY} component calculated from Kermit, Ulysses, and Opus receivers respectively. When presenting hybrid responses, the Y-axis is reduced by an order of magnitude to improve readability.

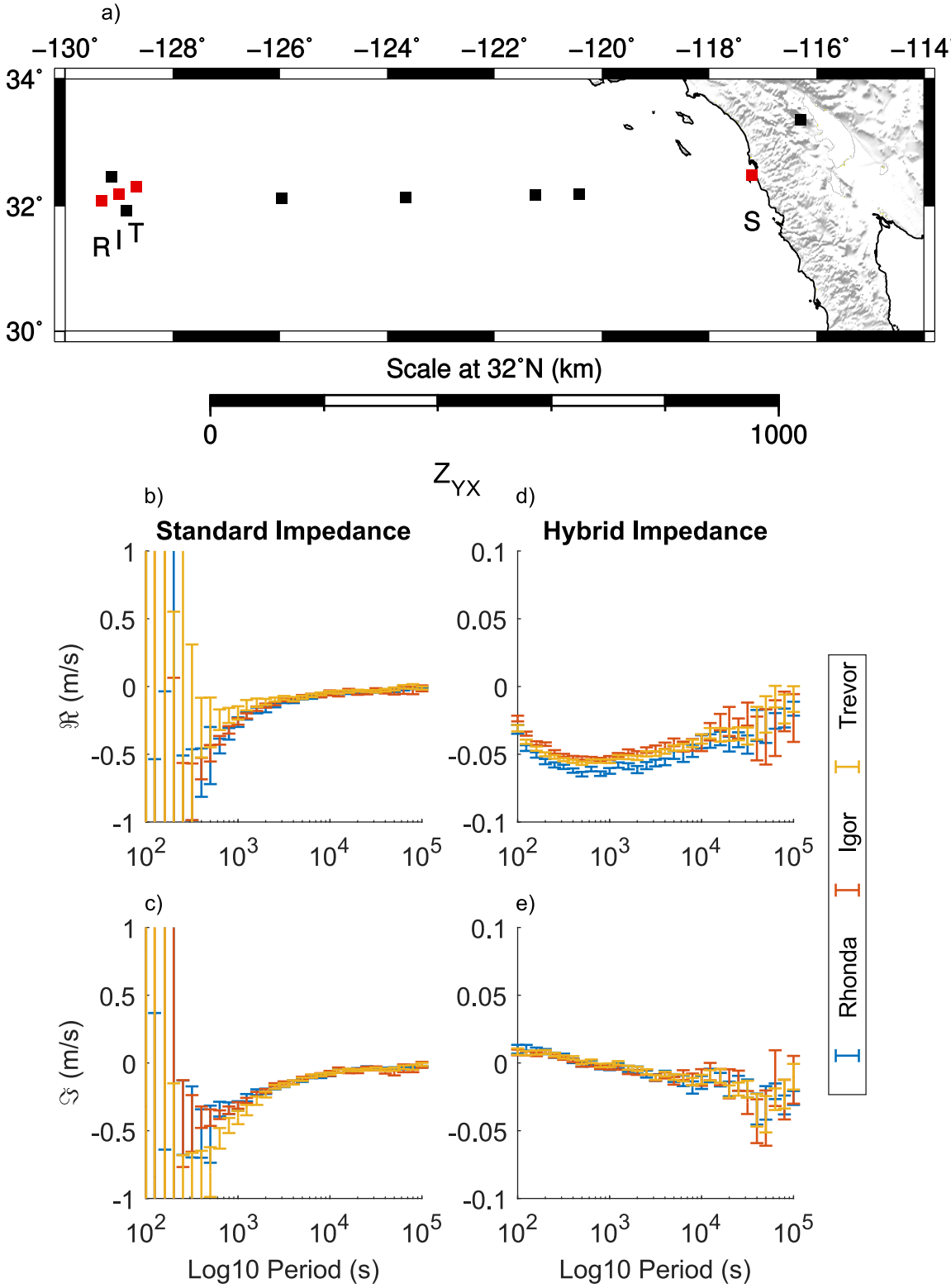

Figure 4.43: a) displays APPLE MT stations as squares. Red squares denote plotted stations. b) and c) display the $\Re$ and $\Im$ for standard impedance. d) and e) display the $\Re$ and $\Im$ for hybrid impedance. Blue, orange, and yellow data points correspond to the Z_{YX} component calculated from Rhonda, Igor, and Trevor receivers respectively. When presenting hybrid responses, the Y-axis is reduced by an order of magnitude to improve readability.

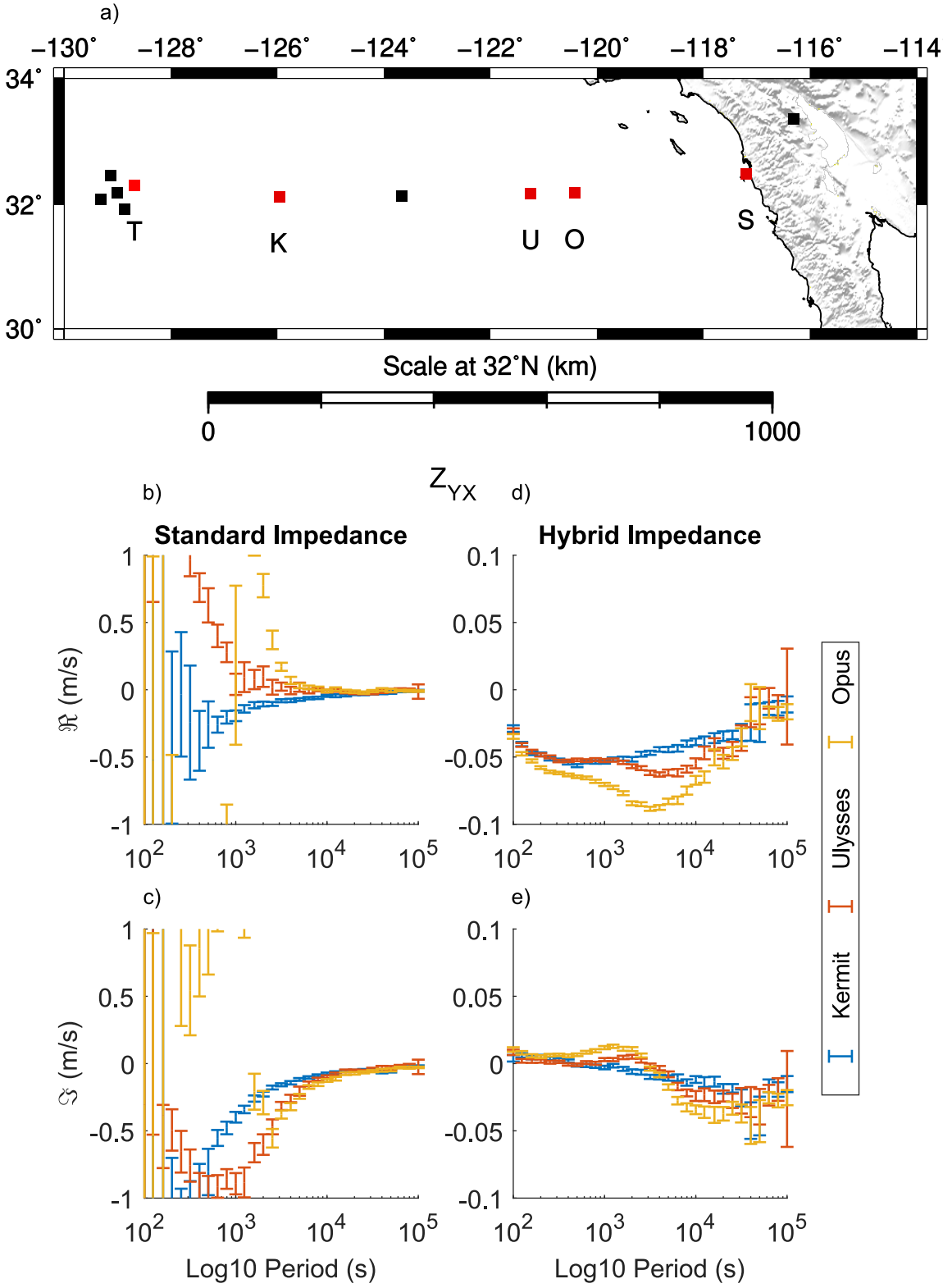

Figure 4.44: a) displays APPLE MT stations as squares. Red squares denote plotted stations. Following instrument issues, Kermit utilises Trevor magnetic fields. b) and c) display the $\Re$ and $\Im$ for standard impedance. d) and e) display the $\Re$ and $\Im$ for hybrid impedance. Blue, orange, and yellow data points correspond to the Z_{XY} component calculated from Kermit, Ulysses, and Opus receivers respectively. When presenting hybrid responses, the Y-axis is reduced by an order of magnitude to improve readability.

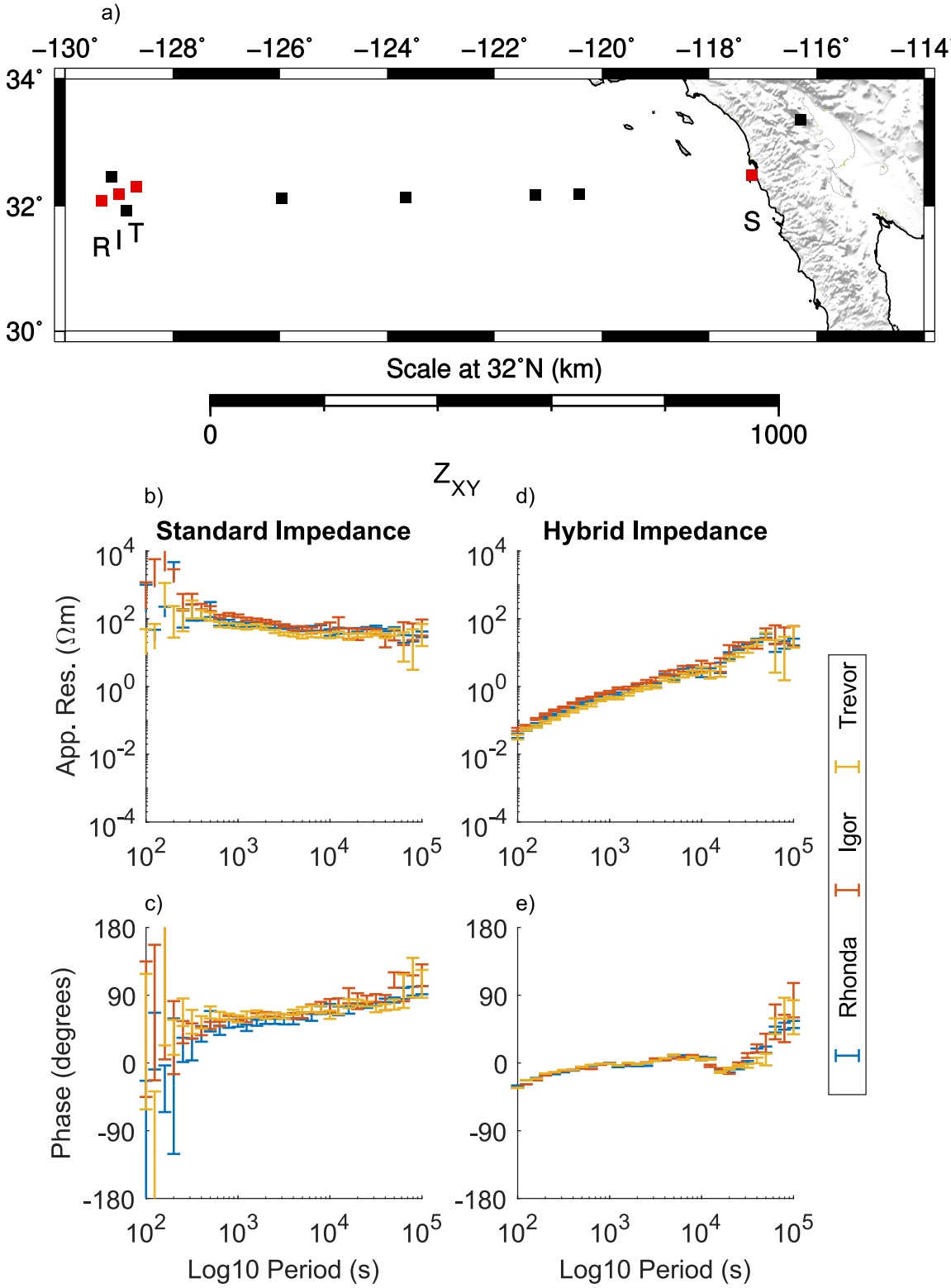

Figure 4.45: a) displays APPLE MT stations as squares. Red squares denote plotted stations. b) and c) display apparent resistivity and phase for a standard impedance. d) and e) display apparent resistivity and phase for a hybrid impedance. Blue, orange, and yellow data points correspond to the Z_{XY} component calculated from Rhonda, Igor, and Trevor receivers respectively.

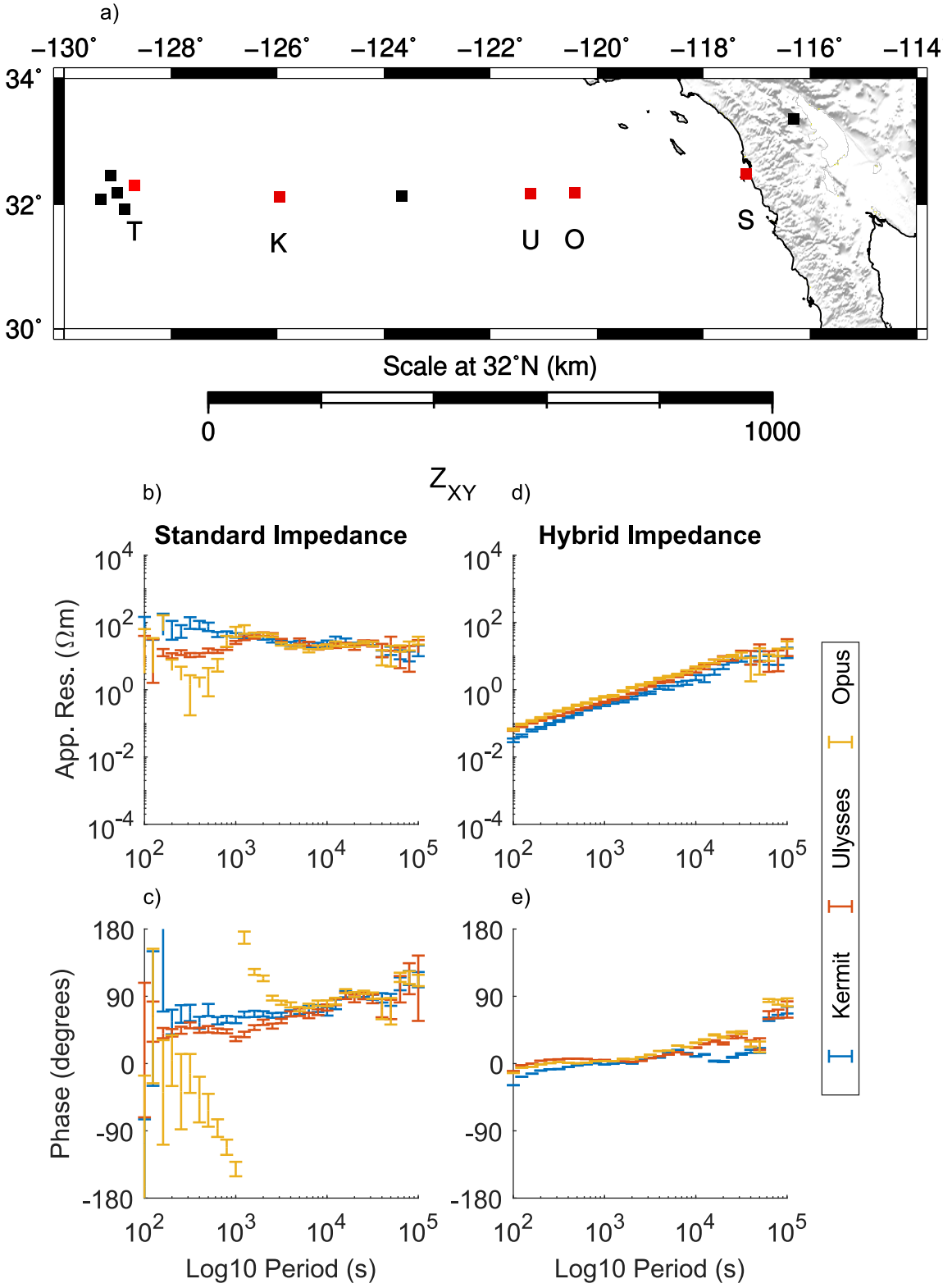

Figure 4.46: a) displays APPLE MT stations as squares. Red squares denote plotted stations. Following instrument issues, Kermit utilises Trevor magnetic fields. b) and c) display apparent resistivity and phase for a standard impedance. d) and e) display apparent resistivity and phase for a hybrid impedance. Blue, orange, and yellow data points correspond to the Z_{XY} component calculated from Kermit, Ulysses, and Opus receivers respectively.

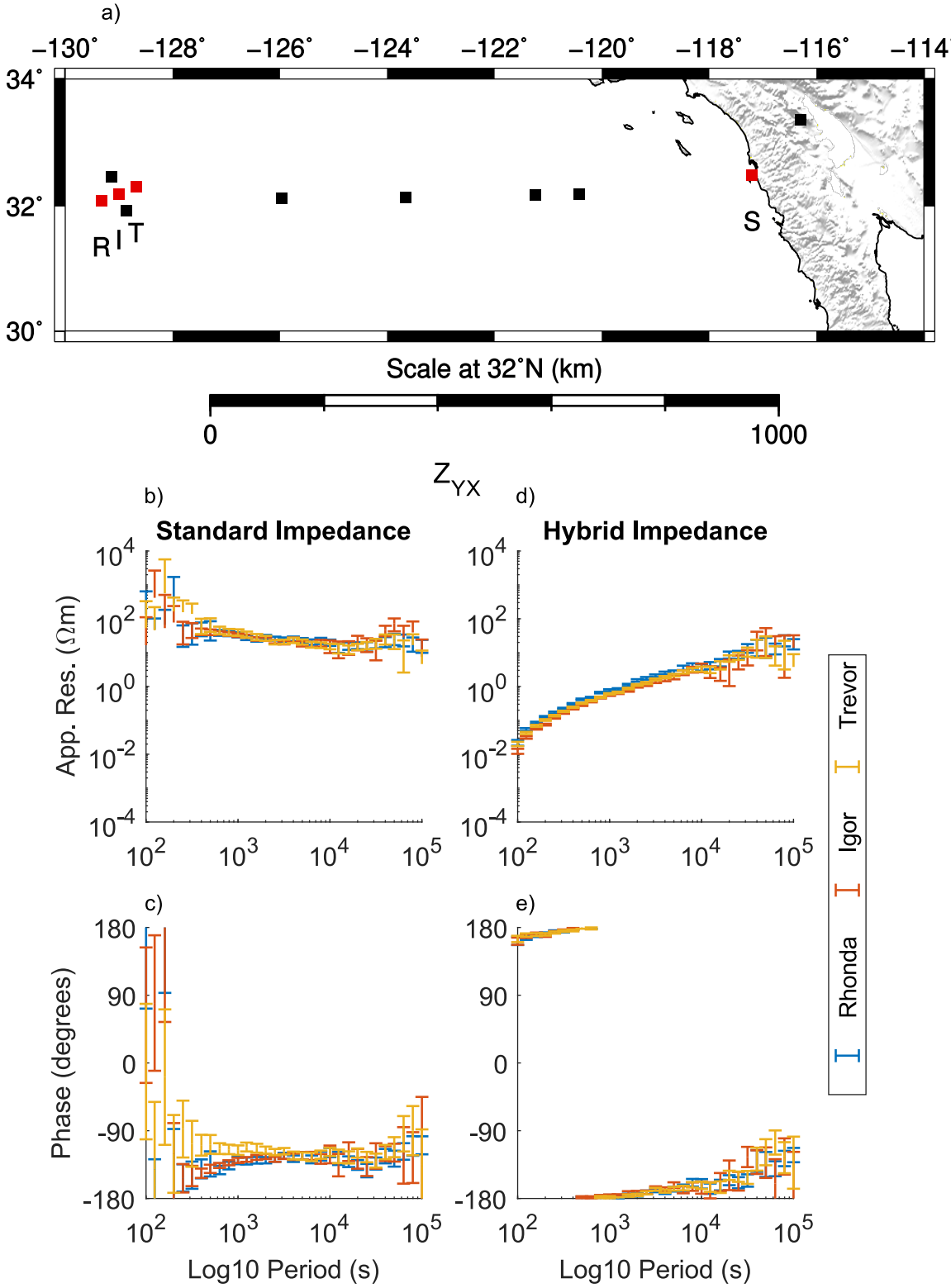

Figure 4.47: a) displays APPLE MT stations as squares. Red squares denote plotted stations. b) and c) display apparent resistivity and phase for a standard impedance. d) and e) display apparent resistivity and phase for a hybrid impedance. Blue, orange, and yellow data points correspond to the Z_{YX} component calculated from Rhonda, Igor, and Trevor receivers respectively.

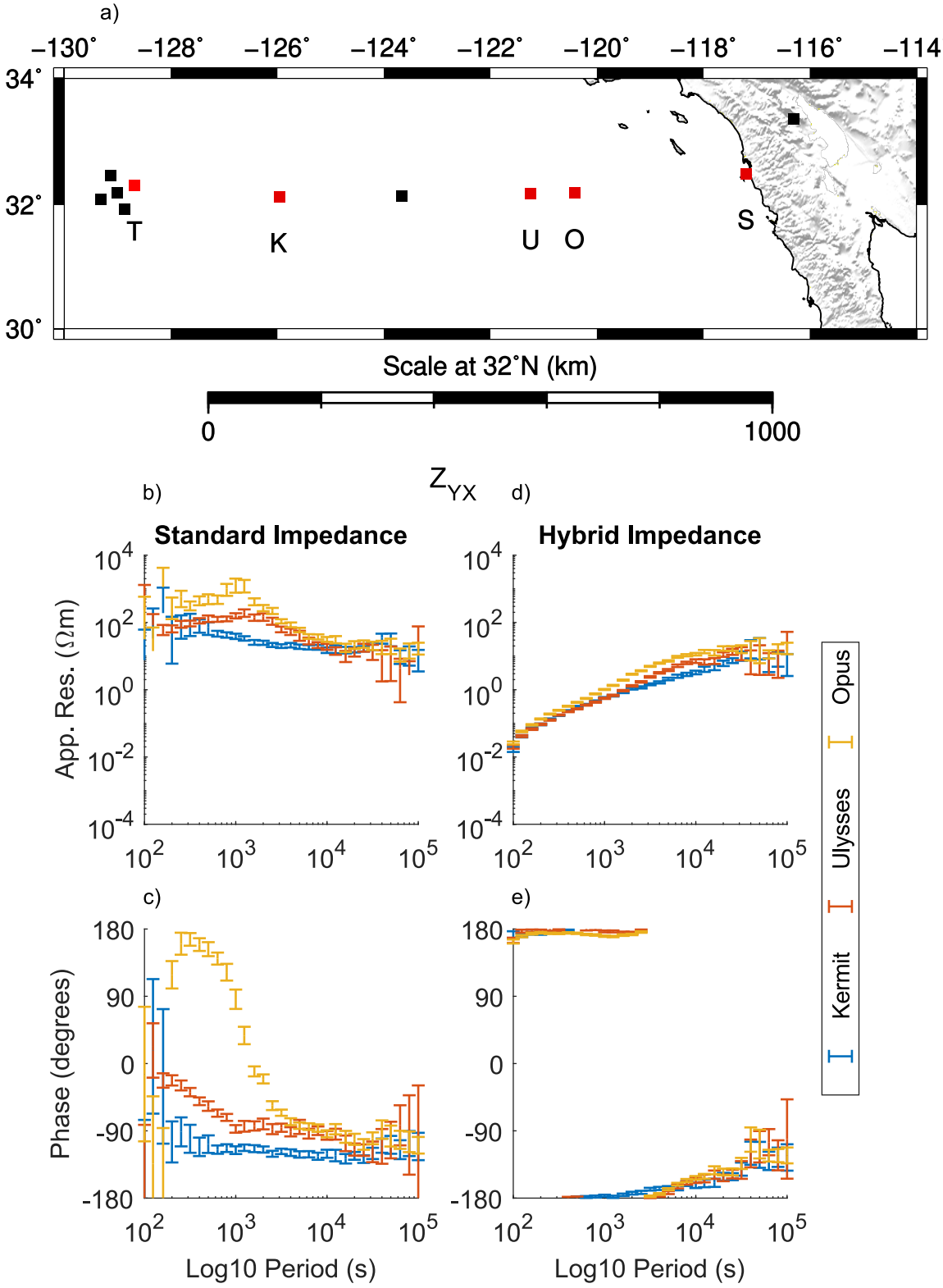

Figure 4.48: a) displays APPLE MT stations as squares. Red squares denote plotted stations. Following instrument issues, Kermit utilises Trevor magnetic fields. b) and c) display apparent resistivity and phase for a standard impedance. d) and e) display apparent resistivity and phase for a hybrid impedance. Blue, orange, and yellow data points correspond to the Z_{YX} component calculated from Kermit, Ulysses, and Opus receivers respectively.

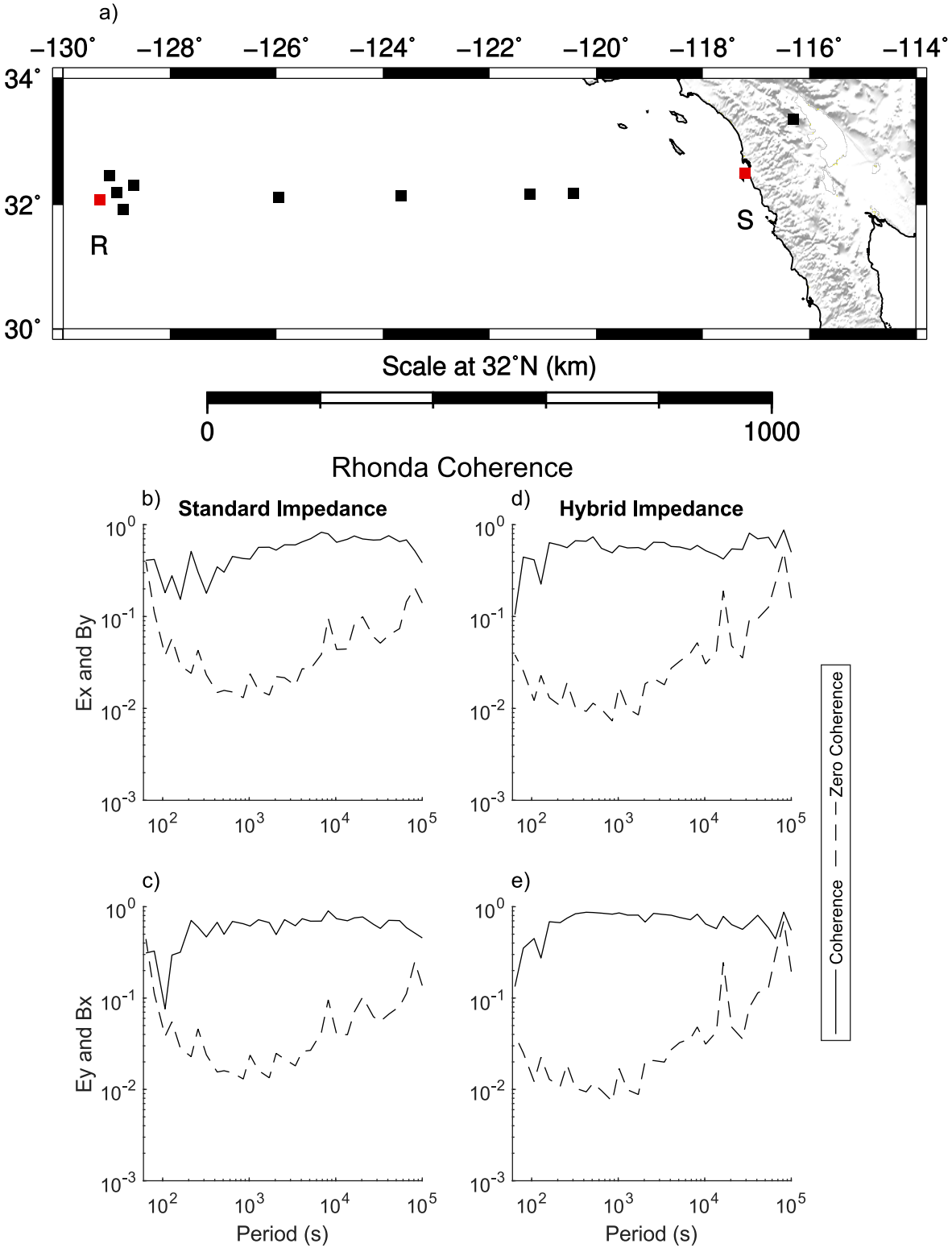

Figure 4.49: a) displays APPLE MT stations as squares. Red squares denote plotted stations. b) and c) display the multiple-squared coherence (solid line) between electric and magnetic fields for standard impedance for the Rhonda receiver. d) and e) display the multiple-squared coherence (solid line) between electric and magnetic fields for hybrid impedance for the Rhonda receiver. The dashed line represents the zero-coherence which is a measure of the random coherence based on the number of windows used.

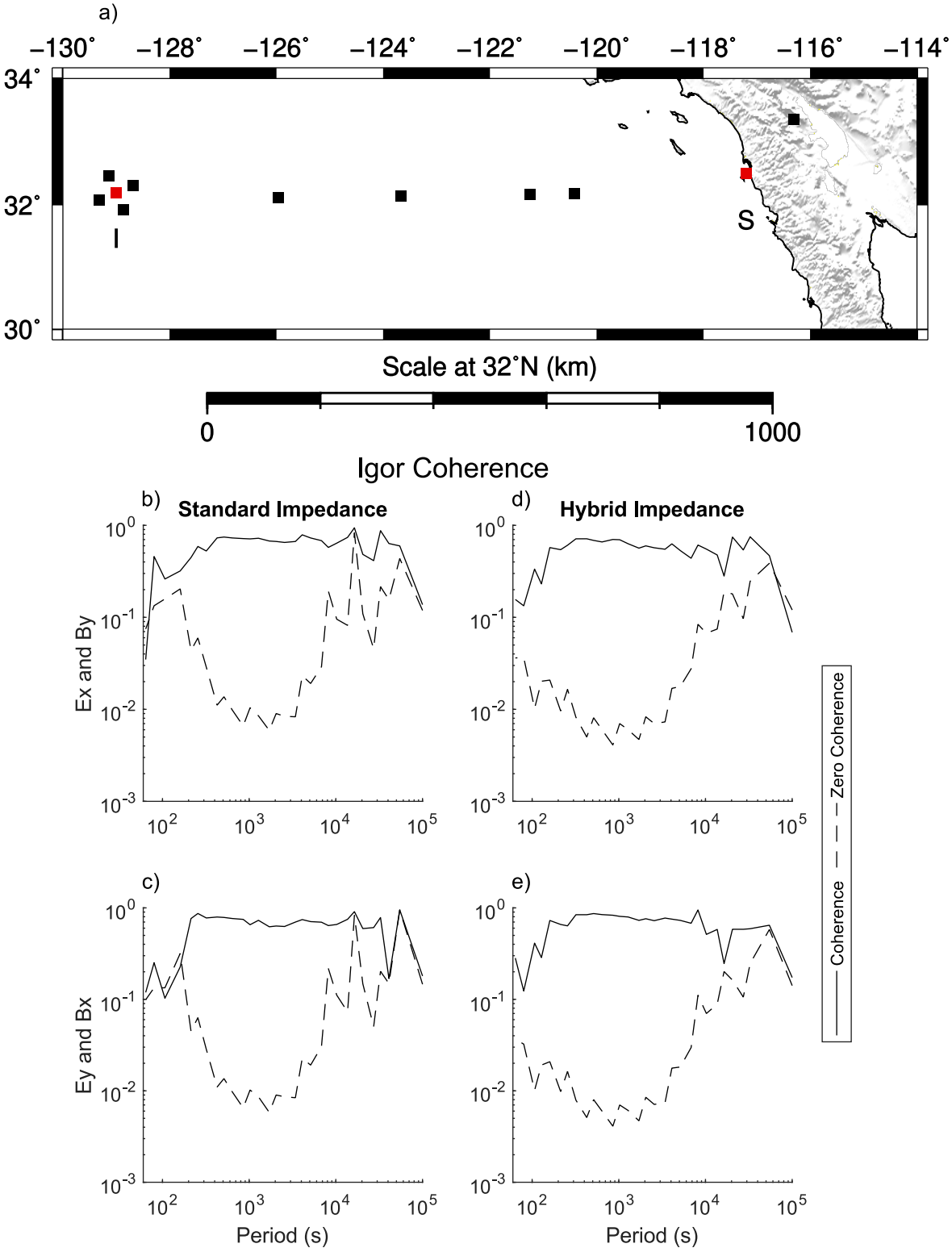

Figure 4.50: a) displays APPLE MT stations as squares. Red squares denote plotted stations. b) and c) display the multiple-squared coherence (solid line) between electric and magnetic fields for standard impedance for the Igor receiver. d) and e) display the multiple-squared coherence (solid line) between electric and magnetic fields for hybrid impedance for the Igor receiver. The dashed line represents the zero-coherence which is a measure of the random coherence based on the number of windows used.

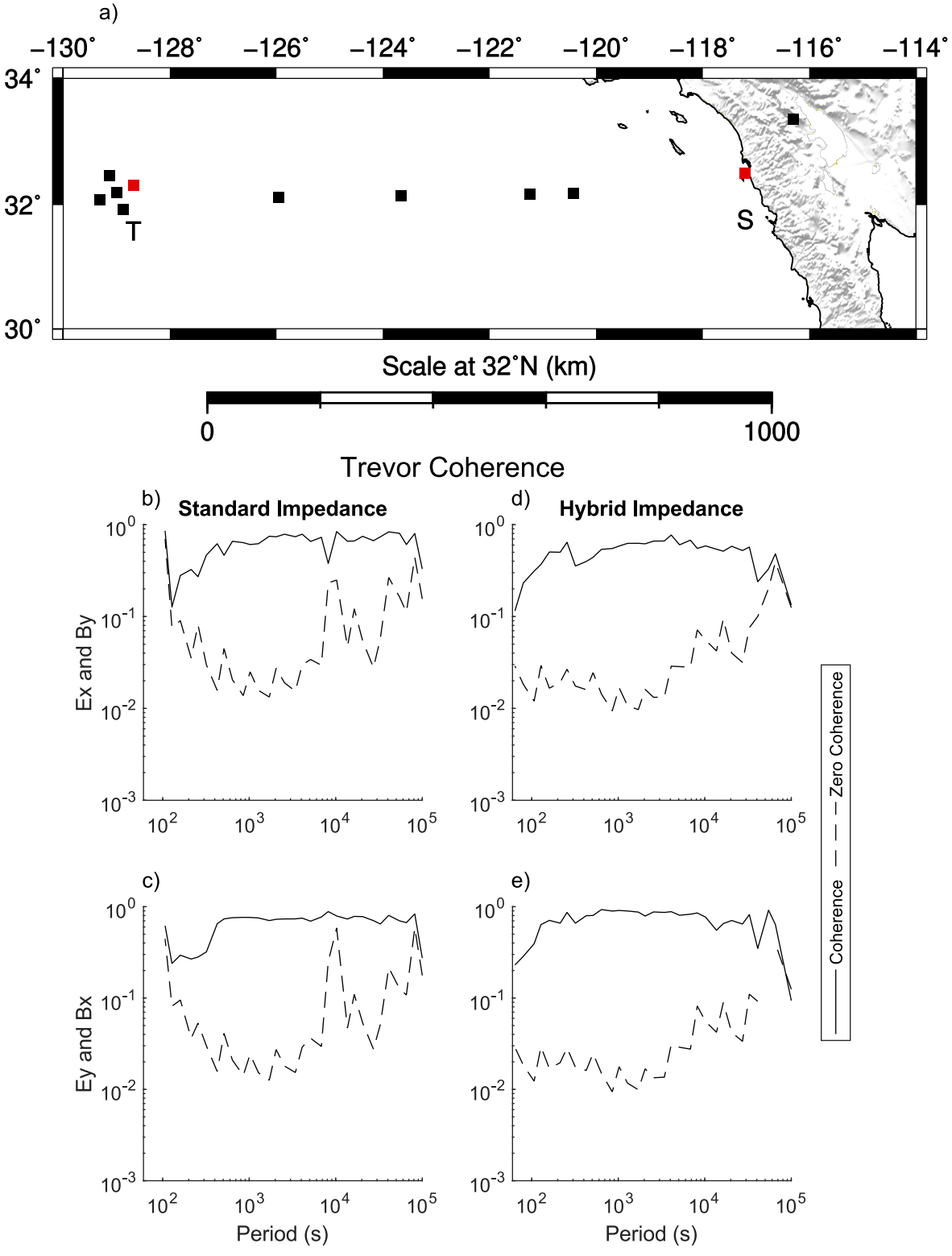

Figure 4.51: a) displays APPLE MT stations as squares. Red squares denote plotted stations. b) and c) display the multiple-squared coherence (solid line) between electric and magnetic fields for standard impedance for the Trevor receiver. d) and e) display the multiple-squared coherence (solid line) between electric and magnetic fields for hybrid impedance for the Trevor receiver. The dashed line represents the zero-coherence which is a measure of the random coherence based on the number of windows used.

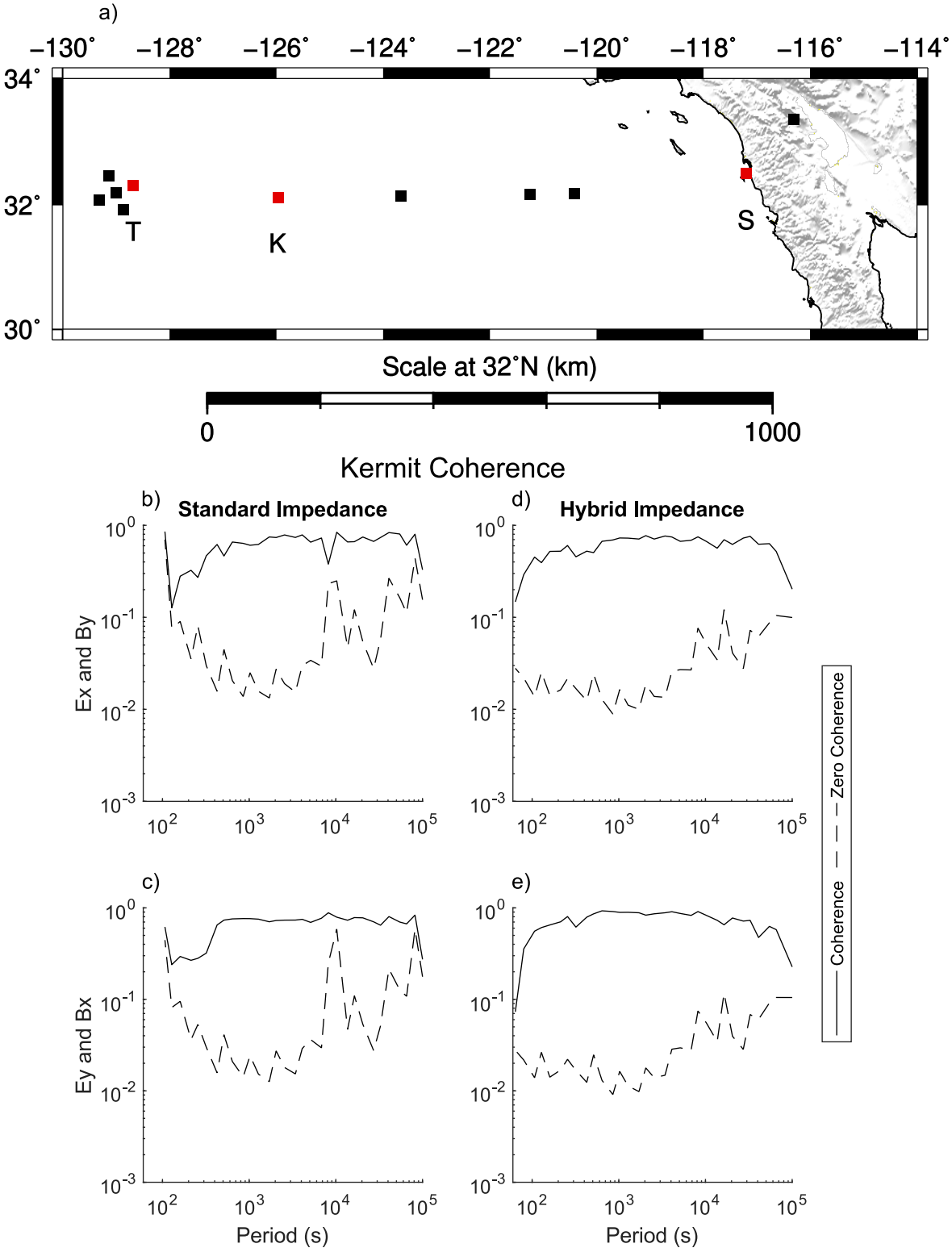

Figure 4.52: a) displays APPLE MT stations as squares. Red squares denote plotted stations. Following instrument issues, Kermit utilises Trevor magnetic fields. b) and c) display the multiple-squared coherence (solid line) between electric and magnetic fields for standard impedance for the Kermit receiver. d) and e) display the multiple-squared coherence (solid line) between electric and magnetic fields for hybrid impedance for the Kermit receiver. The dashed line represents the zero-coherence which is a measure of the random coherence based on the number of windows used.

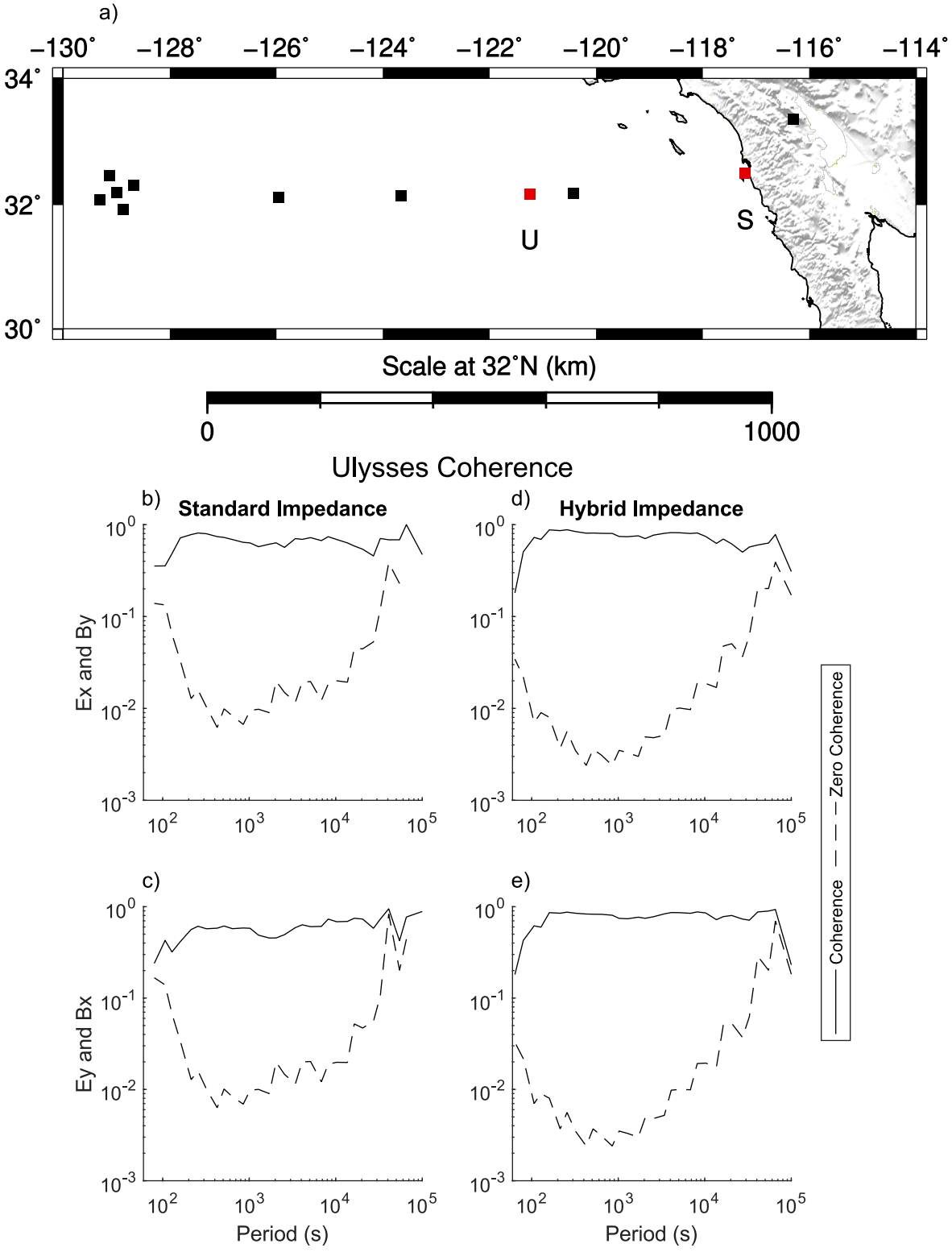

Figure 4.53: a) displays APPLE MT stations as squares. Red squares denote plotted stations. b) and c) display the multiple-squared coherence (solid line) between electric and magnetic fields for standard impedance for the Ulysses receiver. d) and e) display the multiple-squared coherence (solid line) between electric and magnetic fields for hybrid impedance for the Ulysses receiver. The dashed line represents the zero-coherence which is a measure of the random coherence based on the number of windows used.

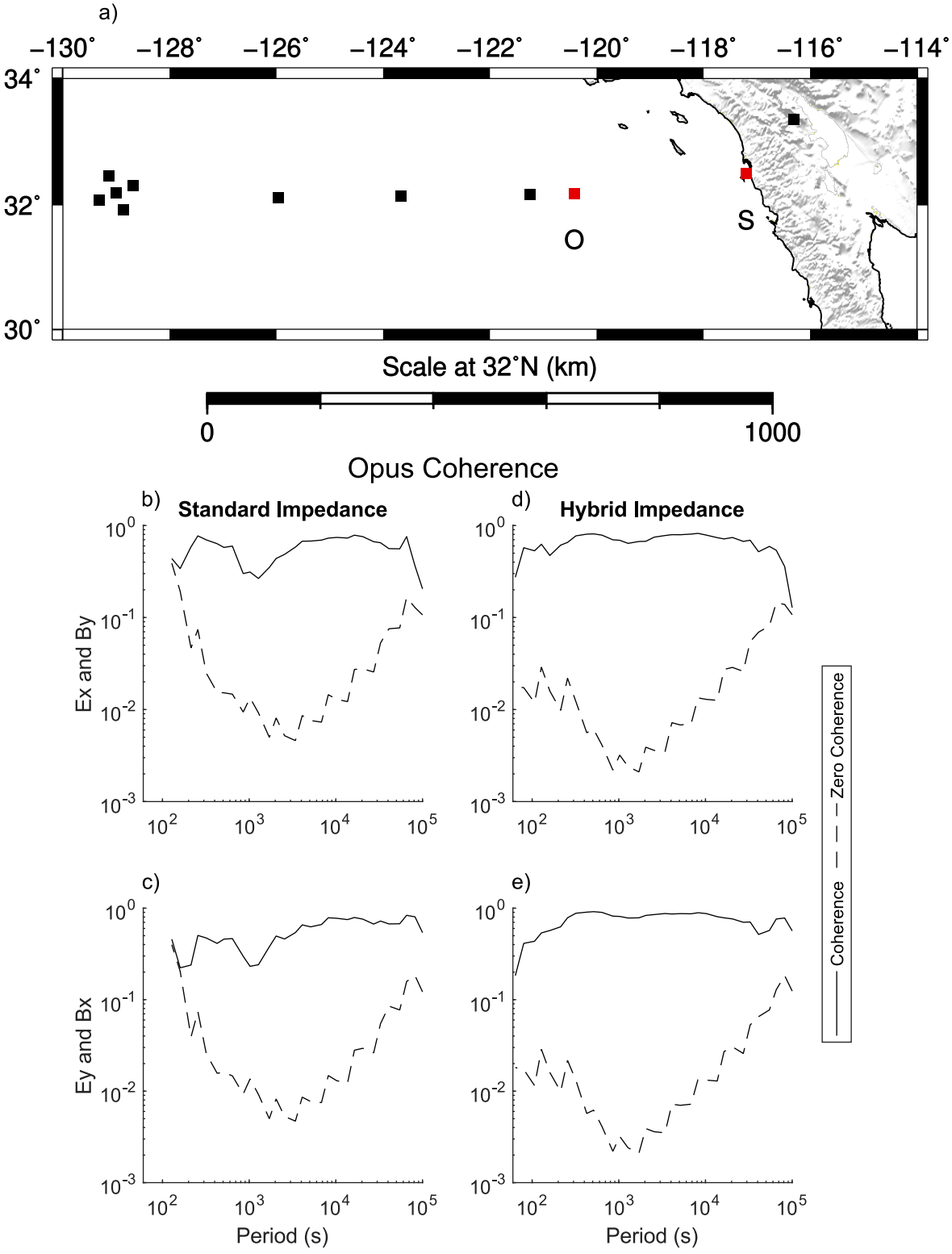

Figure 4.54: a) displays APPLE MT stations as squares. Red squares denote plotted stations. b) and c) display the multiple-squared coherence (solid line) between electric and magnetic fields for standard impedance for the Opus receiver. d) and e) display the multiple-squared coherence (solid line) between electric and magnetic fields for hybrid impedance for the Opus receiver. The dashed line represents the zero-coherence which is a measure of the random coherence based on the number of windows used.

4.8 Conclusions

Covering approximately 70% of the Earth's surface, oceans pose a significant challenge to geophysical studies. The ocean water complicates the use of passive EM geophysical methods, such as the MT method, by distorting the EM fields induced within the Earth. In conjunction with the undulating nature of the Earth's bathymetry and the natural motion of ocean water, this distortion results in unstable ocean-bottom MT data. This instability limits the ability of ocean-bottom MT studies to constrain geodynamic processes. In this chapter, I propose a hybrid MT impedance utilising ocean-bottom electric fields and quasi-surface magnetic fields to address this instability. I anticipate that the adjustment distance represents the distance from the coastline where calculating a hybrid impedance will result in negligible improvements. However, care must be taken to ensure that the plane wave assumption is not violated. Following an analysis of EM fields from offshore California, I conclude that a hybrid MT impedance reduces the instability caused by the Earth's ocean in MT data. Additionally, the hybrid impedance improves the bandwidth of this data from just over one decade to approximately four decades. These conclusions have implications regarding the investigation of geodynamic processes via ocean-bottom MT surveys.

Chapter 5

Insights On The Electrical Conductivity Structure Of The Oceanic Upper Mantle

This chapter aims to assess the conclusions of Chapter 3 and Chapter 4 through a case study. This case study utilises hybrid impedances calculated from data collected during the Anisotropy and Physics of the Pacific Lithosphere Experiment (Chesley et al., 2019). I first constrain the continental portion of my forward model through a 3-Dimensional inversion of USArray MT data across all of California (Fig. 5.1). I then provide an overview of the 2-Dimensional forward modelling algorithm. Following this, I define the general structure common to the forward models used in this chapter. I then calculate an average age for the oceanic lithosphere which I input into my reference model to constrain the upper mantle conductivity structure for this region of the Pacific Ocean. Finally, I calculate responses for both ocean-floor and hybrid impedances and compare them to the measured data.

From this analysis, I find that the upper mantle isn't significantly anisotropic with thermal conduction within upper mantle silicates capable of explaining the conductivity structure within this region of the Earth. In addition, I find that classical ocean-bottom MT responses are poorly reproduced by my forward model as the ocean-bottom magnetic fields are attenuated by undulating bathymetry and sediment thickness which cannot be incorporated into an ocean-bottom MT conductivity model. Consequently, I conclude that these observations validate my electrical conductivity reference model of the upper mantle. Furthermore, I conclude that hybrid impedances improve the stability of both measured and modelled responses over a considerably larger bandwidth.

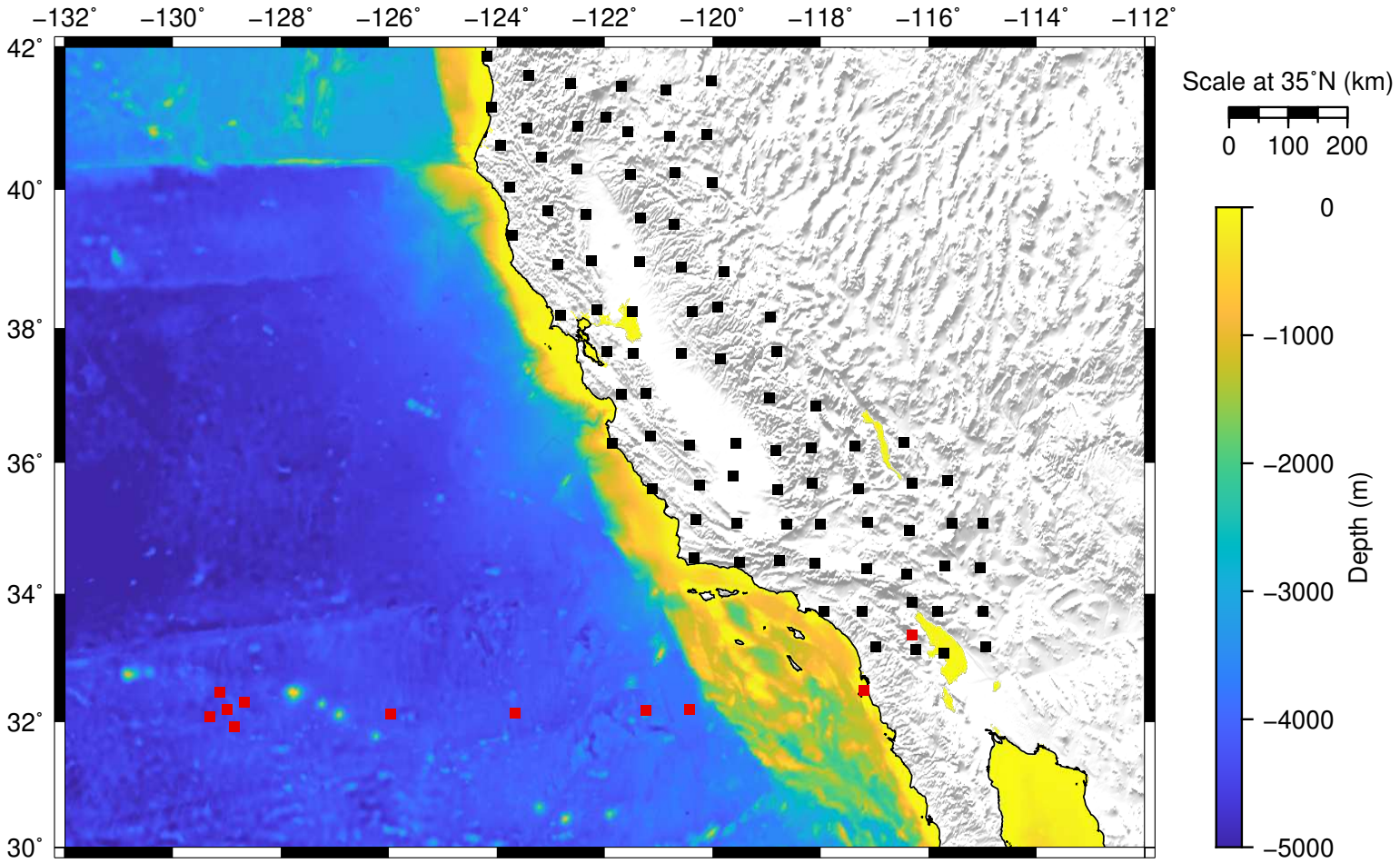

Figure 5.1: Bathymetry location map of California with APPLE data represented as red squares while black squares represent MT data collected during the USArray, CONUS SoCal, and CONUS South projects (Trabant et al., 2012). The basemap utilises the ETOPO1 dataset of Amante and Eakins (2009).

5.1 3-Dimensional Continental Inversion Model

In order to constrain the conductivity of the continental portion of my forward model, I construct a 3-Dimensional inversion of California utilising the RLM-3D code of CGG Multi-Physics Imaging, Milan. This inversion models MT data from the USArray, CONUS SoCal, and CONUS South projects (Trabant et al., 2012). The USArray MT data were collected from 2006 to 2018 as a part of the EarthScope program. This program deployed numerous geophysical instruments to study the structure and evolution of North America. The CONUS MT data, collected from 2019 to 2021, builds upon the EarthScope program by attempting to create a conductivity model of the United States of America which incorporates regional and global electrical conductivity models. Due to the large distance between APPLE and continental receivers, I exclude APPLE MT data from this model. Data collected during the USArray project extending from periods of 7 s to 20,000 s whereas the CONUS SoCal and CONUS South projects collected data extending from periods of 7 s to 30,000 s and 5 s to 30,000 s respectively.

To ensure the mesh is aligned with the regional geoelectric strike, I calculate phase tensors for both oceanic and continental receivers. For 2-Dimensional structures, the phase tensor becomes symmetric with its principal axis aligned parallel or perpendicular to the strike of the regional conductivity distribution. Figs 5.2 to 5.5 display the resulting phase tensors calculated at 1,000 s, 3,000 s, 7,000 s, and 30,000 s respectively. These periods are sensitive to depths characteristic of the lithosphere (1,000 s) and asthenosphere transition zone (30,000 s). From these Figs, I observe the alignment of elliptical phase tensors perpendicular to the continental margin at all periods. From these observations, I conclude that the regional geoelectric strike for this region is the coastline which is primarily 2-Dimensional. I therefore rotate the mesh to be aligned with this coastline.

I then define the horizontal mesh size of this inversion model to be 20 km while covering the continental MT sites. This 20 km mesh size extends an additional 200 km to the ocean side to incorporate changes in seafloor depth. Beyond this central portion, the mesh was padded to a distance of 500 km with the mesh size increasing incrementally by 130%. The vertical mesh size includes topography and begins at 100 m which increases incrementally by 106% to 10 km at which point it increases by 104% to 100 km. The vertical mesh size then increases by 120% to 800 km. In addition, this model includes a further 10 air layers. The resulting model has 80 cells in the x-direction, 59 cells in the y-direction, and 111 cells in the z-direction for a total of 523,920 cells (Fig. 5.6).

The initial conductivity structure for my inversion model is defined by 3 laterally continuous layers and an ocean with a conductivity of 0.3 Ωm. The first layer extends

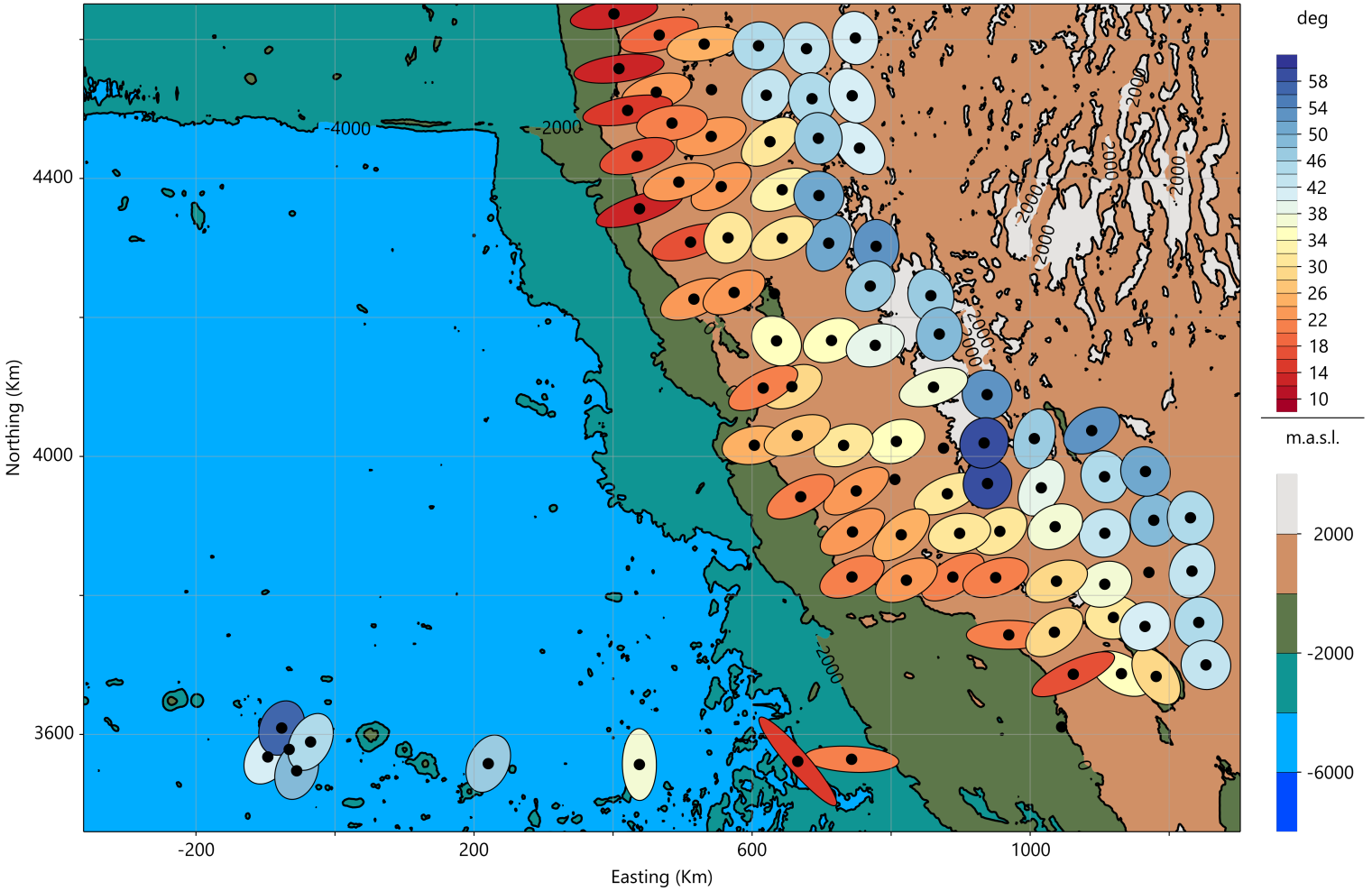

Figure 5.2: Phase tensor diagram of APPLE, USArray, CONUS SoCal, and CONUS South data at 1,000 s period. The colour of the phase tensor represents the minimum phase. Black circles denote the location of plotted receivers. The basemap utilises the SRTM15+ dataset of Tozer et al. (2019).

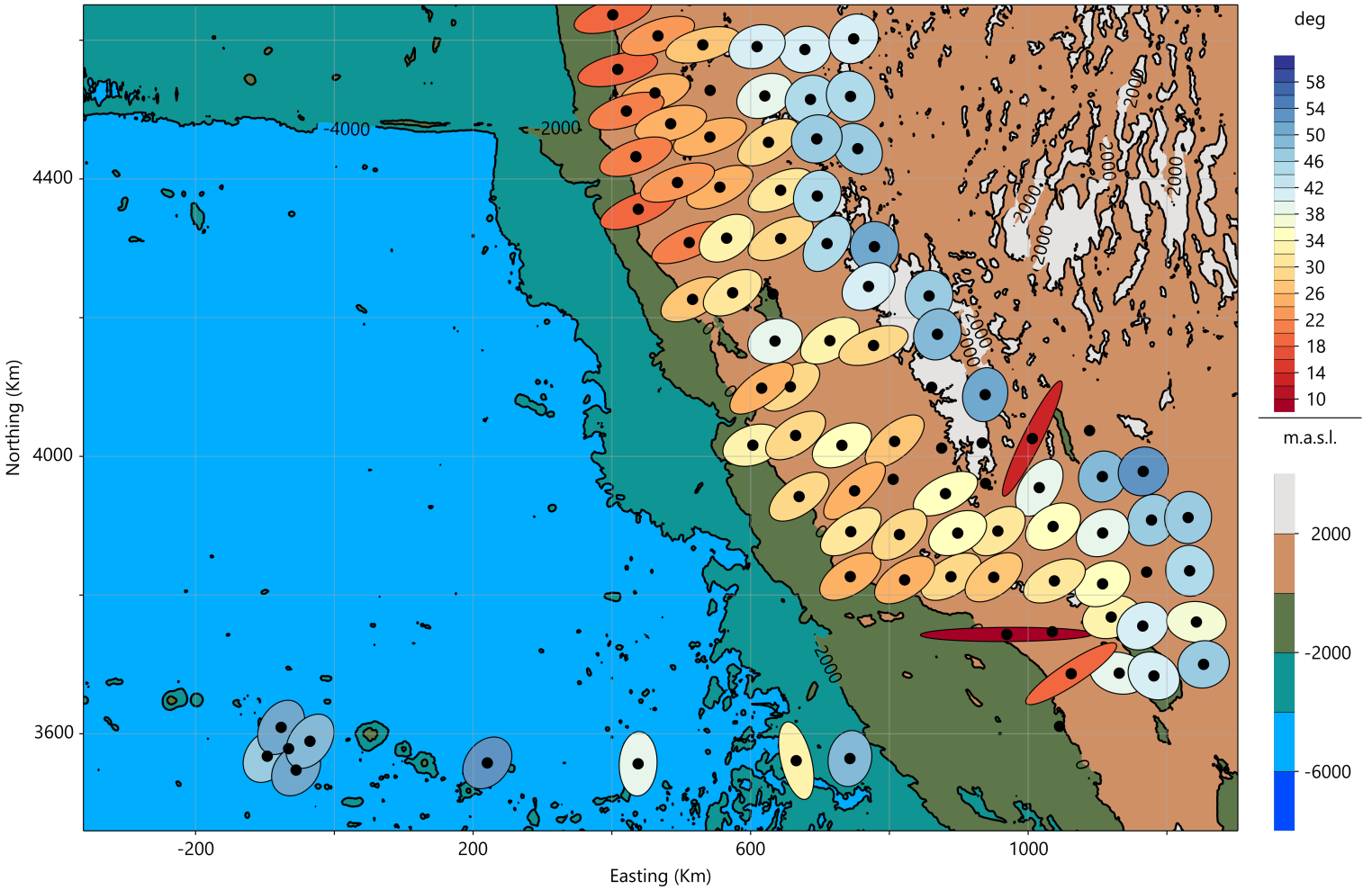

Figure 5.3: Phase tensor diagram of APPLE, USArray, CONUS SoCal, and CONUS South data at 3,000 s period. The colour of the phase tensor represents the minimum phase. Black circles denote the location of plotted receivers. The basemap utilises the SRTM15+ dataset of Tozer et al. (2019).

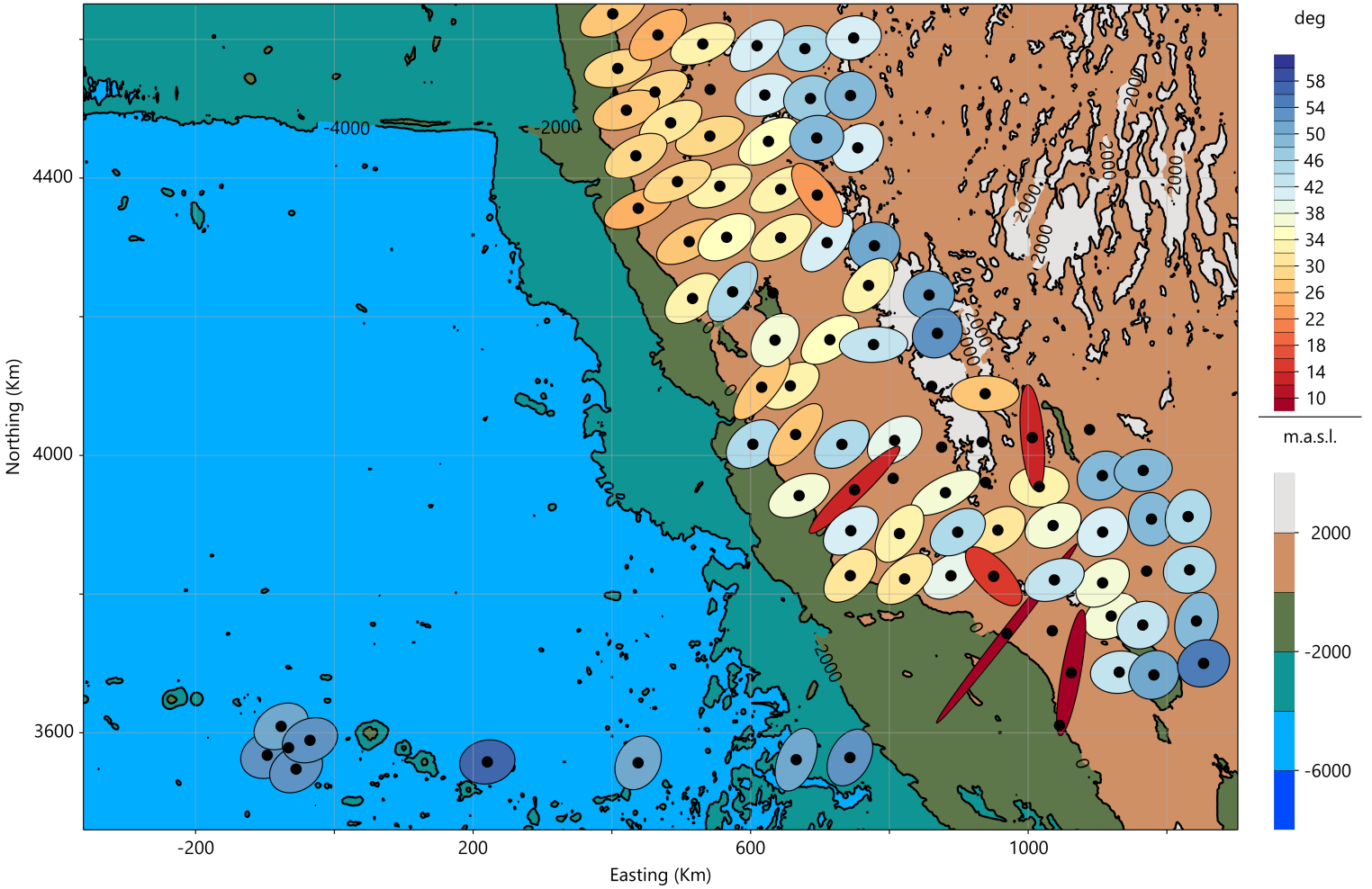

Figure 5.4: Phase tensor diagram of APPLE, USArray, CONUS SoCal, and CONUS South data at 7,000 s period. The colour of the phase tensor represents the minimum phase. Black circles denote the location of plotted receivers. The basemap utilises the SRTM15+ dataset of Tozer et al. (2019).

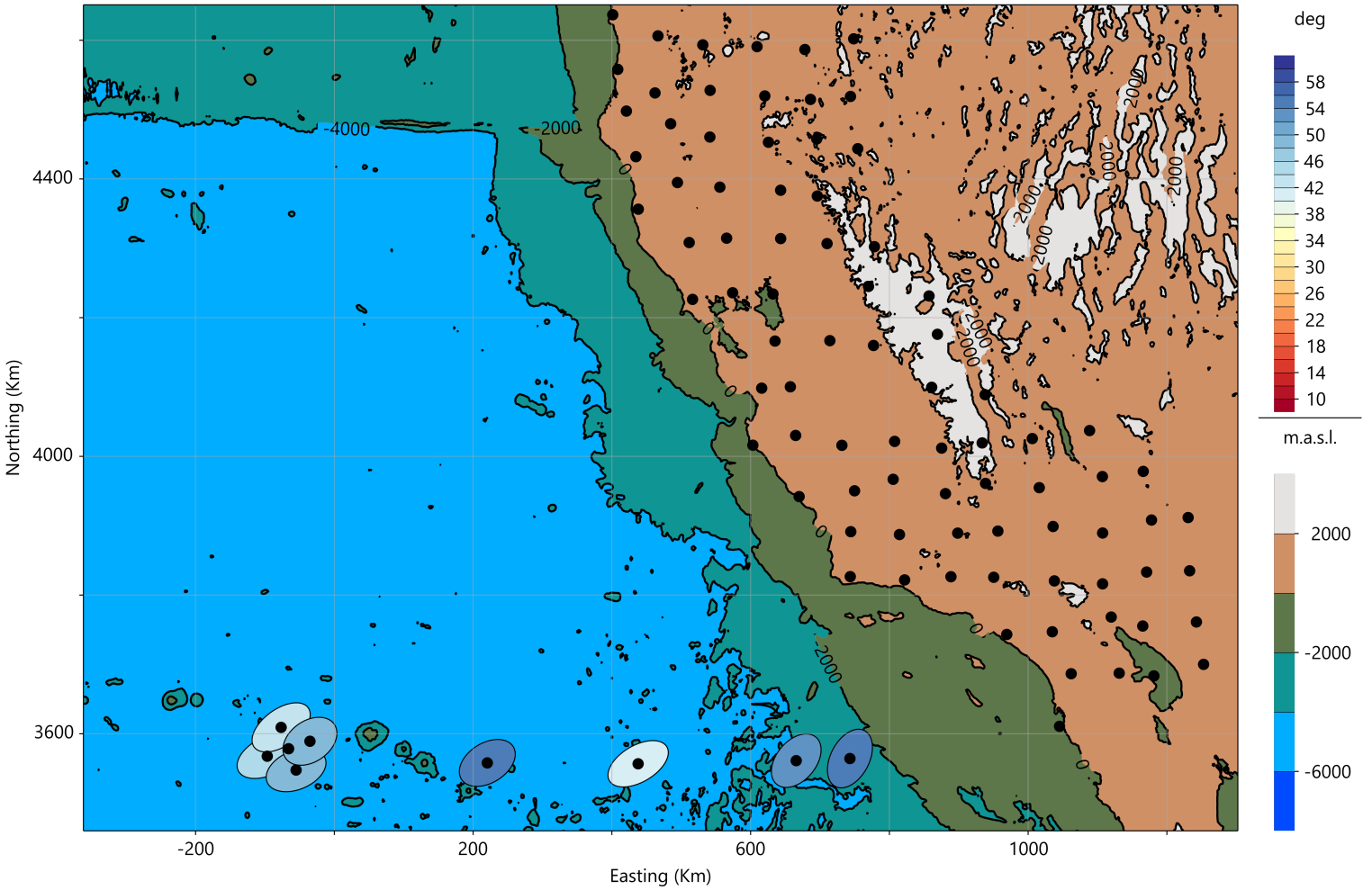

Figure 5.5: Phase tensor diagram of APPLE, USArray, CONUS SoCal, and CONUS South data at 30,000 s period. The colour of the phase tensor represents the minimum phase. Black circles denote the location of plotted receivers. The basemap utilises the SRTM15+ dataset of Tozer et al. (2019).

to a depth of 400 km and is defined by a resistivity of 100 Ωm. The second layer extends to a depth of 670 km and is characterised by a conductivity of 10 Ωm. The final layer is a half space with a conductivity of 1 Ωm. The depths of these layers are defined by the global conductivity model of Grayver et al. (2017). Grayver et al. (2017) generated this conductivity model by model by inverting time-varying magnetospheric and tidal magnetic fields. From this inversion, both a structurally smooth L_2-norm and a structurally sparse L_1-norm solution was calculated. The resulting C-responses were subsequently converted to apparent resistivity and phase using the following equations:

$$\rho_a(\omega) = \omega\mu_0|C(\omega)|^2, \tag{5.1}$$

$$\phi(\omega) = \frac{\pi}{2} + \arctan\left(\frac{\Im C(\omega)}{\Re C(\omega)}\right). \tag{5.2}$$

After 50 iterations, the inversion reduced the RMS misfit to 2 assuming an error floor of 5% of the impedances. Figs 5.7 and 5.8 present the 3-Dimensional inversion resistivity as horizontal slices. In addition, I plot three cross-sections orientated perpendicular to the coastline (Figs 5.9). These cross-sections display the electrical resistivity as a function of depth through the northern, central, and southern region of my 3-Dimensional inversion solution (Figs 5.10, 5.11, and 5.12 respectively).

From these Figs, I observe a zone of approximately 10 Ωm resistivity within the top 5 kilometres of my inversion adjacent to the coastline (Fig. 5.7). Further inland, the resistivity increases to approximately 10,000 Ωm. From the cross-sections, I observe that the near surface conductive structure extends from the coastline to the base of the Sierra Nevada ranges. At which point, a resistive structure becomes dominant. I interpret this lateral variation to be an expression of marine and continental sediments within the Great Valley and the resistive Sierra Nevada batholith which corroborates the results of Zandt et al. (2004) and Ostos and Park (2012) (Fig. 5.13).

Beneath this surface layer, I observe a laterally continuous increase in resistivity to approximately 1,000 Ωm from 5 km to between 20 km to 30 km (Figs. 5.7 and 5.8). This laterally homogeneous resistivity structure is observed within in all cross-sections. Godfrey and Klemperer (1998) utilised seismic reflection, seismic refraction, gravity, borehole, and aeromagnetic data to identify the Coast Range ophiolite beneath the Great Valley basin which is corroborated by the tectonostratigraphic cross section of Williams and Graham (2013). As a consequence, I interpret the laterally homogeneous conductivity structure observed throughout our model to be the Coast Range ophiolite.

As depth increases, I observe an increase in conductivity to approximately 30 Ωm. This conductive anomaly extends to the base of my model (Fig. 5.8).

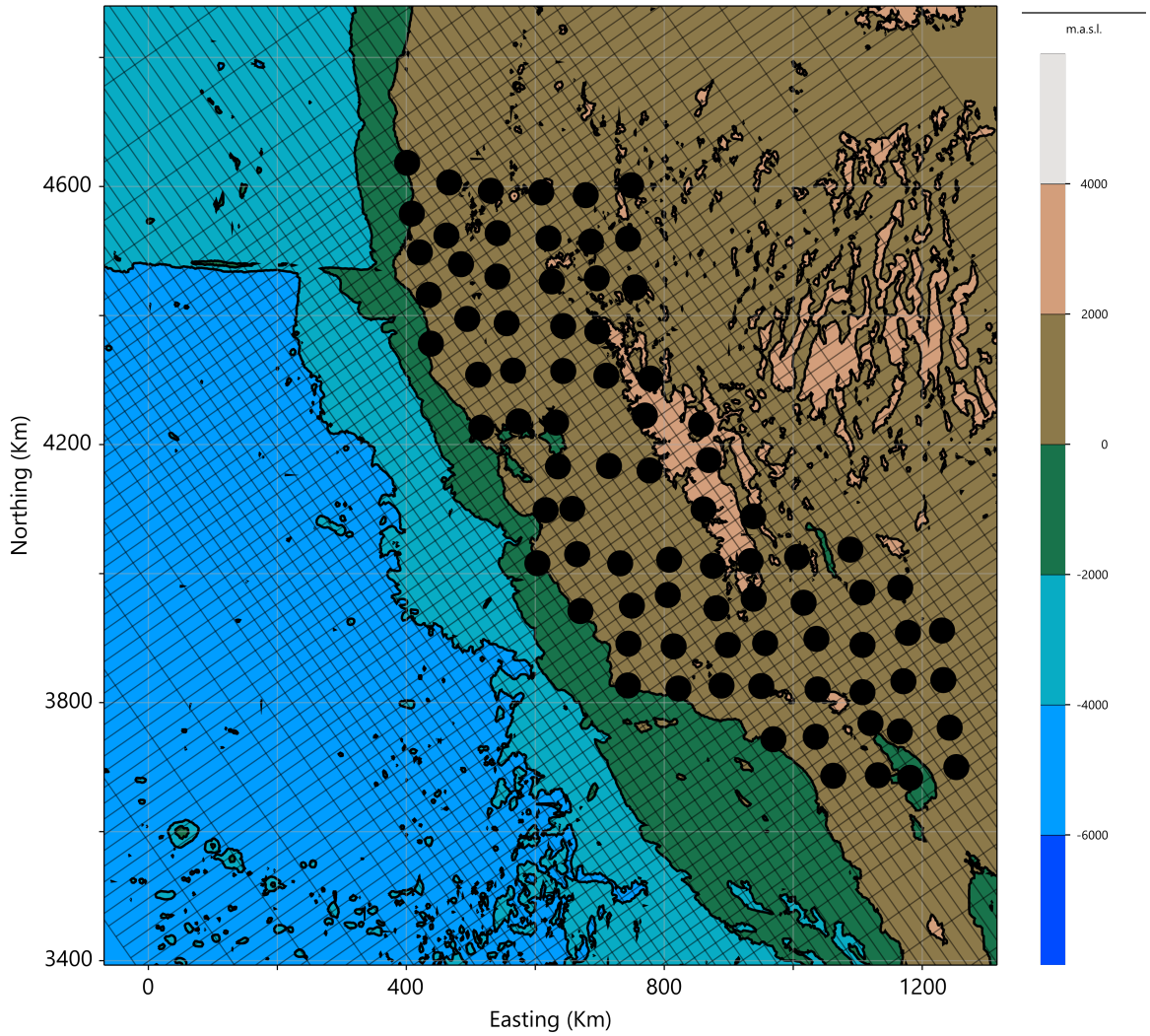

Figure 5.6: Bathymetry location map of the USArray, CONUS SoCal, and CONUS South receiver locations (Trabant et al., 2012). The lines represent the mesh utilised during my 3-Dimensional inversion. The basemap utilises the SRTM15+ dataset of Tozer et al. (2019).

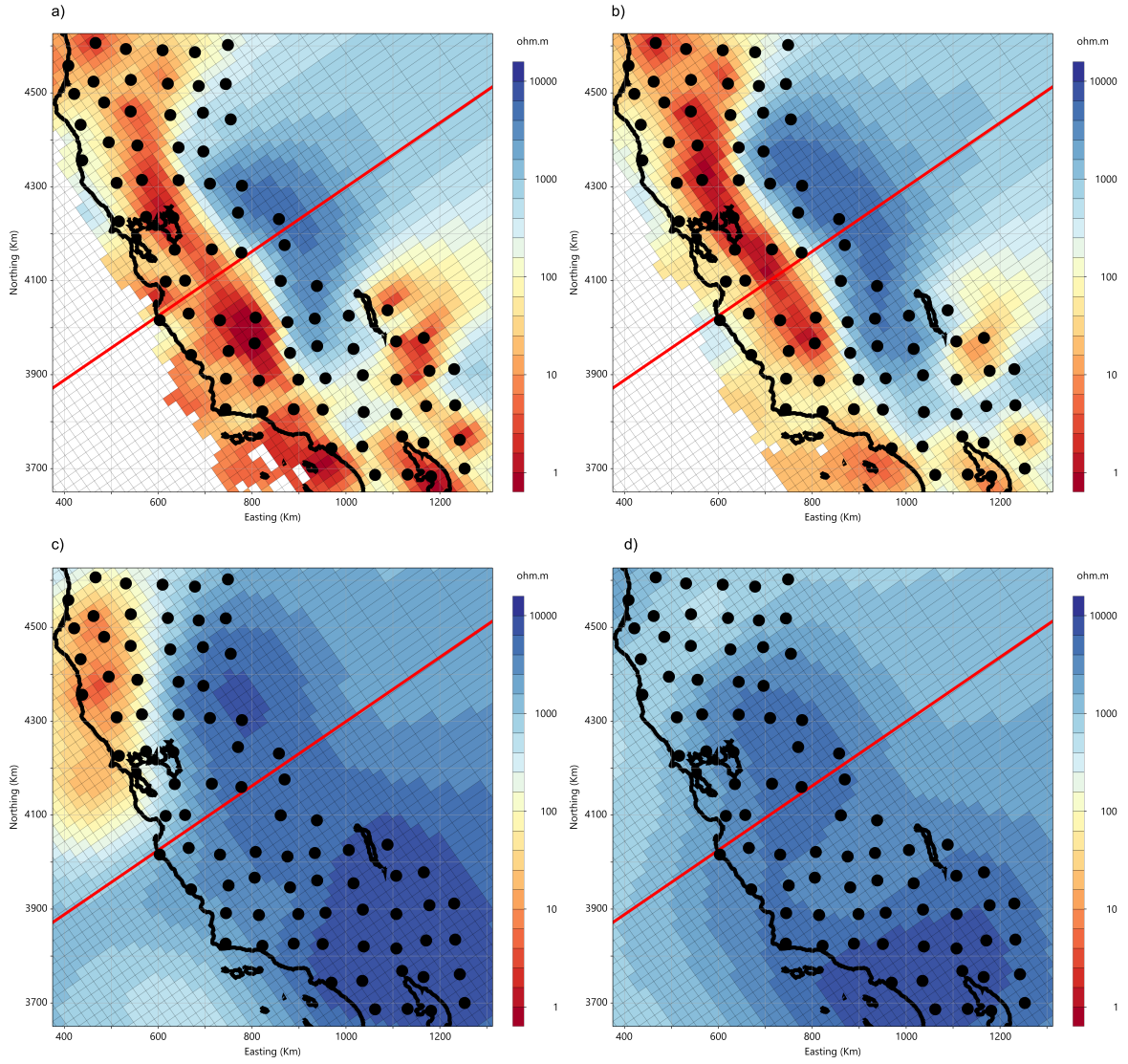

Figure 5.7: Horizontal slice of the 3-Dimensional inversion resistivity at upper crustal depths of a) 1 km depth, b) 2 km depth, c) 5 km depth, and d) 10 km depth. Black circles denote the location of USArray, CONUS SoCal, and CONUS South data. The red line denotes the strike of the central cross-section in Fig. 5.11.

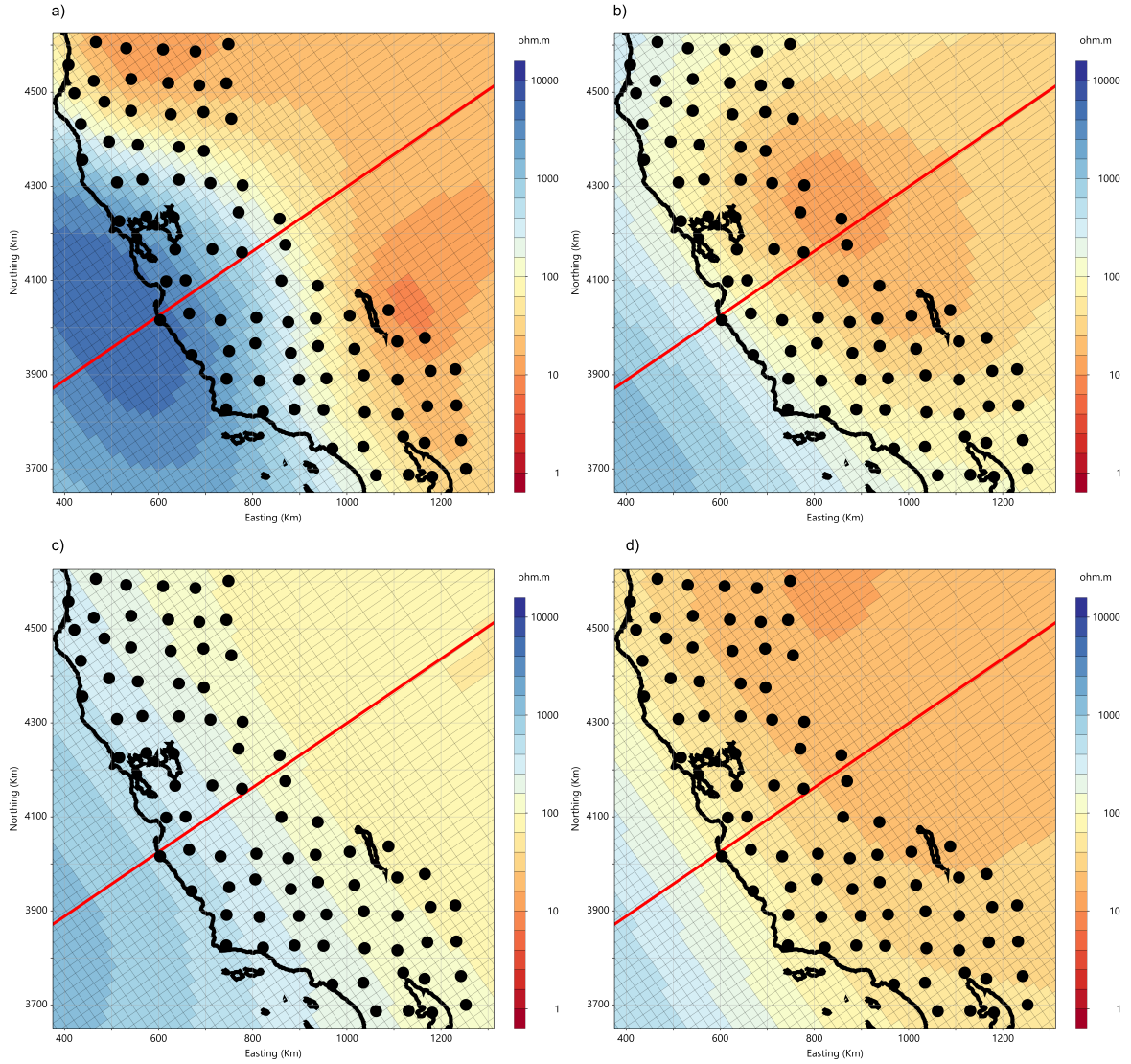

Figure 5.8: Horizontal slice of the 3-Dimensional inversion resistivity at a) 20 km depth, b) 50 km depth, c) 100 km depth, and d) 200 km depth. Black circles denote the location of USArray, CONUS SoCal, and CONUS South data. The red line denotes the strike of the central cross-section in Fig. 5.11.

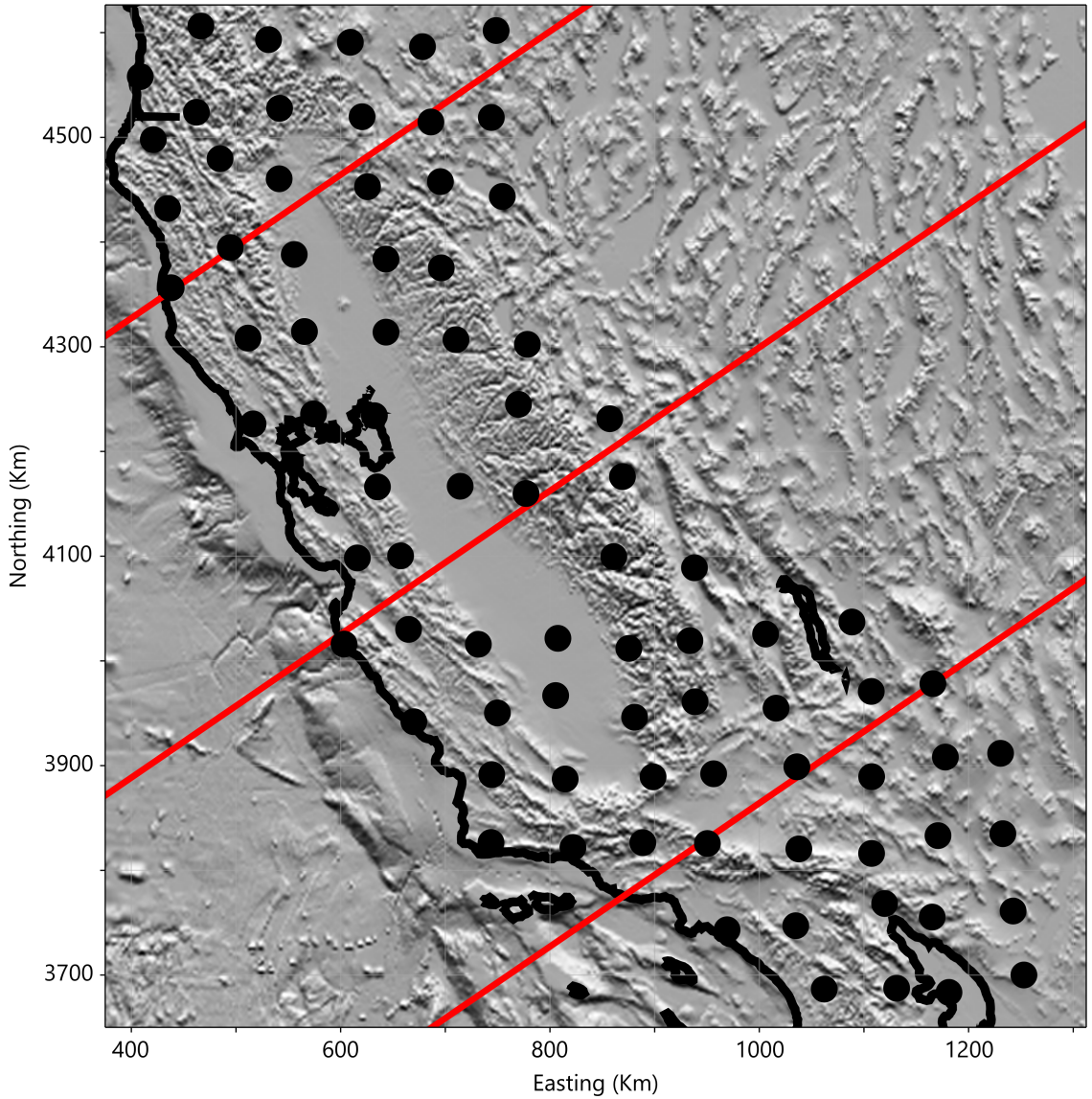

Figure 5.9: Synthetic sunshade bathymetry location map of the USArray, CONUS SoCal, and CONUS South receiver locations (Trabant et al., 2012). The red line denotes the strike of the three cross-sections in Figs 5.10 to 5.12). The basemap utilises the SRTM15+ dataset of Tozer et al. (2019).

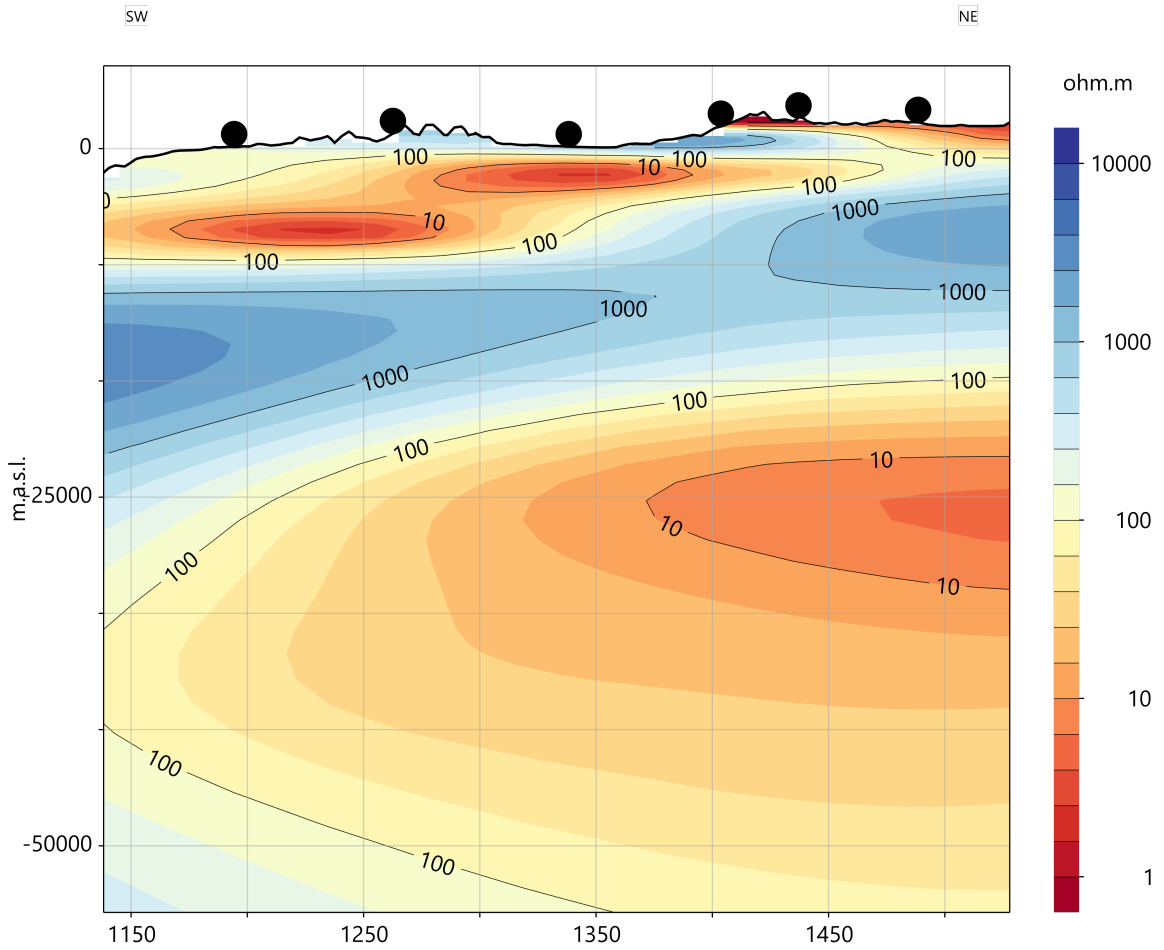

Figure 5.10: Northern cross-section of resistivity as a function of depth (Fig. 5.9). Black circles denote the location of USArray, CONUS SoCal, and CONUS South data along this profile.

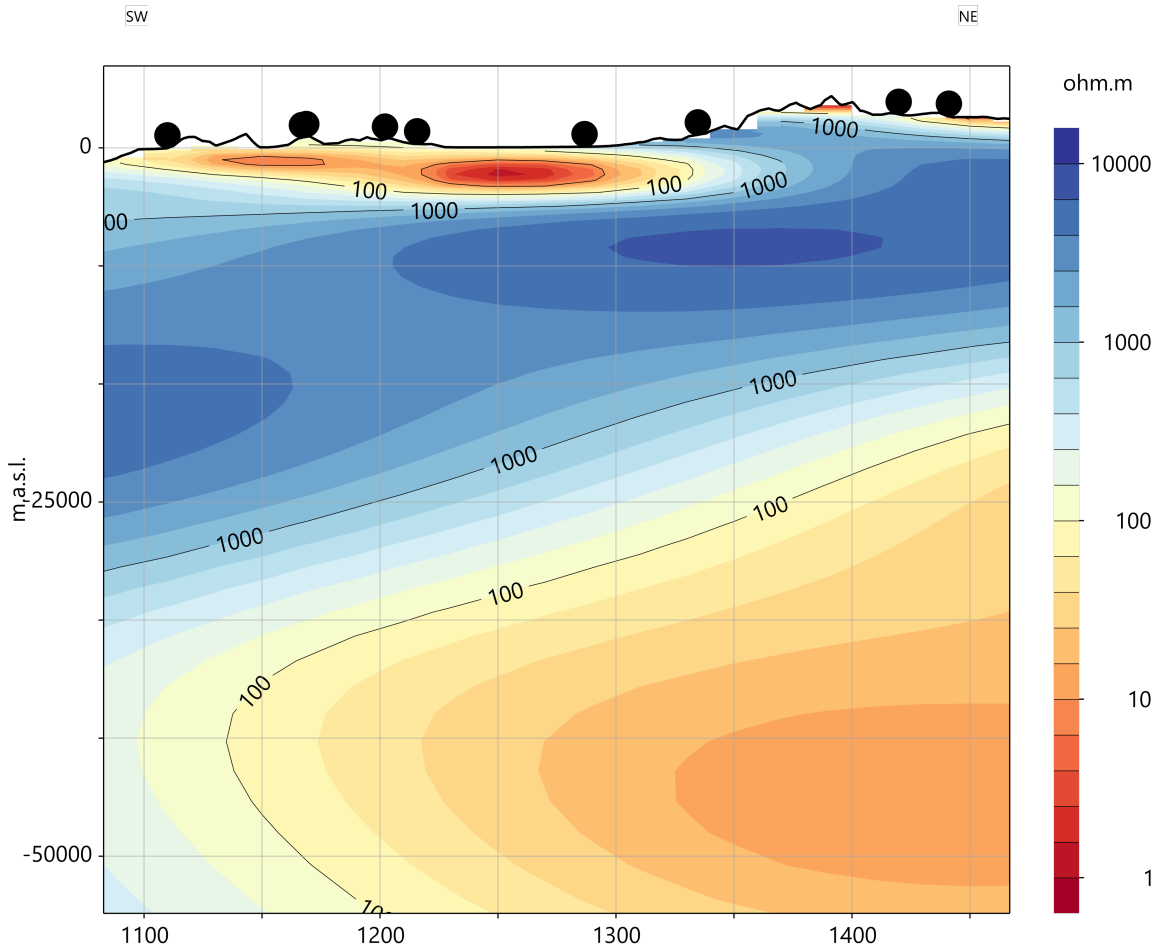

Figure 5.11: Central cross-section of resistivity as a function of depth (Fig. 5.9). Black circles denote the location of USArray, CONUS SoCal, and CONUS South data along this profile.

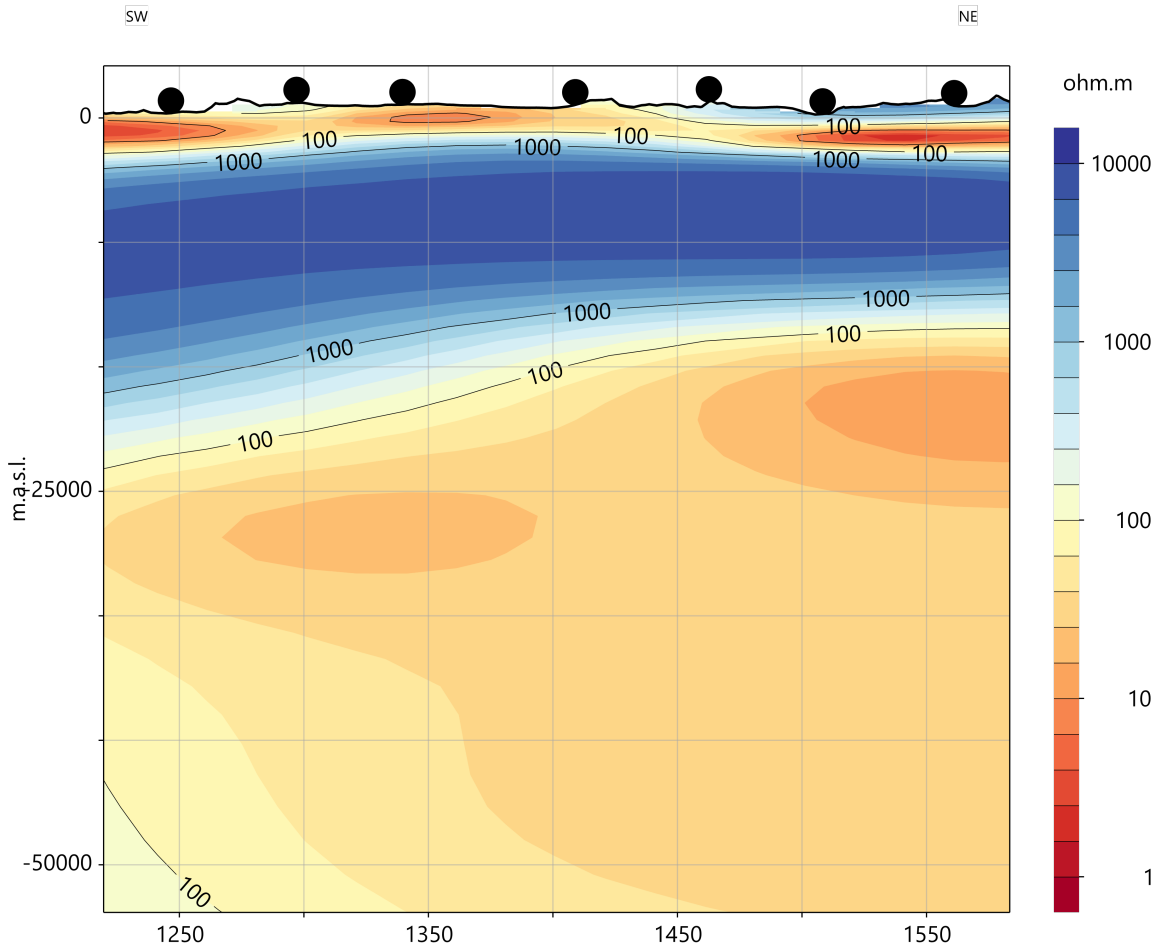

Figure 5.12: Southern cross-section of resistivity as a function of depth (Fig. 5.9). Black circles denote the location of USArray, CONUS SoCal, and CONUS South data along this profile.

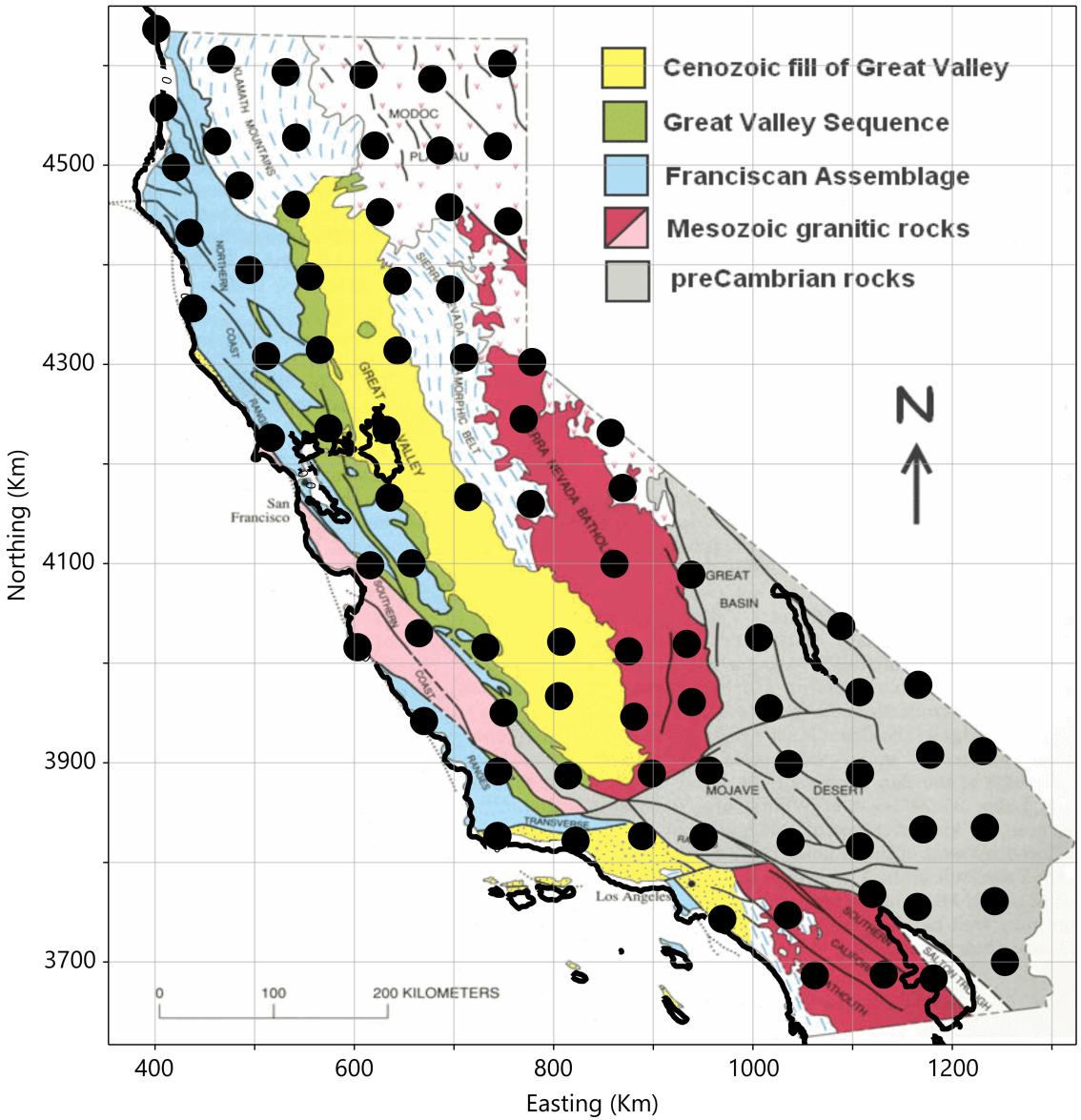

Figure 5.13: Geological map of California. Black circles denote the location of USArray, CONUS SoCal, and CONUS South receiver (Trabant et al., 2012). Geological map is adapted from Ludington et al. (2005).

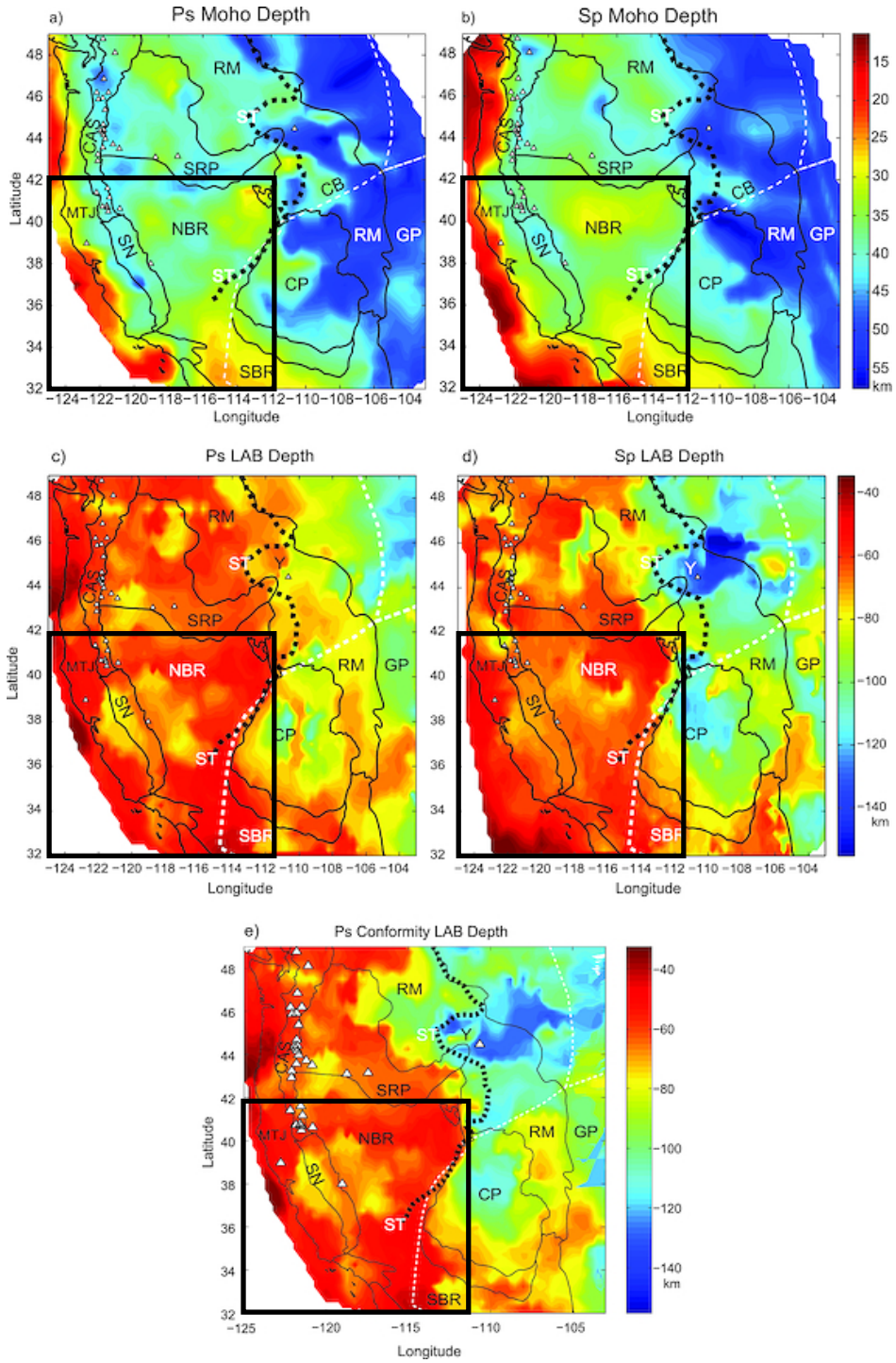

Figure 5.14: Depth to the Mohorovičić discontinuity and LAB maps as determined from seismic receiver functions by Levander and Miller (2012). a) displays the Moho estimated from Ps receiver functions. b) displays the Moho estimated from Sp receiver functions. c) displays the LAB interpreted from the Ps receiver functions. d) displays the LAB interpreted from the Sp receiver functions. e) displays the LAB interpreted using the Sp receiver functions as a guide east of the Sevier Thrust. The black square in each Fig. corresponds to the region of my 3-Dimensional inversion model.

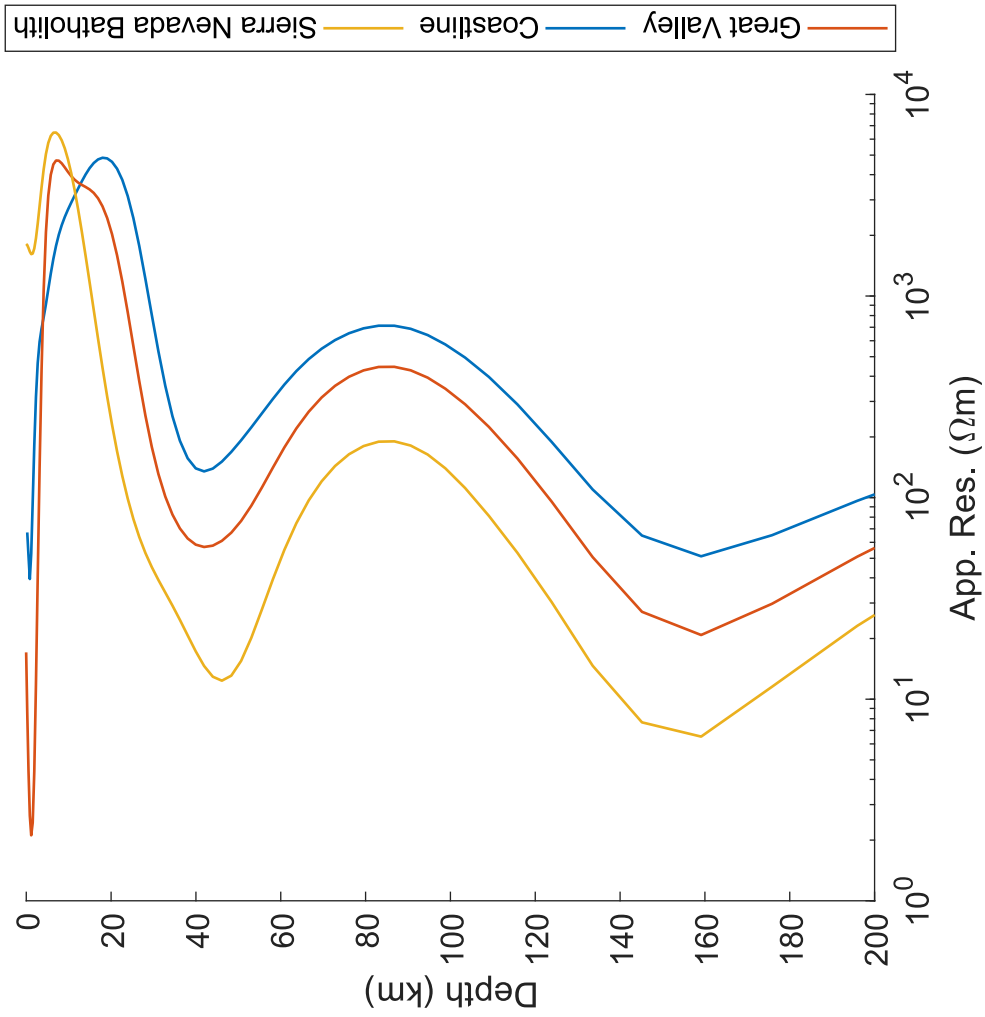

Figure 5.15: Resistivity as a function of depth as extracted from the central cross-section. Data was extracted beneath the coastline, Great Valley, and Sierra Nevada batholith. Each profile is approximately 100 km from the other and shows that the continental lithosphere becomes conductive inland from the coast.

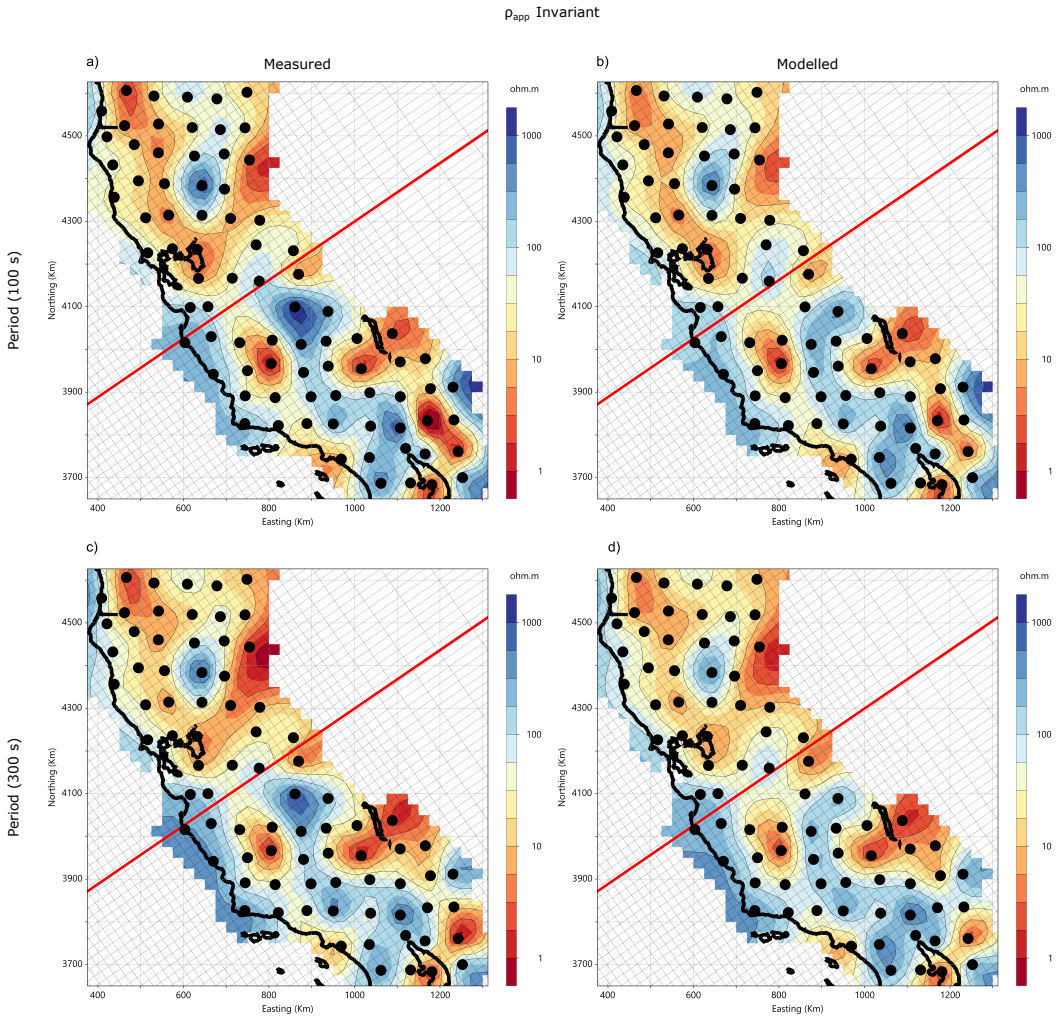

Figure 5.16: a) and b) display the invariant of apparent resistivity for measured and modelled responses at 100 s. c) and d) display the invariant of apparent resistivity for measured and modelled responses at 300 s. Black circles denote the location of USArray, CONUS SoCal, and CONUS South receiver (Trabant et al., 2012). The lines represent the mesh utilised during my 3-Dimensional inversion.

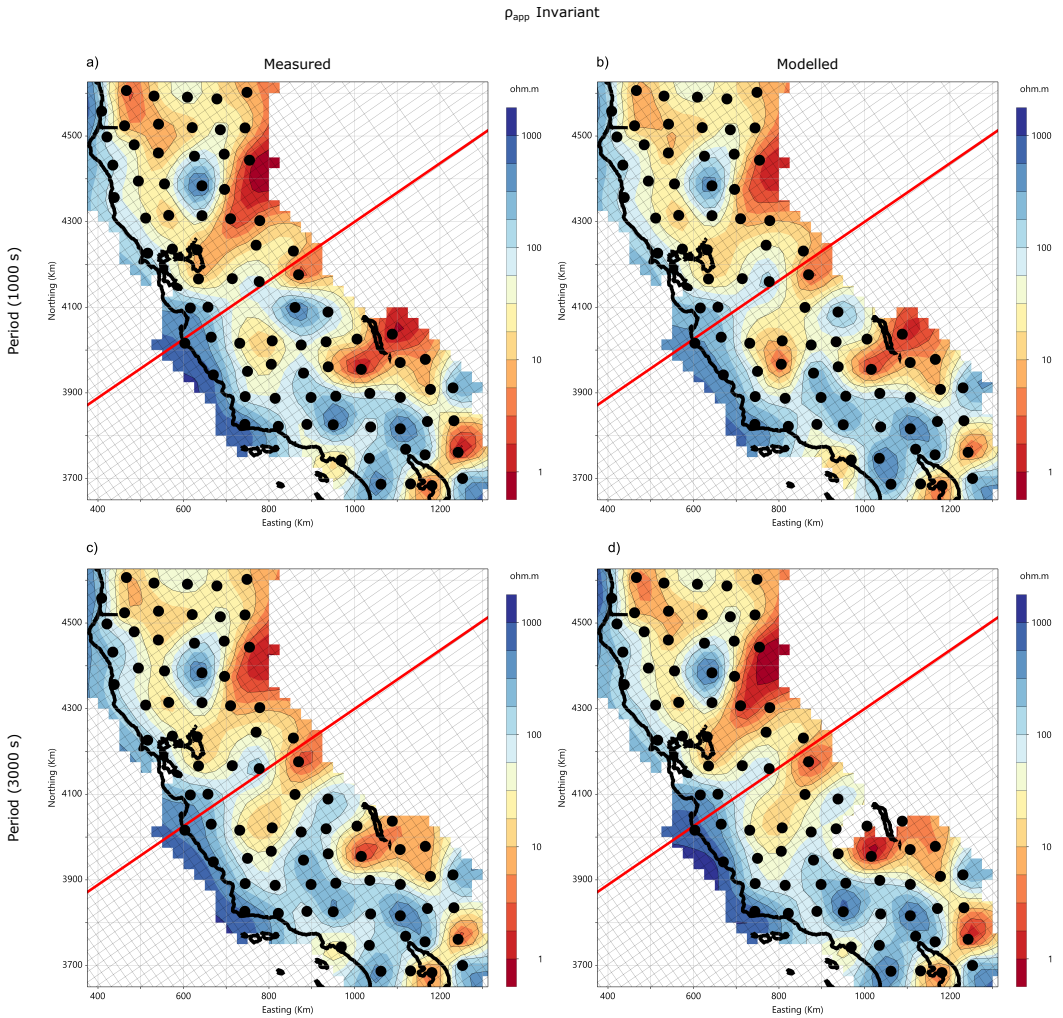

Figure 5.17: a) and b) display the invariant of apparent resistivity for measured and modelled responses at 1,000 s. c) and d) display the invariant of apparent resistivity for measured and modelled responses at 3,000 s. Black circles denote the location of USArray, CONUS SoCal, and CONUS South receiver (Trabant et al., 2012). The lines represent the mesh utilised during my 3-Dimensional inversion.

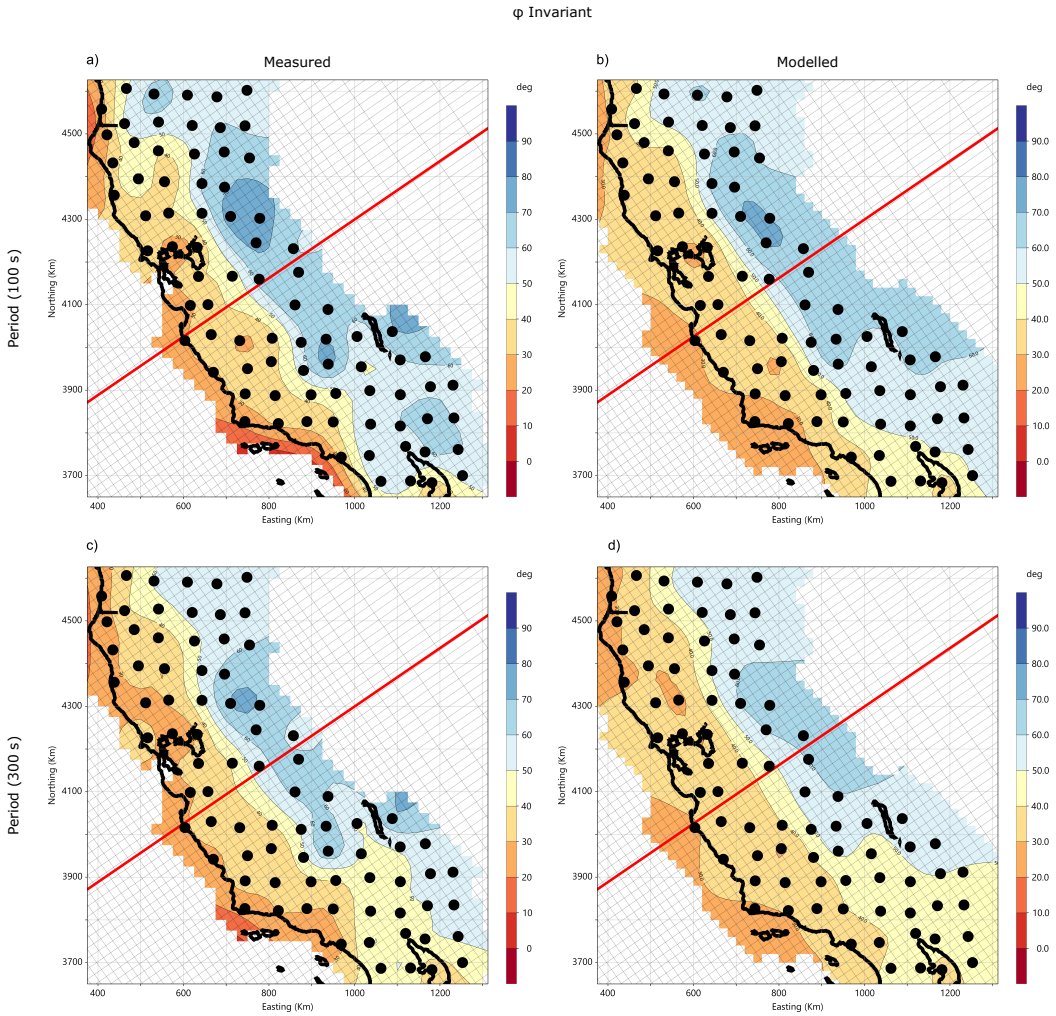

Figure 5.18: a) and b) display the invariant of phase for measured and modelled responses at 100 s. c) and d) display the invariant of phase for measured and modelled responses at 300 s. Black circles denote the location of USArray, CONUS SoCal, and CONUS South receiver (Trabant et al., 2012). The lines represent the mesh utilised during my 3-Dimensional inversion.

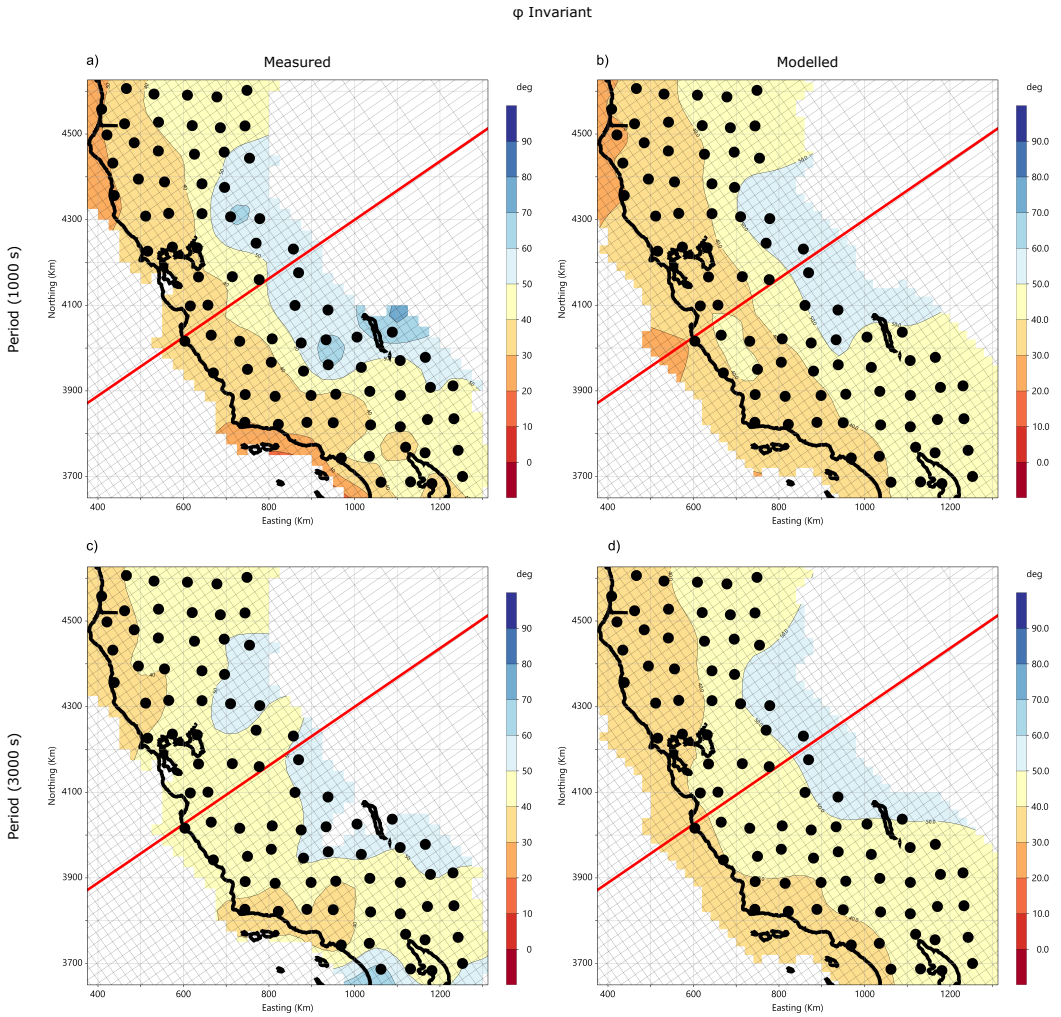

Figure 5.19: a) and b) display the invariant of phase for measured and modelled responses at 1,000 s. c) and d) display the invariant of phase for measured and modelled responses at 3,000 s. Black circles denote the location of USArray, CONUS SoCal, and CONUS South receiver (Trabant et al., 2012). The lines represent the mesh utilised during my 3-Dimensional inversion.

However below 200 km, I observe that the data utilised in my inversion is insensitive to conductivity variations. As such, the resistivity structure of this inversion model remains ambiguous for depths beyond 200 km. Despite this, the depth at which conductivity begins to increase is observed to coincide with the Mohorovičić (Moho) discontinuity beneath California (Wannamaker et al., 2008; Lowry and Pérez-Gussinyé, 2011; Levander and Miller, 2012) (Fig. 5.14). The Moho discontinuity is a change in seismic impedance at the interface between the Earth's crust and mantle (Chave et al., 2012). As a consequence, I interpret this zone of enhanced conductivity to be an expression of the mantle beneath California.

Finally, I define the conductivity model for my 2-Dimensional forward model by extracting the geoelectric structures beneath the coastline ρ_C, the Great Valley ρ_{GV}, and the Sierra Nevada batholith ρ_{SNB} (Fig. 5.15). For the first 5 km of my continental forward model, I utilise a resistivity of approximately 70 Ωm for ρ_C, 10 Ωm for ρ_{GV}, and 2,000 Ωm for ρ_{SNB}. To a depth of 20 km, this model is characterised by a resistivity of 4,000 Ωm for all geoelectric structures. Between the depths of 20 km and 400 km, I utilise a resistivity of 200 Ωm for ρ_C, 100 Ωm for ρ_{GV}, and 30 Ωm for ρ_{SNB}. As my 3-Dimensional inversion model is insensitive to geoelectric structures deeper than 400 km, I characterise this portion of my 2-Dimensional forward model using a resistivity of 1 Ωm as per the global model of Grayver et al. (2017).

To assess how the 3-Dimensional inversion reproduces measured responses, I compare the invariants of apparent resistivity and phase calculated from measured and modelled EM fields (Figs 5.16 to 5.19). These responses are calculated from a rotationally invariant determinant of the impedance tensor and are relatively robust to the effects of near-surface 3-Dimensional resistivity structures Szarka and Menvielle (1997). From these Figs, I observe remarkably similar responses in both the measured and modelled invariant apparent resistivity and phase at all period ranges. As a consequence, I conclude that this inversion appropriately reproduces measured responses.

5.2 2-Dimensional Forward Modelling

To begin, the 2-Dimensional modelling algorithm I use is an altered version of the algorithm published by Wannamaker et al. (1987). This modification allows for the calculation of both standard and hybrid impedance by allowing the user to source magnetic fields from either sea-floor or onshore locations. Models of standard and hybrid impedance calculated from data collected during the APPLE survey were run to investigate the effect of standardising electric fields using quasi-surface magnetic fields.

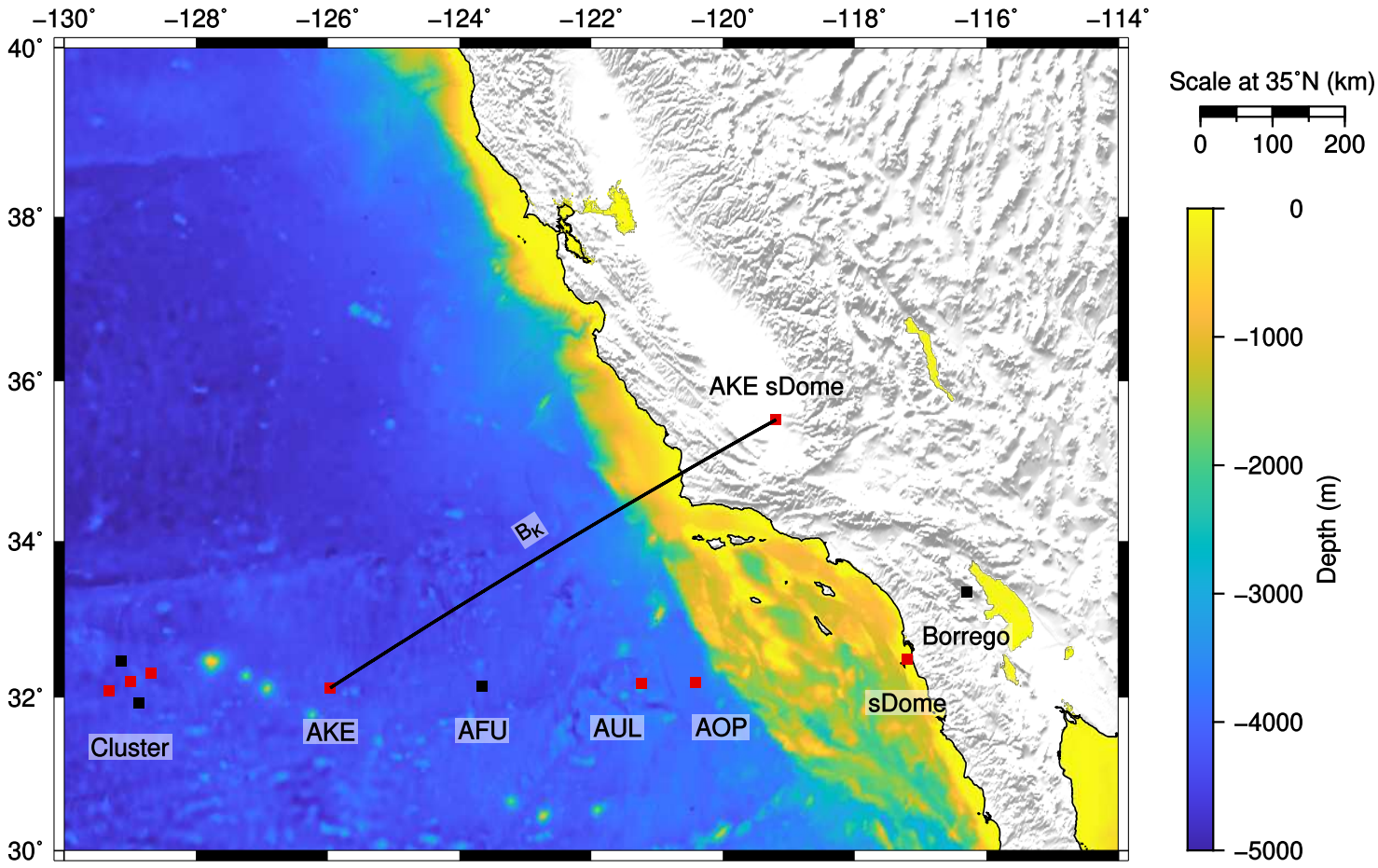

Figure 5.20: Bathymetry location map of the APPLE survey from offshore California with MT stations displayed as squares. Red squares correspond to stations utilised during Chapter 4 and Chapter 5. B_K denotes the path of the bathymetry profile for Kermit (AKE). The basemap utilises the ETOPO1 dataset of Amante and Eakins (2009).

To model the normalisation of ocean-bottom electric fields using continental magnetic fields, I first rotate all receivers to 327° to be perpendicular to the coastline. A profile is then generated which extends from each ocean-bottom receiver location to the continent. The sDome receiver is then projected onto each profile.

This results in a unique profile for each ocean-bottom receiver which is defined by a distinct coastline distance, sDome receiver, and bathymetry (Fig. 5.20, B_{AKE} for Kermit). However, the rotation of consequence of this projection is the inflation of the distance between MT receivers and the coastline. For example, the distance to the coastline decreases by approximately 260 km for the Kermit (AKE) receiver following this projection. Furthermore, this projection places the continental sDome receiver within the ocean when projecting to the Opus (AOP) receiver profile. As a consequence, I shifted the modelled sDome receiver one node inland. Figs 5.21 to 5.22 display bathymetry (Ryan et al., 2009), receiver location, and modelled receiver location. Here, $\mathbf{B_i}$ references the bathymetry profile for receiver $\mathbf{i}$. Following limitations imposed by the modelling algorithm, I choose to reconstruct the bathymetry using the simplest representation possible.

Beginning with the abyssal plain, the bathymetry remains constant until the coastline and represents an average approximation of the abyssal plain bathymetry for each profile (Figs 5.21 to 5.22). The location of the coastline was determined from the GMRT Grid v3.8 (Ryan et al., 2009). In addition, I represent the gradual reduction in bathymetry associated with the continental rise and continental slope using up to two steps from the ocean depth associated with the abyssal plain in each profile to the surface of my model. Furthermore, the horizontal distances modelled for each profile vary from Ryan et al. (2009) by a maximum of 20 km as a consequence of the horizontal mesh chosen for centre portion of the model.

In addition to the 20 km horizontal mesh spacing for the centre portion of the model, additional meshing of over 10,000 km was added to each side as padding to ensure the fields satisfy the boundary conditions applied at external mesh boundaries. Vertical mesh spacing was made to increase gradually with mesh spacings of up to a few hundred metres for the first few kilometres. Furthermore, the vertical mesh spacing was reduced when approaching the sea floor to ensure adequate discretisation across this prominent boundary. The horizontal dimensions of the models vary depending on the length of the profile from a 120 to a 136 node-wide mesh, including 22 padding nodes. In contrast, the vertical dimensions of the model remain a constant 57 node-wide mesh which includes 8 padding nodes. The EM fields calculated at the ocean-bottom and continental receiver locations are then utilised to calculate the standard and hybrid impedances predicted by our forward model.

5.3 Reference Model

To calculate the subsurface conductivity structure used throughout my forward modelling, I must first determine the representative age of oceanic lithosphere for the APPLE region. To do so I calculate the arithmetic mean of oceanic crust age from a dataset published by Müller et al. (2016). To limit the influence of distortions when sampling this grid, I utilise Generic Mapping Tools v5.4.3 to project the data to an equidistant azimuthal projection with a radial distance of 200 km (Fig. 5.23), far exceeding the 30 km radius of the cluster. This projection has the advantage of maintaining the distance and azimuth of a projected location with respect to the centre point. For this, the centre point was chosen to be the centre of the cluster. From this method I calculate the age representative of the APPLE region to be 32.5 Ma which I round to 33 Ma for the purposes of my subsurface conductivity modelling. To verify my predictions, I compare results calculated by my reference model to MT studies from 33 ± 10 Ma regions of the Pacific Ocean.

Through an analysis of melt fractions predicted by the conductivity model from Chapter 3, I observe the absence of silicate melt and < 10 ppm of carbonatite melt between 60 km and 100 km depth (Fig. 5.24). Such amounts of carbonatite melt deep within the Earth are unlikely to be resolved by the MT method. As such, I interpret this as evidence supporting a conduction mechanism which is free of melt beneath the APPLE region. This corroborates the study of Baba et al. (2010), situated on 25.56 Ma oceanic crust, who concluded that partial melt is not required to reproduce Pacific Ocean subsurface conductivity structures. However, my reference model is unable to corroborate the presence of melt beneath 23.45 Ma oceanic crust as predicted by Naif et al. (2013). However the authors concluded that the partial melt is a consequence of subduction. As such, I'm unlikely to reproduce this using my reference model.

From my reference model, I calculate Hashin-Shtrikman (HS) limits for 33 Ma oceanic lithosphere (Fig. 5.25). These limits represent the narrowest conductivity bounds for a multiphase system with an interconnected (σ^{+}_{HS}) and disconnected (σ^{-}_{HS}) conductive phase (Hashin and Shtrikman, 1962). The two HS limits for a dry upper mantle are approximately equal, I utilise a geometric mean of these HS limits within my forward model (Fig. 5.25 solid black line and Figs 5.28 to 5.39 blue circles). In contrast, the lower and upper HS limits calculated for a hydrated upper mantle vary by an order of magnitude. As such, I utilise both within my forward model (Fig. 5.25 dashed and dotted black lines and Figs 5.28 to 5.39 orange and yellow circles respectively).

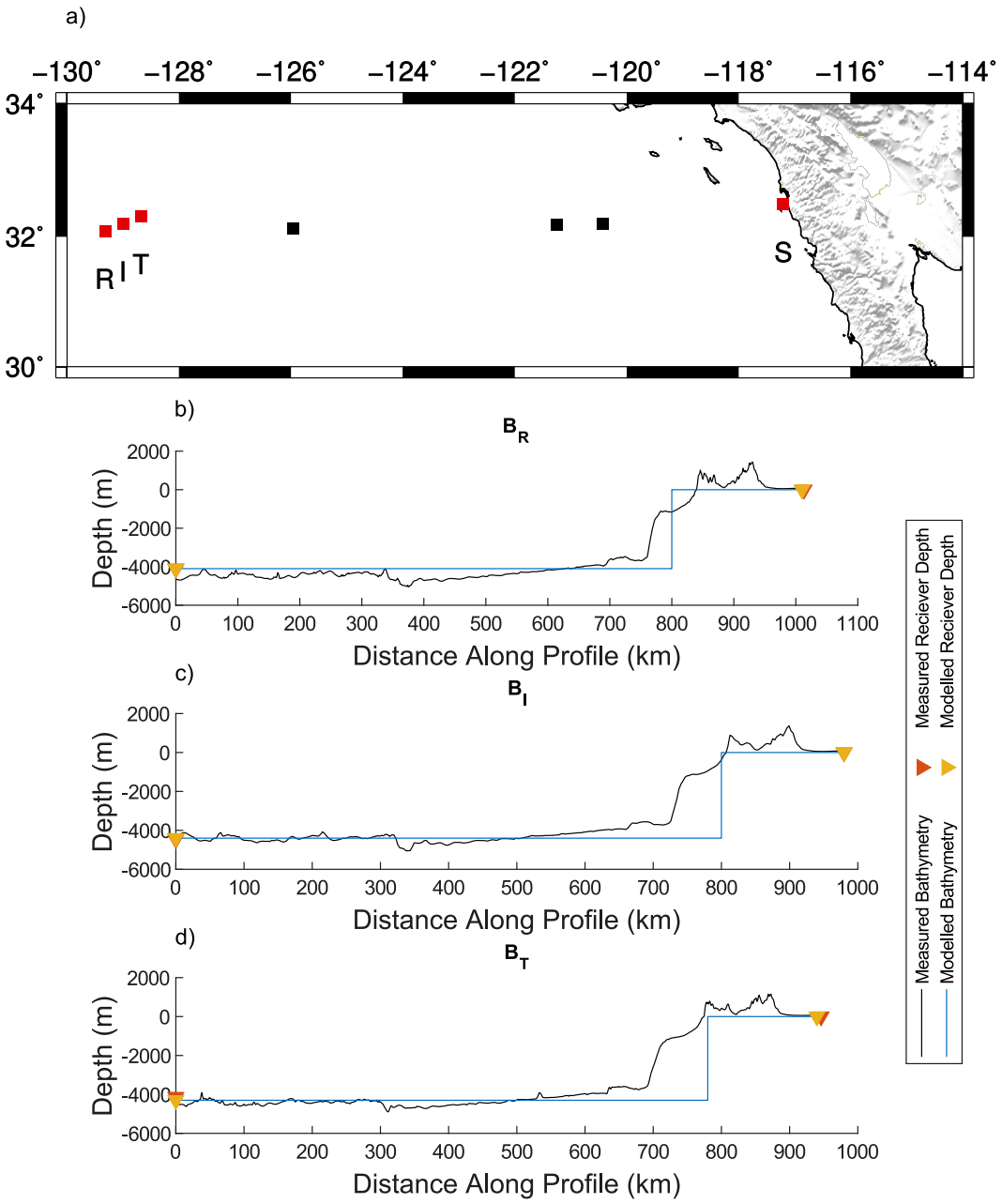

Figure 5.21: 2-Dimensional bathymetry profile for Rhonda (B_R), Igor (B_I), and Trevor (B_T) receivers of the APPLE survey. The black line corresponds to bathymetry as per the GMRT Grid v3.8 of Ryan et al. (2009) while the blue line corresponds to a forward modelled approximation. The orange triangles correspond to the bathymetry measured by the receivers during their deployment while the yellow triangles correspond to a forward modelled approximation. The profile utilises the GMRT Grid v3.8 of Ryan et al. (2009) to determine bathymetry.

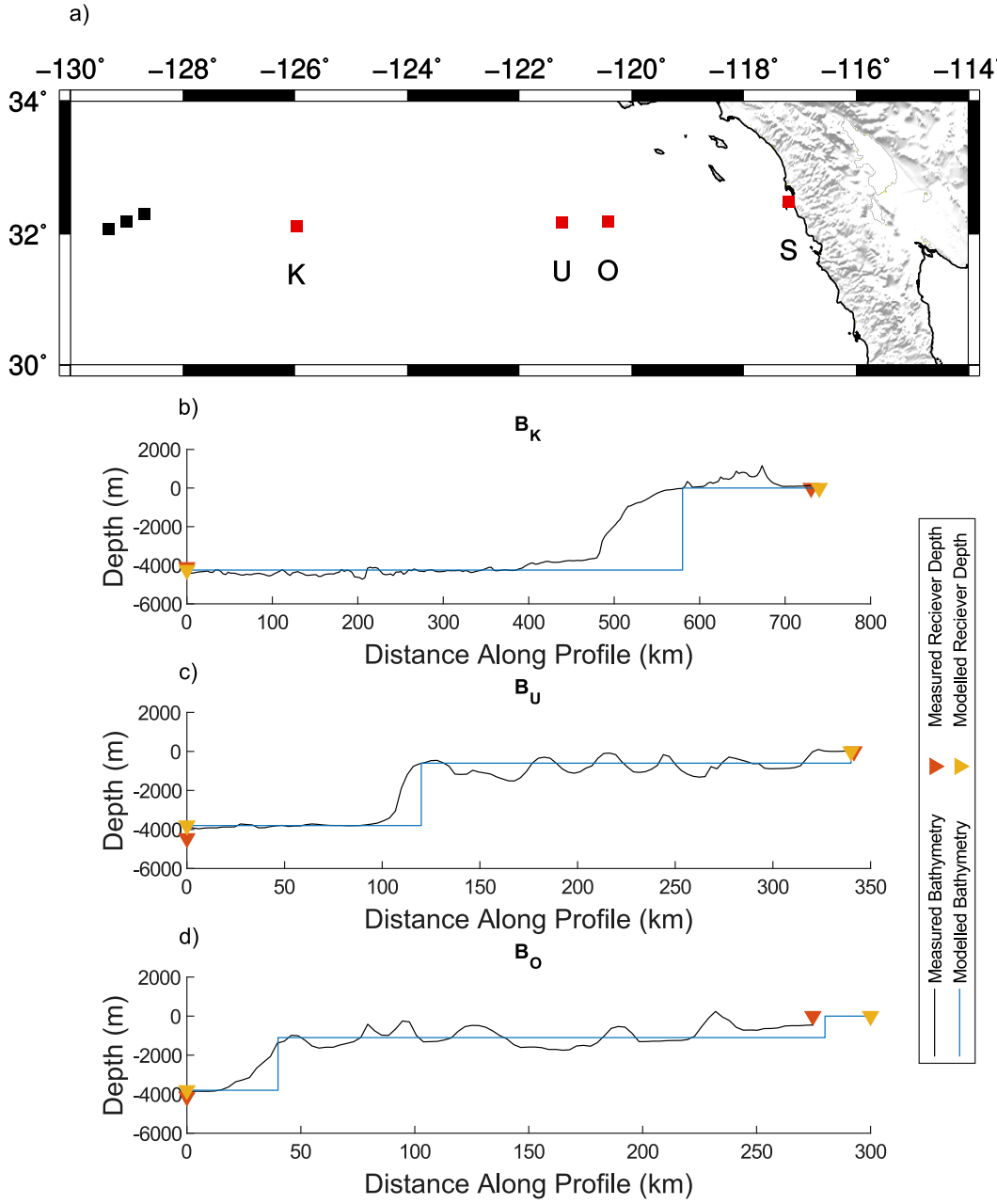

Figure 5.22: 2-Dimensional bathymetry profile for Kermit (B_K), Ulysses (B_U), and Opus (B_O) receivers of the APPLE survey. The black line corresponds to bathymetry as per the GMRT Grid v3.8 of Ryan et al. (2009) while the blue line corresponds to a forward modelled approximation. The orange triangles correspond to the bathymetry measured by the receivers during their deployment while the yellow triangles correspond to a forward modelled approximation. The profile utilises the GMRT Grid v3.8 of Ryan et al. (2009) to determine bathymetry. As the Opus (AOP) projection places the continental sDome receiver is placed within the ocean, the modelled sDome receiver is shifted one node inland.

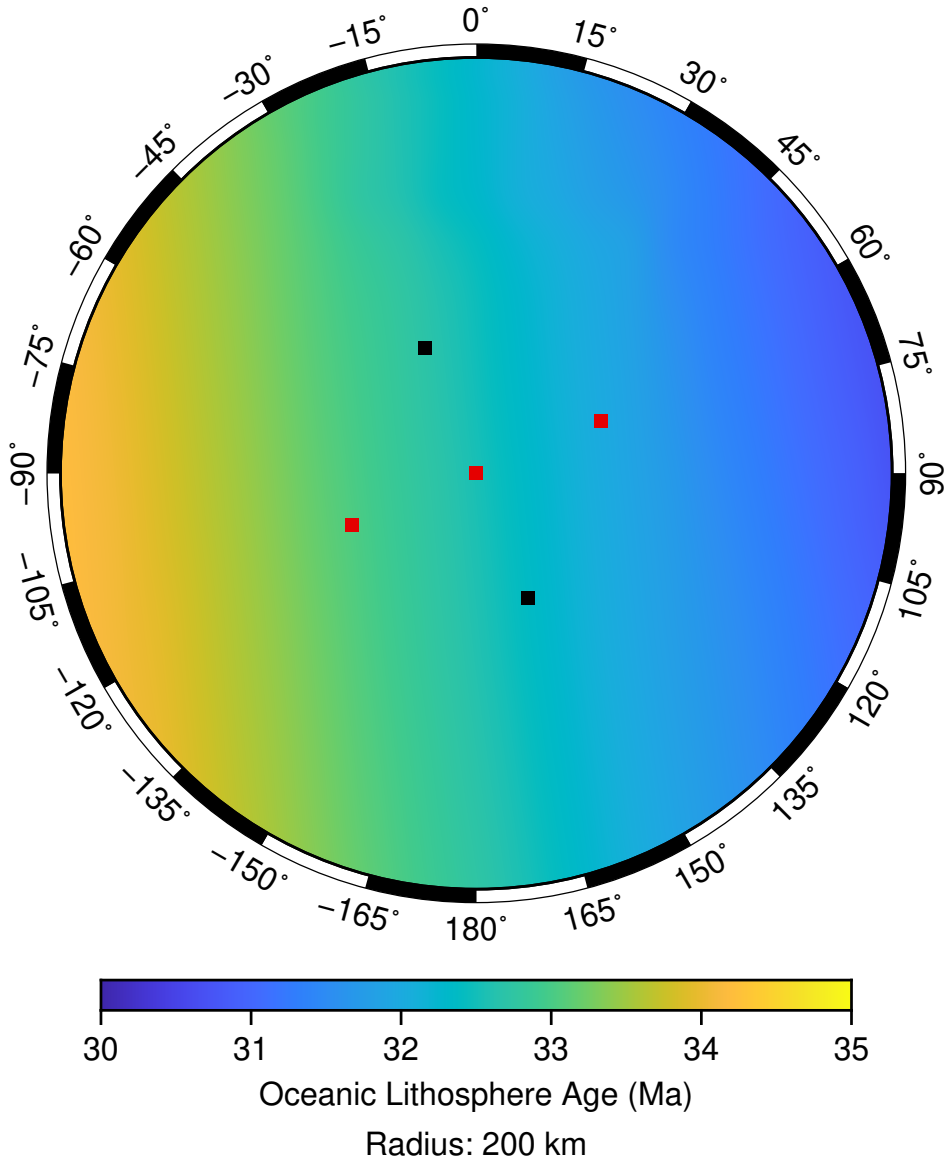

Figure 5.23: Azimuthal equidistant projection of ocean age data focusing on the cluster portion of the APPLE survey from offshore California with MT stations displayed as squares. The projection is centred on the middle of the cluster. The basemap utilises oceanic crust age data published by Müller et al. (2016).

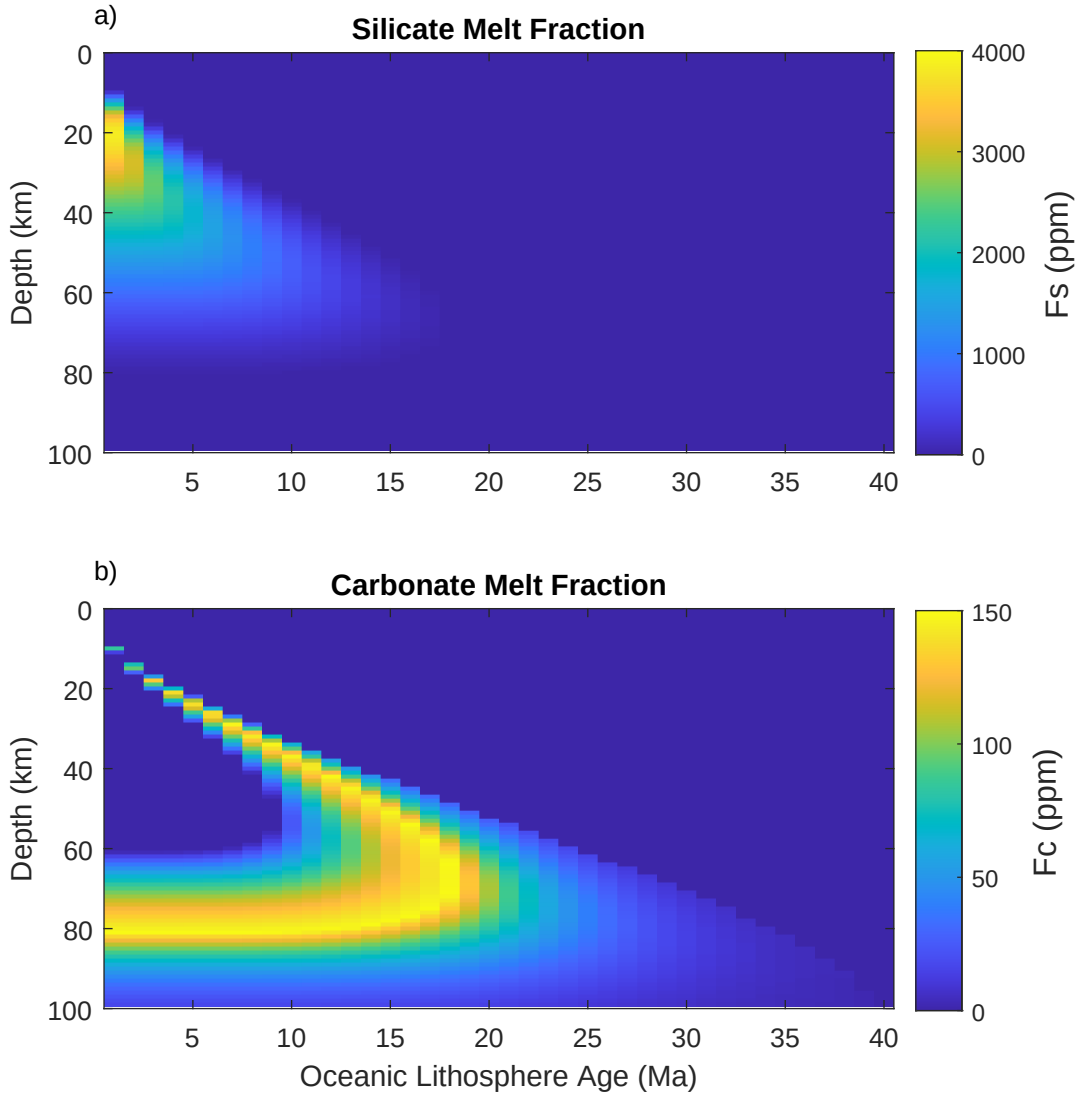

Figure 5.24: a) & b) display the melt fraction as a function of depth beneath the ocean floor (km) and oceanic lithosphere age (Ma) for silicate and carbonatite based melt respectively as calculated by the two-layer standard conductivity model in Chapter 3.

As my reference model is unable to predict the conductivity structure for depths shallower than the base of the oceanic lithosphere, I utilise the results of Chesley et al. (2019) (Fig. 5.26). Chesley et al. (2019) inverted CSEM data collected alongside the APPLE MT data to determine the conductivity structure for this region to a depth of 25 km. As the maximum depth of the model is situated within the highly resistive oceanic lithosphere, I utilise this model as the basis of my forward models near-surface conductivity structure (Fig. 5.27). However, it is worth noting that the spatial resolution of CSEM at these depths far exceeds that of MT measurements. Therefore, I utilise a coarse approximation of this conductivity structure within my forward model.

The upper and lower HS limits for a dry upper mantle represent an interconnected garnet and clinopyroxene phase respectively. These limits are observed to corroborate the global conductivity model of Grayver et al. (2017). However, they are incapable of reproducing the results of Baba et al. (2010) and Naif et al. (2013). Instead, these limits predict a more resistive subsurface beneath 33 $\pm$ 10 Ma oceanic lithosphere. In contrast, the HS limits for hydrated upper mantle corroborate the interpretation of Baba et al. (2010) who proposed the presence of hydration beneath 25.56 Ma oceanic crust. Additionally, these limits also show hydration is incapable of reproducing the conductive features beneath 23.45 Ma oceanic crust as predicted by Naif et al. (2013). It is important to note however that the younger lithosphere beneath the study of Baba et al. (2010) would shift HS limits for a hydrated upper mantle to higher conductivities. As such, the conductivity structure presented by Baba et al. (2010) for depths greater than 100 km is unlikely to be within the disconnected HS limits for a hydrated upper mantle. Subsequently, I interpret a dry upper mantle for depths beyond 100 km beneath for the study of Baba et al. (2010). Following these results, I conclude that a dry or hydrous upper mantle is required to constrain my 2-Dimensional forward model of the APPLE region.

5.4 Discussion

For standard impedance, the apparent resistivity and phase varies between TE- and TM-modes suggesting a complex subsurface conductivity structure for the APPLE region which varies in multiple spatial dimensions (Figs 5.28 to 5.39). In contrast, hybrid impedance predicts a simple apparent resistivity and phase for both TE- and TM-modes indicative of a 1-Dimensional subsurface conductivity structure. Following the simple bathymetry of the APPLE region and its distance from major tectonic boundaries, I interpret these observations to be evidence supporting the use of hybrid impedances.

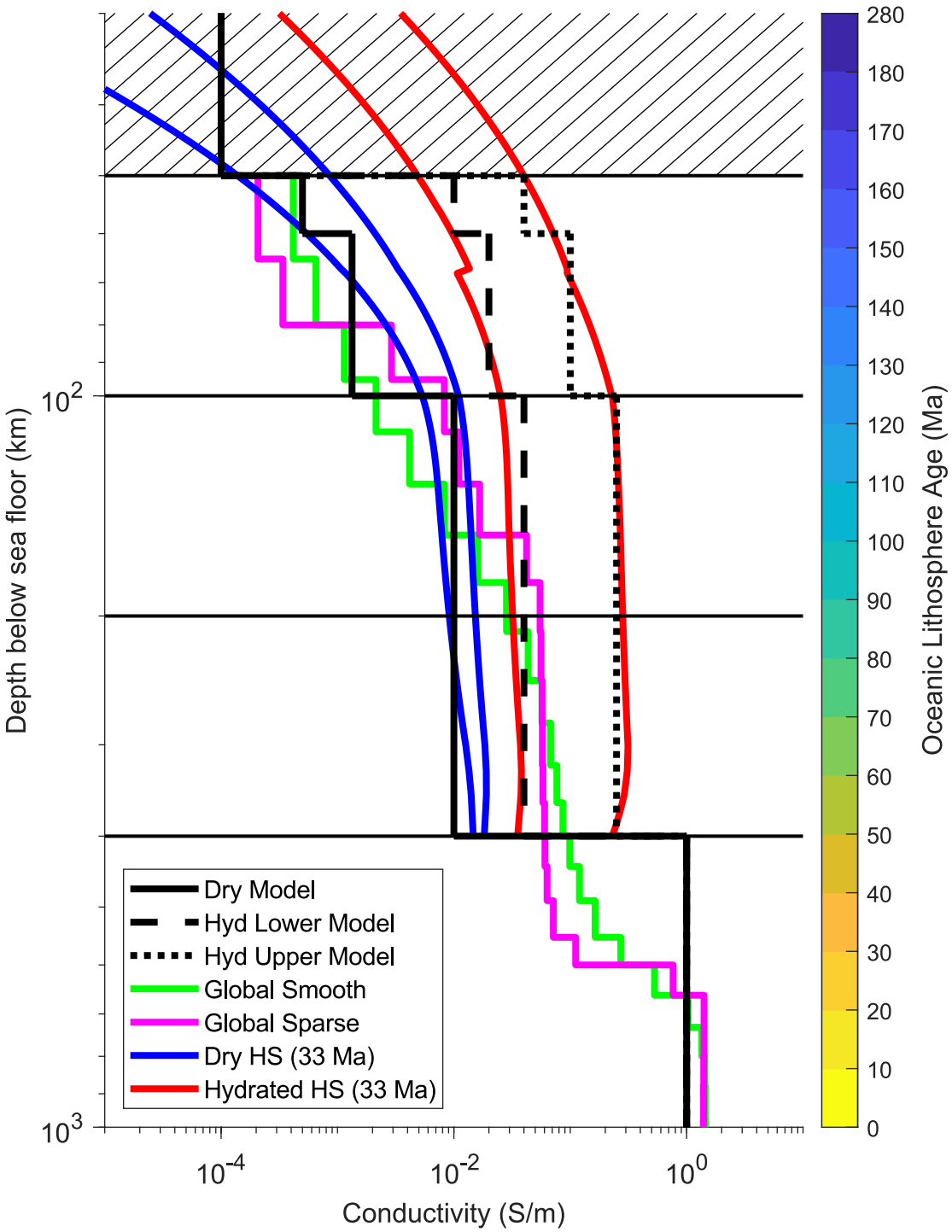

Figure 5.25: Red and blue lines correspond to Hashin-Shtrikman limits as calculated by my two-layer standard conductivity model for 33 Ma oceanic crust by my conductivity model. The HS limits displayed by red and blue lines correspond to a hydrated upper mantle and dry upper mantle respectively. Green and magenta lines correspond to the global conductivity model of Grayver et al. (2017).

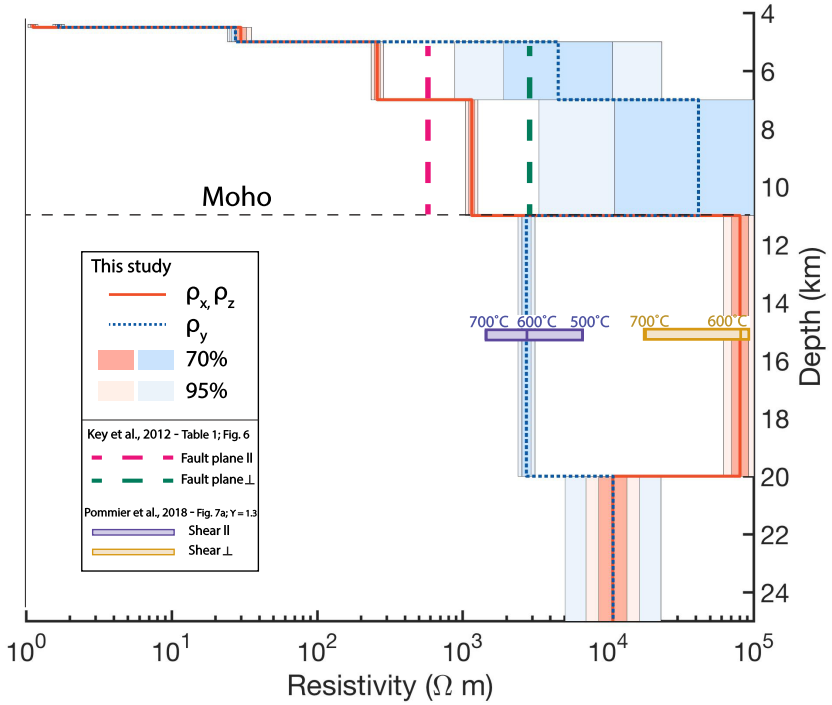

Figure 5.26: Preferred resistivity model with 70% and 95% confidence intervals derived from a linearised uncertainty analysis of Chesley et al. (2019). Orange, solid, and blue, dashed lines show resistivity in the paleo-ridge-parallel (x-z) plane and paleo-spreading (y) direction, respectively, for this study. Overlain dashed pink and green lines are resistivities for hydrated bending fault plane parallel and perpendicular directions, respectively, from the Middle America Trench (Key et al., 2012). Experimentally measured conductivity for sheared olivine samples (Pommier et al. (2018); shear strain = 1.3) extrapolated to lower temperatures for the shear parallel direction (purple rectangle) and shear plane perpendicular direction (gold rectangle).

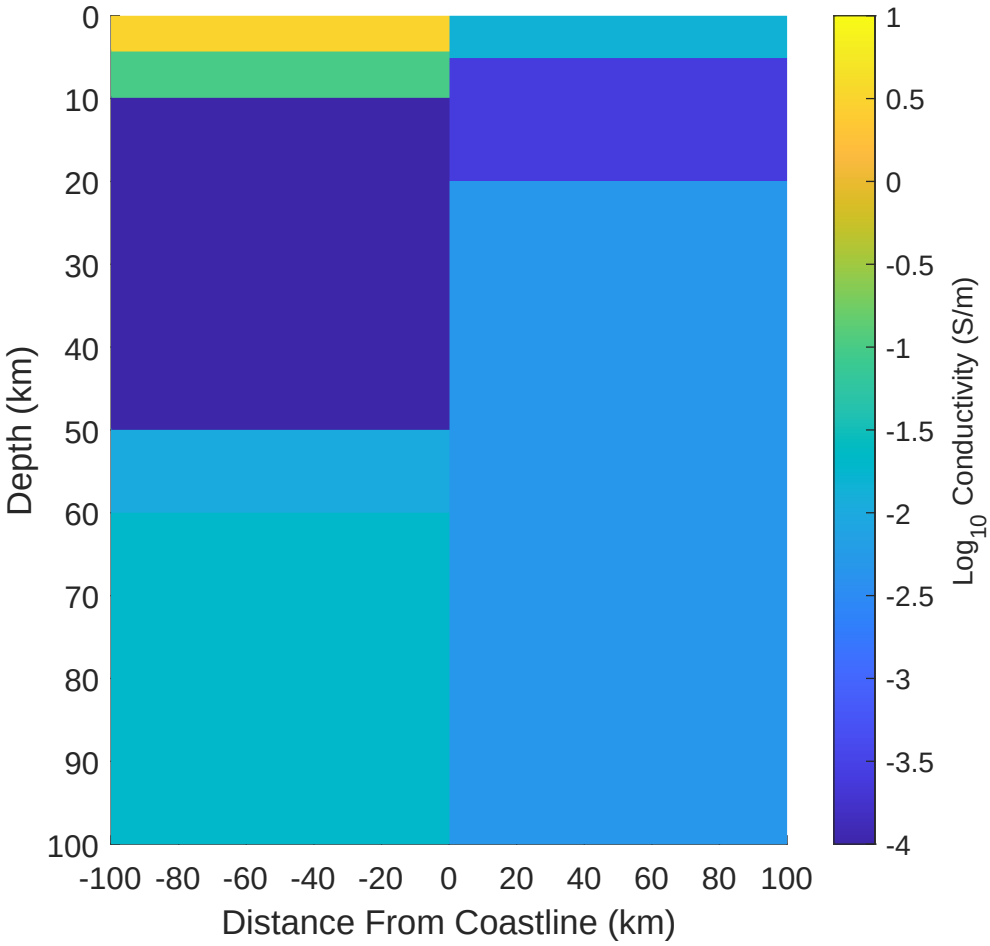

Figure 5.27: 2-Dimensional forward model structure for the Igor receiver. To define the bathymetry, I utilise the profiles in Figs 5.21 to 5.22. Excluding the vertical boundary between oceanic and continental lithosphere, conductivity only varies along the z-axis. The oceanic conductivity structure presented in this figure corresponds to the hydrated lower limit model presented in Fig. 5.25.

Furthermore, all three forward models are unable to reproduce measured responses when utilising standard impedances. In comparison, the dry forward model is capable of reproducing apparent resistivities and phases for the entire period range of 100 s to 10,000 s for measured data. In addition, this forward model predicts responses which are contiguous with the global conductivity model of Grayver et al. (2017) for the TE-mode when utilising hybrid impedance.

I interpret the discontinuity between TM-mode responses and the global conductivity model of Grayver et al. (2017) to be a consequence of my coarse approximation of the coastline. This limits my ability to model the electric fields perpendicular to the coastline which comprise the TM-mode. As such, I conclude that these observations further support the calculation of hybrid impedance. Additionally, I interpret these observations to be evidence supporting my proposed reference model of the upper mantle conductivity structure. Finally, I interpret these responses as evidence supporting a primarily isotropic upper mantle beneath the oceanic lithosphere of the Pacific Ocean.

5.5 Conclusions

Following the adoption of plate tectonic theory, geophysicists have sought to constrain the conditions which result in the LARC. To investigate this, geophysicists utilise the MT method due to its sensitivity to enhanced electrical conductivity caused by partial melt, hydration, and temperature. By analysing ocean-bottom MT data collected from the Pacific Ocean, I have identified a conductivity model which represents the Earth's oceanic lithosphere and asthenosphere. In addition, I identified a strategy to address instability in ocean-bottom MT impedance. In this chapter, I conduct a case study which concludes that the aforementioned conductivity model is capable of reproducing measured responses when utilising hybrid impedances. In contrast, standard impedances are unable to reproduce measured responses.

From this evidence, I conclude that the upper mantle for this region of the Pacific Ocean is primarily isotropic with thermal conduction within upper mantle silicates capable of explaining the observed conductivity structure. As such, I conclude that my reference model realistically represents the Earth's oceanic lithosphere and asthenosphere. Additionally, I conclude that these results support the hybrid impedance as an alternative to traditional MT impedance when conducting ocean-bottom MT studies.

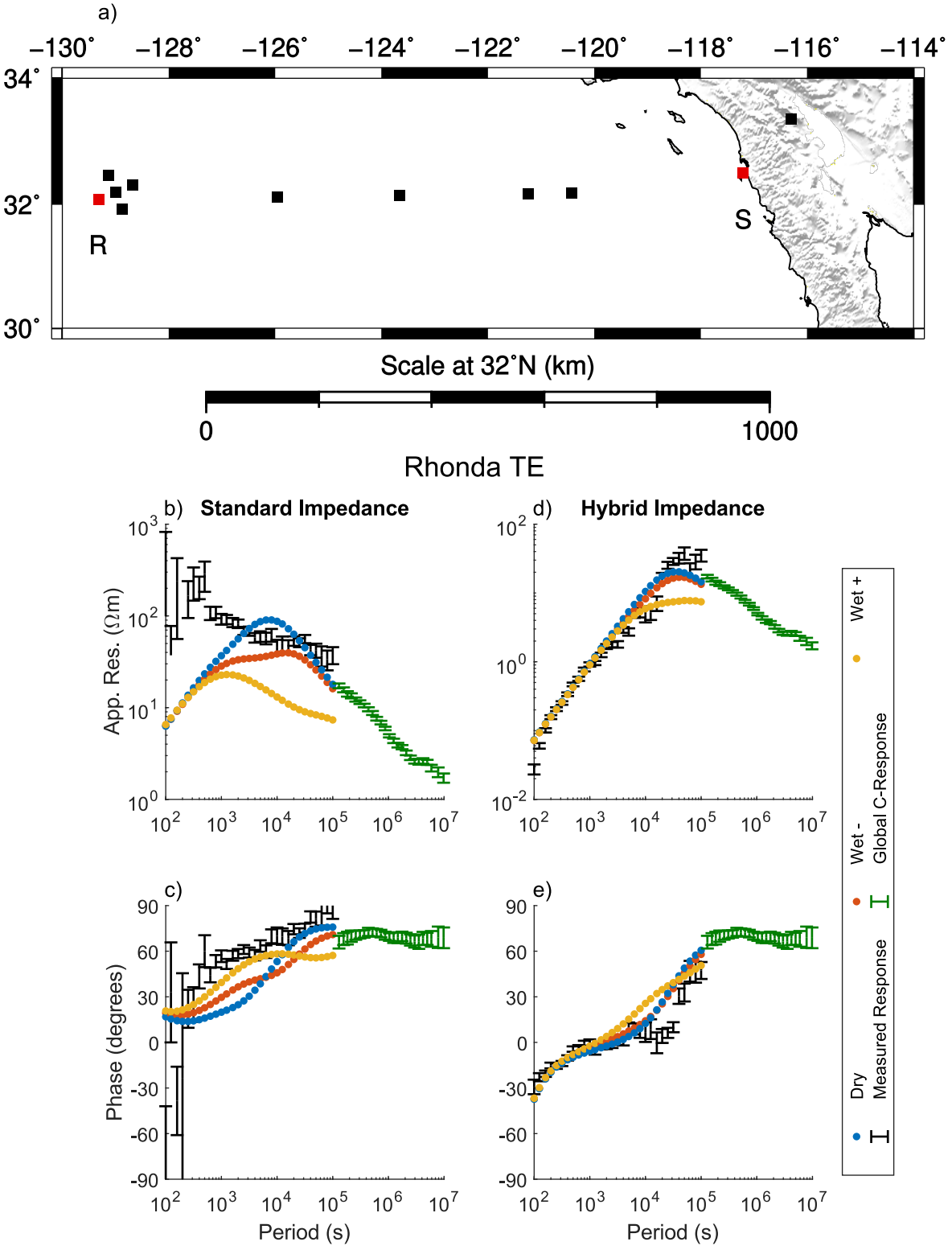

Figure 5.28: a) displays APPLE MT stations as squares. Red squares correspond to plotted stations. b) and c) display standard impedance ρ_{app} and ϕ. d) and e) display hybrid impedance ρ_{app} and ϕ. Blue, orange, and yellow points represent modelled responses for dry, hydrated lower, and hydrated upper limits. Black and green points represent the Rhonda receiver data and the global conductivity model of Grayver et al. (2017) respectively.

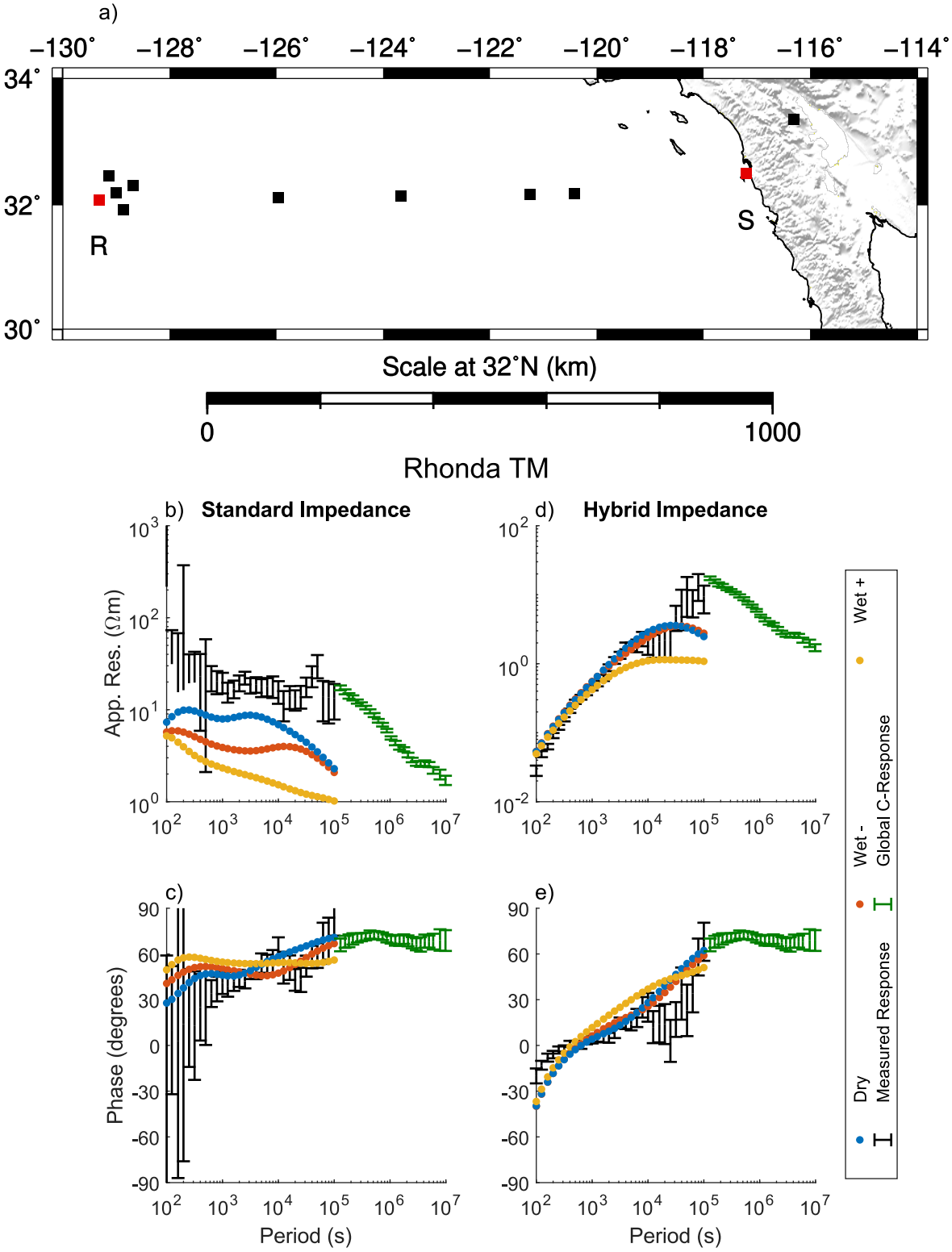

Figure 5.29: a) displays APPLE MT stations as squares. Red squares correspond to plotted stations. b) and c) display standard impedance ρ_{app} and ϕ. d) and e) display hybrid impedance ρ_{app} and ϕ. Blue, orange, and yellow points represent modelled responses for dry, hydrated lower, and hydrated upper limits. Black and green points represent the Rhonda receiver data and the global conductivity model of Grayver et al. (2017) respectively.

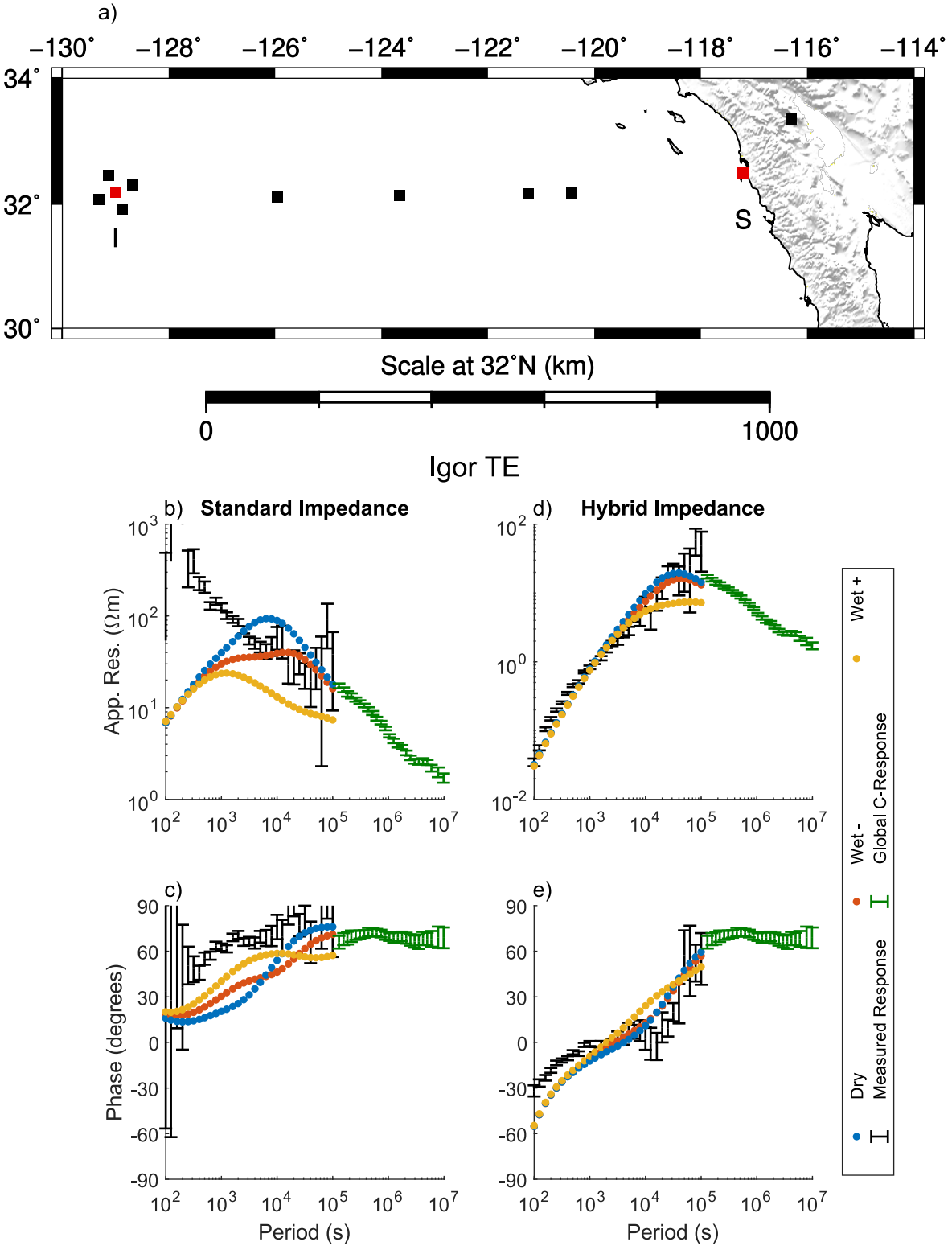

Figure 5.30: a) displays APPLE MT stations as squares. Red squares correspond to plotted stations. b) and c) display standard impedance ρ_{app} and ϕ. d) and e) display hybrid impedance ρ_{app} and ϕ. Blue, orange, and yellow points represent modelled responses for dry, hydrated lower, and hydrated upper limits. Black and green points represent the Igor receiver data and the global conductivity model of Grayver et al. (2017) respectively.

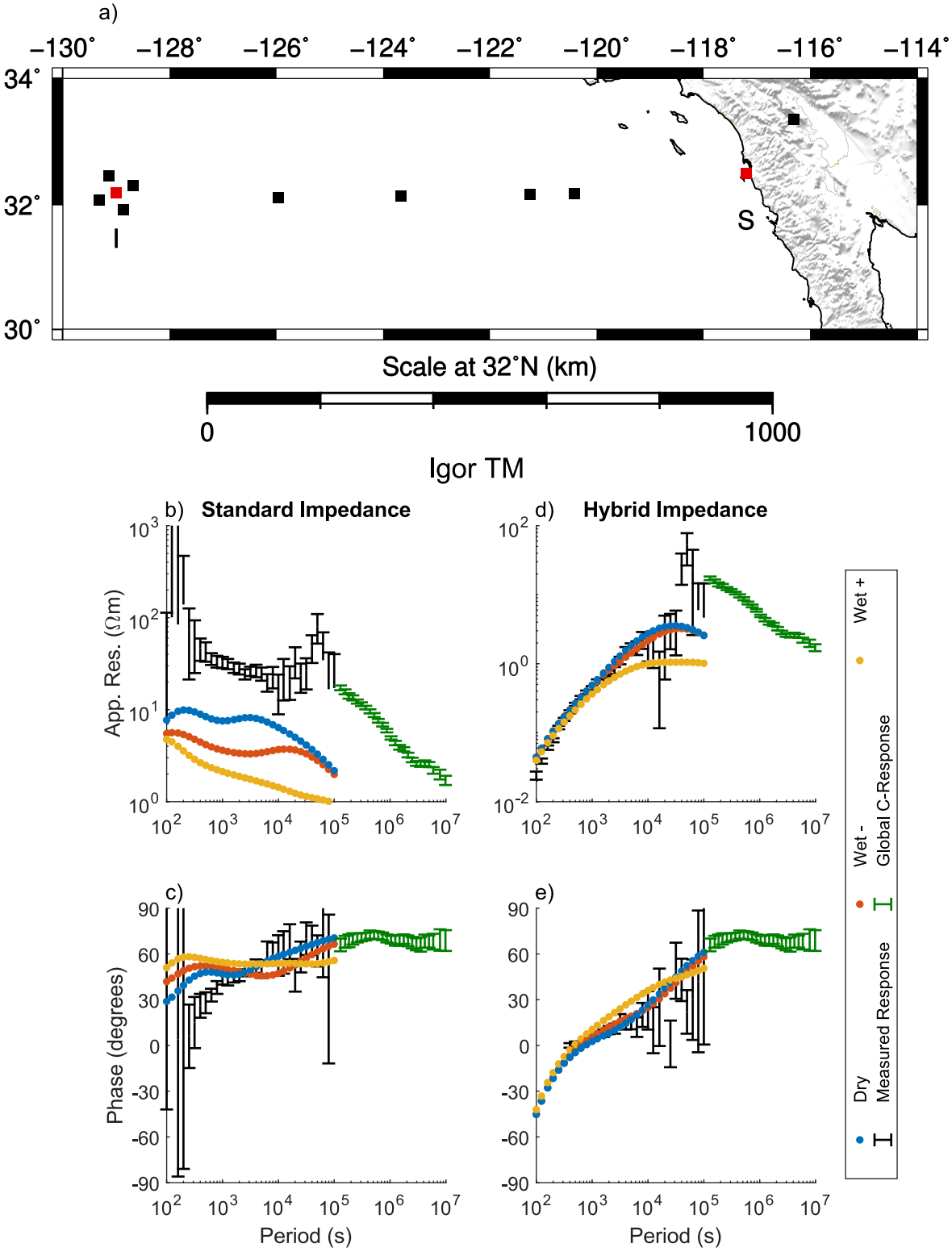

Figure 5.31: a) displays APPLE MT stations as squares. Red squares correspond to plotted stations. b) and c) display standard impedance ρ_{app} and ϕ. d) and e) display hybrid impedance ρ_{app} and ϕ. Blue, orange, and yellow points represent modelled responses for dry, hydrated lower, and hydrated upper limits. Black and green points represent the Igor receiver data and the global conductivity model of Grayver et al. (2017) respectively.

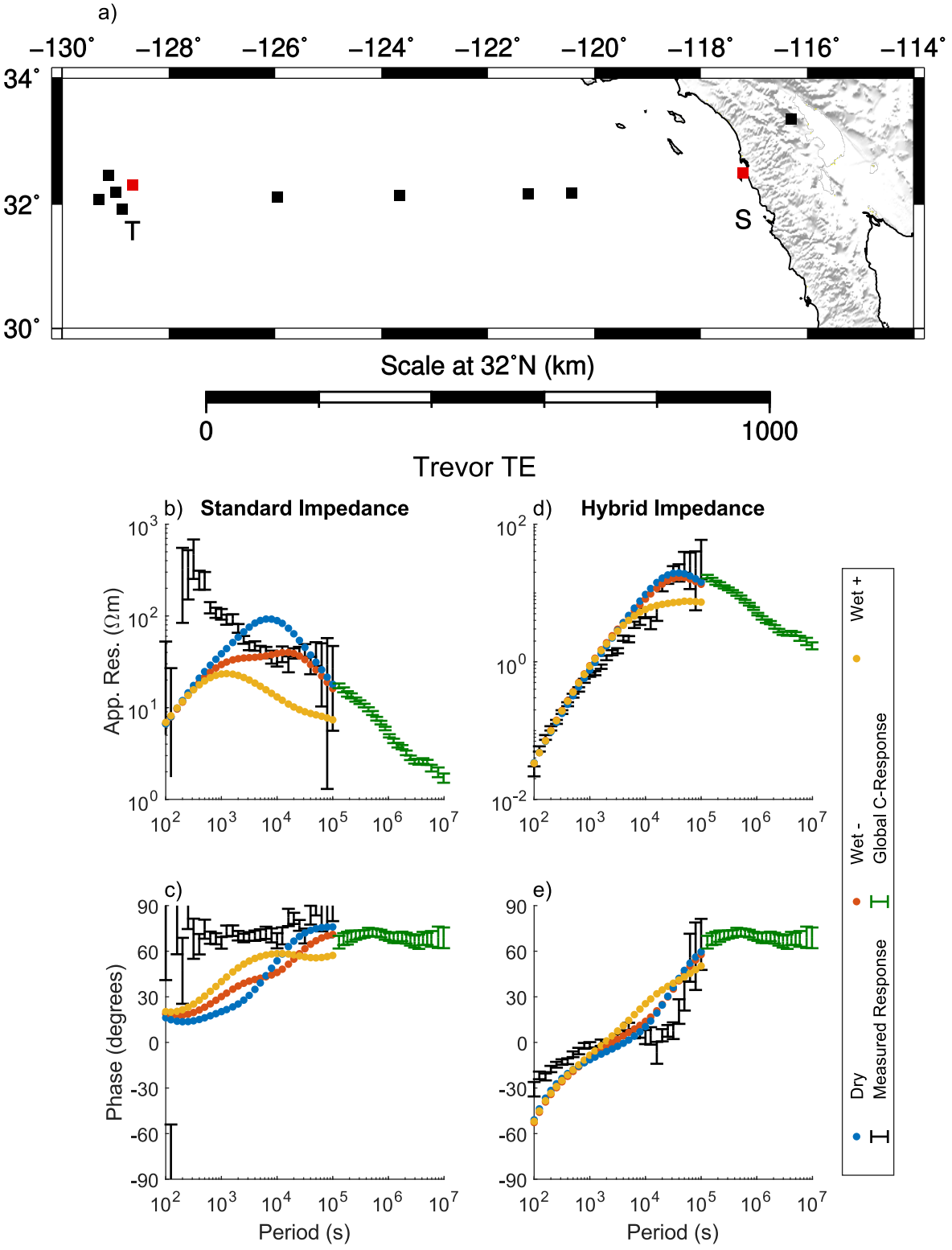

Figure 5.32: a) displays APPLE MT stations as squares. Red squares correspond to plotted stations. b) and c) display standard impedance ρ_{app} and ϕ. d) and e) display hybrid impedance ρ_{app} and ϕ. Blue, orange, and yellow points represent modelled responses for dry, hydrated lower, and hydrated upper limits. Black and green points represent the Trevor receiver data and the global conductivity model of Grayver et al. (2017) respectively.

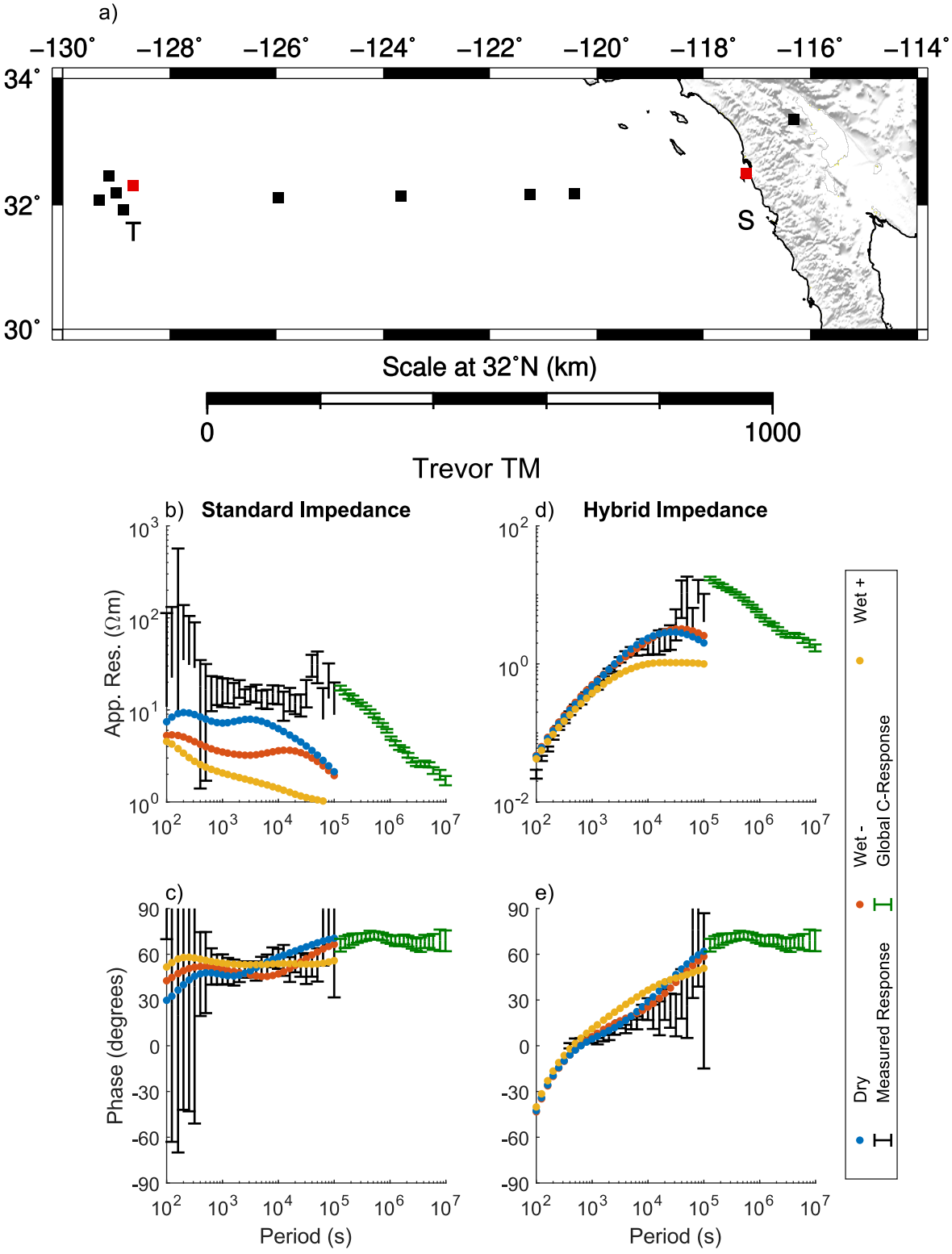

Figure 5.33: a) displays APPLE MT stations as squares. Red squares correspond to plotted stations. b) and c) display standard impedance ρ_{app} and ϕ. d) and e) display hybrid impedance ρ_{app} and ϕ. Blue, orange, and yellow points represent modelled responses for dry, hydrated lower, and hydrated upper limits. Black and green points represent the Trevor receiver data and the global conductivity model of Grayver et al. (2017) respectively.

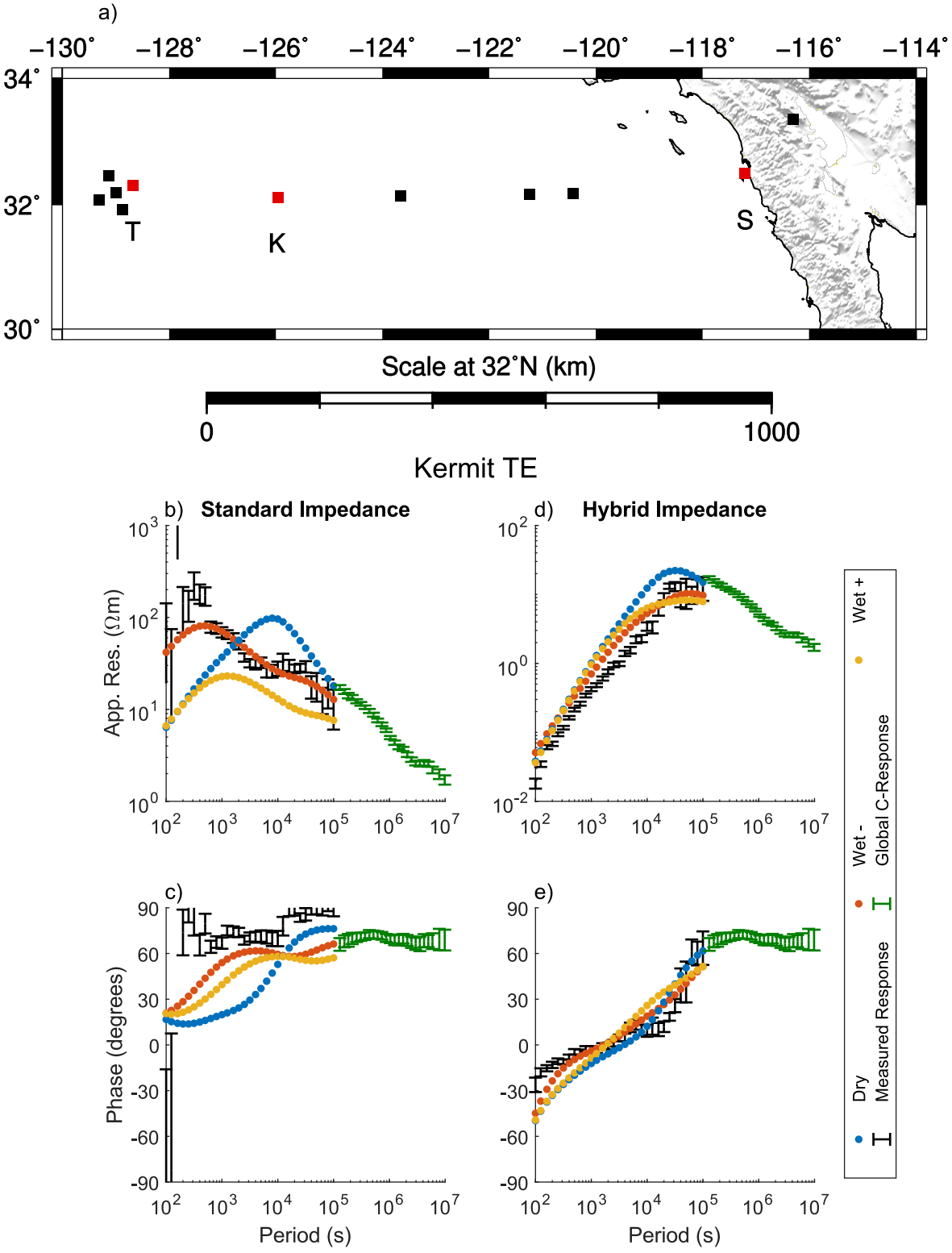

Figure 5.34: a) displays APPLE MT stations as squares. Red squares correspond to plotted stations. b) and c) display standard impedance ρ_{app} and ϕ. d) and e) display hybrid impedance ρ_{app} and ϕ. Blue, orange, and yellow points represent modelled responses for dry, hydrated lower, and hydrated upper limits. Black and green points represent the Kermit receiver data and the global conductivity model of Grayver et al. (2017) respectively.

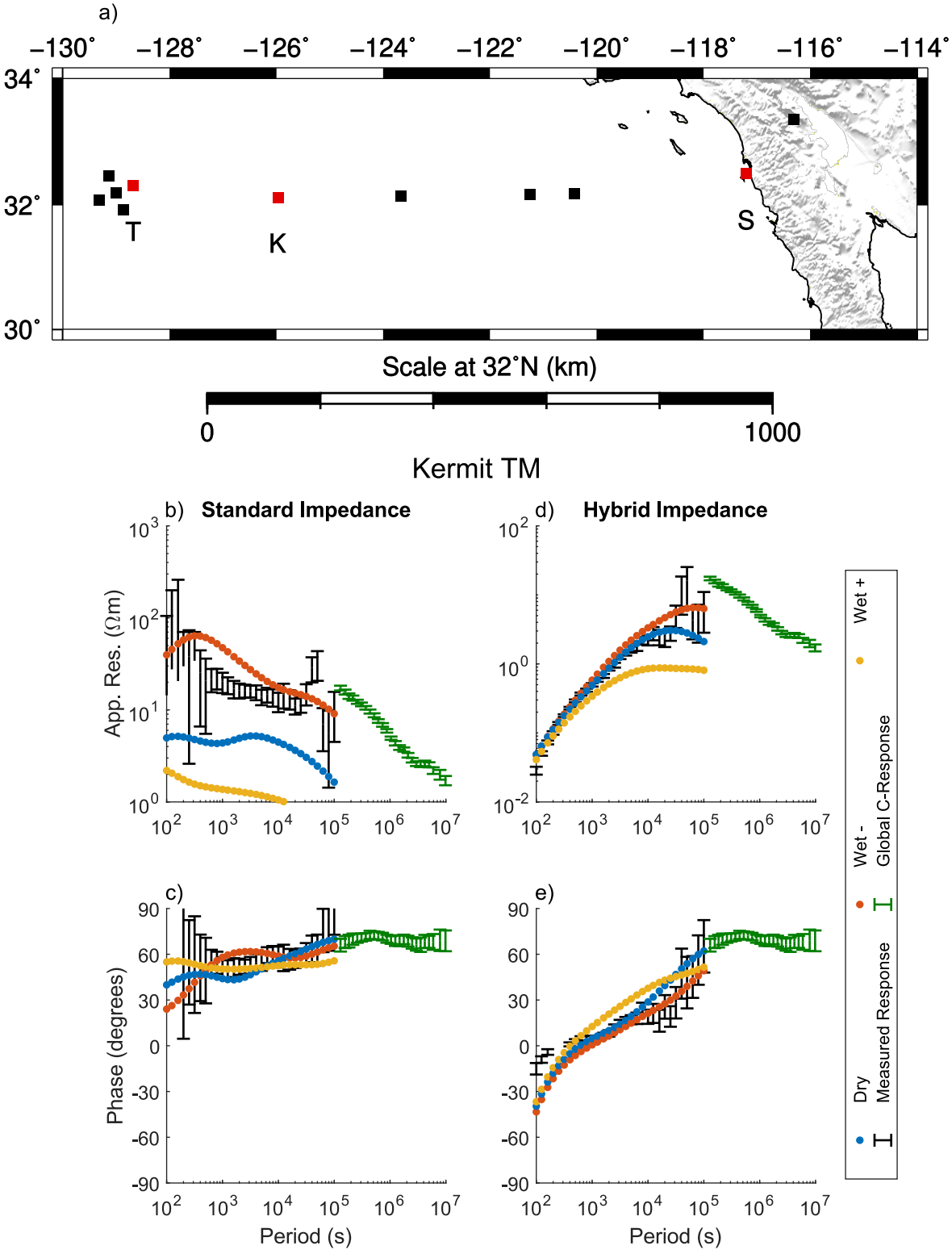

Figure 5.35: a) displays APPLE MT stations as squares. Red squares correspond to plotted stations. b) and c) display standard impedance ρ_{app} and ϕ. d) and e) display hybrid impedance ρ_{app} and ϕ. Blue, orange, and yellow points represent modelled responses for dry, hydrated lower, and hydrated upper limits. Black and green points represent the Kermit receiver data and the global conductivity model of Grayver et al. (2017) respectively.

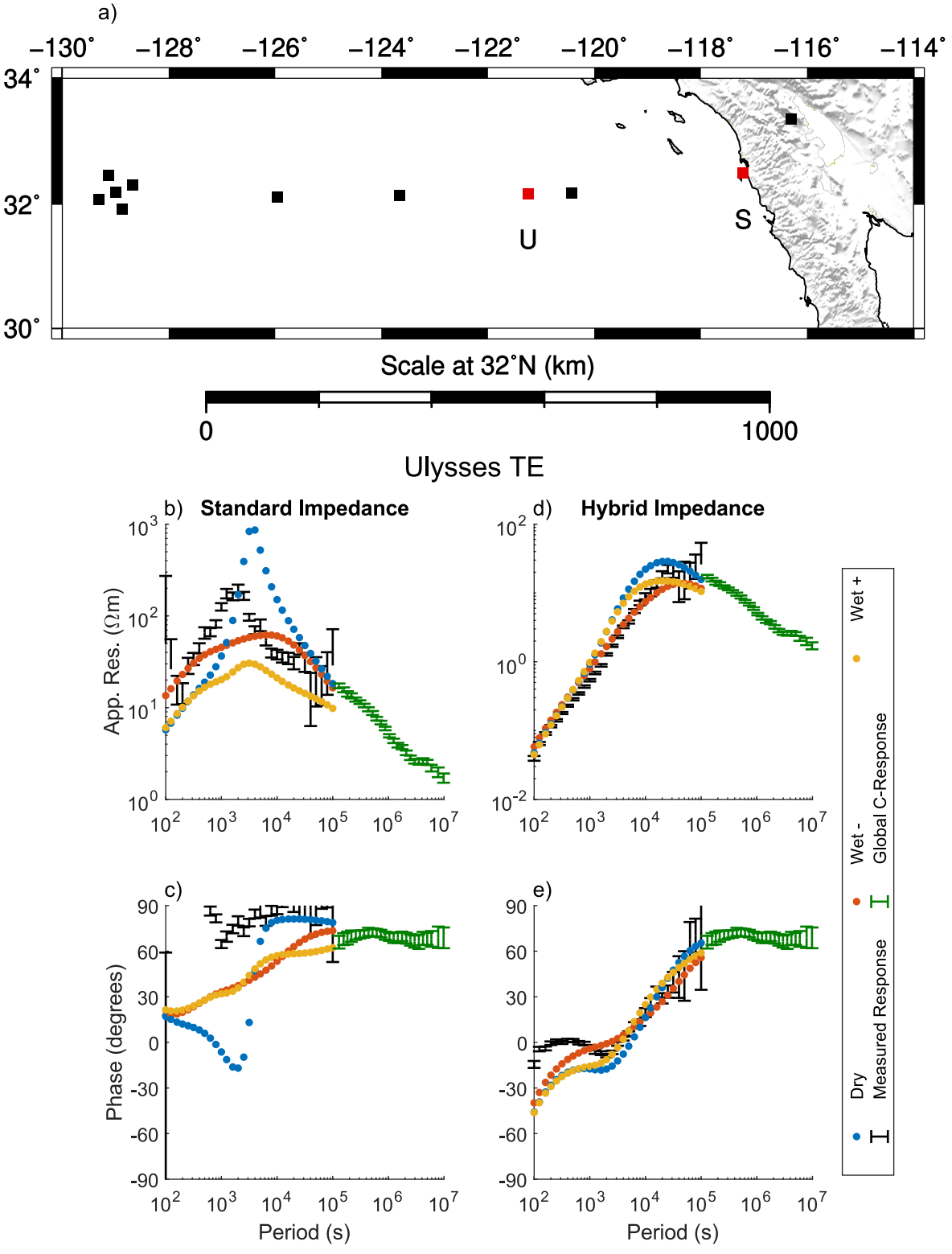

Figure 5.36: a) displays APPLE MT stations as squares. Red squares correspond to plotted stations. b) and c) display standard impedance ρ_{app} and ϕ. d) and e) display hybrid impedance ρ_{app} and ϕ. Blue, orange, and yellow points represent modelled responses for dry, hydrated lower, and hydrated upper limits. Black and green points represent the Ulysses receiver data and the global conductivity model of Grayver et al. (2017) respectively.

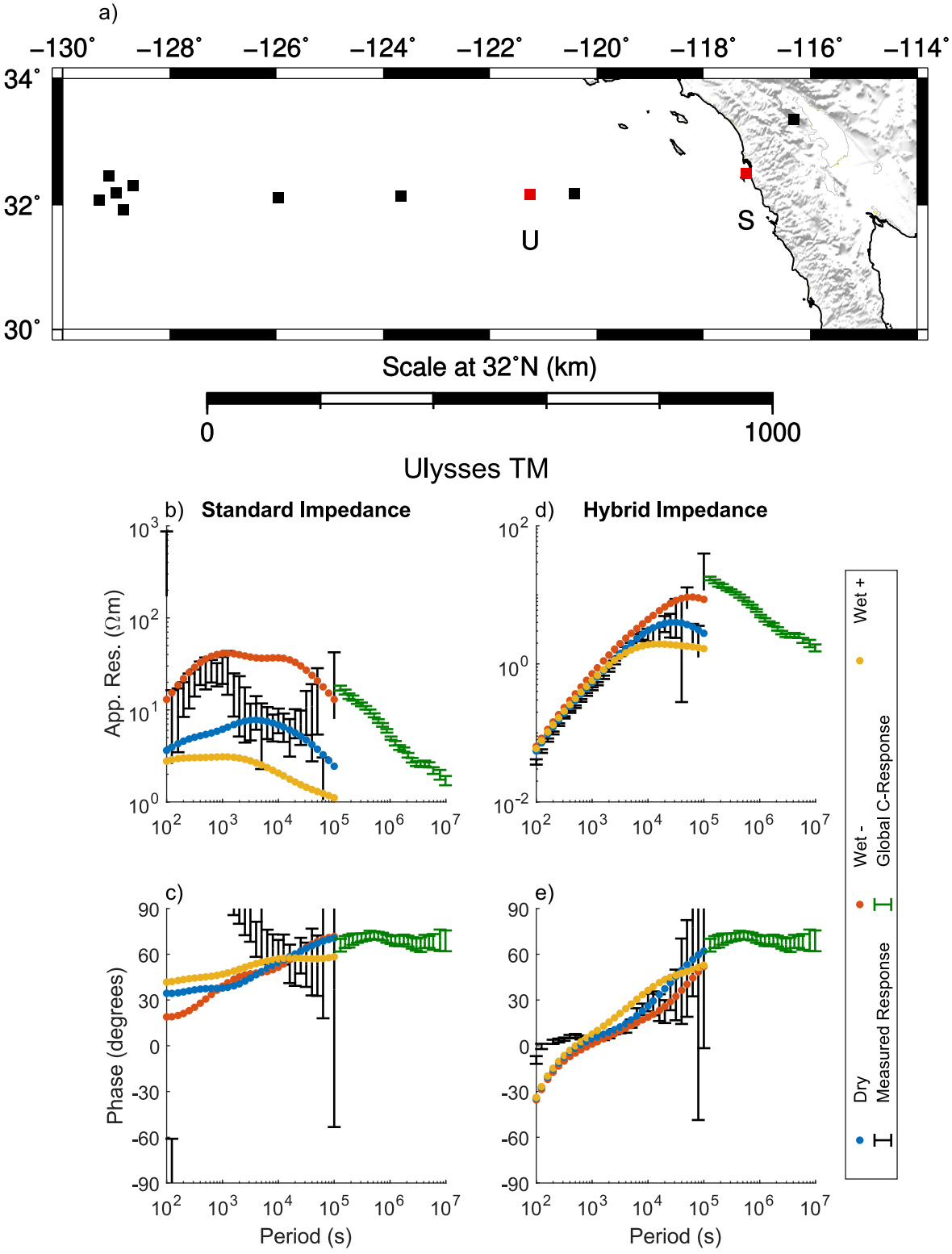

Figure 5.37: a) displays APPLE MT stations as squares. Red squares correspond to plotted stations. b) and c) display standard impedance ρ_{app} and ϕ. d) and e) display hybrid impedance ρ_{app} and ϕ. Blue, orange, and yellow points represent modelled responses for dry, hydrated lower, and hydrated upper limits. Black and green points represent the Ulysses receiver data and the global conductivity model of Grayver et al. (2017) respectively.

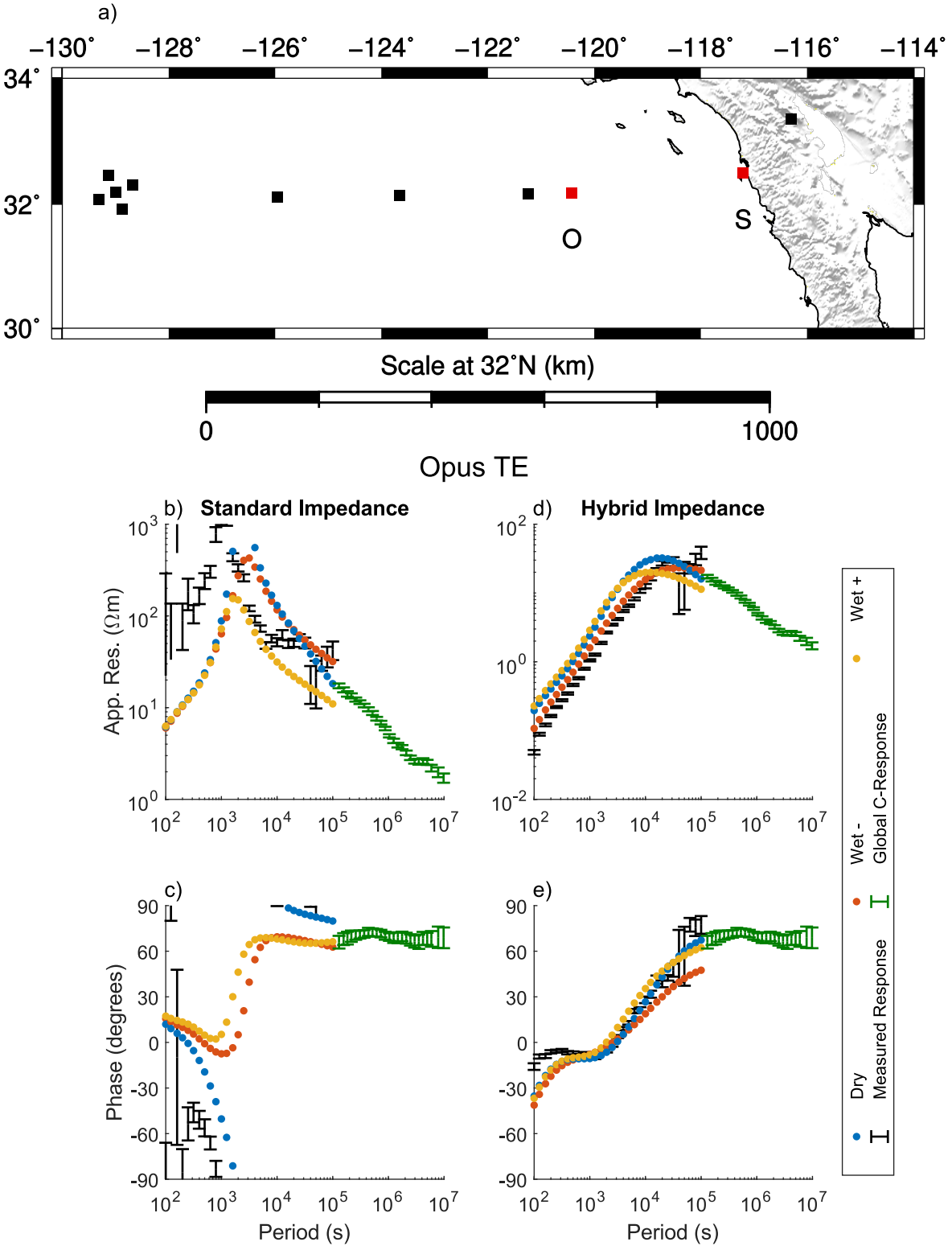

Figure 5.38: a) displays APPLE MT stations as squares. Red squares correspond to plotted stations. b) and c) display standard impedance ρ_{app} and ϕ. d) and e) display hybrid impedance ρ_{app} and ϕ. Blue, orange, and yellow points represent modelled responses for dry, hydrated lower, and hydrated upper limits. Black and green points represent the Opus receiver data and the global conductivity model of Grayver et al. (2017) respectively.

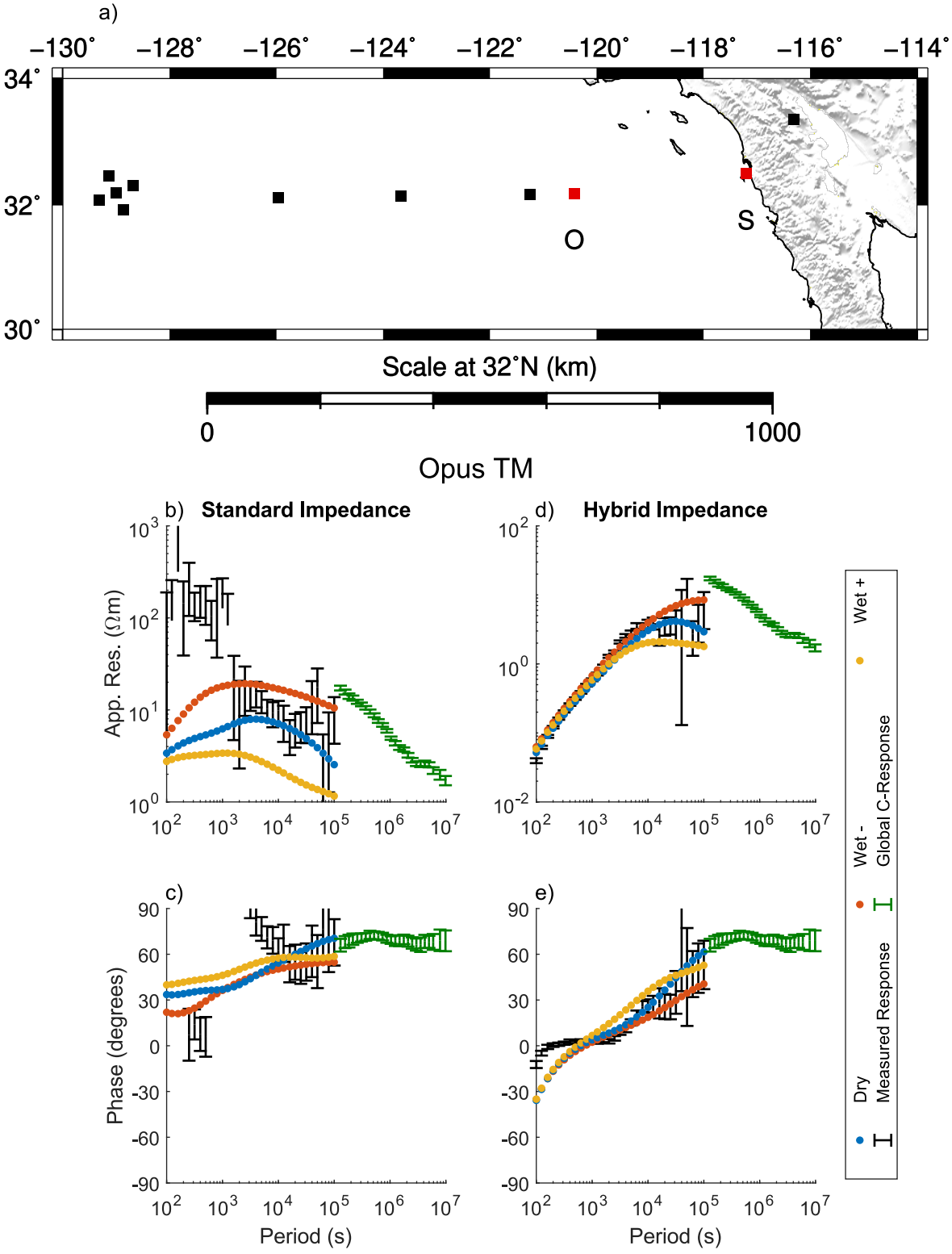

Figure 5.39: a) displays APPLE MT stations as squares. Red squares correspond to plotted stations. b) and c) display standard impedance ρ_{app} and ϕ. d) and e) display hybrid impedance ρ_{app} and ϕ. Blue, orange, and yellow points represent modelled responses for dry, hydrated lower, and hydrated upper limits. Black and green points represent the Opus receiver data and the global conductivity model of Grayver et al. (2017) respectively.

Chapter 6

Summary and Conclusion

Since the adoption of plate tectonic theory, numerous studies have attempted to ascertain the nature of the rheological contrast between the lithosphere and asthenosphere using the MT method. This geophysical technique is sensitive to enhanced electrical conductivity and allows geophysicists to constrain the temperature, pressure, physical and chemical state, porosity, and permeability of the Earth. From these studies, geophysicists propose the rheological discontinuity is the result of hydration or partial melt, however, a consensus is yet to be reached.

6.1 An Oceanic Mantle Electrical Conductivity Reference Model

Furthermore, these studies fail to consider how the conductivity structure of the rheological contrast evolves with respect to lithospheric age. To address this issue, I formulated a representative conductivity model of the Earth's oceanic crust and mantle in Chapter 3. This model characterise the bulk conductivity of the upper mantle in terms of a resistive matrix, comprised of either dry or hydrated upper mantle minerals, and partial melt, comprised of silicate and carbonatite melt. This bulk conductivity varies with respect to lithospheric age via the calculation of the upper mantle temperature gradient which subsequently controls the melt fraction. To ensure accuracy, the model is derived from laboratory conductivity models and then analysed using 40 years of MT studies from the Pacific Ocean.

From this analysis, I draw the following conclusions. Firstly, a simple model consisting of upper mantle minerals, hydration, and partial melt is capable of predicting four decades worth of data collected from the Pacific Ocean. Secondly, the conductivity structure between 50 km and 100 km is consistent with the hypothesis of partial melt for young lithospheric ages otherwise hydration is required. Thirdly, the conductivity

structure between 200 km and 400 km is consistent with the hypothesis of hydration. These conclusions constrain the rheological contrast at the base of the lithosphere its evolution with lithospheric age from partial melt to hydration.

6.2 A Hybrid Oceanic-Continental MT Response Approach

Further compromising my ability to constrain the geodynamic process which produces the rheological contrast using the MT method is the interaction between induced EM fields and the saline water of the Earth's oceans. Chapter 4 presents a solution to this problem in the form of a hybrid MT impedance. Considered one of the principal problems of modern geomagnetism, this interaction distorts the EM fields measured by MT receivers and results in erratic impedances.

A comparison of ocean-bottom electric fields, ocean-bottom magnetic fields, and onshore magnetic fields reveals that the source of the instability observed in standard impedances is the ocean-bottom magnetic field. Furthermore, I observe that the ocean-bottom magnetic field is a long-wavelength approximation of onshore magnetic fields. A subsequent analysis of standard and hybrid impedances, reveals that hybrid impedances are immune to instabilities introduced into ocean-bottom MT studies by interactions between EM fields and the Earth's oceans.

6.3 Insights On The Electrical Conductivity Structure Of The Oceanic Upper Mantle

Finally, Chapter 5 assesses the conclusions of Chapter 3 and Chapter 4 through a forward modelling case study using data collected during the APPLE study. The structure of this forward model represents the abyssal plain, continental slope, and continental lithosphere of California. For the conductivity structure, I calculate Hashin-Shtrikman bounds using the conductivity model proposed in Chapter 3 for a representative lithospheric age of 32.5 Ma. To assess my model, I analyse forward modelled responses calculated for both standard and hybrid impedances.

For standard impedances, my forward model is unable to reproduce measured responses for all receivers. In contrast, hybrid impedances calculated from the anhydrous and disconnected hydrous forward model are observed to reproduce measured responses for all receivers in addition to a global conductivity model derived from satellite magnetic field measurements. From this, I conclude that the calculation of hybrid impedances

as outlined in Chapter 4 is an appropriate method for improving the stability of ocean-bottom MT responses. Similarly, I conclude that the representative conductivity model of Chapter 3 accurately represents the conductivity structure of the lithosphere, asthenosphere, and the rheological contrast between the two.

Appendix A

Reference Model Electrical structure Versus Depth

The electrical structure versus depth profiles presented in Chapter 3 and Chapter 5. The profiles are output from my reference model defined in Chapter 3.

Table A.1: Hashin-Shtrikman lower (HSL) and upper (HSU) limits calculated for a dry, hydrated, and partially melted upper mantle from my reference model in Chapter 3.

Depth (km)	HSL_{Dry}^{140Ma}		HSL_{Dry}^{33Ma}		HSU_{Dry}^{33Ma}	
	(S/m)	(Ωm)	(S/m)	(Ωm)	(S/m)	(Ωm)
1.0	2.2E+18	4.6E-19	4.7E+29	2.1E-30	2.2E+18	4.6E-19
2.0	3.3E+17	3.0E-18	7.5E+26	1.3E-27	5.7E+16	1.7E-17
3.0	6.0E+16	1.7E-17	3.1E+24	3.2E-25	2.6E+15	3.8E-16
4.0	1.2E+16	8.2E-17	2.8E+22	3.6E-23	1.9E+14	5.4E-15
5.0	2.8E+15	3.6E-16	4.6E+20	2.2E-21	1.9E+13	5.4E-14
6.0	7.1E+14	1.4E-15	1.3E+19	7.8E-20	2.5E+12	4.1E-13
7.0	2.0E+14	5.0E-15	5.4E+17	1.9E-18	4.1E+11	2.4E-12
8.0	6.1E+13	1.6E-14	3.2E+16	3.1E-17	8.5E+10	1.2E-11
9.0	2.0E+13	4.9E-14	2.6E+15	3.8E-16	2.0E+10	4.9E-11
10.0	7.1E+12	1.4E-13	2.8E+14	3.5E-15	5.7E+09	1.8E-10
11.0	2.7E+12	3.7E-13	3.8E+13	2.6E-14	1.8E+09	5.6E-10
12.0	1.1E+12	9.3E-13	6.3E+12	1.6E-13	6.3E+08	1.6E-09
13.0	4.6E+11	2.2E-12	1.3E+12	7.9E-13	2.4E+08	4.1E-09
14.0	2.0E+11	5.0E-12	3.0E+11	3.4E-12	1.0E+08	9.8E-09
15.0	9.3E+10	1.1E-11	8.1E+10	1.2E-11	4.6E+07	2.2E-08
16.0	4.5E+10	2.2E-11	2.5E+10	4.0E-11	2.2E+07	4.6E-08
17.0	2.3E+10	4.4E-11	8.7E+09	1.2E-10	1.1E+07	9.1E-08
18.0	1.2E+10	8.5E-11	3.3E+09	3.0E-10	5.9E+06	1.7E-07
19.0	6.3E+09	1.6E-10	1.4E+09	7.4E-10	3.3E+06	3.1E-07
20.0	3.5E+09	2.9E-10	5.9E+08	1.7E-09	1.9E+06	5.3E-07
21.0	2.0E+09	5.1E-10	2.7E+08	3.6E-09	1.1E+06	8.7E-07
22.0	1.2E+09	8.7E-10	1.3E+08	7.5E-09	7.1E+05	1.4E-06
23.0	6.9E+08	1.5E-09	6.8E+07	1.5E-08	4.6E+05	2.2E-06
24.0	4.2E+08	2.4E-09	3.6E+07	2.8E-08	3.0E+05	3.3E-06
25.0	2.6E+08	3.8E-09	2.0E+07	5.1E-08	2.1E+05	4.9E-06
26.0	1.7E+08	5.9E-09	1.1E+07	8.9E-08	1.4E+05	7.0E-06
27.0	1.1E+08	9.1E-09	6.5E+06	1.5E-07	1.0E+05	9.8E-06
28.0	7.2E+07	1.4E-08	4.0E+06	2.5E-07	7.4E+04	1.4E-05
29.0	4.9E+07	2.0E-08	2.6E+06	3.9E-07	5.4E+04	1.9E-05
30.0	3.3E+07	3.0E-08	1.7E+06	6.0E-07	4.1E+04	2.5E-05
31.0	2.3E+07	4.3E-08	1.1E+06	9.1E-07	3.1E+04	3.2E-05
32.0	1.6E+07	6.1E-08	7.5E+05	1.3E-06	2.4E+04	4.2E-05
33.0	1.2E+07	8.6E-08	5.1E+05	2.0E-06	1.9E+04	5.4E-05
34.0	8.4E+06	1.2E-07	3.6E+05	2.8E-06	1.5E+04	6.8E-05
35.0	6.2E+06	1.6E-07	2.6E+05	3.9E-06	1.2E+04	8.4E-05
36.0	4.6E+06	2.2E-07	1.9E+05	5.4E-06	9.6E+03	1.0E-04
37.0	3.4E+06	2.9E-07	1.4E+05	7.3E-06	7.9E+03	1.3E-04
38.0	2.6E+06	3.9E-07	1.0E+05	9.8E-06	6.5E+03	1.5E-04
39.0	2.0E+06	5.1E-07	7.7E+04	1.3E-05	5.4E+03	1.8E-04
40.0	1.5E+06	6.6E-07	5.9E+04	1.7E-05	4.6E+03	2.2E-04

Table A.2: Hashin-Shtrikman limits calculated for a dry, hydrated, and partially melted upper mantle from my reference model in Chapter 3.

Depth (km)	HSL_{Dry}^{140Ma}		HSL_{Dry}^{33Ma}		HSU_{Dry}^{33Ma}	
	(S/m)	(Ωm)	(S/m)	(Ωm)	(S/m)	(Ωm)
41.0	1.2E+06	8.5E-07	4.6E+04	2.2E-05	3.9E+03	2.6E-04
42.0	9.2E+05	1.1E-06	3.6E+04	2.8E-05	3.3E+03	3.0E-04
43.0	7.2E+05	1.4E-06	2.8E+04	3.5E-05	2.8E+03	3.5E-04
44.0	5.7E+05	1.7E-06	2.3E+04	4.4E-05	2.5E+03	4.1E-04
45.0	4.6E+05	2.2E-06	1.8E+04	5.4E-05	2.1E+03	4.7E-04
46.0	3.7E+05	2.7E-06	1.5E+04	6.7E-05	1.9E+03	5.3E-04
47.0	3.0E+05	3.3E-06	1.2E+04	8.1E-05	1.7E+03	6.0E-04
48.0	2.5E+05	4.1E-06	1.0E+04	9.8E-05	1.5E+03	6.8E-04
49.0	2.0E+05	4.9E-06	8.5E+03	1.2E-04	1.3E+03	7.7E-04
50.0	1.7E+05	6.0E-06	7.2E+03	1.4E-04	1.2E+03	8.6E-04
51.0	1.4E+05	7.2E-06	6.1E+03	1.6E-04	1.0E+03	9.5E-04
52.0	1.2E+05	8.6E-06	5.2E+03	1.9E-04	9.4E+02	1.1E-03
53.0	9.8E+04	1.0E-05	4.5E+03	2.2E-04	8.5E+02	1.2E-03
54.0	8.3E+04	1.2E-05	3.9E+03	2.6E-04	7.8E+02	1.3E-03
55.0	7.0E+04	1.4E-05	3.4E+03	2.9E-04	7.1E+02	1.4E-03
56.0	6.0E+04	1.7E-05	3.0E+03	3.4E-04	6.5E+02	1.5E-03
57.0	5.1E+04	2.0E-05	2.6E+03	3.8E-04	6.0E+02	1.7E-03
58.0	4.4E+04	2.3E-05	2.3E+03	4.3E-04	5.5E+02	1.8E-03
59.0	3.8E+04	2.7E-05	2.1E+03	4.9E-04	5.1E+02	2.0E-03
60.0	3.3E+04	3.1E-05	1.8E+03	5.4E-04	4.7E+02	2.1E-03
61.0	2.8E+04	3.5E-05	1.7E+03	6.1E-04	4.4E+02	2.3E-03
62.0	2.5E+04	4.0E-05	1.5E+03	6.7E-04	4.1E+02	2.4E-03
63.0	2.2E+04	4.6E-05	1.3E+03	7.4E-04	3.9E+02	2.6E-03
64.0	1.9E+04	5.3E-05	1.2E+03	8.2E-04	3.6E+02	2.8E-03
65.0	1.7E+04	6.0E-05	1.1E+03	9.0E-04	3.4E+02	2.9E-03
66.0	1.5E+04	6.8E-05	1.0E+03	9.8E-04	3.2E+02	3.1E-03
67.0	1.3E+04	7.6E-05	9.3E+02	1.1E-03	3.0E+02	3.3E-03
68.0	1.1E+04	8.9E-05	8.5E+02	1.2E-03	2.8E+02	3.5E-03
69.0	9.9E+03	1.0E-04	7.8E+02	1.3E-03	2.7E+02	3.7E-03
70.0	8.7E+03	1.2E-04	7.2E+02	1.4E-03	2.5E+02	4.0E-03
71.0	7.7E+03	1.3E-04	6.7E+02	1.5E-03	2.4E+02	4.2E-03
72.0	6.8E+03	1.5E-04	6.3E+02	1.6E-03	2.3E+02	4.4E-03
73.0	6.1E+03	1.7E-04	5.8E+02	1.7E-03	2.1E+02	4.7E-03
74.0	5.4E+03	1.9E-04	5.5E+02	1.8E-03	2.0E+02	4.9E-03
75.0	4.8E+03	2.1E-04	5.1E+02	2.0E-03	1.9E+02	5.2E-03
76.0	4.3E+03	2.3E-04	4.8E+02	2.1E-03	1.9E+02	5.4E-03
77.0	3.9E+03	2.6E-04	4.5E+02	2.2E-03	1.8E+02	5.7E-03
78.0	3.5E+03	2.9E-04	4.3E+02	2.3E-03	1.7E+02	5.9E-03
79.0	3.1E+03	3.2E-04	4.0E+02	2.5E-03	1.6E+02	6.2E-03
80.0	2.8E+03	3.6E-04	3.8E+02	2.6E-03	1.6E+02	6.4E-03

Table A.3: Hashin-Shtrikman limits calculated for a dry, hydrated, and partially melted upper mantle from my reference model in Chapter 3.

Depth (km)	HSL_{Dry}^{140Ma}		HSL_{Dry}^{33Ma}		HSU_{Dry}^{33Ma}	
	(S/m)	(Ωm)	(S/m)	(Ωm)	(S/m)	(Ωm)
81.0	2.5E+03	3.9E-04	3.6E+02	2.8E-03	1.5E+02	6.6E-03
82.0	2.3E+03	4.3E-04	3.5E+02	2.9E-03	1.5E+02	6.9E-03
83.0	2.1E+03	4.8E-04	3.3E+02	3.0E-03	1.4E+02	7.1E-03
84.0	1.9E+03	5.3E-04	3.2E+02	3.2E-03	1.4E+02	7.4E-03
85.0	1.7E+03	5.8E-04	3.0E+02	3.3E-03	1.3E+02	7.6E-03
86.0	1.6E+03	6.3E-04	2.9E+02	3.5E-03	1.3E+02	7.9E-03
87.0	1.4E+03	6.9E-04	2.8E+02	3.6E-03	1.2E+02	8.1E-03
88.0	1.3E+03	7.5E-04	2.7E+02	3.7E-03	1.2E+02	8.4E-03
89.0	1.2E+03	8.2E-04	2.6E+02	3.9E-03	1.2E+02	8.6E-03
90.0	1.1E+03	9.0E-04	2.5E+02	4.0E-03	1.1E+02	8.8E-03
91.0	1.0E+03	9.7E-04	2.4E+02	4.2E-03	1.1E+02	9.1E-03
92.0	9.4E+02	1.1E-03	2.3E+02	4.3E-03	1.1E+02	9.3E-03
93.0	8.7E+02	1.2E-03	2.3E+02	4.4E-03	1.1E+02	9.5E-03
94.0	8.1E+02	1.2E-03	2.2E+02	4.6E-03	1.0E+02	9.7E-03
95.0	7.5E+02	1.3E-03	2.1E+02	4.7E-03	1.0E+02	9.9E-03
96.0	6.9E+02	1.5E-03	2.1E+02	4.8E-03	9.9E+01	1.0E-02
97.0	6.4E+02	1.6E-03	2.0E+02	5.0E-03	9.6E+01	1.0E-02
98.0	6.0E+02	1.7E-03	2.0E+02	5.1E-03	9.4E+01	1.1E-02
99.0	5.5E+02	1.8E-03	1.9E+02	5.2E-03	9.3E+01	1.1E-02
100.0	5.2E+02	1.9E-03	1.9E+02	5.3E-03	9.1E+01	1.1E-02
101.0	4.8E+02	2.1E-03	1.8E+02	5.5E-03	8.9E+01	1.1E-02
102.0	4.5E+02	2.2E-03	1.8E+02	5.6E-03	8.8E+01	1.1E-02
103.0	4.2E+02	2.4E-03	1.8E+02	5.7E-03	8.8E+01	1.1E-02
104.0	4.0E+02	2.5E-03	1.7E+02	5.7E-03	8.7E+01	1.2E-02
105.0	3.7E+02	2.7E-03	1.7E+02	5.8E-03	8.6E+01	1.2E-02
106.0	3.5E+02	2.8E-03	1.7E+02	5.9E-03	8.5E+01	1.2E-02
107.0	3.3E+02	3.0E-03	1.7E+02	6.0E-03	8.5E+01	1.2E-02
108.0	3.1E+02	3.2E-03	1.6E+02	6.1E-03	8.4E+01	1.2E-02
109.0	3.0E+02	3.4E-03	1.6E+02	6.2E-03	8.3E+01	1.2E-02
110.0	2.8E+02	3.6E-03	1.6E+02	6.2E-03	8.3E+01	1.2E-02
111.0	2.7E+02	3.8E-03	1.6E+02	6.3E-03	8.2E+01	1.2E-02
112.0	2.5E+02	4.0E-03	1.6E+02	6.4E-03	8.1E+01	1.2E-02
113.0	2.4E+02	4.2E-03	1.6E+02	6.4E-03	8.1E+01	1.2E-02
114.0	2.3E+02	4.4E-03	1.5E+02	6.5E-03	8.1E+01	1.2E-02
115.0	2.1E+02	4.7E-03	1.5E+02	6.6E-03	8.0E+01	1.3E-02
116.0	2.0E+02	4.9E-03	1.5E+02	6.6E-03	8.0E+01	1.3E-02
117.0	1.9E+02	5.2E-03	1.5E+02	6.7E-03	7.9E+01	1.3E-02
118.0	1.8E+02	5.4E-03	1.5E+02	6.7E-03	7.9E+01	1.3E-02
119.0	1.7E+02	5.7E-03	1.5E+02	6.8E-03	7.9E+01	1.3E-02
120.0	1.7E+02	6.0E-03	1.5E+02	6.8E-03	7.8E+01	1.3E-02

Table A.4: Hashin-Shtrikman limits calculated for a dry, hydrated, and partially melted upper mantle from my reference model in Chapter 3.

Depth (km)	HSL_{Dry}^{140Ma}		HSL_{Dry}^{33Ma}		HSU_{Dry}^{33Ma}	
	(S/m)	(Ωm)	(S/m)	(Ωm)	(S/m)	(Ωm)
121.0	1.6E+02	6.3E-03	1.5E+02	6.9E-03	7.8E+01	1.3E-02
122.0	1.5E+02	6.6E-03	1.4E+02	6.9E-03	7.8E+01	1.3E-02
123.0	1.4E+02	7.0E-03	1.4E+02	6.9E-03	7.8E+01	1.3E-02
124.0	1.4E+02	7.3E-03	1.4E+02	7.0E-03	7.7E+01	1.3E-02
125.0	1.3E+02	7.7E-03	1.4E+02	7.0E-03	7.7E+01	1.3E-02
126.0	1.2E+02	8.1E-03	1.4E+02	7.1E-03	7.6E+01	1.3E-02
127.0	1.2E+02	8.5E-03	1.4E+02	7.1E-03	7.6E+01	1.3E-02
128.0	1.1E+02	8.9E-03	1.4E+02	7.1E-03	7.6E+01	1.3E-02
129.0	1.1E+02	9.3E-03	1.4E+02	7.2E-03	7.6E+01	1.3E-02
130.0	1.0E+02	9.7E-03	1.4E+02	7.2E-03	7.6E+01	1.3E-02
131.0	9.8E+01	1.0E-02	1.4E+02	7.2E-03	7.5E+01	1.3E-02
132.0	9.3E+01	1.1E-02	1.4E+02	7.3E-03	7.5E+01	1.3E-02
133.0	8.9E+01	1.1E-02	1.4E+02	7.3E-03	7.5E+01	1.3E-02
134.0	8.5E+01	1.2E-02	1.4E+02	7.3E-03	7.5E+01	1.3E-02
135.0	8.1E+01	1.2E-02	1.4E+02	7.4E-03	7.5E+01	1.3E-02
136.0	7.8E+01	1.3E-02	1.4E+02	7.4E-03	7.4E+01	1.4E-02
137.0	7.4E+01	1.4E-02	1.3E+02	7.4E-03	7.4E+01	1.4E-02
138.0	7.4E+01	1.4E-02	1.3E+02	7.4E-03	7.4E+01	1.4E-02
139.0	7.4E+01	1.4E-02	1.3E+02	7.5E-03	7.4E+01	1.4E-02
140.0	7.4E+01	1.4E-02	1.3E+02	7.5E-03	7.4E+01	1.4E-02
141.0	7.4E+01	1.4E-02	1.3E+02	7.5E-03	7.4E+01	1.4E-02
142.0	7.3E+01	1.4E-02	1.3E+02	7.5E-03	7.3E+01	1.4E-02
143.0	7.3E+01	1.4E-02	1.3E+02	7.6E-03	7.3E+01	1.4E-02
144.0	7.3E+01	1.4E-02	1.3E+02	7.6E-03	7.3E+01	1.4E-02
145.0	7.2E+01	1.4E-02	1.3E+02	7.6E-03	7.2E+01	1.4E-02
146.0	7.2E+01	1.4E-02	1.3E+02	7.7E-03	7.2E+01	1.4E-02
147.0	7.2E+01	1.4E-02	1.3E+02	7.7E-03	7.2E+01	1.4E-02
148.0	7.2E+01	1.4E-02	1.3E+02	7.7E-03	7.2E+01	1.4E-02
149.0	7.2E+01	1.4E-02	1.3E+02	7.7E-03	7.2E+01	1.4E-02
150.0	7.2E+01	1.4E-02	1.3E+02	7.8E-03	7.2E+01	1.4E-02
151.0	7.2E+01	1.4E-02	1.3E+02	7.8E-03	7.2E+01	1.4E-02
152.0	7.1E+01	1.4E-02	1.3E+02	7.8E-03	7.1E+01	1.4E-02
153.0	7.1E+01	1.4E-02	1.3E+02	7.8E-03	7.1E+01	1.4E-02
154.0	7.1E+01	1.4E-02	1.3E+02	7.9E-03	7.1E+01	1.4E-02
155.0	7.1E+01	1.4E-02	1.3E+02	7.9E-03	7.1E+01	1.4E-02
156.0	7.1E+01	1.4E-02	1.3E+02	7.9E-03	7.1E+01	1.4E-02
157.0	7.1E+01	1.4E-02	1.3E+02	7.9E-03	7.1E+01	1.4E-02
158.0	7.1E+01	1.4E-02	1.3E+02	8.0E-03	7.1E+01	1.4E-02
159.0	7.0E+01	1.4E-02	1.3E+02	8.0E-03	7.0E+01	1.4E-02
160.0	7.0E+01	1.4E-02	1.2E+02	8.0E-03	7.0E+01	1.4E-02

Table A.5: Hashin-Shtrikman limits calculated for a dry, hydrated, and partially melted upper mantle from my reference model in Chapter 3.

Depth (km)	HSL_{Dry}^{140Ma}		HSL_{Dry}^{33Ma}		HSU_{Dry}^{33Ma}	
	(S/m)	(Ωm)	(S/m)	(Ωm)	(S/m)	(Ωm)
161.0	7.0E+01	1.4E-02	1.2E+02	8.0E-03	7.0E+01	1.4E-02
162.0	7.0E+01	1.4E-02	1.2E+02	8.1E-03	7.0E+01	1.4E-02
163.0	7.0E+01	1.4E-02	1.2E+02	8.1E-03	7.0E+01	1.4E-02
164.0	7.0E+01	1.4E-02	1.2E+02	8.1E-03	7.0E+01	1.4E-02
165.0	7.0E+01	1.4E-02	1.2E+02	8.2E-03	7.0E+01	1.4E-02
166.0	7.0E+01	1.4E-02	1.2E+02	8.2E-03	7.0E+01	1.4E-02
167.0	6.9E+01	1.4E-02	1.2E+02	8.2E-03	6.9E+01	1.4E-02
168.0	6.9E+01	1.4E-02	1.2E+02	8.2E-03	6.9E+01	1.4E-02
169.0	6.9E+01	1.4E-02	1.2E+02	8.3E-03	6.9E+01	1.4E-02
170.0	6.9E+01	1.5E-02	1.2E+02	8.3E-03	6.9E+01	1.5E-02
171.0	6.9E+01	1.5E-02	1.2E+02	8.3E-03	6.9E+01	1.5E-02
172.0	6.9E+01	1.5E-02	1.2E+02	8.3E-03	6.9E+01	1.5E-02
173.0	6.9E+01	1.5E-02	1.2E+02	8.4E-03	6.9E+01	1.5E-02
174.0	6.8E+01	1.5E-02	1.2E+02	8.4E-03	6.8E+01	1.5E-02
175.0	6.8E+01	1.5E-02	1.2E+02	8.4E-03	6.8E+01	1.5E-02
176.0	6.8E+01	1.5E-02	1.2E+02	8.4E-03	6.8E+01	1.5E-02
177.0	6.8E+01	1.5E-02	1.2E+02	8.5E-03	6.8E+01	1.5E-02
178.0	6.8E+01	1.5E-02	1.2E+02	8.5E-03	6.8E+01	1.5E-02
179.0	6.8E+01	1.5E-02	1.2E+02	8.5E-03	6.8E+01	1.5E-02
180.0	6.8E+01	1.5E-02	1.2E+02	8.6E-03	6.8E+01	1.5E-02
181.0	6.8E+01	1.5E-02	1.2E+02	8.6E-03	6.8E+01	1.5E-02
182.0	6.8E+01	1.5E-02	1.2E+02	8.6E-03	6.8E+01	1.5E-02
183.0	6.8E+01	1.5E-02	1.2E+02	8.6E-03	6.8E+01	1.5E-02
184.0	6.8E+01	1.5E-02	1.2E+02	8.7E-03	6.8E+01	1.5E-02
185.0	6.7E+01	1.5E-02	1.2E+02	8.7E-03	6.7E+01	1.5E-02
186.0	6.7E+01	1.5E-02	1.1E+02	8.7E-03	6.7E+01	1.5E-02
187.0	6.7E+01	1.5E-02	1.1E+02	8.8E-03	6.7E+01	1.5E-02
188.0	6.7E+01	1.5E-02	1.1E+02	8.8E-03	6.7E+01	1.5E-02
189.0	6.7E+01	1.5E-02	1.1E+02	8.8E-03	6.7E+01	1.5E-02
190.0	6.7E+01	1.5E-02	1.1E+02	8.8E-03	6.7E+01	1.5E-02
191.0	6.7E+01	1.5E-02	1.1E+02	8.9E-03	6.7E+01	1.5E-02
192.0	6.6E+01	1.5E-02	1.1E+02	8.9E-03	6.6E+01	1.5E-02
193.0	6.6E+01	1.5E-02	1.1E+02	8.9E-03	6.6E+01	1.5E-02
194.0	6.6E+01	1.5E-02	1.1E+02	9.0E-03	6.6E+01	1.5E-02
195.0	6.6E+01	1.5E-02	1.1E+02	9.0E-03	6.6E+01	1.5E-02
196.0	6.6E+01	1.5E-02	1.1E+02	9.0E-03	6.6E+01	1.5E-02
197.0	6.6E+01	1.5E-02	1.1E+02	9.0E-03	6.6E+01	1.5E-02
198.0	6.6E+01	1.5E-02	1.1E+02	9.1E-03	6.6E+01	1.5E-02
199.0	6.5E+01	1.5E-02	1.1E+02	9.1E-03	6.5E+01	1.5E-02
200.0	6.5E+01	1.5E-02	1.1E+02	9.1E-03	6.5E+01	1.5E-02

Table A.6: Hashin-Shtrikman limits calculated for a dry, hydrated, and partially melted upper mantle from my reference model in Chapter 3.

Depth (km)	HSL_{Dry}^{140Ma}		HSL_{Dry}^{33Ma}		HSU_{Dry}^{33Ma}	
	(S/m)	(Ωm)	(S/m)	(Ωm)	(S/m)	(Ωm)
201.0	6.5E+01	1.5E-02	1.1E+02	9.2E-03	6.5E+01	1.5E-02
202.0	6.5E+01	1.5E-02	1.1E+02	9.2E-03	6.5E+01	1.5E-02
203.0	6.5E+01	1.5E-02	1.1E+02	9.2E-03	6.5E+01	1.5E-02
204.0	6.5E+01	1.5E-02	1.1E+02	9.3E-03	6.5E+01	1.5E-02
205.0	6.5E+01	1.5E-02	1.1E+02	9.3E-03	6.5E+01	1.5E-02
206.0	6.5E+01	1.6E-02	1.1E+02	9.3E-03	6.5E+01	1.6E-02
207.0	6.5E+01	1.6E-02	1.1E+02	9.3E-03	6.5E+01	1.6E-02
208.0	6.5E+01	1.6E-02	1.1E+02	9.4E-03	6.5E+01	1.6E-02
209.0	6.4E+01	1.6E-02	1.1E+02	9.4E-03	6.4E+01	1.6E-02
210.0	6.4E+01	1.6E-02	1.1E+02	9.4E-03	6.4E+01	1.6E-02
211.0	6.4E+01	1.6E-02	1.1E+02	9.5E-03	6.4E+01	1.6E-02
212.0	6.4E+01	1.6E-02	1.1E+02	9.5E-03	6.4E+01	1.6E-02
213.0	6.4E+01	1.6E-02	1.1E+02	9.5E-03	6.4E+01	1.6E-02
214.0	6.4E+01	1.6E-02	1.0E+02	9.6E-03	6.4E+01	1.6E-02
215.0	6.4E+01	1.6E-02	1.0E+02	9.6E-03	6.4E+01	1.6E-02
216.0	6.3E+01	1.6E-02	1.0E+02	9.6E-03	6.3E+01	1.6E-02
217.0	6.3E+01	1.6E-02	1.0E+02	9.7E-03	6.3E+01	1.6E-02
218.0	6.3E+01	1.6E-02	1.0E+02	9.7E-03	6.3E+01	1.6E-02
219.0	6.3E+01	1.6E-02	1.0E+02	9.7E-03	6.3E+01	1.6E-02
220.0	6.3E+01	1.6E-02	1.0E+02	9.7E-03	6.3E+01	1.6E-02
221.0	6.3E+01	1.6E-02	1.0E+02	9.8E-03	6.3E+01	1.6E-02
222.0	6.3E+01	1.6E-02	1.0E+02	9.8E-03	6.3E+01	1.6E-02
223.0	6.3E+01	1.6E-02	1.0E+02	9.8E-03	6.3E+01	1.6E-02
224.0	6.3E+01	1.6E-02	1.0E+02	9.9E-03	6.3E+01	1.6E-02
225.0	6.3E+01	1.6E-02	1.0E+02	9.9E-03	6.3E+01	1.6E-02
226.0	6.2E+01	1.6E-02	1.0E+02	9.9E-03	6.2E+01	1.6E-02
227.0	6.2E+01	1.6E-02	1.0E+02	1.0E-02	6.2E+01	1.6E-02
228.0	6.2E+01	1.6E-02	1.0E+02	1.0E-02	6.2E+01	1.6E-02
229.0	6.2E+01	1.6E-02	1.0E+02	1.0E-02	6.2E+01	1.6E-02
230.0	6.2E+01	1.6E-02	9.9E+01	1.0E-02	6.2E+01	1.6E-02
231.0	6.2E+01	1.6E-02	9.9E+01	1.0E-02	6.2E+01	1.6E-02
232.0	6.2E+01	1.6E-02	9.9E+01	1.0E-02	6.2E+01	1.6E-02
233.0	6.1E+01	1.6E-02	9.8E+01	1.0E-02	6.1E+01	1.6E-02
234.0	6.1E+01	1.6E-02	9.8E+01	1.0E-02	6.1E+01	1.6E-02
235.0	6.1E+01	1.6E-02	9.8E+01	1.0E-02	6.1E+01	1.6E-02
236.0	6.1E+01	1.6E-02	9.7E+01	1.0E-02	6.1E+01	1.6E-02
237.0	6.1E+01	1.6E-02	9.7E+01	1.0E-02	6.1E+01	1.6E-02
238.0	6.1E+01	1.6E-02	9.7E+01	1.0E-02	6.1E+01	1.6E-02
239.0	6.1E+01	1.7E-02	9.6E+01	1.0E-02	6.1E+01	1.7E-02
240.0	6.1E+01	1.7E-02	9.6E+01	1.0E-02	6.1E+01	1.7E-02

Table A.7: Hashin-Shtrikman limits calculated for a dry, hydrated, and partially melted upper mantle from my reference model in Chapter 3.

Depth (km)	HSL_{Dry}^{140Ma}		HSL_{Dry}^{33Ma}		HSU_{Dry}^{33Ma}	
	(S/m)	(Ωm)	(S/m)	(Ωm)	(S/m)	(Ωm)
241.0	6.1E+01	1.7E-02	9.6E+01	1.0E-02	6.1E+01	1.7E-02
242.0	6.0E+01	1.7E-02	9.5E+01	1.1E-02	6.0E+01	1.7E-02
243.0	6.0E+01	1.7E-02	9.5E+01	1.1E-02	6.0E+01	1.7E-02
244.0	6.0E+01	1.7E-02	9.5E+01	1.1E-02	6.0E+01	1.7E-02
245.0	6.0E+01	1.7E-02	9.4E+01	1.1E-02	6.0E+01	1.7E-02
246.0	6.0E+01	1.7E-02	9.4E+01	1.1E-02	6.0E+01	1.7E-02
247.0	6.0E+01	1.7E-02	9.4E+01	1.1E-02	6.0E+01	1.7E-02
248.0	6.0E+01	1.7E-02	9.3E+01	1.1E-02	6.0E+01	1.7E-02
249.0	6.0E+01	1.7E-02	9.3E+01	1.1E-02	6.0E+01	1.7E-02
250.0	6.0E+01	1.7E-02	9.3E+01	1.1E-02	6.0E+01	1.7E-02
251.0	6.0E+01	1.7E-02	9.3E+01	1.1E-02	6.0E+01	1.7E-02
252.0	5.9E+01	1.7E-02	9.3E+01	1.1E-02	5.9E+01	1.7E-02
253.0	5.9E+01	1.7E-02	9.3E+01	1.1E-02	5.9E+01	1.7E-02
254.0	5.9E+01	1.7E-02	9.2E+01	1.1E-02	5.9E+01	1.7E-02
255.0	5.9E+01	1.7E-02	9.2E+01	1.1E-02	5.9E+01	1.7E-02
256.0	5.9E+01	1.7E-02	9.2E+01	1.1E-02	5.9E+01	1.7E-02
257.0	5.9E+01	1.7E-02	9.1E+01	1.1E-02	5.9E+01	1.7E-02
258.0	5.8E+01	1.7E-02	9.1E+01	1.1E-02	5.8E+01	1.7E-02
259.0	5.8E+01	1.7E-02	9.0E+01	1.1E-02	5.8E+01	1.7E-02
260.0	5.8E+01	1.7E-02	9.0E+01	1.1E-02	5.8E+01	1.7E-02
261.0	5.8E+01	1.7E-02	9.0E+01	1.1E-02	5.8E+01	1.7E-02
262.0	5.8E+01	1.7E-02	8.9E+01	1.1E-02	5.8E+01	1.7E-02
263.0	5.8E+01	1.7E-02	8.9E+01	1.1E-02	5.8E+01	1.7E-02
264.0	5.8E+01	1.7E-02	8.9E+01	1.1E-02	5.8E+01	1.7E-02
265.0	5.8E+01	1.7E-02	8.8E+01	1.1E-02	5.8E+01	1.7E-02
266.0	5.8E+01	1.7E-02	8.8E+01	1.1E-02	5.8E+01	1.7E-02
267.0	5.7E+01	1.7E-02	8.8E+01	1.1E-02	5.7E+01	1.7E-02
268.0	5.7E+01	1.7E-02	8.8E+01	1.1E-02	5.7E+01	1.7E-02
269.0	5.7E+01	1.7E-02	8.8E+01	1.1E-02	5.7E+01	1.7E-02
270.0	5.7E+01	1.7E-02	8.7E+01	1.2E-02	5.7E+01	1.7E-02
271.0	5.7E+01	1.8E-02	8.7E+01	1.2E-02	5.7E+01	1.8E-02
272.0	5.7E+01	1.8E-02	8.7E+01	1.2E-02	5.7E+01	1.8E-02
273.0	5.7E+01	1.8E-02	8.6E+01	1.2E-02	5.7E+01	1.8E-02
274.0	5.7E+01	1.8E-02	8.6E+01	1.2E-02	5.7E+01	1.8E-02
275.0	5.7E+01	1.8E-02	8.6E+01	1.2E-02	5.7E+01	1.8E-02
276.0	5.7E+01	1.8E-02	8.5E+01	1.2E-02	5.7E+01	1.8E-02
277.0	5.6E+01	1.8E-02	8.5E+01	1.2E-02	5.6E+01	1.8E-02
278.0	5.6E+01	1.8E-02	8.5E+01	1.2E-02	5.6E+01	1.8E-02
279.0	5.6E+01	1.8E-02	8.5E+01	1.2E-02	5.6E+01	1.8E-02
280.0	5.6E+01	1.8E-02	8.5E+01	1.2E-02	5.6E+01	1.8E-02

Table A.8: Hashin-Shtrikman limits calculated for a dry, hydrated, and partially melted upper mantle from my reference model in Chapter 3.

Depth (km)	HSL_{Dry}^{140Ma}		HSL_{Dry}^{33Ma}		HSU_{Dry}^{33Ma}	
	(S/m)	(Ωm)	(S/m)	(Ωm)	(S/m)	(Ωm)
281.0	5.6E+01	1.8E-02	8.4E+01	1.2E-02	5.6E+01	1.8E-02
282.0	5.6E+01	1.8E-02	8.4E+01	1.2E-02	5.6E+01	1.8E-02
283.0	5.6E+01	1.8E-02	8.3E+01	1.2E-02	5.6E+01	1.8E-02
284.0	5.6E+01	1.8E-02	8.3E+01	1.2E-02	5.6E+01	1.8E-02
285.0	5.6E+01	1.8E-02	8.3E+01	1.2E-02	5.6E+01	1.8E-02
286.0	5.6E+01	1.8E-02	8.3E+01	1.2E-02	5.6E+01	1.8E-02
287.0	5.6E+01	1.8E-02	8.3E+01	1.2E-02	5.6E+01	1.8E-02
288.0	5.5E+01	1.8E-02	8.2E+01	1.2E-02	5.5E+01	1.8E-02
289.0	5.5E+01	1.8E-02	8.2E+01	1.2E-02	5.5E+01	1.8E-02
290.0	5.5E+01	1.8E-02	8.2E+01	1.2E-02	5.5E+01	1.8E-02
291.0	5.5E+01	1.8E-02	8.1E+01	1.2E-02	5.5E+01	1.8E-02
292.0	5.5E+01	1.8E-02	8.1E+01	1.2E-02	5.5E+01	1.8E-02
293.0	5.5E+01	1.8E-02	8.1E+01	1.2E-02	5.5E+01	1.8E-02
294.0	5.5E+01	1.8E-02	8.1E+01	1.2E-02	5.5E+01	1.8E-02
295.0	5.5E+01	1.8E-02	8.1E+01	1.2E-02	5.5E+01	1.8E-02
296.0	5.5E+01	1.8E-02	8.0E+01	1.3E-02	5.5E+01	1.8E-02
297.0	5.4E+01	1.8E-02	8.0E+01	1.3E-02	5.4E+01	1.8E-02
298.0	5.4E+01	1.8E-02	7.9E+01	1.3E-02	5.4E+01	1.8E-02
299.0	5.4E+01	1.8E-02	7.9E+01	1.3E-02	5.4E+01	1.8E-02
300.0	5.4E+01	1.9E-02	7.9E+01	1.3E-02	5.4E+01	1.9E-02
301.0	5.4E+01	1.9E-02	7.9E+01	1.3E-02	5.4E+01	1.9E-02
302.0	5.4E+01	1.9E-02	7.9E+01	1.3E-02	5.4E+01	1.9E-02
303.0	5.4E+01	1.9E-02	7.9E+01	1.3E-02	5.4E+01	1.9E-02
304.0	5.4E+01	1.9E-02	7.8E+01	1.3E-02	5.4E+01	1.9E-02
305.0	5.4E+01	1.9E-02	7.8E+01	1.3E-02	5.4E+01	1.9E-02
306.0	5.4E+01	1.9E-02	7.8E+01	1.3E-02	5.4E+01	1.9E-02
307.0	5.4E+01	1.9E-02	7.8E+01	1.3E-02	5.4E+01	1.9E-02
308.0	5.4E+01	1.9E-02	7.8E+01	1.3E-02	5.4E+01	1.9E-02
309.0	5.3E+01	1.9E-02	7.8E+01	1.3E-02	5.3E+01	1.9E-02
310.0	5.3E+01	1.9E-02	7.7E+01	1.3E-02	5.3E+01	1.9E-02
311.0	5.3E+01	1.9E-02	7.7E+01	1.3E-02	5.3E+01	1.9E-02
312.0	5.3E+01	1.9E-02	7.7E+01	1.3E-02	5.3E+01	1.9E-02
313.0	5.3E+01	1.9E-02	7.6E+01	1.3E-02	5.3E+01	1.9E-02
314.0	5.3E+01	1.9E-02	7.6E+01	1.3E-02	5.3E+01	1.9E-02
315.0	5.3E+01	1.9E-02	7.6E+01	1.3E-02	5.3E+01	1.9E-02
316.0	5.3E+01	1.9E-02	7.6E+01	1.3E-02	5.3E+01	1.9E-02
317.0	5.3E+01	1.9E-02	7.6E+01	1.3E-02	5.3E+01	1.9E-02
318.0	5.3E+01	1.9E-02	7.6E+01	1.3E-02	5.3E+01	1.9E-02
319.0	5.3E+01	1.9E-02	7.5E+01	1.3E-02	5.3E+01	1.9E-02
320.0	5.3E+01	1.9E-02	7.5E+01	1.3E-02	5.3E+01	1.9E-02

Table A.9: Hashin-Shtrikman limits calculated for a dry, hydrated, and partially melted upper mantle from my reference model in Chapter 3.

Depth (km)	HSL_{Dry}^{140Ma}		HSL_{Dry}^{33Ma}		HSU_{Dry}^{33Ma}	
	(S/m)	(Ωm)	(S/m)	(Ωm)	(S/m)	(Ωm)
321.0	5.3E+01	1.9E-02	7.5E+01	1.3E-02	5.3E+01	1.9E-02
322.0	5.3E+01	1.9E-02	7.5E+01	1.3E-02	5.3E+01	1.9E-02
323.0	5.3E+01	1.9E-02	7.5E+01	1.3E-02	5.3E+01	1.9E-02
324.0	5.3E+01	1.9E-02	7.5E+01	1.3E-02	5.3E+01	1.9E-02
325.0	5.3E+01	1.9E-02	7.4E+01	1.4E-02	5.3E+01	1.9E-02
326.0	5.3E+01	1.9E-02	7.4E+01	1.4E-02	5.3E+01	1.9E-02
327.0	5.3E+01	1.9E-02	7.4E+01	1.4E-02	5.3E+01	1.9E-02
328.0	5.3E+01	1.9E-02	7.4E+01	1.4E-02	5.3E+01	1.9E-02
329.0	5.3E+01	1.9E-02	7.4E+01	1.4E-02	5.3E+01	1.9E-02
330.0	5.3E+01	1.9E-02	7.4E+01	1.4E-02	5.3E+01	1.9E-02
331.0	5.3E+01	1.9E-02	7.4E+01	1.4E-02	5.3E+01	1.9E-02
332.0	5.3E+01	1.9E-02	7.4E+01	1.4E-02	5.3E+01	1.9E-02
333.0	5.3E+01	1.9E-02	7.3E+01	1.4E-02	5.3E+01	1.9E-02
334.0	5.3E+01	1.9E-02	7.3E+01	1.4E-02	5.3E+01	1.9E-02
335.0	5.3E+01	1.9E-02	7.3E+01	1.4E-02	5.3E+01	1.9E-02
336.0	5.3E+01	1.9E-02	7.3E+01	1.4E-02	5.3E+01	1.9E-02
337.0	5.3E+01	1.9E-02	7.2E+01	1.4E-02	5.3E+01	1.9E-02
338.0	5.3E+01	1.9E-02	7.2E+01	1.4E-02	5.3E+01	1.9E-02
339.0	5.3E+01	1.9E-02	7.2E+01	1.4E-02	5.3E+01	1.9E-02
340.0	5.3E+01	1.9E-02	7.2E+01	1.4E-02	5.3E+01	1.9E-02
341.0	5.3E+01	1.9E-02	7.2E+01	1.4E-02	5.3E+01	1.9E-02
342.0	5.3E+01	1.9E-02	7.2E+01	1.4E-02	5.3E+01	1.9E-02
343.0	5.3E+01	1.9E-02	7.2E+01	1.4E-02	5.3E+01	1.9E-02
344.0	5.3E+01	1.9E-02	7.2E+01	1.4E-02	5.3E+01	1.9E-02
345.0	5.3E+01	1.9E-02	7.2E+01	1.4E-02	5.3E+01	1.9E-02
346.0	5.3E+01	1.9E-02	7.1E+01	1.4E-02	5.3E+01	1.9E-02
347.0	5.3E+01	1.9E-02	7.1E+01	1.4E-02	5.3E+01	1.9E-02
348.0	5.3E+01	1.9E-02	7.1E+01	1.4E-02	5.3E+01	1.9E-02
349.0	5.3E+01	1.9E-02	7.1E+01	1.4E-02	5.3E+01	1.9E-02
350.0	5.3E+01	1.9E-02	7.1E+01	1.4E-02	5.3E+01	1.9E-02
351.0	5.3E+01	1.9E-02	7.1E+01	1.4E-02	5.3E+01	1.9E-02
352.0	5.3E+01	1.9E-02	7.1E+01	1.4E-02	5.3E+01	1.9E-02
353.0	5.3E+01	1.9E-02	7.1E+01	1.4E-02	5.3E+01	1.9E-02
354.0	5.3E+01	1.9E-02	7.1E+01	1.4E-02	5.3E+01	1.9E-02
355.0	5.3E+01	1.9E-02	7.1E+01	1.4E-02	5.3E+01	1.9E-02
356.0	5.3E+01	1.9E-02	7.1E+01	1.4E-02	5.3E+01	1.9E-02
357.0	5.3E+01	1.9E-02	7.0E+01	1.4E-02	5.3E+01	1.9E-02
358.0	5.3E+01	1.9E-02	7.0E+01	1.4E-02	5.3E+01	1.9E-02
359.0	5.3E+01	1.9E-02	7.0E+01	1.4E-02	5.3E+01	1.9E-02
360.0	5.3E+01	1.9E-02	7.0E+01	1.4E-02	5.3E+01	1.9E-02

Table A.10: Hashin-Shtrikman limits calculated for a dry, hydrated, and partially melted upper mantle from my reference model in Chapter 3.

Depth (km)	HSL_{Dry}^{140Ma}		HSL_{Dry}^{33Ma}		HSU_{Dry}^{33Ma}	
	(S/m)	(Ωm)	(S/m)	(Ωm)	(S/m)	(Ωm)
361.0	5.3E+01	1.9E-02	7.0E+01	1.4E-02	5.3E+01	1.9E-02
362.0	5.3E+01	1.9E-02	7.0E+01	1.4E-02	5.3E+01	1.9E-02
363.0	5.3E+01	1.9E-02	7.0E+01	1.4E-02	5.3E+01	1.9E-02
364.0	5.3E+01	1.9E-02	7.0E+01	1.4E-02	5.3E+01	1.9E-02
365.0	5.3E+01	1.9E-02	7.0E+01	1.4E-02	5.3E+01	1.9E-02
366.0	5.3E+01	1.9E-02	7.0E+01	1.4E-02	5.3E+01	1.9E-02
367.0	5.3E+01	1.9E-02	7.0E+01	1.4E-02	5.3E+01	1.9E-02
368.0	5.3E+01	1.9E-02	7.0E+01	1.4E-02	5.3E+01	1.9E-02
369.0	5.3E+01	1.9E-02	7.0E+01	1.4E-02	5.3E+01	1.9E-02
370.0	5.3E+01	1.9E-02	7.0E+01	1.4E-02	5.3E+01	1.9E-02
371.0	5.3E+01	1.9E-02	7.0E+01	1.4E-02	5.3E+01	1.9E-02
372.0	5.3E+01	1.9E-02	7.0E+01	1.4E-02	5.3E+01	1.9E-02
373.0	5.3E+01	1.9E-02	6.9E+01	1.4E-02	5.3E+01	1.9E-02
374.0	5.3E+01	1.9E-02	6.9E+01	1.4E-02	5.3E+01	1.9E-02
375.0	5.4E+01	1.9E-02	6.9E+01	1.4E-02	5.4E+01	1.9E-02
376.0	5.4E+01	1.9E-02	6.9E+01	1.4E-02	5.4E+01	1.9E-02
377.0	5.4E+01	1.9E-02	6.9E+01	1.4E-02	5.4E+01	1.9E-02
378.0	5.4E+01	1.9E-02	6.9E+01	1.4E-02	5.4E+01	1.9E-02
379.0	5.4E+01	1.9E-02	6.9E+01	1.4E-02	5.4E+01	1.9E-02
380.0	5.4E+01	1.9E-02	6.9E+01	1.4E-02	5.4E+01	1.9E-02
381.0	5.4E+01	1.9E-02	6.9E+01	1.4E-02	5.4E+01	1.9E-02
382.0	5.4E+01	1.9E-02	6.9E+01	1.5E-02	5.4E+01	1.9E-02
383.0	5.4E+01	1.9E-02	6.9E+01	1.5E-02	5.4E+01	1.9E-02
384.0	5.4E+01	1.9E-02	6.9E+01	1.5E-02	5.4E+01	1.9E-02
385.0	5.4E+01	1.9E-02	6.9E+01	1.5E-02	5.4E+01	1.9E-02
386.0	5.4E+01	1.9E-02	6.9E+01	1.5E-02	5.4E+01	1.9E-02
387.0	5.4E+01	1.8E-02	6.9E+01	1.5E-02	5.4E+01	1.8E-02
388.0	5.4E+01	1.8E-02	6.9E+01	1.5E-02	5.4E+01	1.8E-02
389.0	5.4E+01	1.8E-02	6.9E+01	1.5E-02	5.4E+01	1.8E-02
390.0	5.4E+01	1.8E-02	6.8E+01	1.5E-02	5.4E+01	1.8E-02
391.0	5.4E+01	1.8E-02	6.8E+01	1.5E-02	5.4E+01	1.8E-02
392.0	5.4E+01	1.8E-02	6.8E+01	1.5E-02	5.4E+01	1.8E-02
393.0	5.5E+01	1.8E-02	6.8E+01	1.5E-02	5.5E+01	1.8E-02
394.0	5.5E+01	1.8E-02	6.8E+01	1.5E-02	5.5E+01	1.8E-02
395.0	5.5E+01	1.8E-02	6.8E+01	1.5E-02	5.5E+01	1.8E-02
396.0	5.5E+01	1.8E-02	6.8E+01	1.5E-02	5.5E+01	1.8E-02
397.0	5.5E+01	1.8E-02	6.8E+01	1.5E-02	5.5E+01	1.8E-02
398.0	5.5E+01	1.8E-02	6.8E+01	1.5E-02	5.5E+01	1.8E-02
399.0	5.5E+01	1.8E-02	6.8E+01	1.5E-02	5.5E+01	1.8E-02
400.0	5.5E+01	1.8E-02	6.8E+01	1.5E-02	5.5E+01	1.8E-02

Table A.11: Hashin-Shtrikman limits calculated for a dry, hydrated, and partially melted upper mantle from my reference model in Chapter 3.

Depth (km)	HSL^{33Ma}_{Wet}		HSU^{33Ma}_{Wet}		HSU^{1Ma}_{Melt}	
	(S/m)	(Ωm)	(S/m)	(Ωm)	(S/m)	(Ωm)
1.0	1.5E+14	6.9E-15	1.1E+12	8.9E-13	1.1E+12	8.9E-13
2.0	8.7E+12	1.2E-13	8.9E+10	1.1E-11	3.1E+07	3.2E-08
3.0	7.9E+11	1.3E-12	1.0E+10	9.6E-11	1.8E+05	5.6E-06
4.0	1.0E+11	9.9E-12	1.6E+09	6.1E-10	8.5E+03	1.2E-04
5.0	1.7E+10	5.9E-11	3.3E+08	3.0E-09	1.2E+03	8.5E-04
6.0	3.5E+09	2.8E-10	8.1E+07	1.2E-08	3.0E+02	3.3E-03
7.0	8.8E+08	1.1E-09	2.3E+07	4.3E-08	1.1E+02	8.8E-03
8.0	2.6E+08	3.9E-09	7.6E+06	1.3E-07	5.5E+01	1.8E-02
9.0	8.5E+07	1.2E-08	2.8E+06	3.5E-07	3.2E+01	3.2E-02
10.0	3.2E+07	3.2E-08	1.2E+06	8.6E-07	7.8E-02	1.3E+01
11.0	1.3E+07	7.8E-08	5.2E+05	1.9E-06	1.8E-07	5.7E+06
12.0	5.7E+06	1.8E-07	2.5E+05	4.0E-06	7.9E-08	1.3E+07
13.0	2.7E+06	3.7E-07	1.3E+05	7.9E-06	1.2E-01	8.0E+00
14.0	1.4E+06	7.2E-07	6.9E+04	1.5E-05	1.2E-01	8.6E+00
15.0	7.4E+05	1.4E-06	3.9E+04	2.5E-05	1.1E-01	9.0E+00
16.0	4.2E+05	2.4E-06	2.4E+04	4.3E-05	1.1E-01	9.4E+00
17.0	2.5E+05	4.1E-06	1.5E+04	6.9E-05	1.0E-01	9.6E+00
18.0	1.5E+05	6.6E-06	9.3E+03	1.1E-04	1.0E-01	9.8E+00
19.0	9.6E+04	1.0E-05	6.2E+03	1.6E-04	1.0E-01	1.0E+01
20.0	6.3E+04	1.6E-05	4.3E+03	2.4E-04	9.9E-02	1.0E+01
21.0	4.2E+04	2.4E-05	3.0E+03	3.4E-04	9.8E-02	1.0E+01
22.0	2.9E+04	3.4E-05	2.1E+03	4.7E-04	9.8E-02	1.0E+01
23.0	2.1E+04	4.8E-05	1.6E+03	6.4E-04	9.7E-02	1.0E+01
24.0	1.5E+04	6.6E-05	1.2E+03	8.5E-04	9.7E-02	1.0E+01
25.0	1.1E+04	9.0E-05	8.9E+02	1.1E-03	9.7E-02	1.0E+01
26.0	8.4E+03	1.2E-04	6.9E+02	1.5E-03	9.7E-02	1.0E+01
27.0	6.5E+03	1.6E-04	5.4E+02	1.8E-03	9.7E-02	1.0E+01
28.0	5.0E+03	2.0E-04	4.3E+02	2.3E-03	9.6E-02	1.0E+01
29.0	4.0E+03	2.5E-04	3.5E+02	2.9E-03	9.6E-02	1.0E+01
30.0	3.2E+03	3.2E-04	2.9E+02	3.5E-03	9.6E-02	1.0E+01
31.0	2.6E+03	3.9E-04	2.4E+02	4.2E-03	9.6E-02	1.0E+01
32.0	2.1E+03	4.8E-04	2.0E+02	5.1E-03	9.6E-02	1.0E+01
33.0	1.7E+03	5.8E-04	1.7E+02	6.0E-03	9.6E-02	1.0E+01
34.0	1.4E+03	6.9E-04	1.4E+02	7.1E-03	9.6E-02	1.0E+01
35.0	1.2E+03	8.2E-04	1.2E+02	8.2E-03	9.6E-02	1.0E+01
36.0	1.0E+03	9.7E-04	1.1E+02	9.5E-03	9.6E-02	1.0E+01
37.0	8.8E+02	1.1E-03	9.2E+01	1.1E-02	9.6E-02	1.0E+01
38.0	7.6E+02	1.3E-03	8.0E+01	1.3E-02	9.6E-02	1.0E+01
39.0	6.7E+02	1.5E-03	7.1E+01	1.4E-02	9.6E-02	1.0E+01
40.0	5.8E+02	1.7E-03	6.3E+01	1.6E-02	9.6E-02	1.0E+01

Table A.12: Hashin-Shtrikman limits calculated for a dry, hydrated, and partially melted upper mantle from my reference model in Chapter 3.

Depth (km)	HSL^{33Ma}_{Wet}		HSU^{33Ma}_{Wet}		HSU^{1Ma}_{Melt}	
	(S/m)	(Ωm)	(S/m)	(Ωm)	(S/m)	(Ωm)
41.0	5.1E+02	2.0E-03	5.6E+01	1.8E-02	9.6E-02	1.0E+01
42.0	4.5E+02	2.2E-03	5.1E+01	2.0E-02	9.6E-02	1.0E+01
43.0	4.0E+02	2.5E-03	4.5E+01	2.2E-02	9.6E-02	1.0E+01
44.0	3.6E+02	2.8E-03	4.1E+01	2.4E-02	9.6E-02	1.0E+01
45.0	3.3E+02	3.1E-03	3.8E+01	2.7E-02	9.6E-02	1.0E+01
46.0	2.9E+02	3.4E-03	3.4E+01	2.9E-02	9.6E-02	1.0E+01
47.0	2.7E+02	3.7E-03	3.2E+01	3.2E-02	9.6E-02	1.0E+01
48.0	2.4E+02	4.1E-03	2.9E+01	3.4E-02	9.6E-02	1.0E+01
49.0	2.2E+02	4.5E-03	2.7E+01	3.7E-02	9.6E-02	1.0E+01
50.0	2.1E+02	4.9E-03	2.5E+01	4.0E-02	9.6E-02	1.0E+01
51.0	1.9E+02	5.3E-03	2.3E+01	4.3E-02	9.6E-02	1.0E+01
52.0	1.8E+02	5.7E-03	2.2E+01	4.6E-02	9.6E-02	1.0E+01
53.0	1.6E+02	6.1E-03	2.0E+01	4.9E-02	9.6E-02	1.0E+01
54.0	1.5E+02	6.6E-03	1.9E+01	5.2E-02	9.6E-02	1.0E+01
55.0	1.4E+02	7.1E-03	1.8E+01	5.5E-02	9.6E-02	1.0E+01
56.0	1.3E+02	7.6E-03	1.7E+01	5.8E-02	9.6E-02	1.0E+01
57.0	1.2E+02	8.1E-03	1.6E+01	6.2E-02	9.6E-02	1.0E+01
58.0	1.2E+02	8.6E-03	1.5E+01	6.5E-02	9.6E-02	1.0E+01
59.0	1.1E+02	9.2E-03	1.5E+01	6.8E-02	9.6E-02	1.0E+01
60.0	1.0E+02	9.7E-03	1.4E+01	7.1E-02	9.6E-02	1.0E+01
61.0	9.8E+01	1.0E-02	1.3E+01	7.5E-02	9.6E-02	1.0E+01
62.0	9.3E+01	1.1E-02	1.3E+01	7.8E-02	9.7E-02	1.0E+01
63.0	8.8E+01	1.1E-02	1.2E+01	8.1E-02	9.8E-02	1.0E+01
64.0	8.4E+01	1.2E-02	1.2E+01	8.4E-02	1.0E-01	1.0E+01
65.0	8.0E+01	1.3E-02	1.1E+01	8.8E-02	1.0E-01	9.9E+00
66.0	7.7E+01	1.3E-02	1.1E+01	9.1E-02	1.0E-01	9.7E+00
67.0	7.4E+01	1.4E-02	1.1E+01	9.4E-02	1.1E-01	9.4E+00
68.0	9.3E+01	1.1E-02	1.1E+01	9.4E-02	1.1E-01	9.2E+00
69.0	8.9E+01	1.1E-02	1.0E+01	9.8E-02	1.1E-01	8.9E+00
70.0	8.5E+01	1.2E-02	9.7E+00	1.0E-01	1.3E-01	7.9E+00
71.0	8.2E+01	1.2E-02	9.3E+00	1.1E-01	1.4E-01	7.0E+00
72.0	7.9E+01	1.3E-02	9.0E+00	1.1E-01	1.6E-01	6.2E+00
73.0	7.6E+01	1.3E-02	8.6E+00	1.2E-01	1.9E-01	5.3E+00
74.0	7.2E+01	1.4E-02	8.3E+00	1.2E-01	2.2E-01	4.6E+00
75.0	7.0E+01	1.4E-02	8.0E+00	1.3E-01	2.6E-01	3.9E+00
76.0	6.8E+01	1.5E-02	7.8E+00	1.3E-01	3.1E-01	3.3E+00
77.0	6.5E+01	1.5E-02	7.5E+00	1.3E-01	3.8E-01	2.7E+00
78.0	6.3E+01	1.6E-02	7.2E+00	1.4E-01	4.8E-01	2.1E+00
79.0	6.1E+01	1.6E-02	7.0E+00	1.4E-01	6.3E-01	1.6E+00
80.0	6.0E+01	1.7E-02	6.8E+00	1.5E-01	8.9E-01	1.1E+00

Table A.13: Hashin-Shtrikman limits calculated for a dry, hydrated, and partially melted upper mantle from my reference model in Chapter 3.

Depth (km)	HSL^{33Ma}_{Wet}		HSU^{33Ma}_{Wet}		HSU^{1Ma}_{Melt}	
	(S/m)	(Ωm)	(S/m)	(Ωm)	(S/m)	(Ωm)
81.0	5.8E+01	1.7E-02	6.6E+00	1.5E-01	1.4E+00	6.9E-01
82.0	5.6E+01	1.8E-02	6.5E+00	1.6E-01	3.4E+00	3.0E-01
83.0	5.5E+01	1.8E-02	6.3E+00	1.6E-01	4.1E+00	2.4E-01
84.0	5.3E+01	1.9E-02	6.1E+00	1.6E-01	4.2E+00	2.4E-01
85.0	5.2E+01	1.9E-02	6.0E+00	1.7E-01	4.2E+00	2.4E-01
86.0	5.1E+01	2.0E-02	5.8E+00	1.7E-01	4.2E+00	2.4E-01
87.0	5.0E+01	2.0E-02	5.7E+00	1.8E-01	4.2E+00	2.4E-01
88.0	4.9E+01	2.1E-02	5.5E+00	1.8E-01	4.2E+00	2.4E-01
89.0	4.8E+01	2.1E-02	5.4E+00	1.9E-01	4.2E+00	2.4E-01
90.0	4.7E+01	2.1E-02	5.3E+00	1.9E-01	4.2E+00	2.4E-01
91.0	4.6E+01	2.2E-02	5.2E+00	1.9E-01	4.2E+00	2.4E-01
92.0	4.5E+01	2.2E-02	5.1E+00	2.0E-01	4.1E+00	2.4E-01
93.0	4.4E+01	2.3E-02	5.0E+00	2.0E-01	4.1E+00	2.4E-01
94.0	4.3E+01	2.3E-02	4.9E+00	2.1E-01	4.1E+00	2.4E-01
95.0	4.3E+01	2.3E-02	4.8E+00	2.1E-01	4.1E+00	2.5E-01
96.0	4.2E+01	2.4E-02	4.7E+00	2.1E-01	4.0E+00	2.5E-01
97.0	4.1E+01	2.4E-02	4.6E+00	2.2E-01	4.0E+00	2.5E-01
98.0	4.1E+01	2.5E-02	4.5E+00	2.2E-01	4.0E+00	2.5E-01
99.0	4.0E+01	2.5E-02	4.5E+00	2.2E-01	4.0E+00	2.5E-01
100.0	4.0E+01	2.5E-02	4.4E+00	2.3E-01	3.9E+00	2.6E-01
101.0	3.9E+01	2.6E-02	4.3E+00	2.3E-01	3.9E+00	2.6E-01
102.0	3.9E+01	2.6E-02	4.3E+00	2.3E-01	3.9E+00	2.6E-01
103.0	3.9E+01	2.6E-02	4.3E+00	2.3E-01	3.9E+00	2.6E-01
104.0	3.8E+01	2.6E-02	4.2E+00	2.4E-01	3.9E+00	2.6E-01
105.0	3.8E+01	2.6E-02	4.2E+00	2.4E-01	3.9E+00	2.6E-01
106.0	3.8E+01	2.7E-02	4.2E+00	2.4E-01	3.9E+00	2.6E-01
107.0	3.7E+01	2.7E-02	4.2E+00	2.4E-01	3.9E+00	2.6E-01
108.0	3.7E+01	2.7E-02	4.1E+00	2.4E-01	3.9E+00	2.6E-01
109.0	3.7E+01	2.7E-02	4.1E+00	2.4E-01	3.9E+00	2.6E-01
110.0	3.7E+01	2.7E-02	4.1E+00	2.4E-01	3.9E+00	2.6E-01
111.0	3.7E+01	2.7E-02	4.1E+00	2.4E-01	3.9E+00	2.6E-01
112.0	3.6E+01	2.7E-02	4.1E+00	2.5E-01	3.9E+00	2.6E-01
113.0	3.6E+01	2.8E-02	4.1E+00	2.5E-01	3.9E+00	2.6E-01
114.0	3.6E+01	2.8E-02	4.0E+00	2.5E-01	3.9E+00	2.6E-01
115.0	3.6E+01	2.8E-02	4.0E+00	2.5E-01	3.9E+00	2.6E-01
116.0	3.6E+01	2.8E-02	4.0E+00	2.5E-01	3.9E+00	2.6E-01
117.0	3.6E+01	2.8E-02	4.0E+00	2.5E-01	3.9E+00	2.6E-01
118.0	3.6E+01	2.8E-02	4.0E+00	2.5E-01	3.9E+00	2.6E-01
119.0	3.5E+01	2.8E-02	4.0E+00	2.5E-01	3.9E+00	2.6E-01
120.0	3.5E+01	2.8E-02	4.0E+00	2.5E-01	3.9E+00	2.6E-01

Table A.14: Hashin-Shtrikman limits calculated for a dry, hydrated, and partially melted upper mantle from my reference model in Chapter 3.

Depth (km)	HSL^{33Ma}_{Wet}		HSU^{33Ma}_{Wet}		HSU^{1Ma}_{Melt}	
	(S/m)	(Ωm)	(S/m)	(Ωm)	(S/m)	(Ωm)
121.0	3.5E+01	2.8E-02	4.0E+00	2.5E-01	3.9E+00	2.6E-01
122.0	3.5E+01	2.8E-02	3.9E+00	2.5E-01	3.9E+00	2.6E-01
123.0	3.5E+01	2.9E-02	3.9E+00	2.5E-01	3.8E+00	2.6E-01
124.0	3.5E+01	2.9E-02	3.9E+00	2.6E-01	3.8E+00	2.6E-01
125.0	3.5E+01	2.9E-02	3.9E+00	2.6E-01	3.8E+00	2.6E-01
126.0	3.5E+01	2.9E-02	3.9E+00	2.6E-01	3.8E+00	2.6E-01
127.0	3.5E+01	2.9E-02	3.9E+00	2.6E-01	3.8E+00	2.6E-01
128.0	3.5E+01	2.9E-02	3.9E+00	2.6E-01	3.8E+00	2.6E-01
129.0	3.5E+01	2.9E-02	3.9E+00	2.6E-01	3.8E+00	2.6E-01
130.0	3.5E+01	2.9E-02	3.9E+00	2.6E-01	3.8E+00	2.6E-01
131.0	3.4E+01	2.9E-02	3.9E+00	2.6E-01	3.8E+00	2.6E-01
132.0	3.4E+01	2.9E-02	3.9E+00	2.6E-01	3.8E+00	2.6E-01
133.0	3.4E+01	2.9E-02	3.8E+00	2.6E-01	3.8E+00	2.6E-01
134.0	3.4E+01	2.9E-02	3.8E+00	2.6E-01	3.8E+00	2.6E-01
135.0	3.4E+01	2.9E-02	3.8E+00	2.6E-01	3.8E+00	2.6E-01
136.0	3.4E+01	2.9E-02	3.8E+00	2.6E-01	3.8E+00	2.6E-01
137.0	3.4E+01	2.9E-02	3.8E+00	2.6E-01	3.8E+00	2.6E-01
138.0	3.4E+01	2.9E-02	3.8E+00	2.6E-01	3.8E+00	2.6E-01
139.0	3.4E+01	2.9E-02	3.8E+00	2.6E-01	3.8E+00	2.6E-01
140.0	3.4E+01	2.9E-02	3.8E+00	2.6E-01	3.8E+00	2.6E-01
141.0	3.4E+01	2.9E-02	3.8E+00	2.6E-01	3.8E+00	2.6E-01
142.0	3.4E+01	2.9E-02	3.8E+00	2.6E-01	3.8E+00	2.6E-01
143.0	3.4E+01	2.9E-02	3.8E+00	2.7E-01	3.8E+00	2.7E-01
144.0	3.4E+01	3.0E-02	3.8E+00	2.7E-01	3.8E+00	2.7E-01
145.0	3.4E+01	3.0E-02	3.8E+00	2.7E-01	3.8E+00	2.7E-01
146.0	3.4E+01	3.0E-02	3.8E+00	2.7E-01	3.8E+00	2.7E-01
147.0	3.4E+01	3.0E-02	3.7E+00	2.7E-01	3.7E+00	2.7E-01
148.0	3.4E+01	3.0E-02	3.7E+00	2.7E-01	3.7E+00	2.7E-01
149.0	3.4E+01	3.0E-02	3.7E+00	2.7E-01	3.7E+00	2.7E-01
150.0	3.4E+01	3.0E-02	3.7E+00	2.7E-01	3.7E+00	2.7E-01
151.0	3.4E+01	3.0E-02	3.7E+00	2.7E-01	3.7E+00	2.7E-01
152.0	3.4E+01	3.0E-02	3.7E+00	2.7E-01	3.7E+00	2.7E-01
153.0	3.4E+01	3.0E-02	3.7E+00	2.7E-01	3.7E+00	2.7E-01
154.0	3.3E+01	3.0E-02	3.7E+00	2.7E-01	3.7E+00	2.7E-01
155.0	3.3E+01	3.0E-02	3.7E+00	2.7E-01	3.7E+00	2.7E-01
156.0	3.3E+01	3.0E-02	3.7E+00	2.7E-01	3.7E+00	2.7E-01
157.0	3.3E+01	3.0E-02	3.7E+00	2.7E-01	3.7E+00	2.7E-01
158.0	3.3E+01	3.0E-02	3.7E+00	2.7E-01	3.7E+00	2.7E-01
159.0	3.3E+01	3.0E-02	3.7E+00	2.7E-01	3.7E+00	2.7E-01
160.0	3.3E+01	3.0E-02	3.7E+00	2.7E-01	3.7E+00	2.7E-01

Table A.15: Hashin-Shtrikman limits calculated for a dry, hydrated, and partially melted upper mantle from my reference model in Chapter 3.

Depth (km)	HSL^{33Ma}_{Wet}		HSU^{33Ma}_{Wet}		HSU^{1Ma}_{Melt}	
	(S/m)	(Ωm)	(S/m)	(Ωm)	(S/m)	(Ωm)
161.0	3.3E+01	3.0E-02	3.7E+00	2.7E-01	3.7E+00	2.7E-01
162.0	3.3E+01	3.0E-02	3.7E+00	2.7E-01	3.7E+00	2.7E-01
163.0	3.3E+01	3.0E-02	3.7E+00	2.7E-01	3.7E+00	2.7E-01
164.0	3.3E+01	3.0E-02	3.7E+00	2.7E-01	3.7E+00	2.7E-01
165.0	3.3E+01	3.0E-02	3.7E+00	2.7E-01	3.7E+00	2.7E-01
166.0	3.3E+01	3.0E-02	3.7E+00	2.7E-01	3.7E+00	2.7E-01
167.0	3.3E+01	3.1E-02	3.7E+00	2.7E-01	3.7E+00	2.7E-01
168.0	3.3E+01	3.1E-02	3.7E+00	2.7E-01	3.7E+00	2.7E-01
169.0	3.3E+01	3.1E-02	3.6E+00	2.7E-01	3.6E+00	2.7E-01
170.0	3.3E+01	3.1E-02	3.6E+00	2.7E-01	3.6E+00	2.7E-01
171.0	3.3E+01	3.1E-02	3.6E+00	2.7E-01	3.6E+00	2.7E-01
172.0	3.3E+01	3.1E-02	3.6E+00	2.7E-01	3.6E+00	2.7E-01
173.0	3.3E+01	3.1E-02	3.6E+00	2.8E-01	3.6E+00	2.8E-01
174.0	3.2E+01	3.1E-02	3.6E+00	2.8E-01	3.6E+00	2.8E-01
175.0	3.2E+01	3.1E-02	3.6E+00	2.8E-01	3.6E+00	2.8E-01
176.0	3.2E+01	3.1E-02	3.6E+00	2.8E-01	3.6E+00	2.8E-01
177.0	3.2E+01	3.1E-02	3.6E+00	2.8E-01	3.6E+00	2.8E-01
178.0	3.2E+01	3.1E-02	3.6E+00	2.8E-01	3.6E+00	2.8E-01
179.0	3.2E+01	3.1E-02	3.6E+00	2.8E-01	3.6E+00	2.8E-01
180.0	3.2E+01	3.1E-02	3.6E+00	2.8E-01	3.6E+00	2.8E-01
181.0	3.2E+01	3.1E-02	3.6E+00	2.8E-01	3.6E+00	2.8E-01
182.0	3.2E+01	3.1E-02	3.6E+00	2.8E-01	3.6E+00	2.8E-01
183.0	3.2E+01	3.1E-02	3.6E+00	2.8E-01	3.6E+00	2.8E-01
184.0	3.2E+01	3.1E-02	3.6E+00	2.8E-01	3.6E+00	2.8E-01
185.0	3.2E+01	3.1E-02	3.6E+00	2.8E-01	3.6E+00	2.8E-01
186.0	3.2E+01	3.1E-02	3.6E+00	2.8E-01	3.6E+00	2.8E-01
187.0	3.2E+01	3.1E-02	3.6E+00	2.8E-01	3.6E+00	2.8E-01
188.0	3.2E+01	3.1E-02	3.6E+00	2.8E-01	3.6E+00	2.8E-01
189.0	3.2E+01	3.2E-02	3.6E+00	2.8E-01	3.6E+00	2.8E-01
190.0	3.2E+01	3.2E-02	3.6E+00	2.8E-01	3.6E+00	2.8E-01
191.0	3.2E+01	3.2E-02	3.6E+00	2.8E-01	3.6E+00	2.8E-01
192.0	3.2E+01	3.2E-02	3.6E+00	2.8E-01	3.6E+00	2.8E-01
193.0	3.2E+01	3.2E-02	3.6E+00	2.8E-01	3.6E+00	2.8E-01
194.0	3.2E+01	3.2E-02	3.6E+00	2.8E-01	3.6E+00	2.8E-01
195.0	3.1E+01	3.2E-02	3.6E+00	2.8E-01	3.6E+00	2.8E-01
196.0	3.1E+01	3.2E-02	3.6E+00	2.8E-01	3.6E+00	2.8E-01
197.0	3.1E+01	3.2E-02	3.5E+00	2.8E-01	3.5E+00	2.8E-01
198.0	3.1E+01	3.2E-02	3.5E+00	2.8E-01	3.5E+00	2.8E-01
199.0	3.1E+01	3.2E-02	3.5E+00	2.8E-01	3.5E+00	2.8E-01
200.0	3.1E+01	3.2E-02	3.5E+00	2.8E-01	3.5E+00	2.8E-01

Table A.16: Hashin-Shtrikman limits calculated for a dry, hydrated, and partially melted upper mantle from my reference model in Chapter 3.

Depth (km)	HSL^{33Ma}_{Wet}		HSU^{33Ma}_{Wet}		HSU^{1Ma}_{Melt}	
	(S/m)	(Ωm)	(S/m)	(Ωm)	(S/m)	(Ωm)
201.0	3.1E+01	3.2E-02	3.5E+00	2.8E-01	3.5E+00	2.8E-01
202.0	3.1E+01	3.2E-02	3.5E+00	2.8E-01	3.5E+00	2.8E-01
203.0	3.1E+01	3.2E-02	3.5E+00	2.8E-01	3.5E+00	2.8E-01
204.0	3.1E+01	3.2E-02	3.5E+00	2.8E-01	3.5E+00	2.8E-01
205.0	3.1E+01	3.2E-02	3.5E+00	2.8E-01	3.5E+00	2.8E-01
206.0	3.1E+01	3.2E-02	3.5E+00	2.8E-01	3.5E+00	2.8E-01
207.0	3.1E+01	3.2E-02	3.5E+00	2.8E-01	3.5E+00	2.8E-01
208.0	3.1E+01	3.2E-02	3.5E+00	2.9E-01	3.5E+00	2.9E-01
209.0	3.1E+01	3.3E-02	3.5E+00	2.9E-01	3.5E+00	2.9E-01
210.0	3.1E+01	3.3E-02	3.5E+00	2.9E-01	3.5E+00	2.9E-01
211.0	3.1E+01	3.3E-02	3.5E+00	2.9E-01	3.5E+00	2.9E-01
212.0	3.1E+01	3.3E-02	3.5E+00	2.9E-01	3.5E+00	2.9E-01
213.0	3.1E+01	3.3E-02	3.5E+00	2.9E-01	3.5E+00	2.9E-01
214.0	3.1E+01	3.3E-02	3.5E+00	2.9E-01	3.5E+00	2.9E-01
215.0	3.0E+01	3.3E-02	3.5E+00	2.9E-01	3.5E+00	2.9E-01
216.0	3.0E+01	3.3E-02	3.5E+00	2.9E-01	3.5E+00	2.9E-01
217.0	3.0E+01	3.3E-02	3.5E+00	2.9E-01	3.5E+00	2.9E-01
218.0	3.0E+01	3.3E-02	3.5E+00	2.9E-01	3.5E+00	2.9E-01
219.0	3.0E+01	3.3E-02	3.5E+00	2.9E-01	3.5E+00	2.9E-01
220.0	3.0E+01	3.3E-02	3.5E+00	2.9E-01	3.5E+00	2.9E-01
221.0	3.0E+01	3.3E-02	3.5E+00	2.9E-01	3.5E+00	2.9E-01
222.0	3.0E+01	3.3E-02	3.5E+00	2.9E-01	3.5E+00	2.9E-01
223.0	3.0E+01	3.3E-02	3.5E+00	2.9E-01	3.5E+00	2.9E-01
224.0	3.0E+01	3.3E-02	3.4E+00	2.9E-01	3.4E+00	2.9E-01
225.0	3.0E+01	3.3E-02	3.4E+00	2.9E-01	3.4E+00	2.9E-01
226.0	3.0E+01	3.3E-02	3.4E+00	2.9E-01	3.4E+00	2.9E-01
227.0	3.0E+01	3.3E-02	3.4E+00	2.9E-01	3.4E+00	2.9E-01
228.0	3.0E+01	3.3E-02	3.4E+00	2.9E-01	3.4E+00	2.9E-01
229.0	3.0E+01	3.4E-02	3.4E+00	2.9E-01	3.4E+00	2.9E-01
230.0	3.0E+01	3.4E-02	3.4E+00	2.9E-01	3.4E+00	2.9E-01
231.0	3.0E+01	3.4E-02	3.4E+00	2.9E-01	3.4E+00	2.9E-01
232.0	3.0E+01	3.4E-02	3.4E+00	2.9E-01	3.4E+00	2.9E-01
233.0	3.0E+01	3.4E-02	3.4E+00	2.9E-01	3.4E+00	2.9E-01
234.0	3.0E+01	3.4E-02	3.4E+00	2.9E-01	3.4E+00	2.9E-01
235.0	3.0E+01	3.4E-02	3.4E+00	2.9E-01	3.4E+00	2.9E-01
236.0	3.0E+01	3.4E-02	3.4E+00	2.9E-01	3.4E+00	2.9E-01
237.0	2.9E+01	3.4E-02	3.4E+00	2.9E-01	3.4E+00	2.9E-01
238.0	2.9E+01	3.4E-02	3.4E+00	2.9E-01	3.4E+00	2.9E-01
239.0	2.9E+01	3.4E-02	3.4E+00	2.9E-01	3.4E+00	2.9E-01
240.0	2.9E+01	3.4E-02	3.4E+00	2.9E-01	3.4E+00	2.9E-01

Table A.17: Hashin-Shtrikman limits calculated for a dry, hydrated, and partially melted upper mantle from my reference model in Chapter 3.

Depth (km)	HSL^{33Ma}_{Wet}		HSU^{33Ma}_{Wet}		HSU^{1Ma}_{Melt}	
	(S/m)	(Ωm)	(S/m)	(Ωm)	(S/m)	(Ωm)
241.0	2.9E+01	3.4E-02	3.4E+00	3.0E-01	3.4E+00	3.0E-01
242.0	2.9E+01	3.4E-02	3.4E+00	3.0E-01	3.4E+00	3.0E-01
243.0	2.9E+01	3.4E-02	3.4E+00	3.0E-01	3.4E+00	3.0E-01
244.0	2.9E+01	3.4E-02	3.4E+00	3.0E-01	3.4E+00	3.0E-01
245.0	2.9E+01	3.4E-02	3.4E+00	3.0E-01	3.4E+00	3.0E-01
246.0	2.9E+01	3.4E-02	3.4E+00	3.0E-01	3.4E+00	3.0E-01
247.0	2.9E+01	3.4E-02	3.4E+00	3.0E-01	3.4E+00	3.0E-01
248.0	2.9E+01	3.4E-02	3.4E+00	3.0E-01	3.4E+00	3.0E-01
249.0	2.9E+01	3.5E-02	3.4E+00	3.0E-01	3.4E+00	3.0E-01
250.0	2.9E+01	3.5E-02	3.4E+00	3.0E-01	3.4E+00	3.0E-01
251.0	2.9E+01	3.5E-02	3.4E+00	3.0E-01	3.4E+00	3.0E-01
252.0	2.9E+01	3.5E-02	3.4E+00	3.0E-01	3.4E+00	3.0E-01
253.0	2.9E+01	3.5E-02	3.4E+00	3.0E-01	3.4E+00	3.0E-01
254.0	2.9E+01	3.5E-02	3.3E+00	3.0E-01	3.3E+00	3.0E-01
255.0	2.9E+01	3.5E-02	3.3E+00	3.0E-01	3.3E+00	3.0E-01
256.0	2.9E+01	3.5E-02	3.3E+00	3.0E-01	3.3E+00	3.0E-01
257.0	2.9E+01	3.5E-02	3.3E+00	3.0E-01	3.3E+00	3.0E-01
258.0	2.9E+01	3.5E-02	3.3E+00	3.0E-01	3.3E+00	3.0E-01
259.0	2.9E+01	3.5E-02	3.3E+00	3.0E-01	3.3E+00	3.0E-01
260.0	2.8E+01	3.5E-02	3.3E+00	3.0E-01	3.3E+00	3.0E-01
261.0	2.8E+01	3.5E-02	3.3E+00	3.0E-01	3.3E+00	3.0E-01
262.0	2.8E+01	3.5E-02	3.3E+00	3.0E-01	3.3E+00	3.0E-01
263.0	2.8E+01	3.5E-02	3.3E+00	3.0E-01	3.3E+00	3.0E-01
264.0	2.8E+01	3.5E-02	3.3E+00	3.0E-01	3.3E+00	3.0E-01
265.0	2.8E+01	3.5E-02	3.3E+00	3.0E-01	3.3E+00	3.0E-01
266.0	2.8E+01	3.5E-02	3.3E+00	3.0E-01	3.3E+00	3.0E-01
267.0	2.8E+01	3.6E-02	3.3E+00	3.0E-01	3.3E+00	3.0E-01
268.0	2.8E+01	3.6E-02	3.3E+00	3.0E-01	3.3E+00	3.0E-01
269.0	2.8E+01	3.6E-02	3.3E+00	3.0E-01	3.3E+00	3.0E-01
270.0	2.8E+01	3.6E-02	3.3E+00	3.0E-01	3.3E+00	3.0E-01
271.0	2.8E+01	3.6E-02	3.3E+00	3.0E-01	3.3E+00	3.0E-01
272.0	2.8E+01	3.6E-02	3.3E+00	3.0E-01	3.3E+00	3.0E-01
273.0	2.8E+01	3.6E-02	3.3E+00	3.0E-01	3.3E+00	3.0E-01
274.0	2.8E+01	3.6E-02	3.3E+00	3.1E-01	3.3E+00	3.1E-01
275.0	2.8E+01	3.6E-02	3.3E+00	3.1E-01	3.3E+00	3.1E-01
276.0	2.8E+01	3.6E-02	3.3E+00	3.1E-01	3.3E+00	3.1E-01
277.0	2.8E+01	3.6E-02	3.3E+00	3.1E-01	3.3E+00	3.1E-01
278.0	2.8E+01	3.6E-02	3.3E+00	3.1E-01	3.3E+00	3.1E-01
279.0	2.8E+01	3.6E-02	3.3E+00	3.1E-01	3.3E+00	3.1E-01
280.0	2.8E+01	3.6E-02	3.3E+00	3.1E-01	3.3E+00	3.1E-01

Table A.18: Hashin-Shtrikman limits calculated for a dry, hydrated, and partially melted upper mantle from my reference model in Chapter 3.

Depth (km)	HSL^{33Ma}_{Wet}		HSU^{33Ma}_{Wet}		HSU^{1Ma}_{Melt}	
	(S/m)	(Ωm)	(S/m)	(Ωm)	(S/m)	(Ωm)
281.0	2.8E+01	3.6E-02	3.3E+00	3.1E-01	3.3E+00	3.1E-01
282.0	2.8E+01	3.6E-02	3.3E+00	3.1E-01	3.3E+00	3.1E-01
283.0	2.7E+01	3.6E-02	3.3E+00	3.1E-01	3.3E+00	3.1E-01
284.0	2.7E+01	3.6E-02	3.2E+00	3.1E-01	3.2E+00	3.1E-01
285.0	2.7E+01	3.7E-02	3.2E+00	3.1E-01	3.2E+00	3.1E-01
286.0	2.7E+01	3.7E-02	3.2E+00	3.1E-01	3.2E+00	3.1E-01
287.0	2.7E+01	3.7E-02	3.2E+00	3.1E-01	3.2E+00	3.1E-01
288.0	2.7E+01	3.7E-02	3.2E+00	3.1E-01	3.2E+00	3.1E-01
289.0	2.7E+01	3.7E-02	3.2E+00	3.1E-01	3.2E+00	3.1E-01
290.0	2.7E+01	3.7E-02	3.2E+00	3.1E-01	3.2E+00	3.1E-01
291.0	2.7E+01	3.7E-02	3.2E+00	3.1E-01	3.2E+00	3.1E-01
292.0	2.7E+01	3.7E-02	3.2E+00	3.1E-01	3.2E+00	3.1E-01
293.0	2.7E+01	3.7E-02	3.2E+00	3.1E-01	3.2E+00	3.1E-01
294.0	2.7E+01	3.7E-02	3.2E+00	3.1E-01	3.2E+00	3.1E-01
295.0	2.7E+01	3.7E-02	3.2E+00	3.1E-01	3.2E+00	3.1E-01
296.0	2.7E+01	3.7E-02	3.2E+00	3.1E-01	3.2E+00	3.1E-01
297.0	2.7E+01	3.7E-02	3.2E+00	3.1E-01	3.2E+00	3.1E-01
298.0	2.7E+01	3.7E-02	3.2E+00	3.1E-01	3.2E+00	3.1E-01
299.0	2.7E+01	3.7E-02	3.2E+00	3.1E-01	3.2E+00	3.1E-01
300.0	2.7E+01	3.7E-02	3.2E+00	3.1E-01	3.2E+00	3.1E-01
301.0	2.7E+01	3.7E-02	3.2E+00	3.1E-01	3.2E+00	3.1E-01
302.0	2.7E+01	3.7E-02	3.2E+00	3.1E-01	3.2E+00	3.1E-01
303.0	2.7E+01	3.7E-02	3.2E+00	3.1E-01	3.2E+00	3.1E-01
304.0	2.7E+01	3.8E-02	3.2E+00	3.1E-01	3.2E+00	3.1E-01
305.0	2.7E+01	3.8E-02	3.2E+00	3.1E-01	3.2E+00	3.1E-01
306.0	2.7E+01	3.8E-02	3.2E+00	3.1E-01	3.2E+00	3.1E-01
307.0	2.7E+01	3.8E-02	3.2E+00	3.1E-01	3.2E+00	3.1E-01
308.0	2.7E+01	3.8E-02	3.2E+00	3.1E-01	3.2E+00	3.1E-01
309.0	2.7E+01	3.8E-02	3.2E+00	3.1E-01	3.2E+00	3.1E-01
310.0	2.7E+01	3.8E-02	3.2E+00	3.1E-01	3.2E+00	3.1E-01
311.0	2.7E+01	3.8E-02	3.2E+00	3.1E-01	3.2E+00	3.1E-01
312.0	2.7E+01	3.8E-02	3.2E+00	3.1E-01	3.2E+00	3.1E-01
313.0	2.7E+01	3.8E-02	3.2E+00	3.1E-01	3.2E+00	3.1E-01
314.0	2.7E+01	3.8E-02	3.2E+00	3.1E-01	3.2E+00	3.1E-01
315.0	2.6E+01	3.8E-02	3.2E+00	3.1E-01	3.2E+00	3.1E-01
316.0	2.6E+01	3.8E-02	3.2E+00	3.1E-01	3.2E+00	3.1E-01
317.0	2.6E+01	3.8E-02	3.2E+00	3.1E-01	3.2E+00	3.1E-01
318.0	2.6E+01	3.8E-02	3.2E+00	3.1E-01	3.2E+00	3.1E-01
319.0	2.6E+01	3.8E-02	3.2E+00	3.1E-01	3.2E+00	3.1E-01
320.0	2.6E+01	3.8E-02	3.2E+00	3.1E-01	3.2E+00	3.1E-01

Table A.19: Hashin-Shtrikman limits calculated for a dry, hydrated, and partially melted upper mantle from my reference model in Chapter 3.

Depth (km)	HSL^{33Ma}_{Wet}		HSU^{33Ma}_{Wet}		HSU^{1Ma}_{Melt}	
	(S/m)	(Ωm)	(S/m)	(Ωm)	(S/m)	(Ωm)
321.0	2.6E+01	3.8E-02	3.2E+00	3.1E-01	3.2E+00	3.1E-01
322.0	2.6E+01	3.8E-02	3.2E+00	3.1E-01	3.2E+00	3.1E-01
323.0	2.6E+01	3.8E-02	3.2E+00	3.1E-01	3.2E+00	3.1E-01
324.0	2.6E+01	3.8E-02	3.2E+00	3.1E-01	3.2E+00	3.1E-01
325.0	2.6E+01	3.8E-02	3.2E+00	3.1E-01	3.2E+00	3.1E-01
326.0	2.6E+01	3.8E-02	3.2E+00	3.1E-01	3.2E+00	3.1E-01
327.0	2.6E+01	3.8E-02	3.2E+00	3.1E-01	3.2E+00	3.1E-01
328.0	2.6E+01	3.8E-02	3.3E+00	3.1E-01	3.3E+00	3.1E-01
329.0	2.6E+01	3.8E-02	3.3E+00	3.1E-01	3.3E+00	3.1E-01
330.0	2.6E+01	3.8E-02	3.3E+00	3.1E-01	3.3E+00	3.1E-01
331.0	2.6E+01	3.8E-02	3.3E+00	3.1E-01	3.3E+00	3.1E-01
332.0	2.6E+01	3.8E-02	3.3E+00	3.0E-01	3.3E+00	3.0E-01
333.0	2.6E+01	3.8E-02	3.3E+00	3.0E-01	3.3E+00	3.0E-01
334.0	2.6E+01	3.8E-02	3.3E+00	3.0E-01	3.3E+00	3.0E-01
335.0	2.6E+01	3.8E-02	3.3E+00	3.0E-01	3.3E+00	3.0E-01
336.0	2.6E+01	3.8E-02	3.3E+00	3.0E-01	3.3E+00	3.0E-01
337.0	2.6E+01	3.8E-02	3.3E+00	3.0E-01	3.3E+00	3.0E-01
338.0	2.6E+01	3.8E-02	3.3E+00	3.0E-01	3.3E+00	3.0E-01
339.0	2.6E+01	3.8E-02	3.3E+00	3.0E-01	3.3E+00	3.0E-01
340.0	2.6E+01	3.8E-02	3.3E+00	3.0E-01	3.3E+00	3.0E-01
341.0	2.6E+01	3.8E-02	3.4E+00	3.0E-01	3.4E+00	3.0E-01
342.0	2.6E+01	3.8E-02	3.4E+00	3.0E-01	3.4E+00	3.0E-01
343.0	2.6E+01	3.8E-02	3.4E+00	3.0E-01	3.4E+00	3.0E-01
344.0	2.6E+01	3.8E-02	3.4E+00	3.0E-01	3.4E+00	3.0E-01
345.0	2.6E+01	3.8E-02	3.4E+00	3.0E-01	3.4E+00	3.0E-01
346.0	2.6E+01	3.8E-02	3.4E+00	3.0E-01	3.4E+00	3.0E-01
347.0	2.6E+01	3.8E-02	3.4E+00	2.9E-01	3.4E+00	2.9E-01
348.0	2.6E+01	3.8E-02	3.4E+00	2.9E-01	3.4E+00	2.9E-01
349.0	2.7E+01	3.8E-02	3.4E+00	2.9E-01	3.4E+00	2.9E-01
350.0	2.7E+01	3.8E-02	3.4E+00	2.9E-01	3.4E+00	2.9E-01
351.0	2.7E+01	3.8E-02	3.4E+00	2.9E-01	3.4E+00	2.9E-01
352.0	2.7E+01	3.8E-02	3.4E+00	2.9E-01	3.4E+00	2.9E-01
353.0	2.7E+01	3.8E-02	3.5E+00	2.9E-01	3.5E+00	2.9E-01
354.0	2.7E+01	3.8E-02	3.5E+00	2.9E-01	3.5E+00	2.9E-01
355.0	2.7E+01	3.8E-02	3.5E+00	2.9E-01	3.5E+00	2.9E-01
356.0	2.7E+01	3.8E-02	3.5E+00	2.9E-01	3.5E+00	2.9E-01
357.0	2.7E+01	3.7E-02	3.5E+00	2.8E-01	3.5E+00	2.8E-01
358.0	2.7E+01	3.7E-02	3.5E+00	2.8E-01	3.5E+00	2.8E-01
359.0	2.7E+01	3.7E-02	3.6E+00	2.8E-01	3.6E+00	2.8E-01

Table A.20: Hashin-Shtrikman limits calculated for a dry, hydrated, and partially melted upper mantle from my reference model in Chapter 3.

Depth (km)	HSL^{33Ma}_{Wet}		HSU^{33Ma}_{Wet}		HSU^{1Ma}_{Melt}	
	(S/m)	(Ωm)	(S/m)	(Ωm)	(S/m)	(Ωm)
361.0	2.7E+01	3.7E-02	3.6E+00	2.8E-01	3.6E+00	2.8E-01
362.0	2.7E+01	3.7E-02	3.6E+00	2.8E-01	3.6E+00	2.8E-01
363.0	2.7E+01	3.7E-02	3.6E+00	2.8E-01	3.6E+00	2.8E-01
364.0	2.7E+01	3.7E-02	3.6E+00	2.8E-01	3.6E+00	2.8E-01
365.0	2.7E+01	3.7E-02	3.6E+00	2.7E-01	3.6E+00	2.7E-01
366.0	2.7E+01	3.7E-02	3.7E+00	2.7E-01	3.7E+00	2.7E-01
367.0	2.7E+01	3.7E-02	3.7E+00	2.7E-01	3.7E+00	2.7E-01
368.0	2.7E+01	3.7E-02	3.7E+00	2.7E-01	3.7E+00	2.7E-01
369.0	2.7E+01	3.7E-02	3.7E+00	2.7E-01	3.7E+00	2.7E-01
370.0	2.7E+01	3.7E-02	3.7E+00	2.7E-01	3.7E+00	2.7E-01
371.0	2.7E+01	3.7E-02	3.8E+00	2.7E-01	3.8E+00	2.7E-01
372.0	2.7E+01	3.7E-02	3.8E+00	2.7E-01	3.8E+00	2.7E-01
373.0	2.7E+01	3.7E-02	3.8E+00	2.6E-01	3.8E+00	2.6E-01
374.0	2.7E+01	3.7E-02	3.8E+00	2.6E-01	3.8E+00	2.6E-01
375.0	2.7E+01	3.7E-02	3.8E+00	2.6E-01	3.8E+00	2.6E-01
376.0	2.7E+01	3.6E-02	3.8E+00	2.6E-01	3.8E+00	2.6E-01
377.0	2.7E+01	3.6E-02	3.9E+00	2.6E-01	3.9E+00	2.6E-01
378.0	2.7E+01	3.6E-02	3.9E+00	2.6E-01	3.9E+00	2.6E-01
379.0	2.8E+01	3.6E-02	3.9E+00	2.6E-01	3.9E+00	2.6E-01
380.0	2.8E+01	3.6E-02	3.9E+00	2.6E-01	3.9E+00	2.6E-01
381.0	2.8E+01	3.6E-02	3.9E+00	2.5E-01	3.9E+00	2.5E-01
382.0	2.8E+01	3.6E-02	4.0E+00	2.5E-01	4.0E+00	2.5E-01
383.0	2.8E+01	3.6E-02	4.0E+00	2.5E-01	4.0E+00	2.5E-01
384.0	2.8E+01	3.6E-02	4.0E+00	2.5E-01	4.0E+00	2.5E-01
385.0	2.8E+01	3.6E-02	4.0E+00	2.5E-01	4.0E+00	2.5E-01
386.0	2.8E+01	3.6E-02	4.0E+00	2.5E-01	4.0E+00	2.5E-01
387.0	2.8E+01	3.6E-02	4.1E+00	2.5E-01	4.1E+00	2.5E-01
388.0	2.8E+01	3.6E-02	4.1E+00	2.5E-01	4.1E+00	2.5E-01
389.0	2.8E+01	3.6E-02	4.1E+00	2.4E-01	4.1E+00	2.4E-01
390.0	2.8E+01	3.6E-02	4.1E+00	2.4E-01	4.1E+00	2.4E-01
391.0	2.8E+01	3.6E-02	4.1E+00	2.4E-01	4.1E+00	2.4E-01
392.0	2.8E+01	3.6E-02	4.2E+00	2.4E-01	4.2E+00	2.4E-01
393.0	2.8E+01	3.6E-02	4.2E+00	2.4E-01	4.2E+00	2.4E-01
394.0	2.8E+01	3.6E-02	4.2E+00	2.4E-01	4.2E+00	2.4E-01
395.0	2.8E+01	3.6E-02	4.2E+00	2.4E-01	4.2E+00	2.4E-01
396.0	2.8E+01	3.6E-02	4.3E+00	2.4E-01	4.3E+00	2.4E-01
397.0	2.8E+01	3.5E-02	4.3E+00	2.3E-01	4.3E+00	2.3E-01
398.0	2.8E+01	3.5E-02	4.3E+00	2.3E-01	4.3E+00	2.3E-01
399.0	2.8E+01	3.5E-02	4.3E+00	2.3E-01	4.3E+00	2.3E-01
400.0	2.8E+01	3.5E-02	4.4E+00	2.3E-01	4.4E+00	2.3E-01

Appendix B

3-Dimensional Inversion Versus Depth

The electrical structure extracted from my 3-Dimensional inversion model beneath the coastline ρ_C, the Great Valley ρ_{GV}, and the Sierra Nevada batholith ρ_{SNB} in Chapter 5.

Table B.1: Electrical structure beneath the coastline ρ_C, the Great Valley ρ_{GV}, and the Sierra Nevada batholith ρ_{SNB}.

Depth (km)	σ_C (S/m)	ρ_C (Ωm)	σ_{GV} (S/m)	ρ_{GV} (Ωm)	σ_{SNB} (S/m)	ρ_{SNB} (Ωm)
0.2	1.2E-01	8.6E+00	5.6E-04	1.8E+03	1.5E-02	6.7E+01
0.5	2.3E-01	4.4E+00	5.8E-04	1.7E+03	1.9E-02	5.2E+01
0.8	3.8E-01	2.6E+00	6.0E-04	1.7E+03	2.5E-02	4.0E+01
1.2	4.8E-01	2.1E+00	6.2E-04	1.6E+03	1.9E-02	5.3E+01
1.5	4.2E-01	2.4E+00	6.2E-04	1.6E+03	1.1E-02	9.5E+01
1.9	2.3E-01	4.4E+00	5.8E-04	1.7E+03	5.5E-03	1.8E+02
2.3	8.4E-02	1.2E+01	5.2E-04	1.9E+03	3.2E-03	3.2E+02
2.7	2.5E-02	4.0E+01	4.4E-04	2.3E+03	2.1E-03	4.7E+02
3.1	7.1E-03	1.4E+02	3.6E-04	2.8E+03	1.7E-03	5.9E+02
3.6	2.3E-03	4.3E+02	2.9E-04	3.5E+03	1.4E-03	6.9E+02
4.1	9.3E-04	1.1E+03	2.3E-04	4.3E+03	1.3E-03	7.9E+02
4.6	4.8E-04	2.1E+03	2.0E-04	5.1E+03	1.1E-03	9.1E+02
5.2	3.2E-04	3.1E+03	1.7E-04	5.8E+03	9.3E-04	1.1E+03
5.8	2.5E-04	4.0E+03	1.6E-04	6.2E+03	7.7E-04	1.3E+03
6.4	2.2E-04	4.5E+03	1.5E-04	6.5E+03	6.5E-04	1.5E+03
7.0	2.1E-04	4.7E+03	1.5E-04	6.5E+03	5.6E-04	1.8E+03
7.7	2.1E-04	4.7E+03	1.6E-04	6.3E+03	5.0E-04	2.0E+03
8.4	2.2E-04	4.6E+03	1.7E-04	5.9E+03	4.5E-04	2.2E+03
9.1	2.3E-04	4.3E+03	1.9E-04	5.4E+03	4.1E-04	2.5E+03
9.8	2.4E-04	4.1E+03	2.1E-04	4.8E+03	3.7E-04	2.7E+03
10.6	2.5E-04	3.9E+03	2.5E-04	4.1E+03	3.4E-04	2.9E+03
11.4	2.6E-04	3.8E+03	3.0E-04	3.4E+03	3.2E-04	3.1E+03
12.2	2.7E-04	3.7E+03	3.7E-04	2.7E+03	2.9E-04	3.4E+03
13.1	2.8E-04	3.6E+03	4.8E-04	2.1E+03	2.7E-04	3.7E+03
14.0	2.9E-04	3.5E+03	6.3E-04	1.6E+03	2.5E-04	4.0E+03
14.9	3.0E-04	3.4E+03	8.6E-04	1.2E+03	2.3E-04	4.3E+03
15.9	3.1E-04	3.2E+03	1.2E-03	8.5E+02	2.2E-04	4.6E+03
16.9	3.3E-04	3.1E+03	1.6E-03	6.1E+02	2.1E-04	4.8E+03
18.0	3.6E-04	2.8E+03	2.3E-03	4.4E+02	2.1E-04	4.9E+03
19.1	4.1E-04	2.4E+03	3.2E-03	3.2E+02	2.1E-04	4.8E+03
20.2	4.9E-04	2.0E+03	4.3E-03	2.3E+02	2.2E-04	4.6E+03
21.4	6.3E-04	1.6E+03	5.9E-03	1.7E+02	2.3E-04	4.3E+03
22.6	8.5E-04	1.2E+03	7.8E-03	1.3E+02	2.7E-04	3.8E+03
23.9	1.2E-03	8.3E+02	1.0E-02	9.9E+01	3.2E-04	3.1E+03
25.3	1.8E-03	5.6E+02	1.3E-02	7.8E+01	4.1E-04	2.4E+03
26.6	2.6E-03	3.8E+02	1.6E-02	6.4E+01	5.7E-04	1.8E+03
28.1	3.9E-03	2.6E+02	1.9E-02	5.3E+01	8.2E-04	1.2E+03
29.6	5.6E-03	1.8E+02	2.2E-02	4.5E+01	1.2E-03	8.1E+02
31.2	7.6E-03	1.3E+02	2.6E-02	3.9E+01	1.9E-03	5.3E+02
32.8	9.9E-03	1.0E+02	3.0E-02	3.4E+01	2.8E-03	3.6E+02
34.5	1.2E-02	8.2E+01	3.4E-02	2.9E+01	3.9E-03	2.5E+02
36.2	1.4E-02	7.0E+01	4.0E-02	2.5E+01	5.2E-03	1.9E+02
38.1	1.6E-02	6.3E+01	4.8E-02	2.1E+01	6.4E-03	1.6E+02
40.0	1.7E-02	5.8E+01	5.8E-02	1.7E+01	7.2E-03	1.4E+02

Table B.2: Electrical structure beneath the coastline ρ_C, the Great Valley ρ_{GV}, and the Sierra Nevada batholith ρ_{SNB} (continued).

Depth (km)	σ_C (S/m)	ρ_C (Ωm)	σ_{GV} (S/m)	ρ_{GV} (Ωm)	σ_{SNB} (S/m)	ρ_{SNB} (Ωm)
41.9	1.8E-02	5.7E+01	6.8E-02	1.5E+01	7.4E-03	1.3E+02
44.0	1.7E-02	5.8E+01	7.8E-02	1.3E+01	7.2E-03	1.4E+02
46.1	1.6E-02	6.1E+01	8.1E-02	1.2E+01	6.6E-03	1.5E+02
48.3	1.5E-02	6.7E+01	7.6E-02	1.3E+01	5.9E-03	1.7E+02
50.7	1.3E-02	7.7E+01	6.5E-02	1.6E+01	5.2E-03	1.9E+02
53.1	1.1E-02	9.1E+01	5.0E-02	2.0E+01	4.5E-03	2.2E+02
55.6	8.9E-03	1.1E+02	3.6E-02	2.8E+01	3.8E-03	2.6E+02
58.2	7.1E-03	1.4E+02	2.5E-02	3.9E+01	3.2E-03	3.1E+02
60.9	5.6E-03	1.8E+02	1.8E-02	5.5E+01	2.7E-03	3.6E+02
63.7	4.5E-03	2.2E+02	1.3E-02	7.5E+01	2.4E-03	4.2E+02
66.6	3.7E-03	2.7E+02	1.0E-02	9.7E+01	2.1E-03	4.9E+02
69.6	3.2E-03	3.1E+02	8.3E-03	1.2E+02	1.8E-03	5.5E+02
72.8	2.8E-03	3.6E+02	7.0E-03	1.4E+02	1.7E-03	6.0E+02
76.1	2.5E-03	4.0E+02	6.1E-03	1.6E+02	1.5E-03	6.5E+02
79.5	2.3E-03	4.3E+02	5.6E-03	1.8E+02	1.4E-03	6.9E+02
83.1	2.2E-03	4.4E+02	5.3E-03	1.9E+02	1.4E-03	7.1E+02
86.8	2.2E-03	4.5E+02	5.3E-03	1.9E+02	1.4E-03	7.1E+02
90.6	2.3E-03	4.3E+02	5.5E-03	1.8E+02	1.5E-03	6.9E+02
94.6	2.5E-03	3.9E+02	6.1E-03	1.6E+02	1.6E-03	6.4E+02
98.8	2.9E-03	3.5E+02	7.2E-03	1.4E+02	1.7E-03	5.8E+02
103.5	3.4E-03	2.9E+02	9.0E-03	1.1E+02	2.0E-03	4.9E+02
109.1	4.5E-03	2.2E+02	1.2E-02	8.1E+01	2.5E-03	4.0E+02
115.8	6.4E-03	1.6E+02	1.9E-02	5.3E+01	3.4E-03	2.9E+02
123.9	1.0E-02	9.6E+01	3.3E-02	3.0E+01	5.3E-03	1.9E+02
133.5	2.0E-02	5.1E+01	6.8E-02	1.5E+01	9.1E-03	1.1E+02
145.2	3.7E-02	2.7E+01	1.3E-01	7.7E+00	1.5E-02	6.5E+01
159.1	4.8E-02	2.1E+01	1.5E-01	6.5E+00	2.0E-02	5.1E+01
175.8	3.4E-02	3.0E+01	8.7E-02	1.2E+01	1.5E-02	6.5E+01
195.9	2.0E-02	5.1E+01	4.3E-02	2.3E+01	1.0E-02	9.6E+01
220.0	1.1E-02	9.1E+01	2.1E-02	4.8E+01	6.7E-03	1.5E+02
248.9	7.1E-03	1.4E+02	1.3E-02	7.8E+01	4.8E-03	2.1E+02
283.6	5.3E-03	1.9E+02	8.9E-03	1.1E+02	3.8E-03	2.6E+02
325.2	4.1E-03	2.5E+02	6.3E-03	1.6E+02	3.1E-03	3.2E+02
375.2	3.6E-03	2.8E+02	5.2E-03	1.9E+02	2.9E-03	3.4E+02
435.2	4.2E-01	2.4E+00	5.3E-01	1.9E+00	3.4E-01	2.9E+00
507.1	2.8E-01	3.6E+00	3.7E-01	2.7E+00	2.4E-01	4.2E+00
593.4	2.8E-01	3.6E+00	3.7E-01	2.7E+00	2.4E-01	4.1E+00
697.0	1.4E+00	7.0E-01	1.7E+00	6.0E-01	1.4E+00	7.0E-01
821.4	1.4E+00	7.0E-01	1.7E+00	6.0E-01	1.4E+00	7.0E-01

Bibliography

Amante, C. and Eakins, B. (2009). ETOPO1 arc-minute global relief model: procedures, data sources and analysis. *NOAA Technical Memorandum NESDIS NGDC-24. 19*.

Ashour, A. (1950). The induction of electric currents in a uniform circular disk. *The Quarterly Journal of Mechanics and Applied Mathematics*, 3(1):119–128.

Baba, K., Chave, A., Evans, R., Hirth, G., and Mackie, R. (2006). Mantle dynamics beneath the East Pacific Rise at 17°S: Insights from the Mantle Electromagnetic and Tomography (MELT) experiment. *Journal of Geophysical Research: Solid Earth*, 111(B2).

Baba, K., Chen, J., Sommer, M., Utada, H., Geissler, W., Jokat, W., and Jegen, M. (2017a). Marine magnetotellurics imaged no distinct plume beneath the Tristan da Cunha hotspot in the southern Atlantic Ocean. *Tectonophysics*, 716:52–63.

Baba, K., Tada, N., Matsuno, T., Liang, P., Li, R., Zhang, L., Shimizu, H., Abe, N., Hirano, N., Ichiki, M., and Utada, H. (2017b). Electrical conductivity of old oceanic mantle in the northwestern Pacific I: 1-D profiles suggesting differences in thermal structure not predictable from a plate cooling model. *Earth, Planets and Space*, 69(1).

Baba, K., Utada, H., Goto, T., Kasaya, T., Shimizu, H., and Tada, N. (2010). Electrical conductivity imaging of the Philippine Sea upper mantle using seafloor magnetotelluric data. *Physics of the Earth and Planetary Interiors*, 183(1-2):44–62.

Bullard, E. and Parker, R. (1970). Electromagnetic induction in the oceans. *The Sea, IV, part I*, pages 695–730.

Cagniard, L. (1953). Basic theory of the magneto-telluric method of geophysical prospecting. *Geophysics*, 18(3):605–635.

Chapman, S. (1923). The influence of electrically conducting material within the Earth on various phenomena of terrestrial magnetism. *Trans. Camb. Phil. Soc.*, 22:463–482.

Chave, A., Jones, A., Mackie, R., and Rodi, W. (2012). *The Magnetotelluric Method*. Cambridge University Press.

Chesley, C., Key, K., Constable, S., Behrens, J., and MacGregor, L. (2019). Crustal cracks and frozen flow in oceanic lithosphere inferred from electrical anisotropy. *Geochemistry, Geophysics, Geosystems*, 20(12):5979–5999.

Constable, S. (2006). SEO3: a new model of olivine electrical conductivity. *Geophysical Journal International*, 166(1):435–437.

Constable, S. (2013). Review paper: Instrumentation for marine magnetotelluric and controlled source electromagnetic sounding. *Geophysical Prospecting*, 61:505–532.

Constable, S. and Heinson, G. (2004). Hawaiian hot-spot swell structure from seafloor MT sounding. *Tectonophysics*, 389(1-2):111–124.

Cox, C. (1981). On the electrical conductivity of the oceanic lithosphere. *Physics of the Earth and Planetary Interiors*, 25(3):196–201.

Cox, C., Constable, S., Chave, A., and Webb, S. (1986). Controlled-source electromagnetic sounding of the oceanic lithosphere. *Nature*, 320(6057):52–54.

Dasgupta, R., Hirschmann, M., and Smith, N. (2007). Water follows carbon: CO2 incites deep silicate melting and dehydration beneath mid-ocean ridges. *Geology*, 35(2):135.

Dasgupta, R., Hirschmann, M., and Stalker, K. (2005). Immiscible transition from carbonate-rich to silicate-rich melts in the 3 GPa melting interval of eclogite + CO2 and genesis of silica-undersaturated ocean island lavas. *Journal of Petrology*, 47(4):647–671.

Dawson, T. (1979). *Three-dimensional electromagnetic induction in thin sheets*. PhD thesis, University of Victoria.

Dawson, T. (1983). E-polarization induction in two thin half-sheets. *Geophysical Journal International*, 73(1):83–107.

Dawson, T., Weaver, J., and Raval, U. (1982). B-polarization induction in two generalized thin sheets at the surface of a conducting half-space. *Geophysical Journal International*, 69(1):209–234.

De Wet, J. (1949). *Numerical Methods of Solving Electromagnetic Induction Problems, with Applications to the Theory of Electric Currents Induced in the Oceans and Their Influence on Observed Geomagnetic Variations*. PhD thesis, University of London (Imperial College of Science and Technology).

Dietz, R. (1961). Continent and ocean basin evolution by spreading of the sea floor. *Nature*, 190(4779):854–857.

Evans, R., Hirth, G., Baba, K., Forsyth, D., Chave, A., and Mackie, R. (2005). Geophysical evidence from the MELT area for compositional controls on oceanic plates. *Nature*, 437(7056):249–252.

Fainberg, E. (1980). Electromagnetic induction in the world ocean. *Geophysical Surveys*, 4(1-2):157–171.

Ferguson, I., Filloux, J., Lilley, F., Bindoff, N., and Mulhearn, P. (1985). A seafloor magnetotelluric sounding in the Tasman Sea. *Geophysical Research Letters*, 12(9):545–548.

Filloux, J. (1977). Ocean-floor magnetotelluric sounding over North Central Pacific. *Nature*, 269(5626):297–301.

Filloux, J. (1981). Magnetotelluric exploration of the North Pacific: progress report and preliminary soundings near a spreading ridge. *Physics of the Earth and Planetary Interiors*, 25(3):187–195.

Filloux, J. (1982). Magnetotelluric experiment over the ROSE area. *Journal of Geophysical Research*, 87(B10):8364.

Filloux, J. (1983). Seafloor magnetotelluric soundings in the Mariana Island Arc area. In *The Tectonic and Geologic Evolution of Southeast Asian Seas and Islands: Part 2*, pages 255–265. American Geophysical Union.

Gaillard, F., Malki, M., Iacono-Marziano, G., Pichavant, M., and Scaillet, B. (2008). Carbonatite melts and electrical conductivity in the asthenosphere. *Science*, 322(5906):1363–1365.

Gallardo, L., Fontes, S., Meju, M., Buonora, M., and de Lugao, P. (2012). Robust geophysical integration through structure-coupled joint inversion and multispectral fusion of seismic reflection, magnetotelluric, magnetic, and gravity images: Example from Santos Basin, offshore Brazil. *Geophysics*, 77(5):B237–B251.

Gardés, E., Gaillard, F., and Tarits, P. (2014). Toward a unified hydrous olivine electrical conductivity law. *Geochemistry, Geophysics, Geosystems*, 15(12):4984–5000.

Geiermann, J. and Schill, E. (2010). 2-D Magnetotellurics at the geothermal site at Soultz-sous-Forêts: Resistivity distribution to about 3000m depth. *Comptes Rendus Geoscience*, 342(7-8):587–599.

Godfrey, N. and Klemperer, S. (1998). Ophiolitic basement to a forearc basin and implications for continental growth: The Coast Range/Great Valley ophiolite, California. *Tectonics*, 17(4):558–570.

Grayver, A., Munch, F., Kuvshinov, A., Khan, A., Sabaka, T., and Tøffner-Clausen, L. (2017). Joint inversion of satellite-detected tidal and magnetospheric signals constrains electrical conductivity and water content of the upper mantle and transition zone. *Geophysical Research Letters*, 44(12):6074–6081.

Hashin, Z. and Shtrikman, S. (1962). A variational approach to the theory of the effective magnetic permeability of multiphase materials. *Journal of Applied Physics*, 33(10):3125–3131.

Hasterok, D. (2013). A heat flow based cooling model for tectonic plates. *Earth and Planetary Science Letters*, 361:34–43.

Heezen, B. (1960). The rift in the ocean floor. *Scientific American*, 203(4):98–110.

Heinson, G. and Constable, S. (1992). The electrical conductivity of the oceanic upper mantle. *Geophysical Journal International*, 110(1):159–179.

Heinson, G., Constable, S., and White, A. (2000). Episodic melt transport at mid-ocean ridges inferred from magnetotelluric sounding. *Geophysical Research Letters*, 27(15):2317–2320.

Heinson, G. and Lilley, F. (1993). An application of thin-sheet electromagnetic modelling to the Tasman Sea. *Physics of the Earth and Planetary Interiors*, 81(1-4):231–251.

Heinson, G., White, A., Law, L., Hamano, Y., Utada, H., Yukutake, T., Segawa, J., and Toh, H. (1993). EMRIDGE: The electromagnetic investigation of the Juan de Fuca Ridge. *Marine Geophysical Researches*, 15(2):77–100.

Hess, H. (1962). History of ocean basins. In *Petrologic Studies*, pages 599–620. Geological Society of America.

Hirsch, L., Shankland, T., and Duba, A. (1993). Electrical conduction and polaron mobility in Fe-bearing olivine. *Geophysical Journal International*, 114(1):36–44.

Hirschmann, M. (2010). Partial melt in the oceanic low velocity zone. *Physics of the Earth and Planetary Interiors*, 179(1-2):60–71.

Hirschmann, M. (2018). Comparative deep Earth volatile cycles: The case for C recycling from exosphere/mantle fractionation of major (H2O, C, N) volatiles and from H2O/Ce, CO2/Ba, and CO2/Nb exosphere ratios. *Earth and Planetary Science Letters*, 502:262–273.

Hirschmann, M. and Dasgupta, R. (2009). The H/C ratios of Earth's near-surface and deep reservoirs, and consequences for deep Earth volatile cycles. *Chemical Geology*, 262(1-2):4–16.

Hirschmann, M., Ghiorso, M., Wasylenki, L., Asimow, P., and Stolper, E. (1998). Calculation of peridotite partial melting from thermodynamic models of minerals and melts. I. Review of methods and comparison with experiments. *Journal of Petrology*, 39(6):1091–1115.

Hirschmann, M., Tenner, T., Aubaud, C., and Withers, A. (2009). Dehydration melting of nominally anhydrous mantle: The primacy of partitioning. *Physics of the Earth and Planetary Interiors*, 176(1):54–68.

Holtzman, B. (2016). Questions on the existence, persistence, and mechanical effects of a very small melt fraction in the asthenosphere. *Geochemistry, Geophysics, Geosystems*, 17(2):470–484.

Jegen, M., Avdeeva, A., Berndt, C., Franz, G., Heincke, B., Hölz, S., Neska, A., Marti, A., Planert, L., Chen, J., Kopp, H., Baba, K., Ritter, O., Weckmann, U., Meqbel, N., and Behrmann, J. (2016). 3-D magnetotelluric image of offshore magmatism at the Walvis Ridge and rift basin. *Tectonophysics*, 683:98–108.

Jegen, M., Hobbs, R., Tarits, P., and Chave, A. (2009). Joint inversion of marine magnetotelluric and gravity data incorporating seismic constraints: Preliminary results of sub-basalt imaging off the Faroe Shelf. *Earth and Planetary Science Letters*, 282(1-4):47–55.

Junge, A. (1994). Induced telluric fields—new observations in North Germany and the Bramwald. Habilitation thesis. Göttingen.

Kapinos, G., Weckmann, U., Jegen-Kulcsar, M., Meqbel, N., Neska, A., Katjiuongua, T., Hoelz, S., and Ritter, O. (2016). Electrical resistivity image of the South Atlantic continental margin derived from onshore and offshore magnetotelluric data. *Geophysical Research Letters*, 43(1):154–160.

Karato, S. (2012). On the origin of the asthenosphere. *Earth and Planetary Science Letters*, 321-322:95–103.

Karato, S. (2014). Does partial melting explain geophysical anomalies? *Physics of the Earth and Planetary Interiors*, 228:300–306.

Karato, S. and Jung, H. (1998). Water, partial melting and the origin of the seismic low velocity and high attenuation zone in the upper mantle. *Earth and Planetary Science Letters*, 157(3-4):193–207.

Karato, S. and Jung, H. (2003). Effects of pressure on high-temperature dislocation creep in olivine. *Philosophical Magazine*, 83(3):401–414.

Katz, R., Spiegelman, M., and Langmuir, C. (2003). A new parameterization of hydrous mantle melting. *Geochemistry, Geophysics, Geosystems*, 4(9).

Kawakatsu, H., Kumar, P., Takei, Y., Shinohara, M., Kanazawa, T., Araki, E., and Suyehiro, K. (2009). Seismic evidence for sharp lithosphere-asthenosphere boundaries of oceanic plates. *Science*, 324(5926):499–502.

Key, K. (2003). *Application of broadband marine magnetotelluric exploration to a 3D salt structure and a fast-spreading ridge*. PhD thesis, Citeseer.

Key, K. and Constable, S. (2011). Coast effect distortion of marine magnetotelluric data: Insights from a pilot study offshore northeastern Japan. *Physics of the Earth and Planetary Interiors*, 184(3-4):194–207.

Key, K., Constable, S., Liu, L., and Pommier, A. (2013). Electrical image of passive mantle upwelling beneath the northern East Pacific Rise. *Nature*, 495(7442):499–502.

Key, K., Constable, S., Matsuno, T., Evans, R., and Myer, D. (2012). Electromagnetic detection of plate hydration due to bending faults at the Middle America Trench. *Earth and Planetary Science Letters*, 351-352:45–53.

Khan, A. (2016). On Earth's mantle constitution and structure from joint analysis of geophysical and laboratory-based data: An example. *Surveys in Geophysics*, 37(1):149–189.

Kirkby, A. and Heinson, G. (2017). Three-dimensional resistor network modeling of the resistivity and permeability of fractured rocks. *Journal of Geophysical Research: Solid Earth*, 122(4):2653–2669.

Kohlstedt, D. (2002). Partial melting and deformation. *Reviews in Mineralogy and Geochemistry*, 51(1):121–135.

Levander, A. and Miller, M. (2012). Evolutionary aspects of lithosphere discontinuity structure in the western U.S. *Geochemistry, Geophysics, Geosystems*, 13(7).

Lizarralde, D., Chave, A., Hirth, G., and Schultz, A. (1995). Northeastern Pacific mantle conductivity profile from long-period magnetotelluric sounding using Hawaii-to-California submarine cable data. *Journal of Geophysical Research: Solid Earth*, 100(B9):17837–17854.

Lowry, A. and Pérez-Gussinyé, M. (2011). The role of crustal quartz in controlling Cordilleran deformation. *Nature*, 471(7338):353–357.

Ludington, S., Moring, B., Miller, R., Flynn, K., Hopkins, M., Stone, P., Bedford, D., and Haxel, G. (2005). Preliminary integrated geologic map databases for the United States - western states: California, Nevada, Arizona, and Washington.

Mammerickx, J., Herron, E., and Dorman, L. (1980). Evidence for two fossil spreading ridges in the southeast Pacific. *Geological Society of America Bulletin*, 91(5):263–271.

MATLAB (2019). *9.7.0.1296695 (R2019b) Update 4*. The MathWorks Inc., Natick, Massachusetts.

Matsuno, T., Baba, K., and Utada, H. (2020). Probing 1-D electrical anisotropy in the oceanic upper mantle from seafloor magnetotelluric array data. *Geophysical Journal International*, 222(3):1502–1525.

Matsuno, T., Seama, N., Evans, R., Chave, A., Baba, K., White, A., Goto, T., Heinson, G., Boren, G., Yoneda, A., and Utada, H. (2010). Upper mantle electrical resistivity structure beneath the central Mariana subduction system. *Geochemistry Geophysics Geosystems*, 11(9).

Matthews, K., Müller, D., Wessel, P., and Whittaker, J. (2011). The tectonic fabric of the ocean basins. *Journal of Geophysical Research*, 116(B12).

McKenzie, D., Jackson, J., and Priestley, K. (2005). Thermal structure of oceanic and continental lithosphere. *Earth and Planetary Science Letters*, 233(3-4):337–349.

Mei, S. and Kohlstedt, D. (2000). Influence of water on plastic deformation of olivine aggregates: 1. Diffusion creep regime. *Journal of Geophysical Research: Solid Earth*, 105(B9):21457–21469.

Michaud, F., Royer, J., Bourgois, J., Dyment, J., Calmus, T., Bandy, W., Sosson, M., Mortera-Gutiérrez, C., Sichler, B., Rebolledo-Viera, M., and Pontoise, B. (2006). Oceanic-ridge subduction vs. slab break off: Plate tectonic evolution along the Baja California Sur continental margin since 15 Ma. *Geology*, 34(1):13.

Morley, L. and Larochelle, A. (1964). Palaeomagnetism as a means of dating geological events. In *Geochronology in Canada*, pages 39–51. University of Toronto Press.

Müller, D., Seton, M., Zahirovic, S., Williams, S., Matthews, K., Wright, N., Shephard, G., Maloney, K., Barnett-Moore, N., Hosseinpour, M., Bower, D., and Cannon, J. (2016). Ocean basin evolution and global-scale plate reorganization events since Pangea breakup. *Annual Review of Earth and Planetary Sciences*, 44(1):107–138.

Myer, D., Constable, S., and Key, K. (2013). Magnetotelluric evidence for layered mafic intrusions beneath the Vøring and Exmouth rifted margins. *Physics of the Earth and Planetary Interiors*, 220:1–10.

Naif, S., Key, K., Constable, S., and Evans, R. (2013). Melt-rich channel observed at the lithosphere–asthenosphere boundary. *Nature*, 495(7441):356–359.

Nolasco, R., Tarits, P., Filloux, J., and Chave, A. (1998). Magnetotelluric imaging of the Society Islands hotspot. *Journal of Geophysical Research: Solid Earth*, 103(B12):30287–30309.

Oldenburg, D., Whittall, K., and Parker, R. (1984). Inversion of ocean bottom magnetotelluric data revisited. *Journal of Geophysical Research: Solid Earth*, 89(B3):1829–1833.

Ostos, L. and Park, S. (2012). Foundering lithosphere imaged with magnetotelluric data beneath Yosemite National Park, California. *Geosphere*, 8(1):98–104.

Özaydın, S. and Selway, K. (2020). MATE: an analysis tool for the interpretation of magnetotelluric models of the mantle. *Geochemistry, Geophysics, Geosystems*, 21(9):e2020GC009126.

Poehls, K. and von Herzen, R. (1976). Electrical resistivity structure beneath the north-west Atlantic Ocean. *Geophysical Journal International*, 47(2):331–346.

Pommier, A., Kohlstedt, D., Hansen, L., Mackwell, S., Tasaka, M., Heidelbach, F., and Leinenweber, K. (2018). Transport properties of olivine grain boundaries from electrical conductivity experiments. *Contributions to Mineralogy and Petrology*, 173(5).

Pommier, A. and Le-Trong, E. (2011). "SIGMELTS": A web portal for electrical conductivity calculations in geosciences. *Computers & Geosciences*, 37(9):1450–1459.

Price, A. (1949). The induction of electric currents in non-uniform thin sheets and shells. *The Quarterly Journal of Mechanics and Applied Mathematics*, 2(3):283–310.

Pulkkinen, A., Klimas, A., Vassiliadis, D., Uritsky, V., and Tanskanen, E. (2006). Spatiotemporal scaling properties of the ground geomagnetic field variations. *Journal of Geophysical Research*, 111(A3).

Ranganayaki, R. (1978). *Generalized thin sheet approximation for magnetotelluric modelling.* PhD thesis, Massachusetts Institute of Technology.

Ranganayaki, R. and Madden, T. (1980). Generalized thin sheet analysis in magnetotellurics: an extension of Price's analysis. *Geophysical Journal International*, 60(3):445–457.

Reinke-Kunze, C. (1994). *Die Entstehung der Kontinente und Ozeane*, pages 53–71. Birkhäuser Basel, Basel.

Richards, F., Hoggard, M., Cowton, L., and White, N. (2018). Reassessing the thermal structure of oceanic lithosphere with revised global inventories of basement depths and heat flow measurements. *Journal of Geophysical Research: Solid Earth*, 123(10):9136–9161.

Ryan, W., Carbotte, S., Coplan, J., O'Hara, S., Melkonian, A., Arko, R., Weissel, R., Ferrini, V., Goodwillie, A., Nitsche, F., Bonczkowski, J., and Zemsky, R. (2009). Global multi-resolution topography synthesis. *Geochemistry, Geophysics, Geosystems*, 10(3).

Sarafian, E., Evans, R., Collins, J., Elsenbeck, J., Gaetani, G., Gaherty, J., Hirth, G., and Lizarralde, D. (2015). The electrical structure of the central Pacific upper mantle constrained by the NoMelt experiment. *Geochemistry, Geophysics, Geosystems*, 16(4):1115–1132.

Schmucker, U. (1973). Regional induction studies: A review of methods and results. *Physics of the Earth and Planetary Interiors*, 7(3):365–378.

Schnepf, N., Kuvshinov, A., and Sabaka, T. (2015). Can we probe the conductivity of the lithosphere and upper mantle using satellite tidal magnetic signals? *Geophysical Research Letters*, 42(9):3233–3239.

Schnepf, N., Manoj, C., Kuvshinov, A., Toh, H., and Maus, S. (2014). Tidal signals in ocean-bottom magnetic measurements of the northwestern Pacific: observation versus prediction. *Geophysical Journal International*, 198(2):1096–1110.

Selway, K. and O'Donnell, J. (2019). A small, unextractable melt fraction as the cause for the low velocity zone. *Earth and Planetary Science Letters*, 517:117–124.

Shankland, T. and Waff, H. (1977). Partial melting and electrical conductivity anomalies in the upper mantle. *Journal of Geophysical Research*, 82(33):5409–5417.

Simpson, F. and Bahr, K. (2005). *Practical magnetotellurics*. Cambridge University Press.

Sinha, M., Constable, S., Peirce, C., White, A., Heinson, G., MacGregor, L., and Navin, D. (1998). Magmatic processes at slow spreading ridges: implications of the RAMESSES experiment at 57° 45′N on the Mid-Atlantic Ridge. *Geophysical Journal International*, 135(3):731–745.

Sinha, M., Navin, D., MacGregor, L., Constable, S., Peirce, C., White, A., Heinson, G., and Inglis, M. (1997). Evidence for accumulated melt beneath the slow–spreading Mid–Atlantic Ridge. *Philosophical Transactions of the Royal Society of London. Series A: Mathematical, Physical and Engineering Sciences*, 355(1723):233–253.

Srivastava, S. (1965). Method of interpretation of magnetotelluric data when source field is considered. *Journal of Geophysical Research*, 70(4):945–954.

Stixrude, L. and Lithgow-Bertelloni, C. (2011). Thermodynamics of mantle minerals - II. Phase equilibria. *Geophysical Journal International*, 184(3):1180–1213.

Szarka, L. and Menvielle, M. (1997). Analysis of rotational invariants of the magnetotelluric impedance tensor. *Geophysical Journal International*, 129(1):133–142.

Tikhonov, A. (1950). On determining electric characteristics of the deep layers of the Earth's crust. *Dolk. Acad. Nauk. SSSR*, 73:295–297.

Tozer, B., Sandwell, D., Smith, W., Olson, C., Beale, J., and Wessel, P. (2019). Global bathymetry and topography at 15 arc sec: SRTM15+. *Earth and Space Science*, 6(10):1847–1864.

Trabant, C., Hutko, A., Bahavar, M., Karstens, R., Ahern, T., and Aster, R. (2012). Data products at the IRIS DMC: Stepping stones for research and other applications. *Seismological Research Letters*, 83(5):846–854.

Tyburczy, J. and Fisler, D. (2013). Electrical properties of minerals and melts. In *AGU Reference Shelf*, pages 185–208. American Geophysical Union.

Tyler, R., Boyer, T., Minami, T., Zweng, M., and Reagan, J. (2017). Electrical conductivity of the global ocean. *Earth, Planets and Space*, 69(1).

Umhoefer, P. (2011). Why did the Southern Gulf of California rupture so rapidly?—Oblique divergence across hot, weak lithosphere along a tectonically active margin. *GSA Today*, pages 4–10.

Vine, F. and Matthews, D. (1963). Magnetic anomalies over oceanic ridges. *Nature*, 199(4897):947–949.

Vozoff, K. (1991). The magnetotelluric method. In *Electromagnetic Methods in Applied Geophysics*, chapter 8, pages 641–712. Society of Exploration Geophysicists.

Wait, J. (1954). On the relation between telluric currents and the Earth's magnetic field. *Geophysics*, 19(2):281–289.

Wang, S., Constable, S., Reyes-Ortega, V., and Rychert, C. (2019). A newly distinguished marine magnetotelluric coast effect sensitive to the lithosphere–asthenosphere boundary. *Geophysical Journal International*, 218(2):978–987.

Wannamaker, P., Hasterok, D., Johnston, J., Stodt, J., Hall, D., Sodergren, T., Pellerin, L., Maris, V., Doerner, W., Groenewold, K., and Unsworth, M. (2008). Lithospheric dismemberment and magmatic processes of the Great Basin-Colorado Plateau transition, Utah, implied from magnetotellurics. *Geochemistry, Geophysics, Geosystems*, 9(5).

Wannamaker, P., Stodt, J., and Rijo, L. (1987). A stable finite element solution for two-dimensional magnetotelluric modelling. *Geophysical Journal International*, 88(1):277–296.

Weaver, J. (1994). *Mathematical methods for geo-electromagnetic induction*. Electronic & electrical engineering research studies. Applied and engineering mathematics series 7. Research Studies Press ; New York : Wiley, Taunton, Somerset, England.

Weaver, J. and Dawson, T. (1992). Adjustment distance in TM mode electromagnetic induction. *Geophysical Journal International*, 108(1):293–300.

Wegener, A. (1912). Die Entstehung der Kontinente. *Geologische Rundschau*, 3(4):276–292.

Weidelt, P. (1973). The inverse problem of geomagnetic induction. *Geophysical Journal International*, 35(1-3):379–379.

Wessel, P. and Smith, W. (1996). A global, self-consistent, hierarchical, high-resolution shoreline database. *Journal of Geophysical Research: Solid Earth*, 101(B4):8741–8743.

Wessel, P., Smith, W., Scharroo, R., Luis, J., and Wobbe, F. (2013). Generic mapping tools: Improved version released. *Eos, Transactions American Geophysical Union*, 94(45):409–410.

Williams, T. and Graham, S. (2013). Controls on forearc basin architecture from seismic and sequence stratigraphy of the Upper Cretaceous Great Valley Group, central Sacramento Basin, California. *International Geology Review*, 55(16):2030–2059.

Worzewski, T., Jegen, M., and Swidinsky, A. (2012). Approximations for the 2-D coast effect on marine magnetotelluric data. *Geophysical Journal International*, 189(1):357–368.

Yang, X., Keppler, H., McCammon, C., Ni, H., Xia, Q., and Fan, Q. (2011). Effect of water on the electrical conductivity of lower crustal clinopyroxene. *Journal of Geophysical Research*, 116(B4).

Yaxley, G., Anenburg, M., Tappe, S., Decree, S., and Guzmics, T. (2022). Carbonatites: Classification, sources, evolution, and emplacement. *Annual Review of Earth and Planetary Sciences*, 50(1).

Yoshino, T., Nishi, M., Matsuzaki, T., Yamazaki, D., and Katsura, T. (2008). Electrical conductivity of majorite garnet and its implications for electrical structure in the mantle transition zone. *Physics of the Earth and Planetary Interiors*, 170(3-4):193–200.

Yukutake, T., Filloux, J., , Segawa, J., Hamano, Y., and Utada, H. (1983). Preliminary report on a magnetotelluric array study in the northwest Pacific. *Journal of geomagnetism and geoelectricity*, 35(11/12):575–587.

Zandt, G., Gilbert, H., Owens, T., Ducea, M., Saleeby, J., and Jones, C. (2004). Active foundering of a continental arc root beneath the southern Sierra Nevada in California. *Nature*, 431(7004):41–46.

Zhang, B., Yoshino, T., Wu, X., Matsuzaki, T., Shan, S., and Katsura, T. (2012). Electrical conductivity of enstatite as a function of water content: Implications for the electrical structure in the upper mantle. *Earth and Planetary Science Letters*, 357-358:11–20.